

DISS. ETH NO. 29332

**SELF-ASSEMBLED ANTIMICROBIAL
AMYLOID-NANOCELLULOSE BIOHYBRIDS**

A thesis submitted to attain the degree of
DOCTOR OF SCIENCES of ETH ZÜRICH

(Dr. sc. ETH Zürich)

presented by

NICO KUMMER

MSc in Food Science, ETH Zürich

born on 13.09.1992

accepted on the recommendation of

Prof. Dr. Peter Fischer

Dr. Gustav Nyström

Prof. Dr. Lucio Isa

Prof. Dr. Wim Thielemans

2023

Copyright © 2023 Nico Kummer
All rights reserved.

Self-assembled Antimicrobial Amyloid-Nanocellulose Biohybrids

<https://doi.org/10.3929/ethz-b-000635622>

Laboratory of Food Process Engineering
Institute of Food, Nutrition and Health
Department of Health Sciences and Technology
ETH Zürich
Schmelzbergstrasse 9, 8092 Zürich, Switzerland

Printed in Switzerland by:
ETH Reprozentrale Hönggerberg
HIL C45
8093 Zurich
Switzerland

Acknowledgements

First and foremost, I would like to thank my supervisor Gustav Nyström for giving me the opportunity to pursue my doctoral studies at the Cellulose & Wood Materials Lab at Empa. Gustav, I cannot thank you enough for the support, encouragement and freedom you gave me, which helped me to become an independent scientist.

I would also like to thank my co-supervisor at Empa Silvia Camponi for her tireless guidance throughout my PhD journey. Silvia, thank you for introducing me to the world of amyloids and protein aggregation. Your mentorship has taught me a lot about determination and ethics in science.

I also want to express my appreciation to Peter Fischer for being my official doctoral supervisor at ETH and always helping with scientific or administrative problems. The environment and openness in your subgroup are great and allowed us to share the challenges we are facing, to complain and laugh about them and find solutions together. Many thanks also to Wim Thielemans and Lucio Isa for reading my thesis and being part of the examination committee.

I would like to acknowledge the support of my co-authors Tingting Wu, Kevin De France, Qun Ren, Flavia Zuber, Caroline Giacomini, Yashoda Chandorkar, Jean Schoeller and Ashutosh Sinha without which this thesis would not have been possible. I would also like to thank my students, Adrian Zeller, Luc Huguenin-Elie, Till Germerdonk and Philip Kneis for their great contribution.

Many thanks to the Cellulose & Wood Materials people at Empa for their scientific support, discussions, group meetings and of course all the lunches and after work beers. Special thanks go to my office mate Xavier Aeby for sweetening my days with

his excessive use of "gros mots" and Christopher Dreimol, for being an excellent conference co-organizer and friend.

Many thanks also to the Food Process Engineering and Sustainable Food Processing group for always welcoming me at ETH, especially because I often only came for their parties. Big thanks go to PeFi subgroup people, namely Pascal Bertsch, Jotam Bergfreund, Kim Mishra, Qiyao Sun, Caroline Giacomini, Natalie Nussbaum and Ciatta Wobill for creating a great atmosphere. Special thanks go to Daniela Peguero, for the ice creams at Eawag and for helping me with the organization of the defense party. Thanks also to Robert Axelrod for sharing Palestinian food and life discussions during lunch breaks.

I am deeply grateful to my roommates Toni, Braida, Fäbu, and Johanna, who supported me with their great company during the pandemic and endured my lows over the course of my doctoral journey.

I would like to thank my childhood friends, Nölu, Flöru, Chrigu, Dävu, Däru, Douni, Löru, and Mätthu, and high school friends, Alexei, Irina, Calum, Milica and Adriana, who all have always welcomed me back home since I left Bern more than ten years ago. Special thanks go to Marius Huber, for being there for me even though you were far away for a long time, really happy that we see each other more often now that you are back in Switzerland. I also need to thank Thomas Rüetschi for sharing his wisdom and giving me advice when I needed it.

Lastly, I would like to express my infinite gratitude to my parents for enabling me all of this. Thank you for your endless support, encouragement and for letting me go my way.

Nico Kummer, April 2023

Contents

Acknowledgements	I
Contents	III
Summary	IV
Zusammenfassung	VII
1 Introduction	1
1.1 Amyloids	3
1.1.1 Amyloid self-assembly	3
1.1.2 Lysozyme amyloid self-assembly	6
1.1.3 Antimicrobial activity of lysozyme and its aggregates	8
1.1.4 Amyloid self-assembly at interfaces	10
1.2 Nanocellulose	11
1.2.1 (Nano)-cellulose chemistry and structure	11
1.2.2 The colloidal properties of nanocellulose	13
1.2.3 Nanocellulose materials and their applications	19
1.2.4 Interactions between cellulose and proteins	19
2 Aims of the thesis	23
First-author publications	25
3 Self-assembly pathways and antimicrobial properties of lysozyme in different aggregation states	26
4 2D foam film coating of antimicrobial lysozyme amyloid fibrils onto cellulose nanopapers	61
5 Amyloid fibril-nanocellulose interactions and self-assembly	92
6 Discussion	126
6.1 Self-assembly in 1D, 2D and 3D	126
6.2 Antimicrobial activity of HEWL amyloids	133
7 Conclusion	135
8 Outlook	137
Selected co-authored publications	140
9 Nanocellulose-lysozyme colloidal gels via electrostatic complexation	141
10 Assembly of Cellulose Nanocrystal–Lysozyme Composite Films with Varied Lysozyme Morphology	170
11 Phase Behavior, Self-Assembly, and Adhesive Potential of Cellulose Nanocrystal–Bovine Serum Albumin Amyloid Composites	198
Bibliography	240
Curriculum Vitae	267

Summary

Amyloids derived from low-cost food proteins and nanocellulose from wood pulp are renewable and biodegradable materials with a wide range of potential applications, including water purification, biomaterials, and bioplastics. When amyloids are made from hen egg white lysozyme (HEWL), they exhibit a non-catalytic broad-spectrum antimicrobial activity based on their positive charge interacting with the negatively charged cell walls and cell membranes of microorganisms. Using disulfide bond reduction to induce self-assembly, colloidally stable amyloid-like, worm-shaped HEWL aggregates (worms) were produced and compared to amyloid fibrils made via an acid hydrolysis pathway. The aggregation kinetics of the HEWL worms was strongly pH-dependent, due to reduced double layer repulsion at higher pH, leading to large aggregates and sedimentation. The aggregation at pH 4.5 led to 1-dimensional worms and induced a structural transition from α -helices to β -sheets. Both HEWL worms and amyloid fibrils showed broad-spectrum antimicrobial activity against *Staphylococcus aureus*, *Escherichia coli*, and *Candida albicans*. Amyloid fibrils exhibit the strongest antimicrobial effect, due to their increased positive charge compared to native HEWL leading to stronger interactions with the negatively charged cell walls and cell membranes of the microorganisms and cell lysis.

The HEWL amyloid fibrils were coated onto TEMPO-oxidized cellulose nanofibril (TO-CNF) nanopapers using a coating mechanism based on the formation of 2D foam films. Exploiting the surface activity of proteins, a 2D foam film was pulled out of a HEWL amyloid fibril suspension using a loop, similar to the one used when blowing bubbles. To enhance the stability of the foam film, different concentrations and pH values of the amyloid suspension were tested. The foam stability was increased drastically at pH 6,

due to the deprotonation of the acidic amino acids, introducing negative charges and reducing the adsorption barrier caused by double layer repulsion. Using ultrafiltration, amyloid fibrils (40% of the protein mass) were separated from unconverted peptides (60%) and tested for their foam stability. It turned out that the unconverted peptides were the main species stabilizing the air-water interface, rather than the amyloid fibrils themselves. By depositing the 2D foam film onto various substrates, a uniform coating layer with a thickness of 30 nm was formed. This thickness was sufficient to produce a positively charged HEWL amyloid coating on negatively charged TO-CNF nanopapers. The coating showed a similar trend in terms of antimicrobial effect against the same pathogens (*S. aureus*, *E. coli* and *C. albicans*) tested before with the amyloid suspensions. However, the charge-mediated antimicrobial effect was not as strong due to the loss of surface area of the amyloid fibrils compressed into the coating layer. Overall, the foam film coating offers a facile method for the functionalization of TO-CNF nanopapers with antimicrobial HEWL amyloids, which could potentially be exploited for the production of wound dressing materials.

In order to enhance the mechanical properties of hybrid hydrogels, the colloidal interactions between amyloid fibrils and nanocellulose and their tunability was studied. Polyelectrolyte complexation was dominating the interactions between positively charged HEWL amyloids and negatively charged cellulose nanocrystals (CNCs), while negatively charged β -lactoglobulin (BLG) amyloids could be co-dispersed with CNCs. The complexation increased the elasticity of the amyloid network by cross-linking individual fibrils. Therefore, concentration-dependent rheological measurements were performed to fit elasticity-concentration scaling laws. The scaling of the elasticity with amyloid concentration was in good agreement with results from literature and theoretical models. The nanocellulose morphology contributes differently to elasticity: CNCs

cause amyloid bundling, while TO-CNFs add to a second network. Finally, a pH-mediated self-assembly approach was used to create homogeneous hydrogels made from HEWL and BLG amyloids in combination with nanocellulose. The mixing was done above the isoelectric point of the proteins, so they would be negatively charged and make stable co-dispersions with nanocellulose. Dialysis was used to reduce the pH to cross the isoelectric point, introducing positive charges on the amyloids and causing polyelectrolyte complexation and gelation. The type of nanocellulose morphology (CNCs or CNFs) did not significantly affect the elastic modulus in shear and compression tests, but hybrid gels with TO-CNFs displayed a higher dynamic yield point, enabling them to withstand greater deformations. These findings promote the understanding of amyloid fibril and nanocellulose interactions and offer valuable strategies for optimizing hybrid material assembly.

Overall, this thesis provides important insights on the self-assembly of HEWL aggregates and their co-assembly with nanocellulose. Due to the high sensitivity of proteins to pH changes, tuning the protonation of amyloid fibrils is the best way to control their self-assembly. With the knowledge gained from this thesis, the design of new hybrid materials based on amyloid fibrils and nanocellulose can be developed.

Zusammenfassung

Amyloide, die aus kostengünstigen Lebensmittelproteinen hergestellt werden und Nanocellulose aus Zellstoff, sind erneuerbare und biologisch abbaubare Materialien mit diversen potenziellen Anwendungsgebieten, darunter Wasserreinigung, Biomaterialien und Biokunststoffe. Amyloidfasern aus Hühnereiweiss-Lysozym (HEWL) haben eine nicht-katalytische antimikrobielle Wirkung gegen ein breites Spektrum von Mikroorganismen, die auf ihrer positiven Ladung beruht, welche mit den negativ geladenen Zellwänden und Zellmembranen von Mikroorganismen interagiert. Mit einem durch die Reduktion von Disulfidbindungen induzierten, supramolekularen Selbstorganisationsprozess wurden kolloidal stabile, amyloidähnliche, wurmförmige HEWL-Aggregate (worms) hergestellt und mit Amyloidfibrillen verglichen, die mittels einen Säurehydrolyseprozess hergestellt wurden. Die Aggregationskinetik der HEWL-Würmer war stark pH-abhängig, was auf eine verringerte Abstossung der elektrischen Doppelschicht bei höherem pH-Wert zurückzuführen ist und zu grossen Aggregaten und Sedimentation führt. Die Aggregation bei pH 4.5 führte zu eindimensionalen worms und induzierte einen strukturellen Übergang von α -Helices zu β -Faltblättern. Sowohl die HEWL-worms als auch die Amyloidfibrillen zeigten ein breites Spektrum an antimikrobieller Aktivität gegen *Staphylococcus aureus*, *Escherichia coli* und *Candida albicans*. Amyloidfibrillen hatten die stärkste antimikrobielle Wirkung, was auf ihre im Vergleich zu nativem HEWL erhöhte positive Ladung zurückzuführen ist, die zu stärkeren Wechselwirkungen mit den negativ geladenen Zellwänden und Zellmembranen der Mikroorganismen und zur Zellyse führt.

Die HEWL-Amyloidfibrillen wurden mit einem Beschichtungsmechanismus, der auf der Bildung von 2D-Schaumfilmen beruht, mit TEMPO-oxidierte Cellulose-Nanofibrillen

(TO-CNF) kombiniert. Die 2D-Schaumfilme konnten dank der Oberflächenaktivität der Proteine mit einem Plastikring aus einer HEWL-Amyloidfibrillen-Suspension gezogen werden, ähnlich wie beim Pusten von Seifenblasen. Um die Stabilität des Schaumfilms zu erhöhen, wurden verschiedene Konzentrationen und pH-Werte der Amyloidsuspension getestet. Die Schaumstabilität wurde bei einem pH-Wert von 6 drastisch erhöht, was auf die Deprotonierung der sauren Aminosäuren zurückzuführen ist, was negative Ladungen induziert und die durch die Doppelschichtabstoßung verursachte Adsorptionsbarriere verringern. Mittels Ultrafiltration wurden die Amyloidfibrillen (40 % der Proteinmasse) von den nicht umgewandelten Peptiden (60 %) getrennt und auf ihre Schaumstabilität getestet. Es stellte sich heraus, dass die nicht umgewandelten Peptide die Spezies waren, die die Luft-Wasser-Grenzfläche stabilisierten, und nicht die Amyloidfibrillen selbst. Durch das Auftragen des 2D-Schaumfilms auf verschiedene Substrate wurde eine einheitliche Beschichtung mit einer Dicke von 30 nm gebildet. Diese Dicke war ausreichend, um eine positiv geladene HEWL-Amyloidbeschichtung auf negativ geladenen TO-CNF-Nanopapieren zu erzeugen. Die Beschichtung zeigte einen ähnlichen Trend in Bezug auf die antimikrobielle Wirkung gegen die gleichen Krankheitserreger (*S. aureus*, *E. coli* und *C. albicans*), die zuvor mit den Amyloid-Suspensionen getestet wurden. Allerdings war die auf positiver Ladung beruhende antimikrobielle Wirkung aufgrund des Oberflächenverlusts der in der Beschichtungsschicht komprimierten Amyloidfibrillen nicht so stark. Insgesamt bietet die Schaumfilmbeschichtung eine einfache Methode für die Funktionalisierung von TO-CNF-Nanopapieren mit antimikrobiellen HEWL-Amyloiden, die möglicherweise für die Herstellung von Wundverbänden genutzt werden könnte.

Um die mechanischen Eigenschaften von Hybrid-Hydrogelen zu verbessern, wurden die kolloidalen Wechselwirkungen zwischen Amyloidfibrillen und Nanocellulose und

deren Beeinflussung durch äussere Parameter untersucht. Die Polyelektrolytkomplexierung dominierte die Wechselwirkungen zwischen positiv geladenen HEWL-Amyloiden und negativ geladenen Cellulose-Nanokristallen (CNCs), während negativ geladene β -Lactoglobulin (BLG)-Amyloide mit den CNCs co-dispergiert werden konnten. Die Komplexierung erhöhte die Elastizität des Amyloidnetzwerks durch die Vernetzung einzelner Fibrillen. Um den Zusammenhang zwischen der Elastizität der Hydrogele und der Konzentration zu verstehen wurden konzentrationsabhängige rheologische Messungen durchgeführt und Potenzgesetze aufgestellt. Die Skalierung der Elastizität mit der Amyloidkonzentration stand in guter Übereinstimmung mit Ergebnissen aus der experimentellen Literatur und theoretischen Modellen. Die Morphologie der Nanocellulose trägt unterschiedlich zur Elastizität bei: CNCs verursachen eine Amyloidbündelung, während TO-CNFs zu einem zweiten Netzwerk beitragen. Schliesslich wurde ein supramolekularer Selbstorganisationsprozess entwickelt, der durch die Veränderung des pH-Werts zu homogenen Hydrogelen aus HEWL- und BLG-Amyloiden in Kombination mit Nanocellulose führte. Das Mischen erfolgte oberhalb des isoelektrischen Punkts der Proteine, so dass sie negativ geladen waren und stabile Co-Dispersionen mit der Nanocellulose bildeten. Durch Dialyse wurde der pH-Wert so weit gesenkt, dass der isoelektrische Punkt überschritten wurde, wodurch die Amyloide positiv geladen wurden und eine Polyelektrolytkomplexierung und Gelierung stattfand. Die Art der Nanocellulose-Morphologie (CNCs oder CNFs) hatte keinen deutlichen Einfluss auf den Elastizitätsmodulus in Scher- und Drucktests, allerdings wiesen die Hybridgele mit TO-CNFs eine höhere dynamische Fließgrenze auf, wodurch sie grösseren Verformungen standhalten konnten. Diese Ergebnisse fördern das Verständnis der Wechselwirkungen zwischen Amyloidfibrillen und Nanocellulose und bieten wertvolle Strategien zur Optimierung des Aufbaus von Hybridmaterialien.

Insgesamt liefert diese Arbeit wichtige Erkenntnisse über die Selbstorganisation von HEWL-Aggregaten und deren Interaktionen mit Nanocellulose. Da Proteine sehr empfindlich auf pH-Änderungen reagieren, ist die Abstimmung der Protonierung von Amyloidfibrillen der beste Weg, um ihre Selbstorganisation zu kontrollieren. Mit den in dieser Arbeit gewonnenen Erkenntnissen kann das Design neuer Hybridmaterialien basierend auf Amyloidfibrillen und Nanocellulose entwickelt werden.

1 Introduction

The term self-assembly describes the autonomous arrangement of individual building blocks into higher-order structures [1]. Self-assembly occurs on multiple length scales ranging from individual molecules, to nano- and micrometer-sized particles, to macroscopic objects and even planets and solar systems forming galaxies [1,2]. Most systems from the molecular scale to the mesoscale can be considered static systems, that do not dissipate energy and tend to reduce the free energy of the system to reach a (meta)-stable equilibrium. The theory of self-assembly has been developed for molecular systems, however, there are several size-independent characteristics of a system enabling self-assembly, which are summarized in **Figure 1**.



Figure 1: Five characteristic factors in a system determining the ability to self-assemble.

The systems discussed in this thesis, consist of nanometer-sized building blocks (I) undergoing supramolecular self-assembly processes. The components undergoing self-assembly can be identical, of the same type (i.e. peptides or cellulose nanoparticles), or of different types (protein and cellulose) and interact (II) with each other because of their physicochemical properties. The interactions between the components are determined by the balance of attractive and repulsive forces. For nanoscale particles, these interactions are usually weak, of non-covalent nature (i.e. van der Waals

interactions, coulombic interactions, hydrogen bonding and hydrophobic interactions). The particles described in this thesis are dispersed in water as a solvent, which contains ions and has a pH, creating a tunable environment (III). The transport (IV) of the individual components is driven by Brownian motion, whereas gravitation and friction forces can be neglected for nanometer-sized particles. Since the interactions between the particles are weak (in the order of the thermal energy), bonds can easily be broken up and rearranged, granting the reversibility and adjustability of the self-assembly structures (V) [2].

When referring to the biological context, self-assembly processes played an essential role in the origin of life, forming vesicles filled with genetic information [3,4]. The biomolecules present in living systems (proteins, polysaccharides, DNA and lipids) self-assemble into different higher order structures within living cells, such as enzymatic complexes, cell walls, chromosomes and cell membranes. In the case of proteins, most newly synthesized chains undergo an intramolecular self-assembly process termed “protein folding” that is crucial to achieve their functional role [3,5]. The primary structure (amino acid sequence) of the polypeptide chain determines its ability to undergo intramolecular interactions leading to the formation of specific secondary structures, such as α -helices and β -sheets, and also tertiary structure, ultimately providing the protein its 3D shape and functionality. Supramolecular (intermolecular) self-assembly occurs when several subunits of the same protein or of different come together to form the quaternary structure of some proteins.

Protein folding is a tightly controlled process; yet, in some cases proteins can also misfold and aggregate, which is often connected to the onset of diseases [5,6]. Notorious examples of protein misfolding diseases are Alzheimer's and Parkinson's, in

which proteins in the brain of the affected patients undergo intermolecular self-assembly into so-called amyloid fibrils [7]. Amyloid fibrils share a common structure of antiparallel β -sheets oriented perpendicular to the fibril axis [8]. Apart from disease-related amyloids, examples of functional amyloids can be found in nature, such as curli fibers in biofilms produced by bacteria and even amyloids fulfilling metabolic functions in the human body [9]. In the following chapters laboratory-made, functional amyloid fibrils made from commercial food proteins will be introduced as a class of bio-based and bio-degradable nanomaterial. These amyloid fibrils are of high interest for the bottom-up assembly of new functional materials with different applications.

1.1 Amyloids

1.1.1 Amyloid self-assembly

Many proteins from various sources, such as milk, egg, blood plasma and plant proteins can be aggregated into amyloid fibrils under certain conditions, most commonly high temperature and low pH [10,11]. Under these conditions, the native proteins denature and undergo acid hydrolysis into short peptide fragments, some of which are able to self-assemble into amyloid fibrils. The term amyloid refers to protein aggregates with cross- β -sheet structure, i.e. stacks of antiparallel β -strands (peptides) arranged perpendicular to the fibril axis [8]. Their cross- β -sheet structure has been resolved by X-ray diffraction, showing interstrand distances of 4.8 Å, associated to N–H...O=C hydrogen bond length between individual peptides, and intersheet distances of around 10 Å, depending on how individual β -sheets are arranged (**Figure 2**) [8].

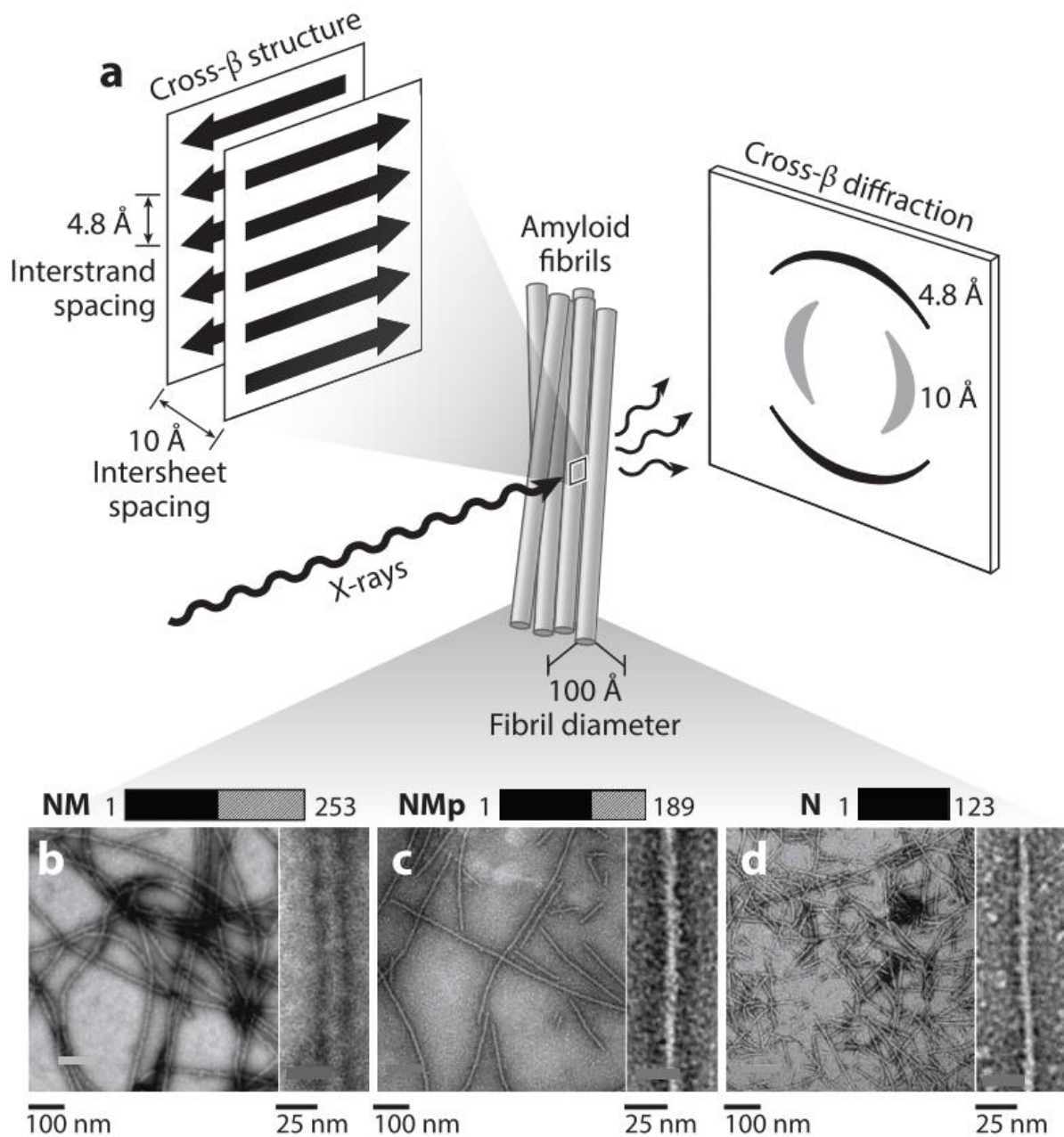


Figure 2: Amyloid aggregation of proteins results in the characteristic cross- β -sheet structure, causing the diffraction pattern associated to interstrand and intersheet spacings (a). The aggregation yields in semi-flexible fibrils (b-d). Figure reprinted with permission from [8].

Protein aggregation is governed by the balance of attractive and repulsive forces between the peptides [12]. Hydrogen bonding, van der Waals interactions, and the entropy gain of released hydration water (hydrophobic effect) promote the attraction of peptides. On the other hand, particularly when the aggregation takes place at low pH,

proteins are strongly positively charged, leading to double layer (electrostatic) repulsion. The repulsion between individual peptides results in a 1-dimensional aggregation rather than random aggregation into "amorphous" micrometer-sized flocs [11,13]. Ionic strength plays an important role in the regulation of the double layer repulsion and shorter more flexible fibrils are typically observed at higher ionic strength [14]. The aggregation kinetics of amyloid formation follow a nucleation-dependent polymerization process (**Figure 3**).

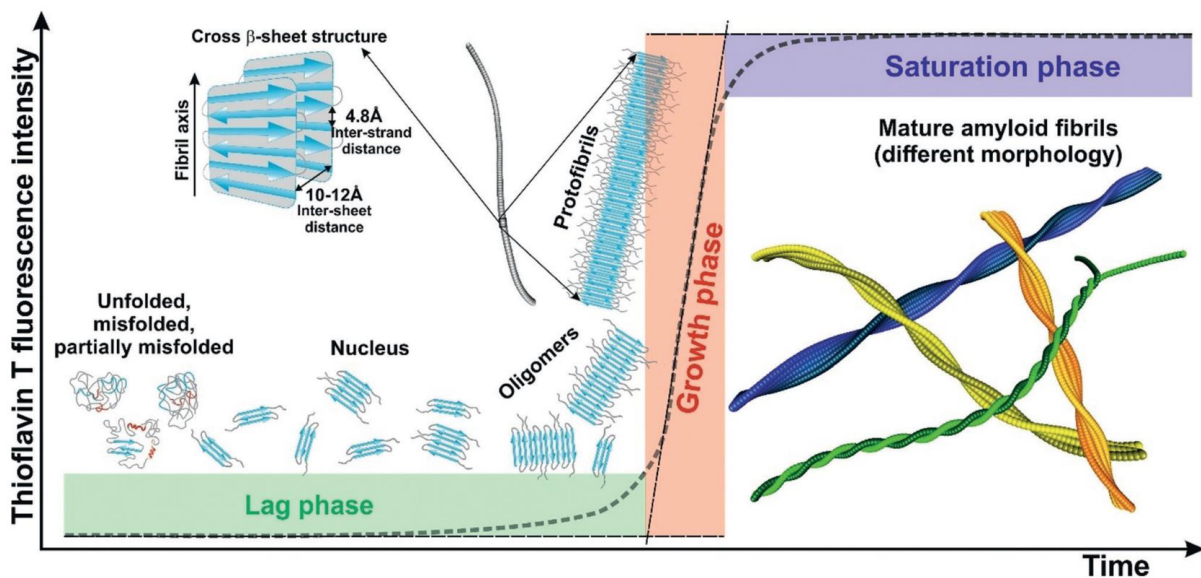


Figure 3: Aggregation kinetics of amyloid fibrils monitored by fluorescence spectroscopy using the amyloid-binding dye thioflavin T. The kinetics follow a typical sigmoidal curve, which can be divided into 3 phases. During the lag phase, denatured proteins nucleate aggregation into cross- β -sheet oligomers. In the growth phase these oligomers elongate to form protofibrils. Lateral assemblies of protofibrils, are present as different polymorphs in the saturation phase. Figure reprinted with permission from [15].

After a lag-phase, the formed oligomer nuclei elongate into fibrils until an equilibrium between fibrils and non-aggregated particles is reached [16,17]. The number concentration of the amyloid fibrils is determined by those processes leading to the formation

of new fibrils, such as primary nucleation (between two peptides), secondary nucleation (nucleation on existing aggregates) and fragmentation (the generation of more fibrils from an existing one) [16,18]. Knowles and co-workers developed a kinetic model including terms for nucleation, elongation, and fragmentation [19], which was extended by Azzari & Mezzenga to describe the influence of the nucleation and elongation rates on the contour length of amyloid fibrils. In short, the faster the nucleation rate, the higher the number concentration of fibrils and the shorter the contour length of the emerging amyloid fibrils [20]. Higher initial protein concentration, higher pH and increased ionic strength decrease the persistence length of amyloid fibrils due to less or no hydrolysis and faster, less ordered aggregation [14,21,22]. Amyloid protofibrils further assemble laterally into polymorphs, such as twisted and helical ribbons and nanotubular shapes [15].

In summary, the acid hydrolysis mediated aggregation into amyloid fibrils, depends mostly on protein concentration, pH, ionic strength and temperature. There are also other mechanisms which can denature proteins and induce the formation of amyloids, namely, disulfide bond reduction by reducing agents (dithiothreitol (DTT) and tris(2-carboxyethyl)phosphine (TCEP)), organic solvents (ethanol, trifluoroethanol), chaotropic agents (guanidine hydrochloride, urea), proteolytic enzymes (trypsin, papain) and harsh mechanical treatments (shear flow, ultrasonication) [11].

1.1.2 Lysozyme amyloid self-assembly

After the discovery of a rare disease related to the aggregation of mutated human lysozyme into amyloid fibrils, more intense research of the amyloid self-assembly of lysozyme was initiated [23]. Similar to other proteins, the aggregation of hen egg white

lysozyme (HEWL) at low pH and high temperatures (after acid hydrolysis into peptides) was observed (**Figure 4**) [24–26].

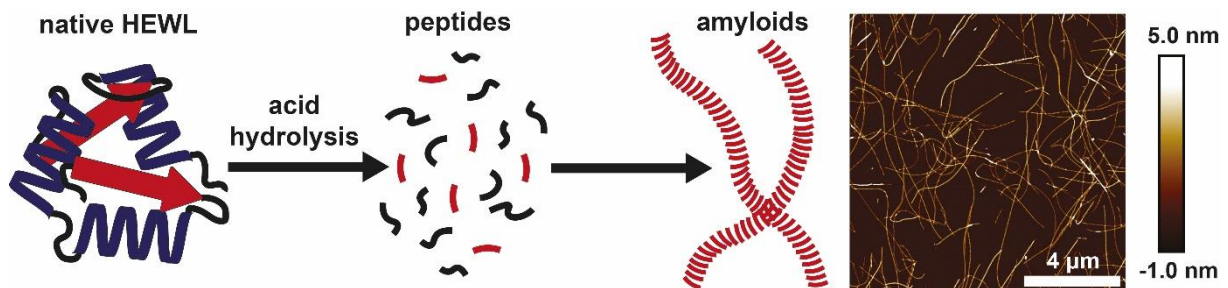


Figure 4: Illustration of the acid hydrolysis pathway cleaving the native protein into short peptides, of which the amyloidogenic fraction converts into semi-flexible, micrometer-long amyloid fibrils.

While the aggregation kinetics at 57-65 °C were in the order of several days [24,25], Lara and co-workers obtained semi-flexible amyloid fibrils (with persistence length of around 1 μm) within 24 hours when heating the protein solution to 90 °C [27]. As described before for β-lactoglobulin (BLG) amyloid fibrils [15,28,29], the HEWL amyloids showed lateral aggregation into twisted and helical ribbons, and even nanotubes, depending on the number of protofilaments [27,30]. HEWL amyloid fibrils obtained by acid hydrolysis have shown excellent biocompatibility [31] and antimicrobial properties [32], and have been used for other applications [33].

As mentioned above, acid hydrolysis is the most common path taken to form lysozyme amyloids, however, there are other possibilities. Yang and co-workers used the reducing agent tris(2-carboxyethyl)phosphine (TCEP) to destabilize the native structure of HEWL by disulfide bond reduction, which resulted in the formation of amyloid-like aggregates with increased β-sheet structure [34,35] (**Figure 5**).

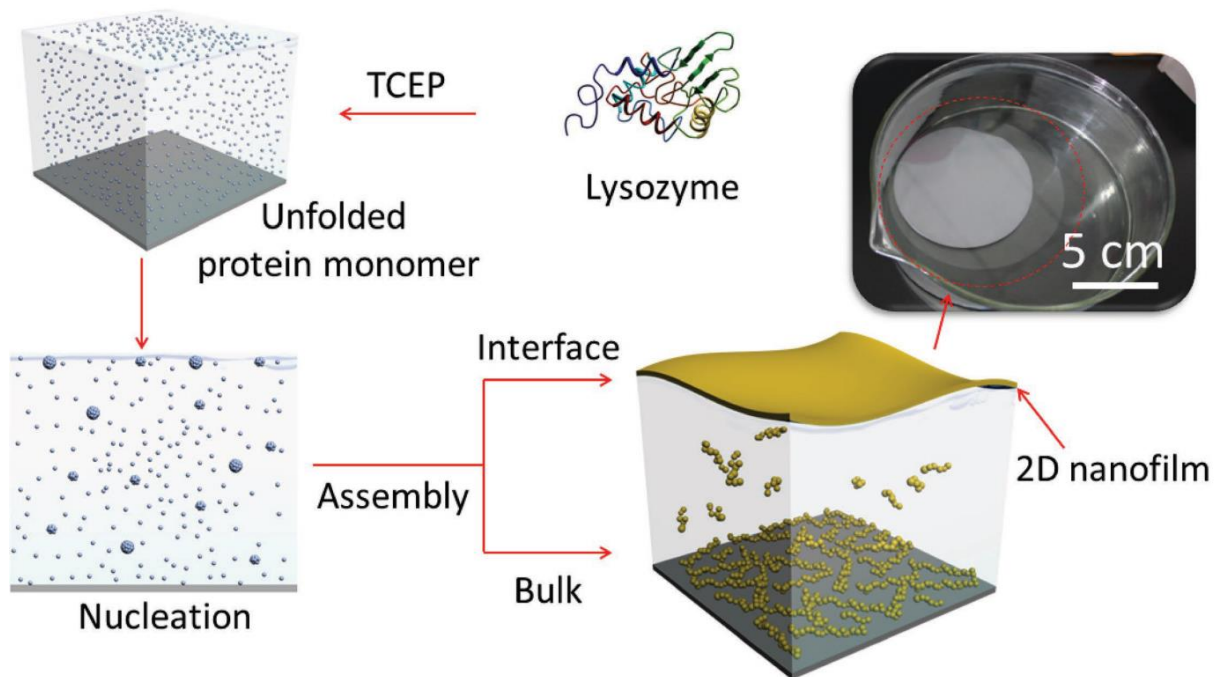


Figure 5: Illustration of the amyloid-like aggregation pathway of HEWL induced by disulfide bond reduction using the reducing agent TCEP. The amyloid-like aggregates adsorb at the air-water interface forming a stable film, while bulk aggregates grow large in size and sediment. Reprinted with permission from [36].

Small HEWL aggregates produced in this way adsorb at the air-water and solid-water interfaces forming an interfacial film, while larger aggregates precipitate. Such interfacial adsorption of HEWL aggregates has been used to coat various materials (polymers, glass, ceramics, metal) and introduce different functionalities including antimicrobial activity [35,37–39]. Due to the lack of a clear fibrillary morphology, the HEWL aggregates were called "amyloid-like" and "phase-transited lysozyme". In contrast to semi-flexible peptide-based amyloids, the amyloid-like aggregates formed with TCEP lacked colloidal stability and therefore the possibility for use in bottom-up assembly.

1.1.3 Antimicrobial activity of lysozyme and its aggregates

At the beginning of the 20th century, the Russian scientist Lashchenko first reported a "germ-killing" effect of hen egg white [40]. Nobody less than the later discoverer of

Penicillin, Scottish physician Alexander Fleming, reported a "remarkable bacteriolytic element" in human secretions and tissues in 1922 [41]. Due to its activity being similar to other "ferments" (enzymes), he named this substance lysozyme. The structure of lysozyme (129 amino acids, 14.3 kDa) was the second protein structure resolved by X-ray diffraction by Blake and co-workers in 1965 [42]. Due to its abundance in hen egg white, facile extraction, known structure and antimicrobial properties, lysozyme has become one of the most studied model proteins [43,44].

The antimicrobial activity of lysozyme originates from the enzymatic catalysis of the hydrolytic degradation of the β -(1,4) glycosidic bonds in the peptidoglycan cell walls of Gram-positive bacteria [44–46]. Peptidoglycan is the main polysaccharide in the cell walls of bacteria, composed of the monomers N-acetylmuramic acid (NAM) and N-acetylglucosamine (NAG) linked by β -(1,4) glycosidic bonds [46]. In Gram-positive bacteria the cell membrane is surrounded by the peptidoglycan cell wall, which can be disrupted by lysozyme, resulting in cell death. Instead, Gram-negative bacteria are insensitive to lysozyme, since their cell wall is physically protected by an outer cell membrane. However, in addition to the enzymatic catalysis of peptidoglycan hydrolysis, lysozyme exhibits a non-enzymatic antimicrobial effect on bacteria [44]. Several studies have shown antimicrobial activity of thermally and chemically denatured as well as mutated forms of lysozyme lacking the active site [37,47–50]. In some cases broadening of the antimicrobial spectrum to Gram-negative bacteria and even yeasts has been reported [37,50]. The non-catalytic mode of antimicrobial activity can be linked to the high abundance of positively charged amino acids in the primary sequence of lysozyme (isoelectric point = 11), which undergo electrostatic interactions with the negatively charged cell walls and membranes, making the membrane permeable and causing cell lysis due to osmotic stress [44,48,49]. Another factor promoting membrane permeability, is the exposure of hydrophobic residues of lysozyme enabling integration and pore

formation in the microbial membranes [37,47,51]. Antimicrobial activity as a consequence of positive charge and amphiphilic properties is also common in antimicrobial peptides [52,53] and cationic polymers [54]. Similarly, lysozyme amyloid fibrils [32,55–59], and amyloid-like lysozyme [37,38,60,61] have a broad-spectrum antimicrobial effect, underlying the same mode of action.

1.1.4 Amyloid self-assembly at interfaces

In general, proteins are surface active particles due to their amphiphilic nature, which arises from the diversity in the chemical functionalities of the amino acid building blocks [62,63]. In the case of amyloids, the ability of self-assembly at interfaces is highly relevant for two reasons: i) triggering amyloid aggregation due to protein unfolding and locally high concentrations at interfaces, and ii) the use of amyloid fibrils to stabilize interfaces in multiphase systems, such as emulsions and foams. As for all proteins, the driving force behind adsorption of amyloid fibrils at interfaces is the overall decrease in free energy in the system, dominated by the entropic component (release of unfavorably trapped water molecules both from hydrophobic patches of the adsorbing amyloids and from the air-water interface) [63]. When native proteins adsorb at interfaces, they may undergo structural changes [63]. The adsorption of protein at interfaces leads to a local increase in concentration, making interactions between individual proteins more likely to occur and leading to the formation of interfacial layers that can behave like 2D networks or granular layers (in the case of less denatured proteins). Lysozyme is a highly stable globular protein and forms weak interfacial layers. However, if the denaturation of lysozyme at the interface is further promoted by disulfide bond reduction, more stable interfacial layers form [36,64].

For some proteins under specific conditions, the formation of amyloid fibrils can be triggered by the presence of interfaces. This is especially relevant for disease-related amyloid fibrils, such as those formed by the amyloid- β peptide and by α -synuclein, that can form at the interface with lipid membranes of cells [65,66]. Similar results of triggering aggregation or accelerating aggregation kinetics, have been found for solid-water [66,67], oil-water [68,69], and air-water interfaces [70–72].

Pre-formed BLG amyloid fibrils can adsorb and self-assemble into 2D liquid crystalline domains at fluid interfaces under the right conditions (pH) and after removal of unconverted peptides [73–75]. The double layer repulsion between individual amyloid fibrils prevents the overlap of fibrils and, in order to reduce the excluded volume, the amyloid fibrils align and form highly elastic interfacial films [75]. Yet, for amyloid fibrils made from soy glycinin, the adsorption at the air-water interface was dominated by the unconverted peptide fraction rather than the amyloid fibrils [76].

1.2 Nanocellulose

1.2.1 (Nano)-cellulose chemistry and structure

Cellulose is a renewable and bio-degradable, light-weight and mechanically strong polymer. It is the main component of the cell walls of plants and therefore the most abundant polymer on the planet. Due to its abundance and low cost, cellulose from different sources (wood, cotton, linen, hemp, etc.) has been used by humankind for thousands of years [77–79]. The building block of the cellulose molecular chains is composed of two anhydroglucose units connected through β -(1,4) glycosidic bonds. During cellulose biosynthesis, the individual polymer chains self-assemble into H-bonded bundles, so called cellulose microfibrils, which in turn are the building blocks of larger cellulose

fibrils that provide structure to the plant cell walls [77]. Cellulose assembles into highly ordered, crystalline stacks of polymeric chains, but also contains less ordered (sometimes called amorphous) regions, which are more flexible (**Figure 6**).

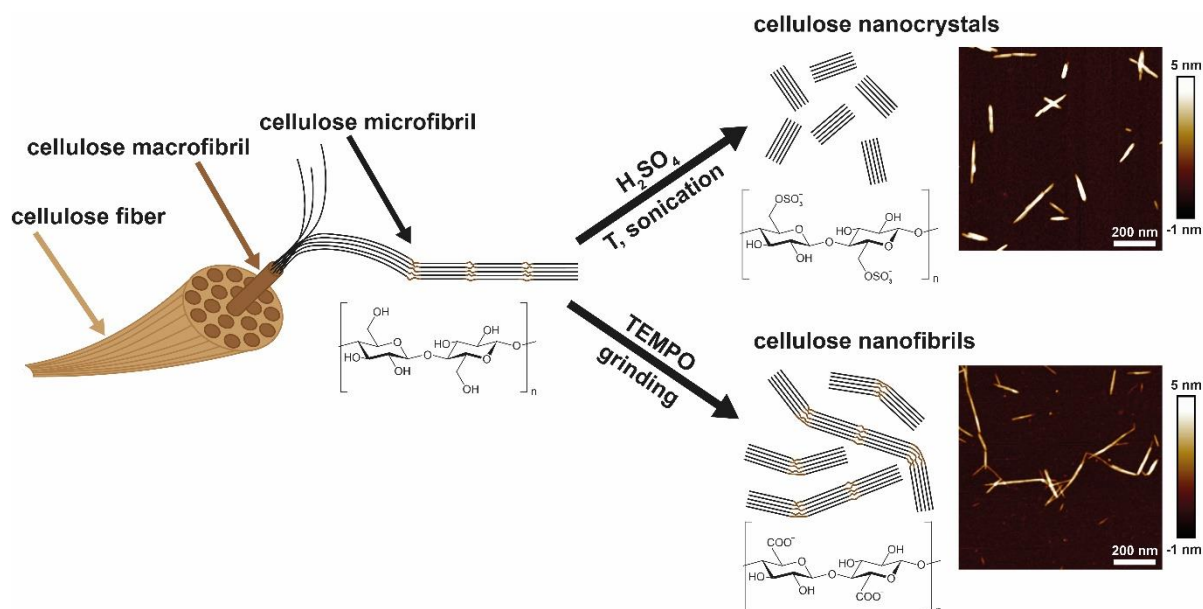


Figure 6: Hierarchical structure of cellulose: cellulose fibers are the structural element of plant cell walls and consist of cellulose fibrils, which are bundles of cellulose nanofibrils. The nanofibrils contain ordered (crystalline) and unordered (amorphous) regions. Depending on the treatment of the nanocellulose, cellulose nanocrystals (acid hydrolysis) or cellulose nanofibrils (TEMPO-oxidation and mechanical treatments) can be isolated and observed by atomic force microscopy.

Nanocelluloses (NC), i.e. cellulose particles with dimensions in the nanoscale, can be isolated from various sources of biomass (wood, cotton, linen, hemp, etc.). There are two common treatments for isolation, acid hydrolysis of the amorphous cellulose to obtain cellulose nanocrystals (CNCs) and mechanical grinding yielding cellulose nanofibrils (CNFs). In both cases the introduction of negatively charged functional groups promotes the isolation process and colloidal stability of the emerging particles [80]. For CNCs the sulfuric acid hydrolysis has become the standard method, introducing sulfate

half-esters on the CNC surface [81]. CNFs instead are usually stabilized by the introduction of carboxylic groups, for instance by TEMPO (2,2,6,6-tetramethylpiperidine-1-oxyl radical)-mediated oxidation (leading to so called TO-CNFs) [82] or carboxymethylation (leading to so-called CM-CNFs) [83]. The hydroxyl groups of the cellulose offer numerous other possibilities for chemical functionalization, as summarized by Habibi [84]. Positively charged CNFs can also be obtained using 2,3-epoxypropyltrimethylammonium chloride (EPTMAC) [85]. The etherification of cellulose with EPTMAC through nucleophilic addition of the cellulose hydroxyl groups to the epoxy group of EPTMAC proceeds under alkaline conditions [86].

1.2.2 The colloidal properties of nanocellulose

The colloidal properties of nanocellulose systems have been summarized in the review paper of the same title as this section, co-authored with Bensefelt and co-workers [80]. The DLVO theory was developed by Derjaguin, Landau, Verwey, and Overbeek in the 1940s and describes the colloidal interactions between dispersed nanoparticles [63,87]. On the nanometer scale the gravitation and inertia experienced by the particles can be neglected and colloidal forces dominate the system. The DLVO theory describes the balance between van der Waals attraction and the repulsion caused by overlapping electrical double layers (dense counter-ion clouds surrounding charged particles), which determines the colloidal stability of the aqueous dispersion [87]. The van der Waals attraction is described by Hamaker [88], introducing a Hamaker constant A to calculate the force F between two spherical particles of the radius R separated by a distance D :

$$F(D) = \frac{-AR}{12D}$$

The Hamaker constant is a measure of the average electrodynamic properties determined by the dielectric constants of the dispersed material and the solvent.

The repulsive forces between the dispersed particles originate in the overlap of electrical double layers, leading to an increased local salt concentration between the particles [87]. The counter-ions in the electrical double layer are confined by the surface potential of the particles and thus the only possibility to reduce this entropically unfavorable high ion concentration is the inflow of water between the particles resulting in their separation. In literature, the term electrostatic repulsion is often used as a synonym for double layer repulsion. The DLVO theory includes a term for the repulsion force F between two charged spherical particles separated by a distance D [87].

$$W(D) = \frac{64\pi k_B T R \rho_\infty \gamma^2}{\kappa^2} \exp(-\kappa D)$$

With k_B being the Boltzmann constant, T the temperature, ρ_∞ the number density of ions in the bulk and γ the reduced surface potential defined as:

$$\gamma = \tanh\left(\frac{ze\psi_0}{4k_b T}\right)$$

With z denominating the valence, e the elementary charge and ψ_0 the potential at the particle surface. The Debye length κ^{-1} describes the decay of the surface potential as a function of ionic strength I :

$$\kappa^{-1} = \sqrt{\frac{\varepsilon_0 \varepsilon_r k_b T}{2e^2 N_A I}} = \frac{0.3nm}{\sqrt{I}}$$

With ε_0 the permittivity in vacuum, and ε_r the relative permittivity of the electrolyte, N_A the Avogadro constant. The ionic strength of the solvent is defined as:

$$I = \frac{1}{2} \sum_i z_i^2 c_i$$

The ionic strength takes into account the valence and ionic concentration c_i of each ionic species i . Expressing the Debye length as a function of I , demonstrates the importance of the electrolyte concentration with respect to the double layer repulsion [89]. At a distance from the charged surface corresponding to the Debye length the electric potential is decreased by $1/e$, due to charge screening.

Under ideal conditions and at low enough concentration, suspensions of nanocellulose (CNCs and TO-CNFs) consist of perfectly isolated particles, due to the strong double layer repulsion originating from the negative functional groups on the surface of the particles. If the concentration is increased the nanocellulose particles will start interacting with each other. Two highly relevant modes of interaction for nanocelluloses are i) network formation determining the properties of nanocellulose gel [90], which are often the starting point for materials design, and ii) liquid crystalline phase transition, resulting in photonic structures [91].

Nanocelluloses, especially CNF, form networks at very low concentrations [90,92,93]. These networks can be considered interlocked systems of fibrils affecting each other over large distances in series of connections. This network formation property is highly dependent on the aspect ratio a of the fibrils, which is defined as the ratio between the length L and the diameter d of the individual particles [94].

$$a = \frac{L}{d}$$

Nanocellulose suspension can be described using the crowding factor N_{3D} , as a function of volume fraction φ and aspect ratio.

$$N_{3D} = \frac{2}{3}\varphi a^2$$

The crowding factor defines the number of particles taking up a spherical volume having the same diameter as the length of the rods [94]. Once the crowding factor exceeds

1, the spherical volumes of rotating nanocellulose rods start to overlap (3D overlap) and the probability of interactions and restrictions is increased (Figure 7) [95]. This results first in increased viscosity and, once the crowding factor reaches 16, in a transition from a Newtonian fluid to a viscoelastic rheological behavior [93]. After further increasing the crowding factor to around 60, percolated networks form with 3 contacts per fibril [96]. At this point the fibrils are still able to rotate freely in a 2D disc and translate parallel. Finally, in concentrated regimes with crowding factors higher than 200, the 2D overlap concentration is reached, which results in so called volume-arrested states (VAS) with a solid behavior [90]. It is important to point out that the nanocellulose particles still form a repulsive network, which should be referred to as colloidal glasses, rather than gels (as it is often done both colloquially and in literature). Gels are systems in which there is attraction between individual particles, which leads to aggregation [97]. Gelation is normally induced by lowering the pH to protonate the negatively charged functional groups or by increasing the ionic strength by adding salt. Typically, the VAS occurs at concentrations of around 1 wt% for CNFs, whereas 8 wt% are required for CNCs [90,93].

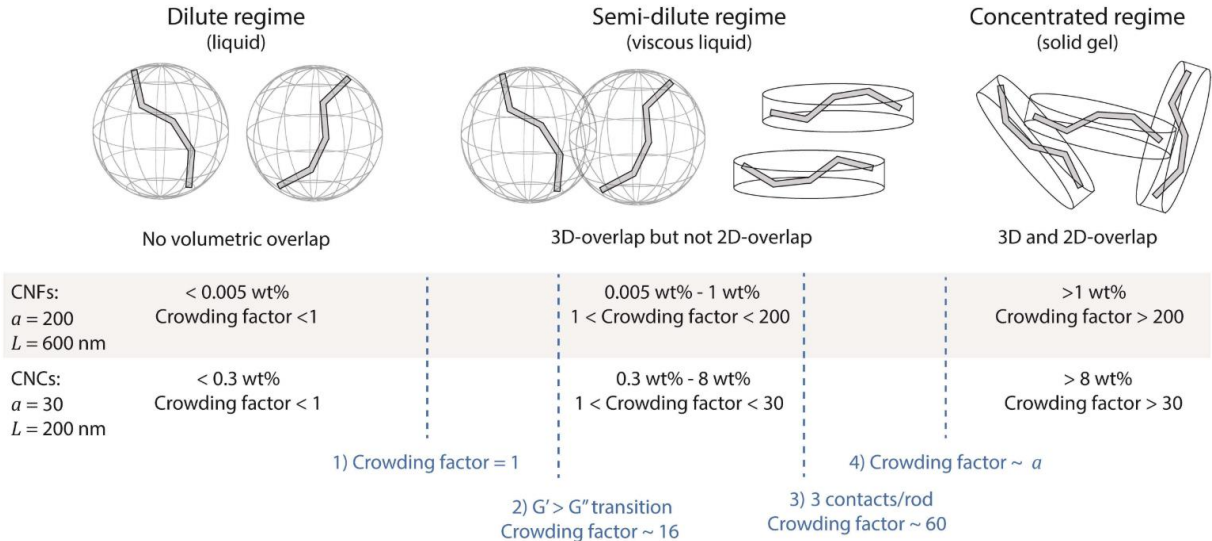


Figure 7: Schematic showing the transitions between concentration regimes as a function of the crowding factor. The figure was reproduced with permission from [80].

Before reaching a VAS, CNC suspensions undergo liquid crystalline phase transitions. When dispersed anisotropic nanoparticles reach a critical volume fraction, their freedom of movement is decreased due to overlapping excluded volumes [91,98]. To reduce the overlapping volume and increase the translational entropy at the expense of rotational entropy, the particles align into parallel nematic phases. The critical volume fraction for this isotropic-nematic phase transition to occur is again depending on the aspect ratio of the anisotropic particles and was defined by Onsager [99].

$$\varphi_{I-N} = 3.3a^{-1}$$

In the case of charged particles, the contribution of the electrical double layer has to be taken into account, which is described with a modification of the original Onsager theory [100,101]. As the critical volume fraction for the phase transition to occur depends on the aspect ratio, the equation has to be corrected using an effective particle diameter d_{eff} , which takes the thickness of the double layer into account.

$$\varphi_{I-N} = 6a^{-1} \frac{d}{d_{eff}}$$

The effective diameter depends on the electrolyte concentration and the surface charge density, which are parameters that can be used to control the phase transition. In the case of nanocelluloses, the distribution of charged surface groups is asymmetric, due to their right-handed twist, which in turn influences the assembly into liquid crystalline phases [102,103]. As a consequence of their asymmetry, CNCs self-assemble into chiral nematic (also called cholesteric) phases, which means that the nematic phase undergoes an additional organization into a helical structure twisting perpendicular to the nematic plane [91,98,103]. The length scale along the helical axis between two CNCs of the same orientation, after the helix performed a 360° twist, is referred to as the cholesteric pitch (**Figure 8f**). In liquid state the pitch is normally in the order of

micrometers, but it can reach sub-micrometer length when a CNC cholesteric phase is dried (evaporation induced self-assembly, EISA). Sub-micrometer pitch lengths are of high interest for optical applications, since the optical reflection band shift to the visible spectrum, resulting in pronounced structural colors. By controlling the cholesteric pitch, which is usually achieved by changing the interactions between the CNCs, the structural color can be tuned [91,104,105].

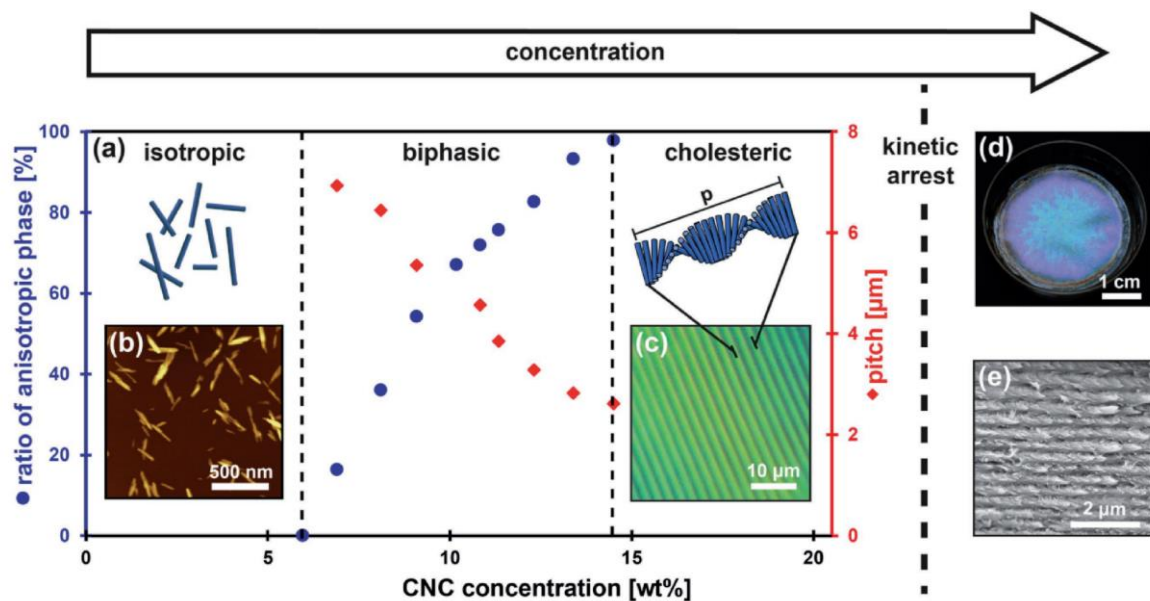


Figure 8: Schematic describing the isotropic-cholesteric phase transition as a function of concentration (a). As the concentration of CNCs (b) is increased the anisotropic phase is preferred and the cholesteric pitch is decreased (c). When the CNC concentration is further increased by solvent evaporation, a kinetic arrest occurs and the pitch decreases to the order of the wavelengths of visible light (d & e), inducing structural color by reflecting certain wavelengths. Reproduced with permission from [91].

In summary, the colloidal interactions in nanocellulose systems are mostly dependent on electrostatics, which can be approximated using the DLVO theory. Furthermore, when the concentration of nanocellulose particles is increased, interactions become more important and determine their self-assembly into networks (mostly CNF gels and glasses) and liquid crystalline phases (mostly applying for CNCs). Note that the DLVO

and the other principles described here also apply for other colloidal systems, such as amyloid fibrils.

1.2.3 Nanocellulose materials and their applications

Nanocellulose has received the attention of materials scientists due to the gigantic mechanical strength of individual nanofibrils and nanocrystals in the order of Gigapascals [106]. The large surface area covered with hydroxyl groups allows for facile chemical modification [84] and promotes the colloidal stability of nanocellulose suspensions and thus the suitability for bottom-up assembly [79,107]. Nanocellulose suspensions can be transformed into different materials, such as hydrogels [108], aerogels [108,109], liquid crystals[91], films/nanopapers [110], foams [111] and emulsions [112,113]. The versatility of nanocellulose based materials is reflected in the wide range of possible applications, such as biomedical engineering, drug delivery, water purification, packaging, electronics, optical devices, and much more [78].

1.2.4 Interactions between cellulose and proteins

Due to the broad diversity in amino acids, proteins are a heterogeneous class of biopolymers. The properties of the 21 different amino acids composing the primary sequence of a protein determine the physical interactions such protein will undergo, including ionic interactions, hydrogen bonds, pi-stacking, or hydrophobic [2,114]. The net charge of proteins is governed by the protonation of pH-responsive functional groups present in some amino acids, such as carboxylic and amino groups. The isoelectric point (pI), i.e. the pH value at which the net charge is zero is an important pa-

parameter to describe proteins. Indeed, at a $\text{pH} < \text{pI}$ the net charge of the protein is positive (due to protonated amines), while at $\text{pH} > \text{pI}$ the net charge turns negative (dominated by deprotonated carboxylic groups) [114]. Therefore, tuning the pH of the environment of the protein can be useful to control the interactions between proteins and oppositely charged colloids, such as polysaccharides. These interactions are the cause of polyelectrolyte complexation, a type of self-assembly observed between oppositely charged polymers, so-called polyelectrolytes [80,115,116].

When complexes between oppositely charged polyelectrolytes are formed through ionic bonds, counter-ions from the electrical double layer surrounding the polyelectrolytes are released. This release of high numbers of counter-ions and hydration water gaining translational entropy increases the entropy in the system, which is the actual driving force of the complexation rather than short-ranged forces between the polyelectrolytes [80,116–118]. Isothermal titration calorimetry (ITC) measurements applied to a solution containing positively charged, native lysozyme and mechanically disintegrated CNFs, showed that the complexation is indeed entropy-driven, and that the negatively charged groups (pH-dependent) of hemicellulose residues still present from the isolation of the CNF fibrils from wood played an important factor [119]. Also in the case of negatively charged bovine serum albumin (BSA) and positively charged pyridinium-grafted CNCs, protein adsorption was driven by the entropic gain resulting from the release of water molecules and counter-ions, as confirmed by ITC [120]. Wu and co-workers studied the complexation of TO-CNF with native HEWL, which resulted in physically cross-linked colloidal hydrogels with tunable rheological properties, depending on amount of added HEWL [121]. Further examples of proteins adsorbed/immobilized on nanocellulose are summarized in the review paper co-authored with Bensselfelt and others [80]. Nanocelluloses can be effectively combined with fibrillary proteins such as gelatin and silk fibroin to create robust composite materials. These composite

materials are particularly promising for use in biomedical applications like drug release and cell scaffolds because they form biocompatible hybrid hydrogels that exhibit superior mechanical properties [122–124]. Even though composite materials made from cellulose and amyloid fibrils can be found in nature in the biofilms of *E. coli* and other bacteria [125], research on lab-made bio-inspired cellulose-amyloid composites has been rare [126]. Recent literature also focused on the combination of amyloid fibrils and other polysaccharides to obtain hybrid materials. Usuelli and co-workers, successfully infiltrated BLG amyloid fibril gels with polysaccharides, forming a second network providing enhanced mechanical strength [127]. Moreover, Chen and co-workers reported the preparation of a amyloid-like HEWL-alginate film with high toughness and demonstrated its use in flexible electronics [128].

De France and co-workers report the effect of amyloid fibrils made from HEWL and bovine serum albumin (BSA) on the chiral nematic self-assembly of CNCs in dried films [104,105]. The positively charged HEWL amyloids disturbed the chiral nematic assembly of negatively charged CNCs at relative concentrations of 1%, due to polyelectrolyte complexation. At lower amyloid concentration the reflection peak was shifted to smaller wavelengths (blue shift), which can be related to a decrease in the cholesteric pitch. For native HEWL the blue shift occurred at much higher relative concentrations, with respect to BSA. Typically, a red shift can be observed upon the addition of polymers due to the self-assembling CNC suspensions because they occupy some volume between the nematic planes [129]. This red shift was also observed by Bast and co-workers, when they infiltrated already dried chiral nematic CNC films with different negatively charged proteins (silk proteins and BSA). In contrast to native BSA, BSA amyloid fibrils caused an unexpected concentration dependent blue shift in chiral nematic CNC films [105]. Despite taking up volume between the nematic planes of CNCs, the incorporation of BSA amyloids resulted in a decreased pitch. This can be associated

to depletion [87]: the BSA amyloids acting as depletants are prevented from entering the excluded volume of the larger CNCs, creating a higher osmotic pressure in the surrounding volume, causing the outflow of water, which brings the CNCs closer together and decreases the pitch. The compression of the pitch of chiral nematic CNC phases after mixing them with non-adsorbing polymers has been observed before for sodium polyacrylate [129]. Bast and co-workers pointed out that there might be a different behavior depending on whether then chiral nematic CNC films were casted first and then infiltrated with polymers, or the two polymers were first pre-mixed and then left for self-assembly by EISA, probably resulting in aggregation and loss of the chiral nematic structure [130].

In summary, the polyelectrolyte complexation drives the interactions between nanocelluloses and proteins. Oppositely charge macromolecules complex with each other due to increasing entropy from released counter-ions and hydration water. In the case of liquid crystalline phases, excluded volume effects causing depletion attraction also have to be taken into account.

2 Aims of the thesis

The overall goal of this thesis was to study and understand interactions between protein aggregates and nanocellulose to identify different self-assembly strategies to create hybrid protein-nanocellulose materials. More specifically, the first goal was the production of HEWL amyloid(-like) aggregates, study their self-assembly, aggregation kinetics, structural changes and test their antimicrobial properties in suspension. With the characterized HEWL amyloids at hand, the further goal was to understand their interactions with nanocellulose to create biohybrid materials using different self-assembly strategies. Ultimately, the amyloids were used with the aim to introduce new functionalities, such as antimicrobial activity, to the nanocellulose.

The thesis is structured into three chapters containing the first-authored publication resulting from this project. Self-assembly is the common theme and each publication deals with a different dimensionality: the **1D** self-assembly of amyloid fibrils, the adsorption of amyloid fibrils at **2D** air-water interfaces and the **3D** self-assembly of amyloid fibrils and nanocellulose into hybrid hydrogels using polyelectrolyte complexation. The publications were each assigned a chapter of the thesis:

Chapter 3 describes the systematic optimization of 1D aggregation conditions to obtain a toolbox of colloidally stable amyloid(-like) particles made of HEWL. The aggregation kinetics, conversion, morphology and structure of the emerging aggregates were characterized in detail. Finally, the antimicrobial potential of the amyloid(-like) aggregates obtained from different pathways were evaluated.

Chapter 4 explores the adsorption of HEWL amyloid fibrils at the air-water interface. The adsorption and foam stability was optimized screening concentration and pH as main parameters. Using the best conditions, 2D films were generated inside a loop and

used to coat various substrates. The dried coating was characterized for its thickness, morphology, and physicochemical properties. As a last step the antimicrobial activity of the coating against different pathogenic microbes was tested to explore its potential for biomedical applications, such as wound dressings.

In **Chapter 5**, the self-assembly of different amyloid fibrils (HEWL and BLG) with nanocellulose into 3D hybrid hydrogels was studied. Rheological characterization was used to elucidate the structure of the hybrid gels. A pH-mediated slow polyelectrolyte complexation process was developed to control the charge of the amyloid fibrils, in order to prepare homogenous self-assembled solid hydrogels.

Further co-authored publications also deal with polyelectrolyte complexation of TO-CNF and native HEWL (**Chapter 9**) and the self-assembly of CNCs into liquid crystalline phases in the presence of amyloids of opposite or same charge (**Chapters 10 and 11**). The main outcomes of these papers were already included in the introduction (subsection 1.2.4) and will be discussed in the main discussion section of the thesis (**Chapter 6**).

First-author publications

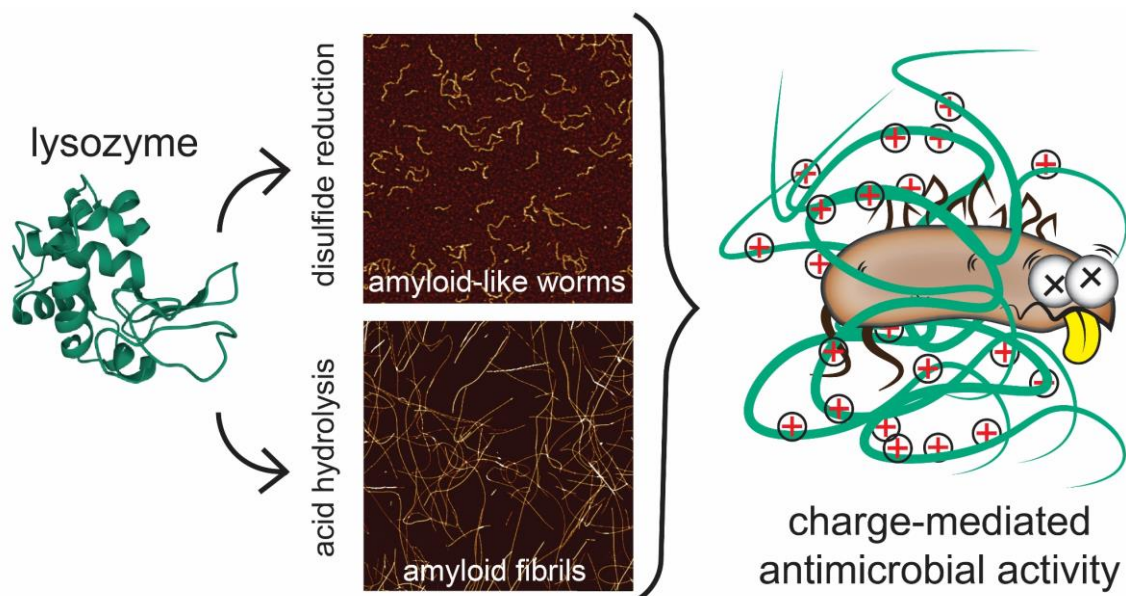
The research conducted during this doctorate has resulted in three first-authored publications. They are included in this thesis as single chapters, without modification from the published version. Permission for reprinting was granted by the publishers.

3 Self-assembly pathways and antimicrobial properties of lysozyme in different aggregations states

Nico Kummer, Tingting Wu, Kevin De France, Flavia Zuber, Qun Ren, Peter Fischer, Silvia Campioni and Gustav Nyström

Biomacromolecules, 2021, 22, 4327-4336

<https://doi.org/10.1021/acs.biomac.1c00870>



Reproduced with permission from authors and publisher [131]

© 2021, American Chemical Society

Self-assembly pathways and antimicrobial properties of lysozyme in different aggregations states

Nico Kummer^{1,2}, Tingting Wu^{1,3†}, Kevin J. De France¹, Flavia Zuber⁴, Qun Ren⁴, Peter Fischer², Silvia Campioni^{1}, Gustav Nyström^{1,2*}*

¹ Laboratory for Cellulose & Wood Materials, Empa – Swiss Federal Laboratories for Materials Science and Technology, Überlandstrasse 129, 8600 Dübendorf, Switzerland

² Institute of Food Nutrition and Health, Schmelzbergstrasse 7, ETH Zurich, 8092 Zurich, Switzerland

³ State Key Laboratory for Modification of Chemical Fibers and Polymer Materials, College of Materials Science and Engineering, Donghua University, Shanghai 201620, P. R. China

⁴ Laboratory for Biointerfaces, Empa – Swiss Federal Laboratories for Materials Science and Technology, Lerchenfeldstrasse 5, 9014 St. Gallen

* To whom correspondence should be addressed

E-mail: silvia.campioni@empa.ch; gustav.nystroem@empa.ch

ABSTRACT

Antimicrobial resistance in microorganisms will cause millions of deaths and pose a vast burden on health systems, therefore alternatives to existing small-molecule antibiotics have to be developed. Lysozyme is an antimicrobial enzyme and has broad-spectrum antimicrobial activity in different aggregated forms. Here, we propose a reductive pathway to obtain colloiddally stable amyloid-like worm-shaped lysozyme nanoparticles (worms) from hen egg white lysozyme (HEWL) and compare them to amyloid fibrils made in an acid hydrolysis pathway. The aggregation of HEWL into worms follows strongly pH-dependent kinetics and induces a structural transition from α -helices to β -sheets. Both HEWL worms and amyloid fibrils show broad-spectrum antimicrobial activity against the bacteria *Staphylococcus aureus* (Gram-positive), *Escherichia coli* (Gram-negative) and the fungus *Candida albicans*. The colloidal stability of the worms allows the determination of minimum inhibitory concentrations (MIC), which are lower than for native HEWL in the case of *S. aureus*. Overall, amyloid fibrils have the strongest antimicrobial effect, likely due to the increased positive charge compared to native HEWL. The structural and functional characterization of HEWL worms and amyloids investigated herein is critical for understanding the detailed mechanisms of antimicrobial activity, and opens up new avenues for the design of broad-spectrum antimicrobial materials for use in various applications.

INTRODUCTION

The excessive use of antibiotics has led to the emergence of antimicrobial resistance (AMR) in multiple microorganisms, ranging from bacteria, to viruses and fungi.[132] Infectious diseases that can no longer be treated with antibiotics cause chronic illnesses, complications, long-term effects and even death.[133] AMR is a global health

problem affecting the healthcare systems in both lower-income countries and in more developed areas. It is projected that without taking action, AMR will cause up to 10 million deaths and cost upwards of 100 trillion dollars per year.[134] However, due to expensive production and challenging approval processes, the development of new antibiotics is relatively unattractive for pharmaceutical companies.[133] Therefore, the demand for alternative strategies against AMR is of pressing importance. Moreover, the development of broad-spectrum antimicrobial materials (such as antimicrobial peptides[53] or nanomaterials[135]) that can target different types of microorganisms is particularly desirable, as this would drastically increase the practical use of such a product in a wide variety of clinical settings. In contrast to traditional small-molecule antibiotics which disrupt specific microbial metabolic functions, broad-spectrum antimicrobials target general features such as the cell wall or membrane, and can therefore inhibit the growth of multiple types of microorganisms.[52,53,135,136]

The antimicrobial activity of lysozyme in hen egg white (HEWL)[40] and human nasal secretions[41] has been known since the early 20th century. Lysozyme is an antimicrobial enzyme which acts by cleaving the peptidoglycan cell wall of Gram-positive bacteria, leading to cell death.[45,46] Studies on heat denatured and mutated forms of lysozyme have demonstrated antimicrobial activity even in absence of an active catalytic site.[47–49] It is believed that this non-catalytic antimicrobial activity is caused by a structural motif[47] consisting of positively charged basic amino acids that interact with negatively charged cell walls or membranes, causing membrane deformation and lysis.[48,49] Furthermore, the exposure of hydrophobic groups has been hypothesized to contribute to this interaction with microbial membranes.[37,47,51]

Lysozyme has been reported to form amyloid aggregates, which are self-assembled nanofibrils composed of β -sheets held together by hydrogen bonds.[8] The possibility

to prepare amyloids in a simple fashion, from inexpensive commercial protein sources (such as HEWL),[11] makes them an attractive bio-based nanomaterial with various potential technological applications ranging from adhesion to water filtration, drug release and biosensing.[9] For instance, HEWL amyloids are easily obtained upon incubation at low pH and high temperature, where native HEWL is first hydrolyzed into shorter peptides, which rapidly self-assemble to form high aspect ratio fibrils with a cross- β structured core having exceptional mechanical properties.[25,27] Another method to produce amyloid-like HEWL aggregates (i.e. aggregates that despite having a different morphology, possess a cross- β structured core) exploits the reduction of the four disulfide bonds present in its native state.[34] Using this methodology, particles with spherical, protofibrillar and irregular/amorphous morphologies have been obtained under different reduction conditions.[137] However, one relatively significant drawback of this method, first described by Yang and co-workers, is that the aggregation kinetics of HEWL with the reducing agent tris-(2-carboxyethyl)phosphine (TCEP) is rapid and uncontrolled, leading to large sedimenting aggregates.[36] Moreover, the lack of control over particle size can lead to decreased particle mobility and loss of relative surface area.

Recently, HEWL amyloid fibrils used in the form of suspensions,[58] hydrogels[32] and hybrid films with nanocellulose[57,104] have shown antimicrobial activity against both Gram-positive and Gram-negative bacteria in *in-vitro* experiments and biocompatibility with human colonic epithelial cells.[32] Moreover, amyloid-like HEWL films coated on medical implants and wound dressings have shown broad spectrum antimicrobial activity against Gram-positive and Gram-negative bacteria, as well as fungi, both *in vitro* and *in vivo*, while keeping excellent biocompatibility.[37–39] However, quantitative

analysis of the concentration-dependent antimicrobial activity is still lacking for amyloid-like HEWL aggregates, which makes a direct comparison to amyloid fibrils impossible. Moreover, the fact that these amyloid particles are relatively unstable in solution hampers the possibility to assess their properties.

Therefore, we investigated the aggregation kinetics of TCEP-reduced HEWL to develop a protocol for a controlled preparation of colloiddally stable amyloid-like "worms". We characterized the yield of the process used to prepare worms/amyloid fibrils and how further processing, such as sonication, dialysis and ultrafiltration change the aggregate/soluble peptide ratio. Moreover, we compared three distinct types of colloiddally stable HEWL aggregates in terms of morphology and dimensions, secondary structure, surface charge and concentration-dependent antimicrobial activity, shedding light on their structure-antimicrobial function relationship. This analysis of the colloiddal and macromolecular nature of HEWL aggregates and its effect on broad-spectrum antimicrobial activity opens new possibilities for the incorporation of these particles into antimicrobial soft biomaterials.

EXPERIMENTAL

Materials

Hen egg white lysozyme (HEWL, >90%), 4-(2-hydroxyethyl)-1-piperazineethanesulfonic acid (HEPES), tryptic soy broth (TSB), plant count agar (PC-agar) were purchased from Sigma Aldrich. Hydrochloric acid, sodium hydroxide, tris-(2-carboxyethyl)phosphine (TCEP), Thioflavin T (ThT) and phosphate buffer (sodium dihydrogen phosphate and sodium hydrogen phosphate) were purchased from VWR Chemicals. Glucose was provided by Fluka. All chemicals were used as received.

Preparation of amyloids by acid hydrolysis

Amyloid fibril aggregation conditions were taken from an established protocol[27] with minor modifications: HEWL was dissolved at 20 mg/mL in 10 mM HCl (pH 2) and incubated for 24 hours at 90°C in 50-mL tubes in a Thermomixer (Eppendorf) under mild shaking (400 rpm). After aggregation, long amyloid fibrils were shortened with a tip sonicator (Digital Sonifier 450, Branson Ultrasonics), using 3 sonication cycles of 2 minutes at 30% amplitude, as reported in a previous protocol[104]. To prevent heating, the tubes were kept in an ice bath during sonication. Fibrils were stored in the fridge at 4°C until further use.

Preparation of flexible amyloid-like aggregates under reducing conditions

Solutions of HEWL and TCEP in MilliQ water at different concentrations were prepared and mixed in equal volumes to initiate the amyloid-like aggregation of HEWL.[34] The pH of the TCEP solution was adjusted using 0.1 M NaOH. The aggregation took place at room temperature without agitation. After the initial parameter screening the following conditions were used to obtain colloidally stable worm-like aggregates (worms): 1 mg/mL HEWL, 12.5 mM TCEP at pH 4.5 after 16 hours. As above, worms were stored in the fridge at 4°C until further use.

Aggregation kinetics under reducing conditions

A ThT binding assay was performed in a fluorescence plate reader (CLARIOstar Plus, BMG LABTECH) using non-binding 96-well plates (Greiner). Eppendorf tubes with 750 µL each of HEWL and pH-adjusted TCEP solutions at different concentrations were prepared. Finally, 30 µL of a 244 µM ThT solution (in 25 mM phosphate buffer pH 6.5) were added to the samples and to control vials with all components except for

HEWL. ThT fluorescence was measured at an excitation and emission wavelength of 450 nm and 488 nm, respectively, collecting data every 15 min over the course of 24 h of incubation at 25 °C. Average kinetic curves with standard deviations were determined in quintuplicate measurements.

Time-resolved dynamic light scattering (DLS) was performed using a Malvern Zetasizer Nano ZS. The HEWL and TCEP solutions were filtered through a 0.02 µm syringe filter (Whatman) to remove aggregates and impurities before mixing equal volumes into a cuvette. The z-average radius diameter describing the intensity weighted mean hydrodynamic size was measured at an interval of two minutes. The kinetic curves are the average of three repetitions of the experiment.

Dialysis, ultrafiltration and yield quantification

Dialysis was performed on 50 mL batches of amyloid fibrils, sonicated amyloids and worms against pH-adjusted MilliQ water (pH 2 for amyloids, pH 4.5 for worms) using a 300 kDa molecular weight cut-off (MWCO) cellulose ester membrane (Repligen, part no. 131420). The MilliQ water was constantly stirred and changed 4 times at intervals of at least 4 hours.

Ultrafiltration using a stirred cell with a 100 kDa regenerated cellulose filter disc (both from Amicon) allowed for simultaneous removal of TCEP or non-aggregated peptides, and up-concentration of the worm samples needed for antimicrobial tests. Batches of 200 mL worms were first filtered with an applied nitrogen pressure of 4 bar under constant stirring to reach a volume of 20 mL. The worms were then washed by adding 180 mL of MilliQ at pH 4.5 and filtered again to the final volume of 20 mL.

The protein concentration of the samples after dialysis/ultrafiltration was determined by measuring the UV-absorbance at 280 nm with a Cary 1E spectrophotometer, using

the molar extinction coefficient at 280 nm of HEWL $\epsilon=38,940 \text{ cm}^{-1}\text{M}^{-1}$. [138] The ratio between aggregates and residual peptides was determined by filtering samples with 100 kDa MWCO centrifugal filters (Amicon) and 0.02 μm syringe filters (Whatman) and measuring the protein concentration in the filtrate. The conversion of HEWL monomer into aggregates was calculated as

$$\text{conversion} = \left(1 - \frac{c_{\text{filtrate}}}{c_{\text{initial}}}\right) \times 100\% \quad (1)$$

where c_{filtrate} is the concentration of protein in the filtrate determined by UV-Vis spectroscopy and c_{initial} is the concentration of protein in the sample before filtration. No aggregates in the filtrate were found by AFM (data not shown).

Atomic force microscopy

Atomic force microscopy (AFM) imaging (Bruker Icon 3 equipped with Bruker RTESPA-150 probes) in tapping mode was performed on samples of worms (0.01 mg/mL) and amyloid fibrils (0.1 mg/mL) on freshly cleaved mica at a resolution of 1024x1024 lines and at a scan rate of 0.5 Hz. Images were flattened with the Bruker Nanoscope software.

Secondary structure analysis

Attenuated total reflectance Fourier-transform infrared (ATR-FTIR) spectroscopy (Bruker Tensor 27) was performed on freeze-dried aggregate samples. Spectra were measured between 4000 and 600 cm^{-1} with a resolution of 4 cm^{-1} and 32 accumulated scans. A background subtraction and normalization to the highest peak were performed.

Circular dichroism (CD) spectroscopy (Jasco J-815) was performed on HEWL aggregate samples in pH-adjusted MilliQ at a concentration of 0.2 mg/mL. Accumulations of 5 spectra were recorded at 25°C and a scan speed of 20 nm/min in the far-UV range (250-190 nm). All CD spectra were smoothed with Jasco Spectra Manager and deconvoluted with BeStSel[139] and CDPPro[140] (CONTINLL).

Zeta potential

Zeta potential of worms and amyloid fibers were measured at a concentration of 0.1 mg/mL in 10 mM HEPES pH 7.2. Samples of native HEWL at 1 mg/mL in 10 mM HEPES pH 7.2 were also measured. A Malvern Zetasizer Nano ZS was used with disposable capillary zeta potential cell. The mean zeta potentials with standard deviation were determined in three single measurements.

Antimicrobial activity testing

The antimicrobial activity of native HEWL and the dialyzed/ultrafiltrated aggregate species was tested against the commonly occurring pathogens, namely Gram-positive *Staphylococcus aureus* (ATCC 6538), Gram-negative *Escherichia coli* (DSMZ 1576), *Pseudomonas aeruginosa* (ATCC 43390) and the fungus *Candida albicans* (ATCC 90028). Pre-cultures of the strains were incubated overnight in 30% TSB with 0.25% glucose. The microorganisms were then centrifuged at 1200 x g for 5 min and the pellet was redispersed in 10 mM HEPES buffer at pH 7.2 and diluted to a concentration of OD₆₀₀=0.2 for *S. aureus* and *E. coli* and OD₆₀₀=2.0 for *C. albicans*. HEWL species were first adjusted to pH 6.0 using 0.1 M NaOH and then diluted in HEPES at concentrations of 1 mg/mL, 0.1 mg/mL, 0.01 mg/mL, and 0.001 mg/mL. The resuspended cells (50 µL) were mixed with HEWL species (950 µL) in a 24-well plate and incubated for 6 hours

at 37°C while shaking at 40 rpm (Infors Multitron). After 6 hours, 20 µL aliquots were taken from the 24-well plate to perform a serial dilution in 180 µL TSB down to a dilution factor of 10⁻⁷. Each dilution was then spotted (20 µL) on PC-agar plates in triplicates, incubated for 37°C overnight and colony forming units (cfu) were evaluated. Regrowth assays were performed in 96-well plates filled with 190 µL TSB, adding 10 µL of the samples in triplicates from the 24-well plate, as described previously.[141] The plates were sealed and incubated in a plate reader (BioTek Instruments Microplate Reader Synergy HT) at 37°C with continuous shaking, measuring OD₅₉₅ every 30 minutes. All experiments included controls without microbial cells or without the addition of HEWL aggregates.

RESULTS AND DISCUSSION

Effect of pH on HEWL aggregation under reducing conditions

In most cases, amyloid fibrils of food proteins are easily prepared *in vitro* by incubating samples at low pH and high temperature, conditions that lead to hydrolysis of the starting polypeptide chain. Yet, HEWL can also undergo an alternative ultrafast aggregation process when incubated with reducing agents that destabilize its globular fold. As this process can also lead to the uncontrolled formation and sedimentation of large HEWL aggregates, the effect of different solution parameters such as HEWL concentration, TCEP concentration and pH on HEWL aggregation was screened in order to determine conditions leading to the formation of colloiddally stable aggregates with a smaller size and larger relative surface area (Figure 1). To this aim, aggregation kinetics were obtained by recording the fluorescence intensity of the amyloid-binding dye Thioflavin T as a function of time.[142,143] Typically, aggregation kinetics of amyloids measured by ThT binding or other methods give a sigmoidal profile with a lag phase, a growth

phase and a plateau phase describing the process on a macroscopic level.[17] On a molecular level, amyloid formation is a nucleated polymerization process in which secondary nucleation events play an important role.[17,18] For instance, it is known that the formation of HEWL amyloid fibrils under conditions of low pH and high temperature follows such sigmoidal behavior.[25,27,144] In the case of HEWL aggregates formed under reducing conditions, the kinetic process has not yet been monitored in detail. Our data show that increasing either HEWL or TCEP concentration influences the measured ThT fluorescence at pH 4.5 (Figures 1A and B), 5.5 and 6.5 (Supporting Information, Figures S1A and S1B, respectively), by shortening the duration of the lag phase and increasing the apparent elongation rate of the process. Increasing the pH from 4.5 to 6.5 had an even more profound effect on the evolution of the measured aggregation kinetics (Figure 1C). A detectable lag phase was observed only at pH 4.5, while at pH 5.5 and 6.5 aggregation occurred within minutes instead of hours. Yet, the samples prepared at pH 5.5 and 6.5 turned turbid and exhibited sedimentation (not shown), indicating an aggregate size in the order of micrometers. Therefore, ideal reaction conditions to obtain colloidally stable β -sheet-rich aggregates were identified at pH 4.5, with concentrations of 12.5 mM TCEP and 1 mg/mL HEWL. Aggregation kinetics monitored under identical conditions by time resolved DLS corroborate the ThT binding data and show a similar lag-phase duration (Figure 1D). Finally, AFM images of aliquots taken after 1, 2, 3 and 4 hours of aggregation show that nuclei form within the first two hours, followed by their one-dimensional elongation (Figure 1E).

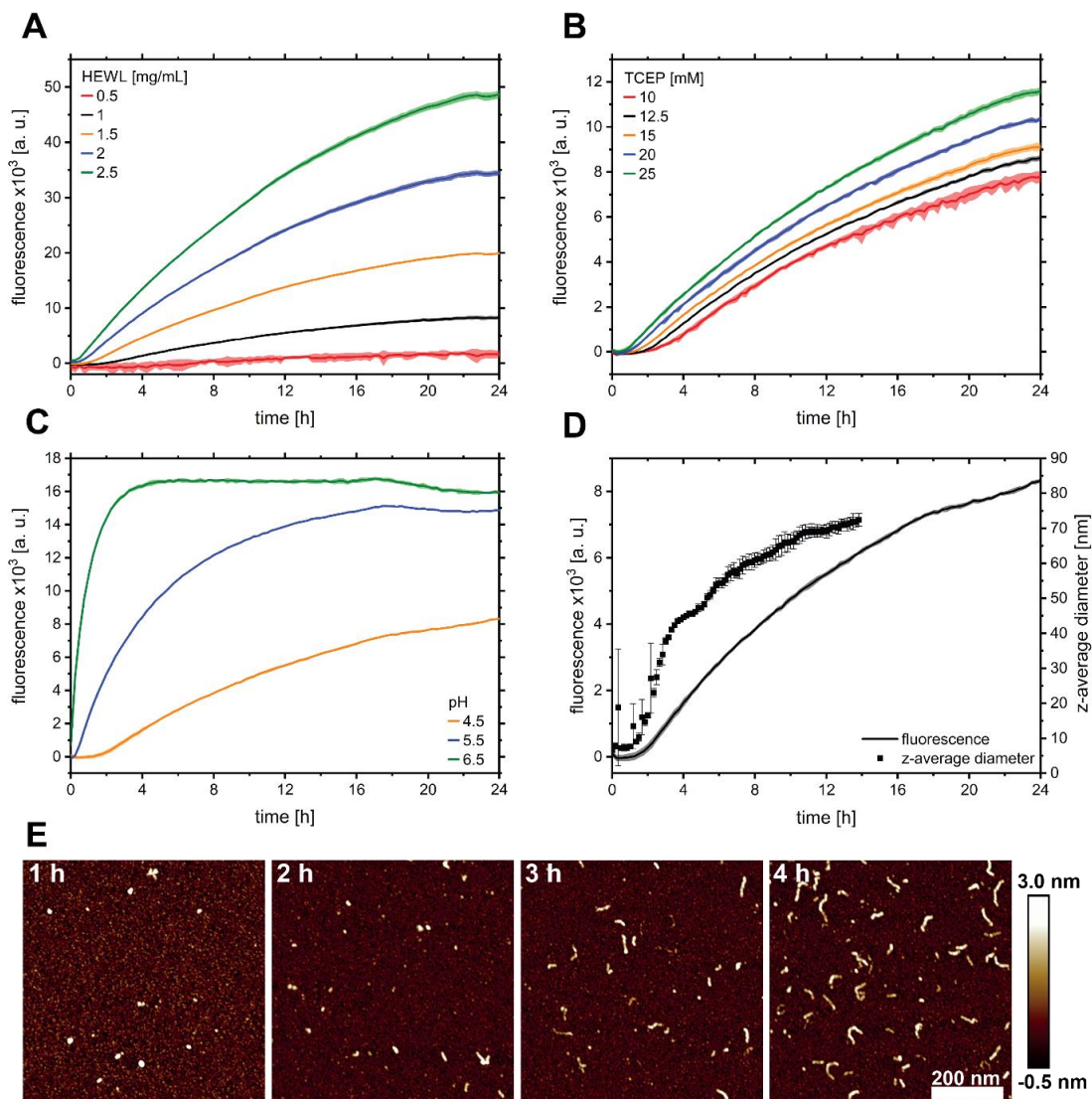


Figure 1: TCEP induced worm aggregation kinetics measured by ThT binding assay at different HEWL concentrations at pH 4.5 and 12.5 mM TCEP (A), different TCEP concentrations at pH 4.5 and 1 mg/mL HEWL (B) and different pH values at 12.5 mM TCEP and 1 mg/mL HEWL (C). Aggregation kinetics at pH 4.5, 12.5 mM TCEP and 1 mg/mL were also measured by time-resolved DLS (D). AFM images showing the first 4 hours of aggregation under the same conditions with the nucleation of aggregates and the start of one-dimensional elongation (E).

Despite the fact that Li and co-workers (who measured HEWL aggregation kinetics at pH values of 6.5 and higher) stated that TCEP-induced aggregation of HEWL does not follow the typical sigmoidal growth curve,[137] our results suggest that the measured kinetic profile changes significantly as a function of the solution pH, which in turn affects the overall net charge of the protein. While sigmoidal growth is observed at pH 4.5, at

higher pH the equilibrium of the reaction is strongly pushed towards the aggregate state, which significantly shortens the lag phase (Figure 1C). This can be explained by the stronger repulsion experienced by unfolded peptide chains at pH 4.5, which leads to a preferential one-dimensional growth of aggregates (elongation). Instead, under conditions of weaker repulsion, large spherical particles that precipitate out of the solution were formed. These observations are well aligned to previous results for β -lactoglobulin, where similar effects were seen through the addition of salt and change in pH, but in absence of reducing agents.[11]

Characterization of different HEWL aggregates

With the detailed knowledge of the aggregation pathway under the reducing conditions at hand, we now focus on a comparison of three types of HEWL aggregates, differing in length, thickness, flexibility and aspect ratio (Figure 2). The amyloid-like aggregation of HEWL with TCEP for 16 hours led to the formation of curvilinear worm-like particles (worms) with an average length of a few hundred nm. These aggregates exhibit a wavy, beaded morphology and are highly flexible. Acid hydrolysis conditions produced semi-flexible amyloid fibrils of a few μm in length (amyloids). Further sonication of amyloids led to short and stiff rod-like particles (sonicated amyloids) with an average length comparable to that of the worms. The three selected types of aggregates differ also in their thickness, here expressed as height obtained from AFM measurements: worms are around 2-3 nm thick, whereas full-length and sonicated amyloids are 3-8 nm thick, as these can be formed by the association of multiple protofibrils.[27]

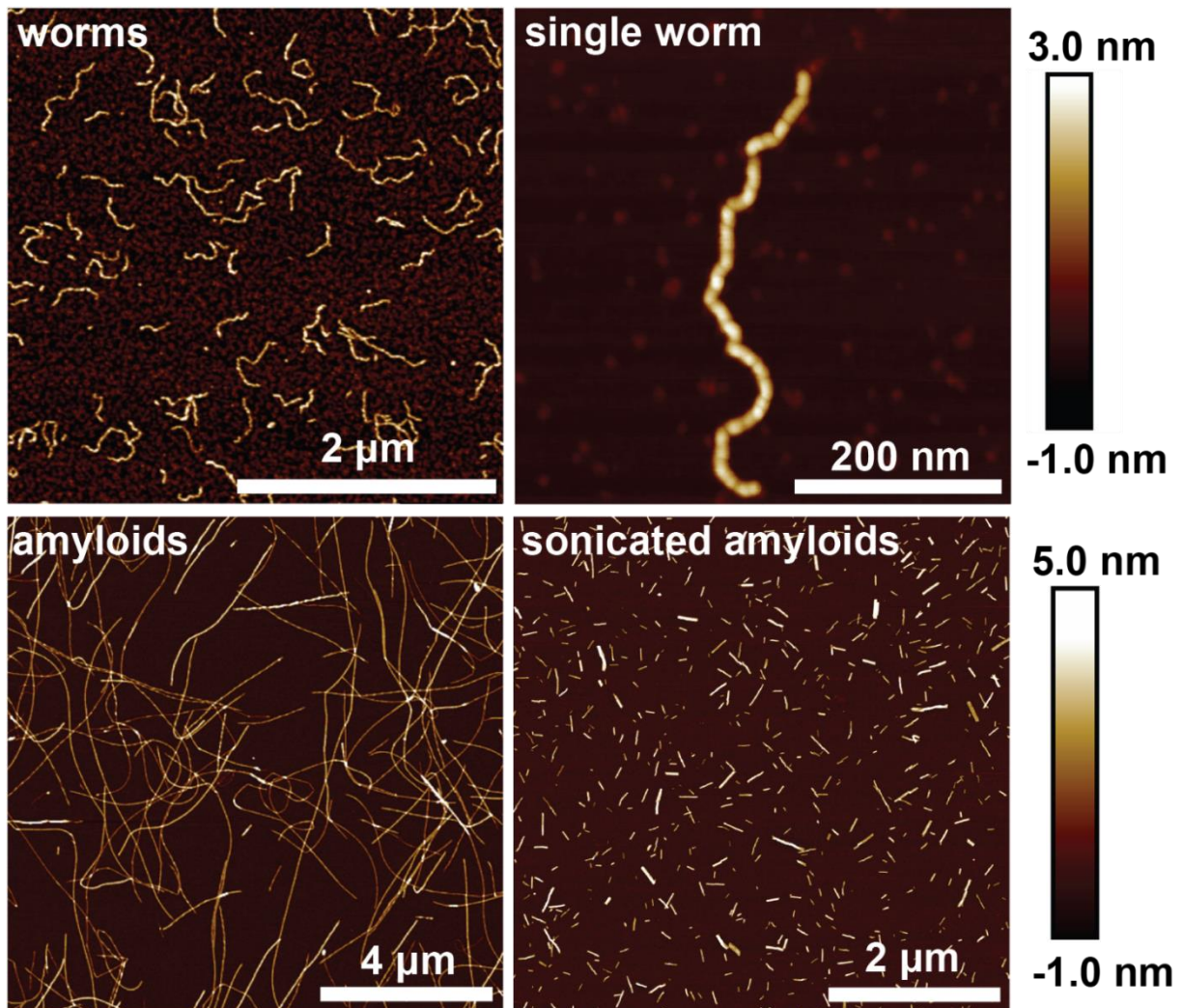


Figure 2: AFM height images of flexible, short worms, a single worm with visible beaded structure, semi-flexible, long amyloid fibrils and stiff, rod-like sonicated amyloid fibrils.

The higher flexibility of the worm-like aggregates compared to the stiff amyloid fibrils could possibly be attributed to the formation of more nuclei and faster aggregation leading to a less ordered secondary structure.[21] For example, worm-like aggregates with decreased β -sheet content have been observed when the aggregation of β -lactoglobulin was accelerated due to increased protein concentration[21,145] or decreased electrostatic repulsion due to ionic strength or increased pH[11]. Generally, amyloid fibrils can be shortened with sonication,[104,146] high-pressure homogenization[147]

and by stirring the solution for extended times.[148] In our case, by tuning the sonication parameters, shorter fibrils of different well-defined lengths (few hundreds nm) could be obtained.

After completion of the aggregation reaction, all samples were dialyzed to remove TCEP (when present) as well as unreacted HEWL species (i.e. monomers or peptide residues in the case of worms or amyloids, respectively). The ratio between the aggregated and the soluble fraction of each sample was determined by filtration of the samples, followed by UV-spectroscopy of the filtrate. In the case of TCEP-induced aggregation, 65% of the initial HEWL mass was converted into worms. The ratio between residual soluble species and aggregates was further improved by dialysis or ultrafiltration to around 80% (Supporting Information, Table S1), most likely reflecting the equilibrium between the two states. However, the total protein concentration decreased from 1 mg/mL to 0.5 mg/mL after dialysis and to ca. 0.7 mg/mL after ultrafiltration. Incubation at pH 2 and 90 °C resulted in 35% mass conversion of initial HEWL and a maximum of 60% fibrils in dialyzed samples, independent of sonication treatment. In this case, the total protein concentration after dialysis decreased to 5 mg/mL, accounting for a loss of 75% of the initial HEWL mass. Despite the previous work characterizing the formation of amyloids from lysozyme, there is still a lack of clarity about the yield of HEWL amyloids following aggregation. This is also the case for other amyloid species; for β -lactoglobulin for example, the same acid hydrolysis pathway (2 wt% protein, pH 2, 90°C) leads to aggregate yield values ranging from 38% to over 80%.[11,147,149,150] The decrease in total protein mass observed after dialysis is higher than the mass of the soluble fraction determined after the reaction. This raises the question about the stability of the aggregates upon prolonged dialysis. Amyloids and related aggregates are described as energy minima in the protein folding land-

scape.[15] However, it is known that a dynamic equilibrium exists between the aggregated and the soluble forms.[151–153] Thus, it is possible that the dialysis process induces a partial disaggregation of amyloids, and to a lesser extent of worms. Moreover, despite using low binding cellulose ester dialysis membranes, a small amount of protein could also be lost due to adsorption at the membrane, leading to the observed decrease in total protein concentration upon dialysis.

Zeta potential measurements providing indirect information about the charge density of the HEWL species (Supporting Information, Table S2) underline that different aggregation pathways lead to changes in the surface charge density of the formed particles. Zeta potential values for HEWL amyloid fibrils in 10 mM HEPES at pH 7.2 were 32.7 ± 1.0 mV and 30.2 ± 0.8 mV before and after sonication, respectively, whereas the free peptides (obtained by centrifugal ultrafiltration) had a zeta potential of 14.2 ± 0.2 mV. The worms and native HEWL had a zeta potential of 24.0 ± 0.6 mV and 13.3 ± 0.8 mV, respectively. The pH-dependent zeta potential of worms and dialyzed amyloids confirmed colloidal stability from pH 2 to 8 (Supporting Information, Figure S2).

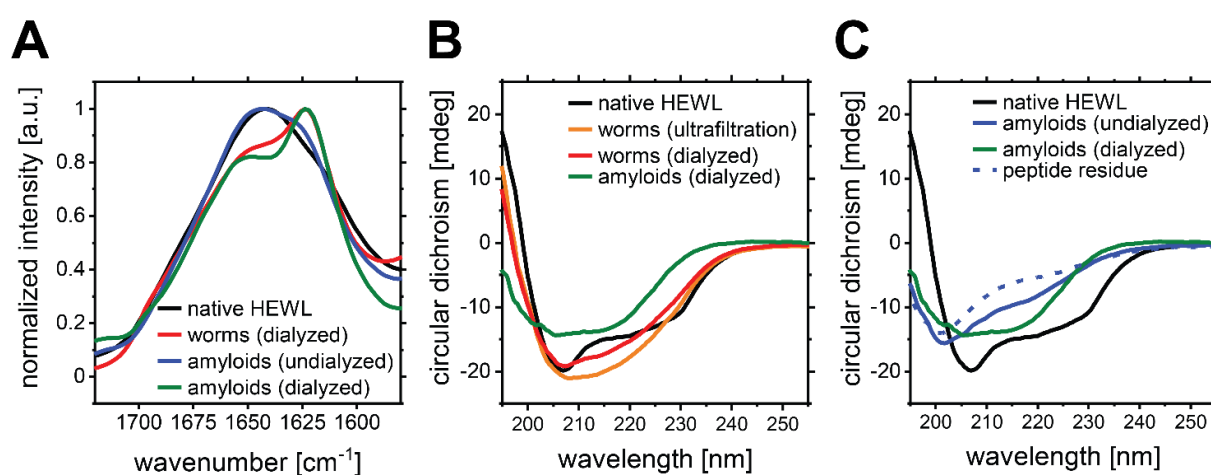


Figure 3: Secondary structure of HEWL aggregates determined by FTIR spectroscopy (A) and CD (B and C).

The structural properties of the various types of HEWL aggregates were investigated by FTIR and CD, which are complementary methods typically used to detect changes in the secondary structure of polypeptides (Figure 3, the full spectra can be found in Supplementary Information, Figure S3). Both techniques allowed for the detection of secondary structure changes between native HEWL and its aggregates, as well as an increase in β -sheet content after dialysis, consistent with the removal of non-aggregated species. In FTIR, the secondary structure of proteins can be estimated from the amide I infrared absorption band (1600-1700 cm^{-1}).^[154] For HEWL monomers, this band has its maximum at a wavelength where α -helices typically adsorb, at ca. 1656 cm^{-1} . Undialyzed amyloids show a prominent signal at around 1650 cm^{-1} due to the presence of a high fraction (65% in mass) of residual hydrolyzed peptides present in solution. Due to the aggregation conditions of pH 2 and 90 °C, these peptides occur in an unordered, random-coil conformation which is reflected by the position of the maximum FTIR signal. (Figure 3A). The shoulder at 1620 cm^{-1} is attributed to intermolecular β -sheets typical for amyloids,^[153,155,156] which become dominant in the spectrum of dialyzed amyloids. Dialyzed worms exhibit a spectrum similar to that of dialyzed amyloids, yet with a slightly higher α -helix contribution. The CD spectra (Figure 3B) are in good agreement with the FTIR data, showing a shift from the minimum at 208 nm attributed to the presence of α -helical structures in native HEWL to a stronger contribution at 218 nm stemming from β -sheets in the HEWL worms.^[157] Also in this case, an increase in β -sheet content was observed in the dialyzed amyloid samples. Indeed, the spectra of undialyzed amyloids and of a control sample containing only the soluble peptide fraction of the sample show a minimum at ca. 200 nm, which is typically observed in largely disordered peptides. The deconvolution of the CD spectra into secondary structure components performed with BeStSel^[139] and

CDPro[140] (CONTINLL) confirmed the transition to β -sheets in worms and the increase in β -sheet content after dialysis for amyloids (Supplementary Information, Table S3).

Antimicrobial activity of HEWL and its aggregates

In order to assess the antimicrobial potential of colloidal HEWL amyloid-like worms, dialyzed amyloids fibrils and peptide residue in comparison with native HEWL, the quantitative analysis of their antimicrobial activities were carried out using different microorganisms: Gram-positive *S. aureus*, Gram-negative *E. coli* and *P. aeruginosa* and the fungus *C. albicans*. These microorganisms were exposed to increasing concentrations of native HEWL, worms, dialyzed amyloid fibrils and peptide residue. Figure 4 shows the colony forming units per mL (cfu/mL) after 6 hours of treatment with the various HEWL species. In the case of *S. aureus*, all HEWL species, including native HEWL, reduced the colony forming units. Importantly, HEWL aggregates (i.e. both worms and amyloids) were more effective than the native protein and peptides at 0.01 mg/mL. However, both the amyloids and peptides eliminated all cells at the 10-fold higher concentration of 0.1 mg/ml. When tested against gram-negative *E. coli*, native HEWL and the worms only showed a 2-log reduction of the cell viability at 0.1 mg/mL, whereas the amyloids and the peptides achieved a 5-log reduction at the same concentration. Nevertheless, amyloids appear to be effective already at a concentration of 0.001 mg/ml, while peptides need to be added in higher amounts in order to detect an effect. The Gram-negative *P. aeruginosa* was more resistant to HEWL and its aggregates (possibly due to the complex nature of the extracellular matrix of these bacteria, which makes them less susceptible to various treatments[158]). Still, a 3-log reduction at 0.1 mg/mL was observed for dialyzed amyloids before and after sonication

(Supporting Information Figure S4). Finally, all HEWL species showed a similar anti-fungal effect against *C. albicans* with complete elimination at 0.1 mg/mL. The increase in the number of viable cells at 1 mg/mL for the aggregated HEWL species when tested against *S. aureus* and *E. coli* might be due to agglomeration of HEWL samples, leading to inhomogeneity and reducing the total surface area. Indeed, although, increased z-average diameters were found in DLS experiments for amyloid fibrils diluted at this concentration: 1670 ± 317 nm in HEPES (the buffer used in the antimicrobial assay), compared to 445 ± 4 nm in pH 2 MilliQ water. Shortening of the amyloid fibrils by sonication did not change the antimicrobial performance (Supporting information Figure S5).

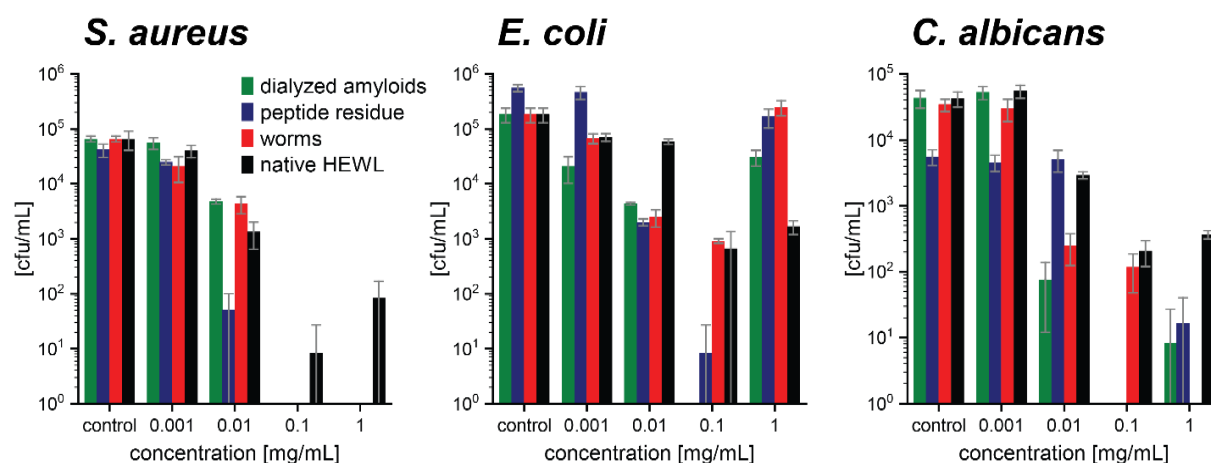


Figure 4: Concentration-dependent antimicrobial activity of dialyzed amyloids, peptide residue, worms and native HEWL against *S. aureus*, *E. coli* and *C. albicans*.

Minimum inhibitory concentrations (MIC) were also determined by measuring the re

growth of the microorganisms by means of optical density (Table 1, regrowth curves in Supporting information Figures S6, S7, S8 and S9). Overall, the MIC determined from the regrowth curves were in good agreement with the colony counting results. This analysis indicates that among the tested species, amyloids appear to be most effective

as broad-spectrum antimicrobial agents. The efficacy of HEWL amyloids becomes even more remarkable considering that 60% of the protein mass was converted into aggregates within these samples. Moreover, due to the large molecular weight of amyloids (megadaltons)[159] the particle concentration is most likely in the low nanomolar range for dialyzed amyloids, versus the micromolar concentration used here for native HEWL (0.1 mg/mL=7 μ M) and peptide residues. The considerable antimicrobial activity of the peptides can possibly be attributed to this high molar concentration, as well as to their net positive charge and hydrophobicity. Even though the amyloid samples contain 40% peptides by mass, the 3-log reduction observed only for the amyloids when tested against *S. aureus* at 0.01 mg/mL and the 1-log reduction against *E. coli* at 0.001 mg/mL indicate that the antimicrobial activity of amyloids cannot be solely attributed to the peptide fraction in equilibrium with the fibrils. Finally, as all experiments were performed at the same mass concentrations, the peptide concentration in the control samples is more than twofold higher than the one present in the amyloid samples.

Table 1: Minimum inhibitory concentrations (MIC) in mg/mL of dialyzed amyloids, peptide residue, worms and native HEWL against *S. aureus*, *E. coli* and *C. albicans* based on regrowth measurement.

	<i>S. aureus</i>	<i>E. coli</i>	<i>C. albicans</i>
dialyzed amyloids	0.01	0.1	0.1
peptide residue	0.01	0.1	0.1
worms	0.01	>1	0.1
native HEWL	0.1	>1	0.1

Overall, the antimicrobial performance of HEWL species against Gram-positive bacteria is in good agreement with results from literature. For amyloid fibrils MIC values of 0.01 mg/mL against *S. aureus*[58] and 0.05 mg/mL against *L. monocytogenes*[32] were reported earlier. To date, MIC values for TCEP-reduced HEWL aggregates in suspension have not been reported, most likely because of their propensity to precipitate in solution. Importantly, under our controlled assembly conditions, a MIC of 0.01 mg/mL of HEWL worms against *S. aureus* was obtained, which demonstrates that these particles are antimicrobial at low concentrations. The small size of colloidal worms leading to high mobility and high surface-to-volume ratio, might even be an advantage over densely packed solid-supported HEWL films formed under reducing conditions, which were able to kill 92% (1-log reduction) of *S. aureus* upon contact.[37] Instead, the antimicrobial potential of native HEWL has been monitored for concentrations up to 5 mg/mL against 25 strains of *S. aureus*, without finding complete inhibition of growth.[160] Due to their outer cell membrane, which protects the peptidoglycan cell wall, Gram-negative bacteria are insensitive to the catalytic antimicrobial activity of HEWL. However, 2-log[58] and 3-log[32] reduction of Gram-negative *E. coli* exposed to 0.05 mg/mL HEWL amyloid fibrils have been reported and attributed to fibril-bacteria interactions responsible for agglomeration of the bacteria and cell disruption. Aggregated HEWL films made by TCEP reduction killed 95% of *E. coli*.[37] Likewise, these films inhibited the growth of *C. albicans* by 94%. This does not come as a surprise, since the concentration-dependent antifungal activity of native lysozyme has long been known.[161]

Overall, the results presented here reinforce the notion that preserving enzymatic activity of HEWL is not necessary to maintain its activity as an antimicrobial protein. Rather, the mechanism used by HEWL amyloids to interact with bacteria seems to be due to electrostatic interactions between these highly cationic HEWL species and negative

charges present in the cell membranes and cell wall of the microorganisms.[37,47–49] The interaction between cells and the amyloid fibrils have been visualized by transmission electron microscopy and AFM imaging.[32,58] Zeta potential measurements of the HEWL species (Supporting Information, Table S2) underline the importance of positive charges for the antimicrobial effect. The differences in charge between the HEWL species could be the explanation for the improved antimicrobial activity of the aggregates over native HEWL. Furthermore, the unfolding of native HEWL during the aggregation might expose more non-polar amino acids leading to increased hydrophobicity of aggregated HEWL and peptides which could promote the interaction with cell membranes and lead to membrane disruption and cell lysis.[32,37,58] Another hypothesis is that the binding of lysozyme on receptors in the cell membrane could influence the regulation of autolytic enzymes in bacteria[47] and *C. albicans*.[161] The charge and hydrophobicity driven killing mechanism of lysozyme aggregates resembles the mode of action of the large group of cationic amphipathic antimicrobial peptides (AMP). Here, the binding of cationic and amphipathic AMP to negatively charged membranes, followed by membrane rearrangements and pore formation, lead to bacterial inactivation.[52,53] Another shared feature of amyloids and AMP is that they can self-assemble into supramolecular structures with immune ligands like DNA and RNA, which play a role in the mediation of immune responses.[162]

Our toolbox containing three different species of colloidal HEWL aggregates (long amyloid fibrils, sonicated amyloids and amyloid-like worms) shares common features with AMP. Apart from the gain in antimicrobial activity compared to native HEWL, the outstanding mechanical properties of HEWL aggregates might impart additional strength to a final composite material. Moreover, previous studies with mammalian cell cultures have shown that amyloid fibrils and worms are also non-cytotoxic and can therefore be considered biocompatible.[32,37,38,163] Furthermore, films of TCEP-reduced

HEWL had a positive effect on wound healing when tested on mice[37,38]. All these appealing properties could be exploited in the formation of new biomaterials. For instance, the colloidal and amphiphilic nature of amyloids allows for facile handling and a wide range of processes, such as self-assembly, interfacial self-assembly, layer-by-layer deposition etc. These processes could be used to form various types of biocompatible soft materials for wound healing applications, such as hydrogels, aerogels or coated films.

CONCLUSION

In summary, solution conditions were established to enable the comparison of different colloidally stable aggregates of HEWL, ranging from highly flexible worm-like particles to stiffer amyloids of different length. The aggregation kinetics of the worms was found to be strongly pH-dependent and stable suspensions could be achieved only at the lowest pH value tested (pH 4.5), where HEWL appears to aggregate in a more controlled fashion. Depending on the protocol used, the aggregation yield varied between 35 and 60% of the initial protein mass, which could be further improved by dialysis/ultrafiltration. In all cases, HEWL aggregation caused significant secondary structure changes, increasing the β -sheet content compared to the native protein. Despite lacking the enzymatic activity of native HEWL; HEWL aggregates showed an improved antimicrobial activity, with amyloids having broad-spectrum antimicrobial activity against Gram-positive and Gram-negative bacteria, as well as fungi. Minimum inhibitory concentrations were found in the range of 0.01 mg/mL against the relevant pathogens *S. aureus* and *C. albicans* for amyloids, peptide residue and worms. Amyloid fibrils also inhibited the growth of Gram-negative *E. coli* and caused a 3-log cfu reduction against *P. aeruginosa* at 0.1 mg/mL. The increased positive charge of the aggregates suggests a mode of action based on electrostatic binding to the cell walls and

membranes of the microorganisms, followed by membrane disruption. In conclusion, our data show that highly active antimicrobial species of different morphology can be prepared from a commercially available food protein such as HEWL, in a simple and up-scalable manner. These protein-based nanomaterials could be a viable alternative to existing antimicrobial agents (such as metal nanoparticles) for applications such as wound management, coatings for biomedical devices and food packaging, due to their macromolecular nature and good biocompatibility.

ASSOCIATED CONTENT

Supporting Information

The following files are available free of charge:

TCEP-induced aggregation kinetics at pH 5.5 and pH 6.5, overview of conversion of HEWL into aggregates, overview of zeta potential values of HEWL species, cfu-based antimicrobial activity measurements of HEWL species against *P. aeruginosa*, cfu-based antimicrobial activity measurements of sonicated amyloids against *S. aureus*, *E. coli*, *P. aeruginosa* and *C. albicans*, regrowth curves of *S. aureus* after exposure to HEWL species, regrowth curves of *E. coli* after exposure to HEWL species, regrowth curves of *C. albicans* after exposure to HEWL species, regrowth curves of *P. aeruginosa* after exposure to HEWL species (PDF).

AUTHOR INFORMATION

Corresponding Author

To whom correspondence should be addressed:

Dr. Silvia Campioni

Laboratory for Cellulose & Wood Materials

Empa – Swiss Federal Laboratories for Materials Science and Technology

Überlandstrasse 129

8600 Dübendorf, Switzerland

E-mail: silvia.campioni@empa.ch

Dr. Gustav Nyström

Laboratory for Cellulose & Wood Materials

Empa – Swiss Federal Laboratories for Materials Science and Technology

Überlandstrasse 129

8600 Dübendorf, Switzerland

E-mail: gustav.nystroem@empa.ch

Present Address

† Laboratory for Building Energy Materials and Components, Empa – Swiss Federal Laboratories for Materials Science and Technology, Überlandstrasse 129, 8600 Dübendorf, Switzerland

Notes

The authors declare no conflicts of interest.

ACKNOWLEDGEMENTS

The authors would like to acknowledge Jason Greenwald and Roland Riek from ETH Zurich for providing the CD spectrophotometer and Brian Sinnet from Eawag for his support with DLS. Mattia Usuelli and Massimo Bagnani (both ETH Zurich) are acknowledged for valuable discussions on amyloid fibers. Xavier Aeby is acknowledged for his help with the design of the TOC. The ThT fluorescence measurements were performed on a demonstration instrument (CLARIOstar Plus) kindly provided by BMG LABTECH. N.K., S.C. and G.N. would like to acknowledge financial support from Swiss National Science Foundation (grant no. 200021_192225). K.J.D. also acknowledges funding

from Natural Sciences and Engineering Research Council of Canada (NSERC) Post-doctoral Fellowship program. T.W. was supported by the China Scholarship Council (CSC).

Supporting Information for:

Self-assembly pathways and antimicrobial properties of lysozyme in different aggregations states

Nico Kummer^{1,2}, Tingting Wu^{1,3†}, Kevin J. De France¹, Flavia Zuber⁴, Qun Ren⁴, Peter Fischer², Silvia Campioni^{1}, Gustav Nyström^{1,2*}*

¹ Laboratory for Cellulose & Wood Materials, Empa – Swiss Federal Laboratories for Materials Science and Technology, Überlandstrasse 129, 8600 Dübendorf, Switzerland

² Institute of Food Nutrition and Health, Schmelzbergstrasse 7, ETH Zurich, 8092 Zurich, Switzerland

³ State Key Laboratory for Modification of Chemical Fibers and Polymer Materials, College of Materials Science and Engineering, Donghua University, Shanghai 201620, P. R. China

⁴ Laboratory for Biointerfaces, Empa – Swiss Federal Laboratories for Materials Science and Technology, Lerchenfeldstrasse 5, 9014 St. Gallen

* To whom correspondence should be addressed

E-mail: silvia.campioni@empa.ch; gustav.nystroem@empa.ch

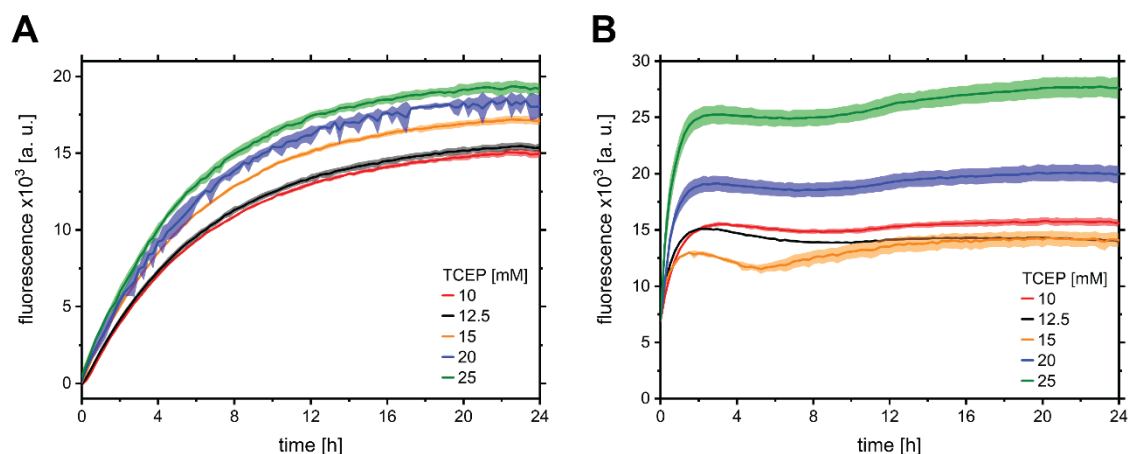


Figure S1: Amyloid-like aggregation kinetics measured by β -sheet-specific ThT fluorescence assay at different TCEP concentrations for pH 5.5 (A) and pH 6.5 (B).

Table S1: Conversion of native HEWL into worms and amyloid fibrils measured with 100 kDa MWCO centrifugal filters, 20 nm pore size syringe filters, the total protein in a sample after each step and the calculated overall loss of protein due to processing.

	Centrifugal filtration (100 kDa MWCO)	syringe (20 nm pore size)	total protein (mg/mL)	protein loss
Worms				
undialyzed	65.0%	not measured	1.0	
dialyzed (300 kDa MWCO)	79.4%	78.5%	0.5	50%
ultrafiltration (100 kDa MWCO)	76.6%	99.0%	0.65	34%
Amyloids				
undialyzed	34.4%	38.5%	20.0	
dialyzed (300 kDa MWCO)	57.5%	55.5%	4.5	78%
sonicated dialyzed (300 kDa MWCO)	59.6%	65.5%	4.8	75%

Table S2: Zeta potential of dialyzed amyloids, sonicated amyloids, peptide residue obtained after centrifugal filtration of amyloid samples, worms and native HEWL in 10 mM HEPES at pH 7.2.

	Zeta potential (mV)
dialyzed amyloids	32.7 \pm 1.0
sonicated amyloids	30.2 \pm 0.8
peptide residue	14.2 \pm 0.2
worms	24.0 \pm 0.6
native HEWL	13.3 \pm 0.8

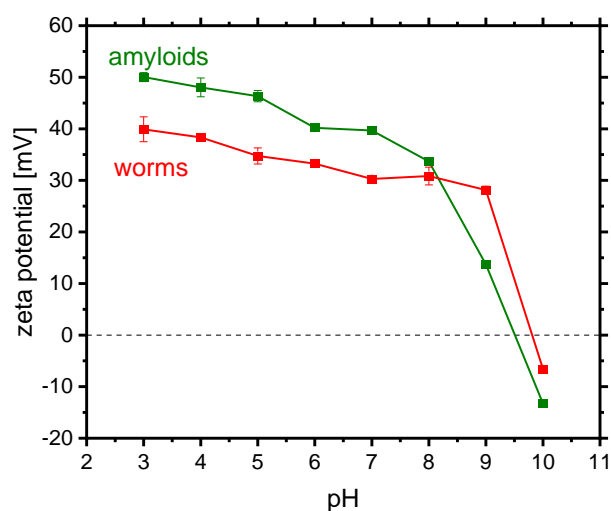


Figure S2: Zeta potential of dialyzed amyloids and worms in 5 mM NaCl as a function of pH.

Table S3: Secondary structure estimations for native HEWL, dialyzed worms, undialyzed and dialyzed amyloids and the peptide obtained through CD spectra deconvolution with BestSel and CDPPro (CONTINLL algorithm).

	BeStSel			CDPro (CONTINLL)		
	α -helix	β -sheet	others	α -helix	β -sheet	unordered
native HEWL	22.2%	19.8%	44.1%	98.4%	0.2%	0.0%
dialyzed worms	15.1%	22.7%	50.5%	92.8%	7.1%	0.0%
undialyzed amyloids	8.2%	28.4%	49.5%	21.6%	3.6%	60.4%
dialyzed amyloids	9.2%	35.9%	43.5%	24.7%	15.3%	28.7%
peptide residue	2.8%	38.9%	43.6%	18.6%	3.7%	70.5%

Note: Due to the unknown molecular weights of the non-native HEWL species, proper scaling and conversion of the data was impossible and compromises the deconvolution of the spectra that had to be made. BeStSel allowed the conversion of the CD data in millidegrees (mdeg) to molar ellipticity ($\text{deg}\cdot\text{cm}^2\cdot\text{dmol}^{-1}$). Independent of the aggrega-

tion state, all spectra were processed using a protein concentration of 14 μM (equivalent to 0.2 mg/mL native HEWL), 129 amino acid residues and a cuvette path length of 0.1 cm. The CDPro analysis was performed on the raw data in mdeg, using Database 7 containing 43 protein datasets and 5 datasets of denatured protein for better assessment of the aggregated samples containing short peptide fragments.

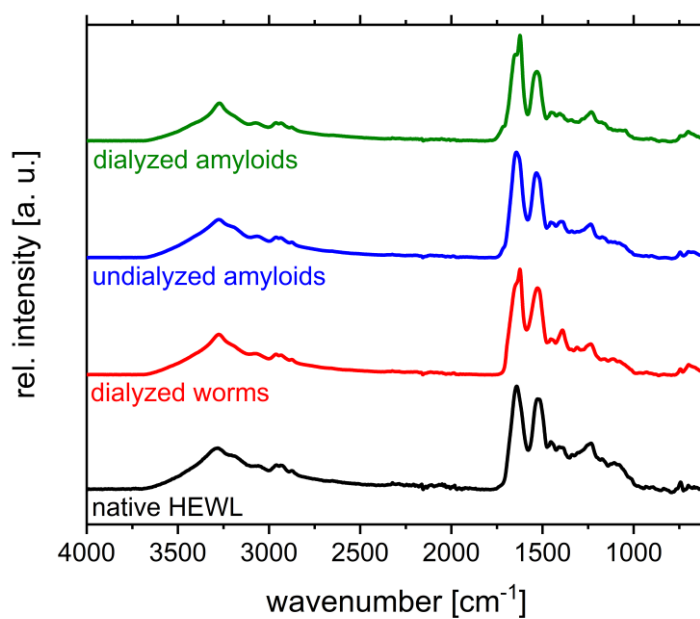


Figure S3: Full FTIR spectra of dialyzed and undialyzed amyloids, dialyzed worms and native HEWL.

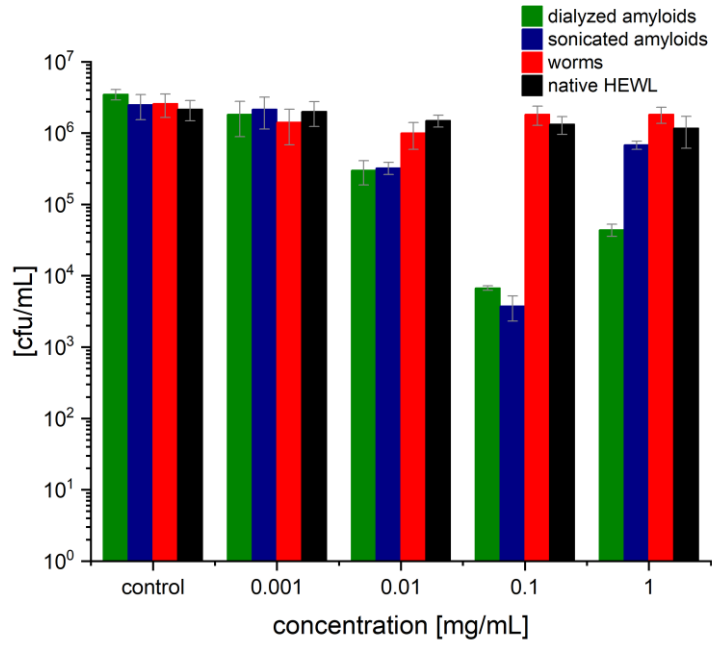


Figure S4: Concentration-dependent cfu-based antimicrobial activity measurements of dialyzed amyloids, sonicated amyloids, worms and native HEWL against *P. aeruginosa*.

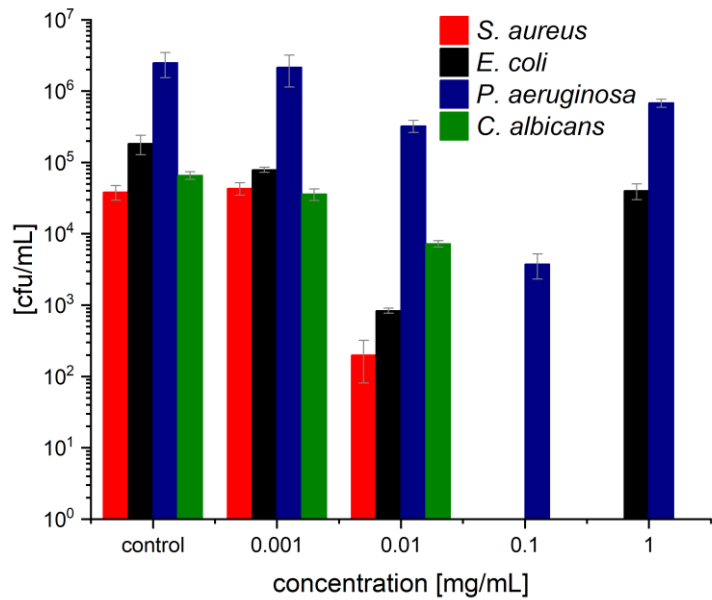


Figure S5: Concentration-dependent cfu-based antimicrobial activity measurements of sonicated amyloids against *S. aureus*, *E. coli*, *P. aeruginosa* and *C. albicans*.

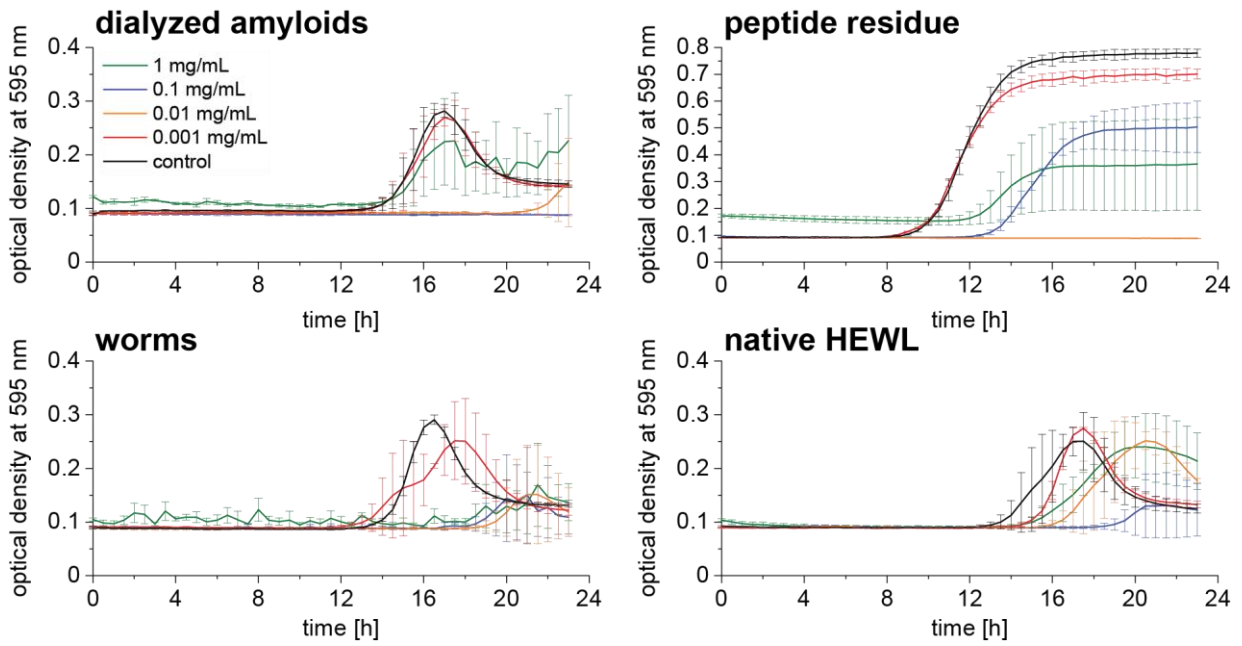


Figure S6: Optical density-based regrowth curves of *S. aureus* after 6 hours exposure to dialyzed amyloids, peptide residue, worms and native HEWL.

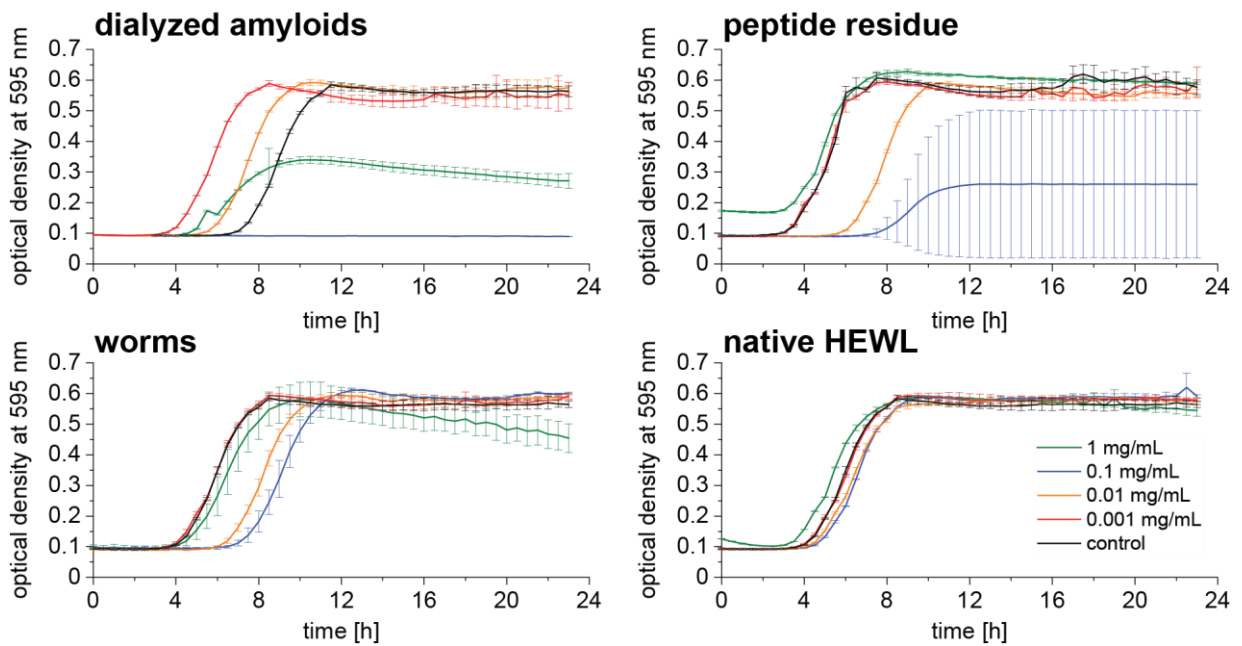


Figure S7: Optical density-based regrowth curves of *E. coli* after 6 hours exposure to dialyzed amyloids, peptide residue, worms and native HEWL.

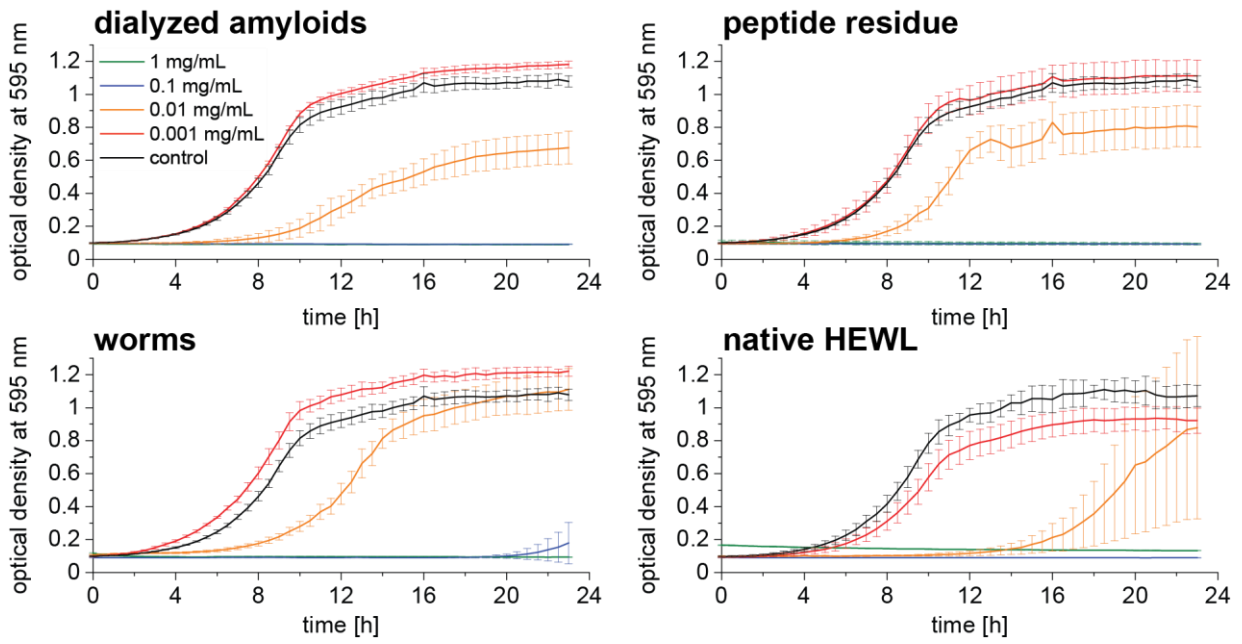


Figure S8: Optical density-based regrowth curves of *C. albicans* after 6 hours exposure to dialyzed amyloids, peptide residue, worms and native HEWL.

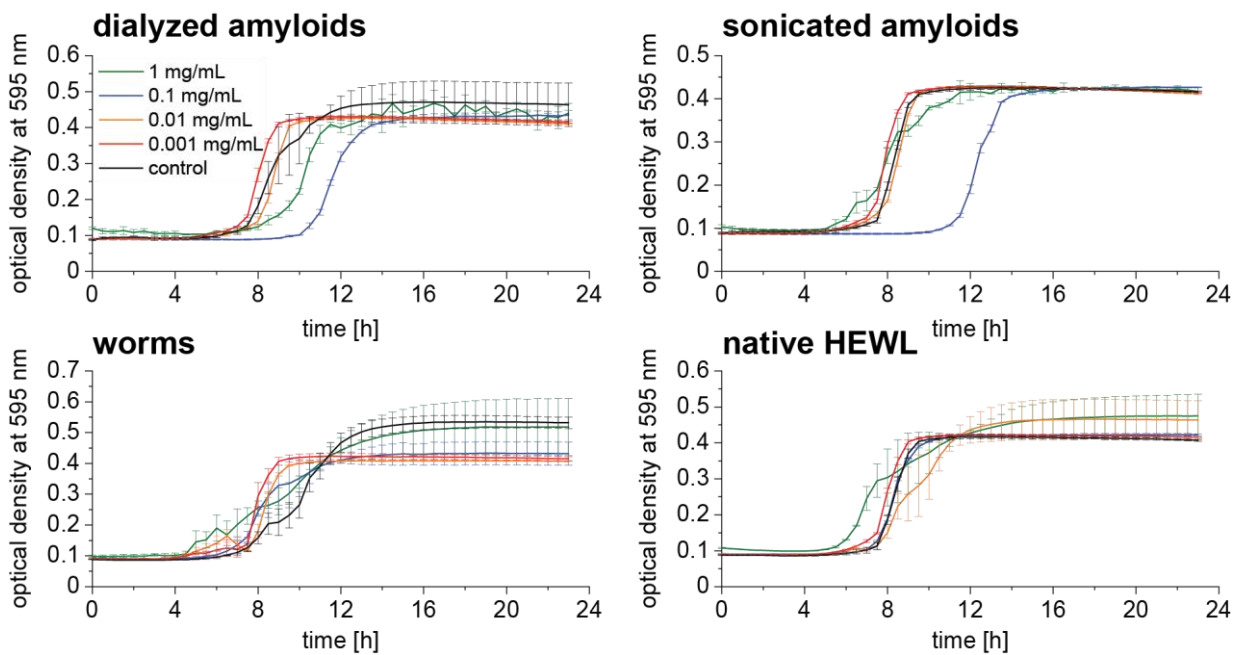


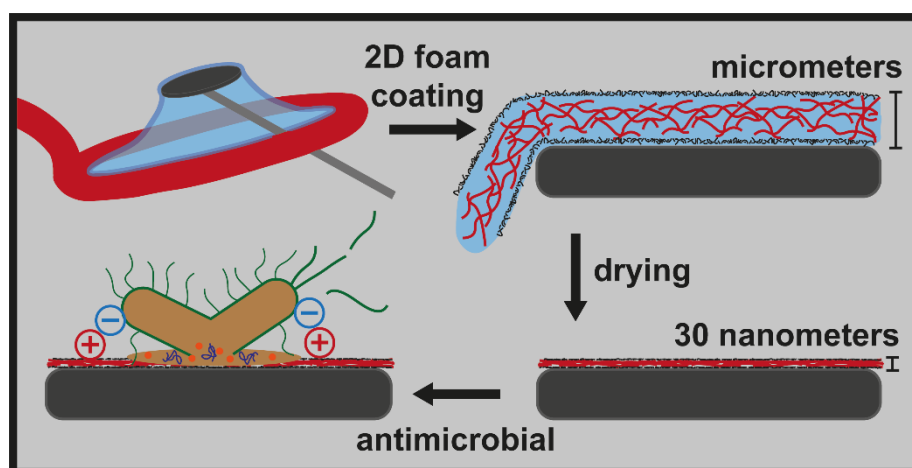
Figure S9: Optical density-based regrowth curves of *P. aeruginosa* after 6 hours exposure to dialyzed amyloids, sonicated amyloids, worms and native HEWL.

4 2D foam film coating of antimicrobial lysozyme amyloid fibrils onto cellulose nanopapers

Nico Kummer, Luc Huguenin-Elie, Adrian Zeller, Ashutosh Sinha, Yashoda Chandorkar, Flavia Zuber, Qun Ren, Jean Schoeller, Kevin de France, Peter Fischer, Silvia Campioni, Gustav Nyström

Nanoscale Advances, 2023, 5, 5276-5285

<https://doi.org/10.1039/D3NA00370A>



Reproduced with permission from authors and publisher

© 2023, Royal Society of Chemistry

2D foam film coating of antimicrobial lysozyme amyloid fibrils onto cellulose nanopapers

Nico Kummer^{1,2}, Luc Huguenin-Elie², Adrian Zeller², Yashoda Chandorkar³, Jean Schoeller^{4,5}, Flavia Zuber³, Qun Ren³, Ashutosh Sinha^{1,2}, Kevin De France^{1,#}, Peter Fischer², Silvia Campioni^{1,}, Gustav Nyström^{1,2,*}*

¹ Laboratory for Cellulose & Wood Materials, Empa – Swiss Federal Laboratories for Materials Science and Technology, Überlandstrasse 129, 8600 Dübendorf, Switzerland

² Institute of Food Nutrition and Health, Schmelzbergstrasse 9, ETH Zurich, 8092 Zurich, Switzerland

³ Laboratory for Biointerfaces, Empa – Swiss Federal Laboratories for Materials Science and Technology, Lerchenfeldstrasse 5, 9014 St. Gallen

⁴ Laboratory for Biomimetic Membranes and Textiles, Empa – Swiss Federal Laboratories for Materials Science and Technology, Lerchenfeldstrasse 5, 9014 St. Gallen

⁵ Institute for Biomechanics, Stefano-Francini-Platz 5, ETH Zürich, 8093 Zürich, Switzerland

* To whom correspondence should be addressed

present address: Department of Chemical Engineering, Queen's University, Kingston, Ontario K7L 3N6, Canada

E-Mail Gustav Nyström.: gustav.nystroem@empa.ch

E-Mail Silvia Campioni.: silvia.campioni@empa.ch

Abstract

Amyloid fibrils made from inexpensive hen egg white lysozyme (HEWL) are bio-based, bio-degradable and bio-compatible colloids with broad-spectrum antimicrobial activity, making them an attractive alternative to existing small-molecule antibiotics. Their surface activity leads to the formation of 2D foam films within a loop, similar to soap films when blowing bubbles. The stability of the foam was optimized by screening concentration and pH, which also revealed that the HEWL amyloid foams were actually stabilized by unconverted peptides unable to undergo amyloid self-assembly rather than the fibrils themselves. The 2D foam film was successfully deposited on different substrates to produce a homogenous coating layer with a thickness of roughly 30 nm. This was thick enough to shield the negative charge of dry cellulose nanopaper substrates, leading to a positively charged HEWL amyloid coating. The coating exhibited a broad-spectrum antimicrobial effect based on the interactions with the negatively charged cell walls and membranes of clinically relevant pathogens (*Staphylococcus aureus*, *Escherichia coli* and *Candida albicans*). The coating method presented here offers an alternative to existing techniques, such as dip and spray coating, in particular when optimized for continuous production. Based on the facile preparation and broad spectrum antimicrobial performance, we anticipate that these biohybrid materials could potentially be used in the biomedical sector as wound dressings.

Introduction

Due to its abundance, affordability, and antimicrobial activity hen egg white lysozyme (HEWL) is a promising candidate for the design of new materials to tackle the severe global health problem of antimicrobial resistance (AMR). Due to the excessive and incorrect use of small-molecule antibiotics, the evolutionary stress on bacteria has led

to the emergence of resistant strains.[132,133] Infections with multidrug-resistant strains are responsible for millions of deaths per year and pose a heavy financial burden on health care systems.[132,134] As such, the development of new materials and implementation of advanced treatment strategies to combat AMR is critical.

Lysozyme naturally occurs in the body fluids of many organisms including humans and contributes to protection against pathogenic bacteria.[40,41] This enzyme catalyzes the degradation of the outer cell wall of Gram-positive bacteria, thus mediating bacterial cell death. However, the antimicrobial potential of lysozyme is not limited to its enzymatic function.[47–49] Due to its high isoelectric point, lysozyme (not only in the native state, but also in denatured states, which do not show any enzymatic activity) is positively charged at neutral/physiological pH, and can therefore interact with the negatively charged bacterial cell walls and membranes, leading to cellular aggregation and eventual cell lysis.[48,49,51,164] Even aggregated forms of HEWL such as amyloid fibrils have demonstrated improved broad-spectrum antimicrobial activity, most likely due to a similar mechanism.[32,37,58,131] Amyloid fibrils are a class of protein aggregates notorious for their role in neurodegenerative diseases such as Alzheimer's or Parkinson's.[6] Research on disease-related misfolded proteins has revealed that they self-assemble into structurally similar morphologies, stabilized by a cross- β motif.[8] This self-assembly of hydrogen-bonded antiparallel β -sheets provides excellent mechanical properties and environmental stability to amyloid fibrils. These properties are exploited by many organisms in nature, particularly microorganism such as bacteria (curli fibers) and fungi (hydrophobin rodlets), to fulfill some functions that are in this case beneficial.[165] Even in humans, some examples of functional amyloids have been described, which are responsible for specific metabolic, storage and transport functions.[9] In the past twenty years, the generic capability of polypeptide chains to self-assemble into amyloids under determined conditions has been used to target a

wide range of applications such as water filtration, bioplastics, and biomedical engineering.[9,11,35,166,167] In some cases, amyloid fibrils have been obtained from inexpensive food proteins under acidic conditions and at high temperature, leading to the hydrolysis of the full-length chain into short peptide fragments, some of which are capable to self-assemble into a cross- β -structure.[11]

So far, the antimicrobial potential of HEWL amyloid fibrils has been assessed in suspension and in the form of coatings on a variety of materials to create antimicrobial surfaces and wound dressings.[32,37,57,59,61,104,131] HEWL amyloid fibrils show an enhanced antimicrobial effect and a broader spectrum of target organisms (Gram-positive and Gram-negative bacteria, fungi) compared to native HEWL (mostly active towards Gram-positive bacteria).[37,131] This is attributed to both the accumulation of positive charge in the HEWL amyloid fibrils which enhances electrostatic interactions with the bacteria and the amphiphilic nature of amyloids which enables penetration into bacterial membranes.[32,37,58,131] The antimicrobial properties of a material can be enhanced by coating its surface with the HEWL amyloid fibrils to expose as much positive charge as possible, rather than incorporating them into the bulk.[57] Amyloid coatings (not only with HEWL amyloids) have been achieved using different methods such as vacuum filtration,[57,166] dip coating,[37,168] or Langmuir-Schaefer/Langmuir-Blodgett[35] deposition.

In this work, we present a novel coating technique for amyloid fibrils, exploiting their tendency to adsorb at air-water interfaces (AWI) and lower the surface tension. Proteins are generally surface active due to their heterogeneous composition of amino acids, which vary in hydrophilicity.[62,63] As such, amyloid fibrils have been shown to efficiently stabilize multiphase systems such as foams and emulsions.[76] Foams are

dispersions of air bubbles within a solvent phase, whereby the solvent tends to organize into lamellae, separating individual air bubbles. This foam formation phenomenon is commonly observed when blowing bubbles through a wand. In this situation, a single foam lamella can be generated by pulling a ring/loop out of a soap solution containing surface active molecules. Similarly, Zhang and co-workers developed a coating method using the surfactant sodium dodecyl sulphate (SDS) to stabilize such a 2D foam film inside a loop. By adding different nanomaterials (silica, polystyrene, titanium dioxide, gold nanoparticles, graphene oxide, ferritin, and nanocellulose) to the SDS solution and pulling a silicon (Si) wafer through the 2D foam film, the surface was efficiently and homogeneously coated.[169] In this work the HEWL amyloid fibrils serve as both the surface active compound stabilizing the AWI of the 2D foam film and the functional nanomaterial to be coated onto different substrates. The adsorption of amyloid fibrils at the AWI leads to dense networks and potentially introduces alignment into 2D nematic phases.[74]

Using mechanically strong nanopapers made from TEMPO-oxidized cellulose nanofibrils (TO-CNFs) as a substrate resulted in a transparent hybrid film composed of bio-based and bio-degradable materials.[80,110] Nanocellulose is an ideal material for wound dressings, due to its high tensile strength, ability to absorb excessive liquid, while providing moisture to the wound and the possibility to incorporate drugs and nanomaterials.[170] CNFs have been used and commercialized as wound dressing materials due to their excellent bio-compatibility and ability to promote wound healing.[171] Combining bio-compatible[31] HEWL amyloid fibrils with nanocellulose introduces additional antimicrobial functionality to these hybrid materials intended for wound dressing applications.[57,104]

Herein, we present a coating method for HEWL amyloid fibrils based on their surface activity, enabling the formation of 2D films within a loop. The stabilization of the 2D interfaces was optimized according to bulk (3D) foam stability tests. Factors such as amyloid concentration, pH, and the composition of the amyloid suspension were assessed, in relation to foam stability. The thickness of each HEWL amyloid layer deposited onto silicon wafers was determined by atomic force microscopy and ellipsometry. The HEWL amyloid fibrils were also successfully coated onto TO-CNF nanopapers, as confirmed by SEM, AFM, FTIR and XPS spectroscopy, and surface ζ potential measurements. Finally, the antimicrobial activity of the amyloid-coated TO-CNF nanopapers was tested.

Materials and Methods

Materials

Hen egg white lysozyme (HEWL), (3-Aminopropyl)triethoxysilane (APTES), 4-(2-hydroxyethyl)-1-piperazineethanesulfonic acid (HEPES), tryptic soy broth (TSB), and plant count agar (PC-agar) were purchased from Sigma-Aldrich. Hydrochloric acid (HCl), sodium hydroxide (NaOH), and sodium chloride (NaCl) were obtained from VWR. Glucose was provided by Fluka. All chemicals were used as received without any further purification. The TO-CNF were prepared according to a procedure published previously by our group.[121]

Methods

Preparation of HEWL amyloid fibrils

The native HEWL (20 mg/mL) was aggregated using acid hydrolysis at pH 2 and 90°C. The samples were incubated in a Thermomixer (Eppendorf) for 24 hours under constant shaking (400 rpm). To quench the aggregation, the test tubes containing the freshly formed amyloid fibrils were cooled in an ice bath. Quantification of the conversion was performed using the method described in a previous publication by our group.[131] The concentration of the peptide fraction after ultrafiltration was measured with UV-Vis spectroscopy using the molar extinction coefficient of 38000 M⁻¹cm⁻¹.

Preparation of TO-CNF nanopapers

10 mL of 1.4 wt% TO-CNF suspension was dried at room temperature in a polystyrene petri dish (diameter 60 mm) in a dust-free environment. Due to the slow drying at low temperature, the nanopapers were flat and suitable for coating. For further experiments, the nanopaper was cut into smaller pieces using a razor blade. The nanopapers were mechanically characterized in tensile tests performed according to a previous publication.[172] The water sorption was tested gravimetrically by comparing the weight of a 1x1 cm² piece of nanopaper before and after immersion in MilliQ water for 48 h.

Foam film coating method

Inspired by the wands/loops used to blow bubbles, a loop with a diameter of 5 cm was 3D printed. With this loop, it was possible to pull out an amyloid film from a polystyrene Petri dish filled with a 1 mg/mL amyloid suspension at pH 6.

Foam stability experiments

The foam stability of the different amyloid fractions, i.e. the original mixed system containing amyloid fibrils and peptides and the separated pure fibrils and peptides obtained by ultrafiltration was tested. The foam stability of the different fractions were assessed at different concentrations and pH in a custom-made foaming setup. For the measurements, 2 mL of the amyloid suspension was foamed through the frit of a chromatography column with a nitrogen flow of 20 cm³/min to reach a column height of 8-10 cm. After the height was reached the main valve of the column was closed and the decay of the foam was monitored over time using a camera. An exponential decay function of the form

$$h_{foam}(t) = h_{foam}(0)e^{-\lambda t}$$

was fitted to the data, with h_{foam} being the foam height, t the time and λ the decay constant. The determined decay constant was used to calculate the foam half-life:

$$t_{1/2}(t) = \frac{\ln(2)}{\lambda}$$

The half-lives were determined for triplicates of each sample and are shown as the mean half-life including the standard deviation.

Interfacial adsorption experiments

The adsorption of amyloids and peptides at the air-water interface (AWI) was measured with a Wilhelmy balance setup (KSV Nima) equipped with a Langmuir-Blodgett trough and movable barriers according to Bertsch and co-workers.[173] After confirming the absence of contamination by closing the barriers without observing an increase in surface pressure, the trough was filled with 64.35 mL MilliQ water. The measurement was started after injecting 0.65 mL of amyloid mix and peptides adjusted to pH 6 and

at a concentration of 1 mg/mL. The final concentration of protein in the trough was 0.01 mg/mL. The change in surface tension $\gamma(t)$ compared to initial surface tension $\gamma(0)$ is defined as the surface pressure $\Pi(t) = \gamma(0) - \gamma(t)$ and was measured with a Wilhelmy plate made from filter paper.

Atomic force microscopy

All AFM images were obtained with a Bruker Icon 3 microscope equipped with RTESPA-300 probes for tapping mode. The resolution of all the images is 1024x1024 pixels, recorded at scan rates of 0.5 Hz. The thickness of the dry coating layers was measured on Si-wafers. After depositing 1, 2, and 3 layers of the foam film coating was scratched gently with a sterile syringe needle (without scratching the Si-wafer). The height difference between the Si-wafer and the coating was analyzed by extracting height profiles in 10 spots of three individual 10x10 μm^2 scans. To account for the tilt in the images and to account for roughness, linear functions were fitted for the Si-wafer background and the coating layer. The height of the coating was calculated by subtracting the y-axis intercepts of the linear functions. AFM imaging of the coated and uncoated side of the TO-CNF nanopapers was performed on a dried sample that was immobilized on a glass slide using carbon tape.

Variable angle spectroscopic ellipsometry (VASE)

The thickness of the dry coating on SI wafers was also determined using ellipsometry to complement the AFM data with a non-invasive method. A JAW M2000 (J A Woollam) variable angle spectroscopic ellipsometer that was equipped with a He-Ne laser source ($\lambda = 633 \text{ nm}$) was used for this purpose. The focusing lenses were at 50 °, 60 ° and 70 ° angles from the surface normal and in a range of 370 -1690 nm (0.7-3.3 eV) and

an integration time of 5 sec to record the amplitude (ψ) and the phase (Δ) components. Fitting of the raw data was performed using software CompleteEase based on a layered model using bulk dielectric functions for Si and SiO₂ of the substrate Si wafer. The amyloid fibril layer was analyzed on the basis of a Cauchy model of the form $n = A + B\lambda^{-2}$, where n is the refractive index and λ is the wavelength, and A and B were considered to be 1.450 and 0.0103 for transparent organic polymeric films.

Scanning electron microscopy

The morphology of the TO-CNF nanopapers with and without the amyloid layer was investigated by SEM. The samples were coated with a layer of platinum (~7 nm) before imaging with the FEI Quanta 650 FEG SEM (10.0 mm working distance, 5.0 kV accelerating voltage).

FTIR spectroscopy

The changes in the composition of the TO-CNF nanopapers with the amyloid coating was investigated via FTIR (Bruker Tensor 27 FT-IR) spectroscopy in attenuated total reflectance (ATR) mode. All spectra were recorded between 4000 and 600 cm⁻¹ with a resolution of 4 cm⁻¹ and 32 scans per sample. A background spectrum was measured before each measurement and subtracted from the sample spectra.

X-ray photoelectron spectroscopy

The atomical concentration at the surface of the specimens was measured using X-ray photoelectron spectroscopy (XPS). The measurements were performed on a Quantum 200 X-ray photoelectron spectrometer (Physical Electronics, MN, US) equipped with an Al K α monochromatic source. Survey and high resolution spectra

were acquired at a pass energy of 117.4 eV and 29.35 eV, respectively. Tougaard backgrounds were subtracted to measure peak intensities.

Suspension ζ potential measurements

The ζ potential measurements were conducted in triplicate utilizing a Malvern Zetasizer nano ZS with a folded capillary cell, and the reported values are the mean and standard deviation of the three measurements. The concentration of the TO-CNF and amyloid containing samples was 0.1 mg/mL, the pure peptide sample (obtained by ultrafiltration, as described above) was measured at a concentration of 1 mg/mL. All samples were measured in MilliQ water containing 1 mM NaCl for better conductivity during the measurements.

Surface ζ potential measurements

The surface ζ potential of the nanopapers was characterized using an Anton Paar Surpass 3 electrokinetic flow-through ζ potential instrument (Anton Paar, Austria). The dry film samples were slightly pre-wetted on the unexposed side of the nanopaper during the measurement and placed in a clamping cell. The system was rinsed with an electrolyte solution (1 mM KCl in milliQ at pH 7) and measured at the ideal gap height of 100-120 μm . The ζ potential was calculated using the formula

$$U_{\zeta} = \frac{\Delta U}{\Delta p} \cdot k_B \cdot \frac{\eta}{\varepsilon_0 \varepsilon_r}$$

where ΔU is the potential difference, Δp the gap-dependent pressure difference, k_B the Boltzmann constant, η the viscosity of the electrolyte, ε_0 the permittivity in vacuum, and ε_r the relative permittivity of the electrolyte.

Antimicrobial activity testing

The coated TO-CNF nanopapers were tested for their antimicrobial activity against common pathogenic strains, namely Gram-positive *Staphylococcus aureus* (ATCC 6538), Gram-negative *Escherichia coli* (DSMZ 1576), and the fungus *Candida albicans* (ATCC 90028). The pre-cultures were prepared according to a previous publication,[131] and diluted to optical densities of 0.01 (*S. aureus* and *E. coli*) and 0.1 (*C. albicans*) using 10 mM HEPES buffer at pH 7.2. The coated TO-CNF nanopapers were cut into samples with a diameter of 5 mm using a biopsy punching tool. The samples were placed into 48-well plates with the active amyloid coated side facing 5 μ L of bacterial culture prepared at the bottom of each well. The samples were incubated for 4 h at room temperature in humidified air to prevent the drying of the samples. After the incubation, 200 μ L HEPES buffer were added and the samples were sonicated for 5 min and vortexed for 15 s to detach the microorganisms. The 200 μ L were then transferred to a fresh 96-well plate to prepare a dilution series down to 10^{-3} . Aliquots of 20 μ L were dropped onto PC-Agar plates, and incubated at 37°C overnight, before counting the colony forming units (CFU). Each sample was tested in triplicate, the antimicrobial activity is reported as the mean growth in CFU/mL including the standard deviation. The killing ratio was calculated as the ratio between the CFU of the coated sample and the uncoated TO-CNF controls.

Results and Discussion

The 2D foam coating

When air is dispersed into a HEWL amyloid fibril suspension, for example by shaking, stable foams are formed. Occasionally, a big bubble spanning the entire rim of the vial

can be observed after opening the lid. Seeing this bubble brought back childhood memories of blowing soap bubbles and gave inspiration to try to blow amyloid fibril bubbles. While creating a 2D amyloid-stabilized film was successful by pulling out the amyloid suspension using a custom-made loop (**Figure 1A**), blowing the film into a bubble was unsuccessful, as the film burst upon blowing. However, the 2D film was successfully transferred onto a silicon wafer (**Figure 1B**) and subsequently dried under ambient conditions to form a homogenous, ultra-thin HEWL amyloid fibril coating (**Figure 1C**).

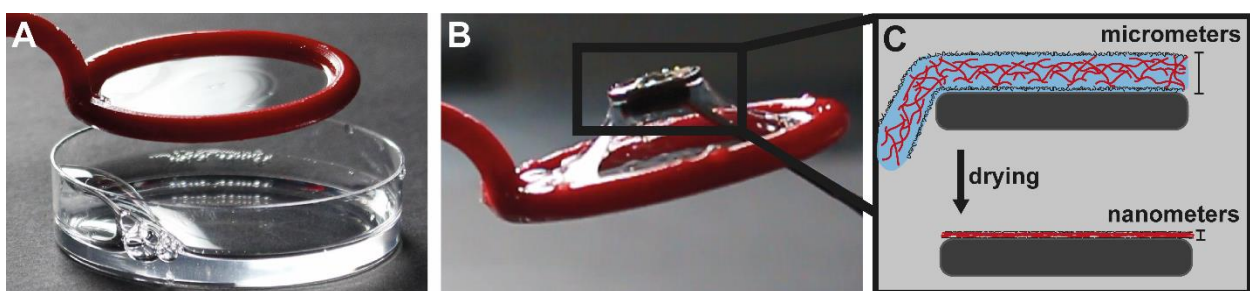


Figure 9: Photo of the 2D HEWL amyloid fibril film spanning the inside of a 3D printed loop (A). Transfer of the elastic 2D foam film onto a substrate (B). Schematic showing the micrometer thick wet deposited foam film compressing into a nanometer thick dried coating on a substrate (C).

Optimization of the foam stability

To optimize the stability of the 2D amyloid fibril foam film inside the loop, a foaming device was created using a fritted chromatography column (**Figure 2A**). By streaming nitrogen at a fixed flux through the frit, the amyloid suspensions were foamed at different concentrations and pH values. At pH 6, the HEWL amyloid fibril foam stability was strongly dependent on the amyloid concentration with foam half-lives in the order of 1 min at 0.1 mg/mL, 1 h at 0.5 mg/mL, and several hours at 1 mg/mL (**Figure 2B**). **Figure 2C** shows the foam stability of the amyloid suspensions at 0.5 mg/mL and at different pH. At pH values lower or equal to 4, a foam was either not obtained at all or highly unstable. The foams only became stable at pH values of 6 and higher. However, at pH 8, small agglomerates of amyloid fibrils were visible to the naked eye (**Figure**

S1). Finally, at constant pH of 6, different fractions, referred to as the original amyloid mix (consisting of 40% fibrils and 60% peptides[131]), and the pure fibrils and the pure peptides (separated by ultrafiltration), were compared (**Figure 2D**). The foam half-lives of the amyloid mix and the pure peptides were similar, while the pure amyloid fibrils did not form stable foams. This finding was also confirmed with surface pressure (Π) measurements in **Figure 2E**, which showed a similar adsorption isotherm for the amyloids mix and the peptide fraction alone. These two experiments lead to the conclusion that the peptides rather than the amyloid fibrils are the species responsible for interfacial stabilization. **Figure 2F** illustrates the amyloid self-assembly pathway mediated by acid hydrolysis of the native protein into short peptide fragments. Only some of these take part in the self-assembly into amyloid fibrils, while the rest remain in the sample as free peptides. The conversion of HEWL into amyloid fibrils and possible purification strategies were discussed in detail in our previous publication.[131] Based on the foam stability and surface pressure measurements (**Figures 2D** and **2E**), which are in good agreement with other findings from literature,[76] we propose the stabilization of the air-water interface by the peptides (illustrated in **Figure 2G**). In agreement with results from amyloid systems made from soy protein isolate, it is thus not the actual amyloid fibrils that stabilize the AWI, but rather the free peptides.[76] In addition to the much lower molecular weight of the peptides, which enables faster diffusion and adsorption to the interface compared to the fibrils,[76] there might be two more factors promoting peptide adsorption. Peptides largely consist of a disordered/unfolded structure,[131] with unfavorably exposed hydrophobic patches enhancing the amphiphilic properties and causing a higher surface activity. Moreover, it was shown that the unfolding of native HEWL adsorbed at the air-water interface (induced by the reduction of disulfide bond by the reducing agent dithiothreitol) resulted in more elastic interfacial layers.[64]

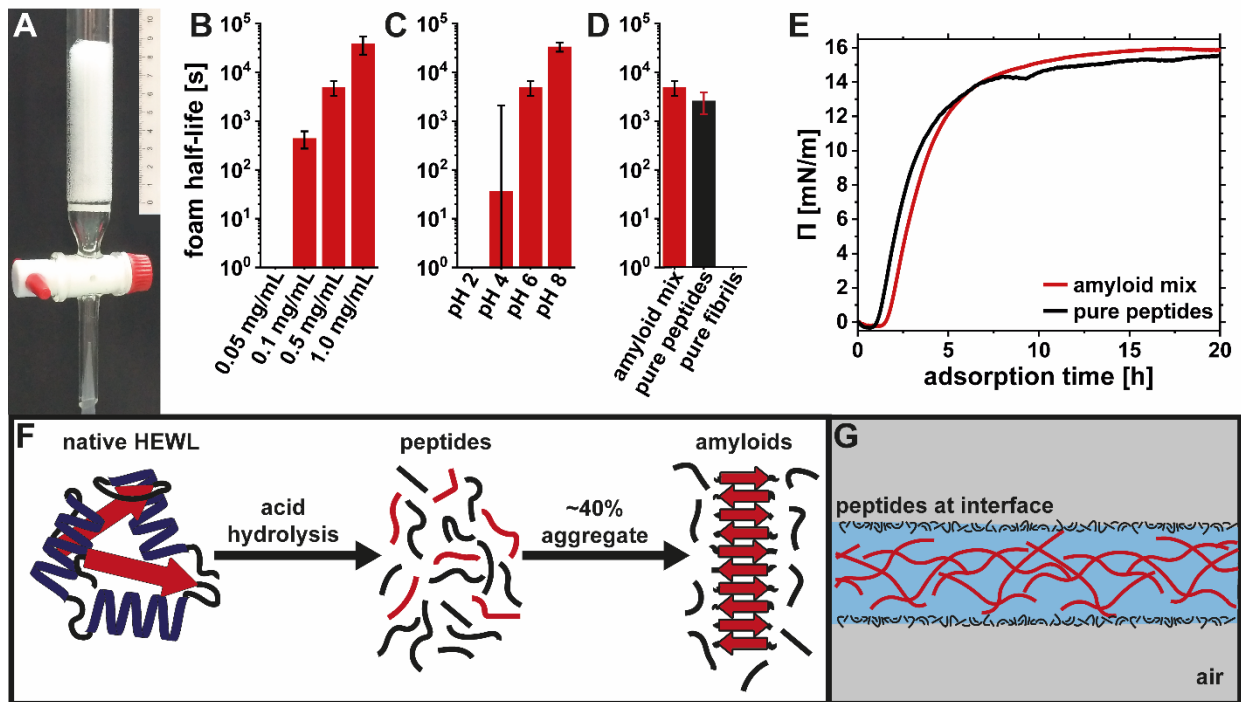


Figure 10: The setup used to measure foam stability consisted of a chromatography column. The samples were foamed by dispersing nitrogen through the frit (A). Amyloid mix foam half-life in dependence of concentration (B) and pH (C). The amyloid mix was separated into pure peptides and pure fibrils using ultrafiltration to measure their individual contribution to foam stability (D). Surface pressure measurement showing similar adsorption kinetics for the amyloid mix and the pure peptides (E). Amyloid self-assembly pathway using acid hydrolysis (F). Schematic illustrating that the air-water interface is stabilized by peptides, while the amyloid fibrils form a network within the foam lamella (G).

Additionally, the ζ potential of the peptides is lower than that of the fibrils (**Figure S2**), which reduces the adsorption barrier caused by the double layer repulsion between adsorbed peptides at the interface and peptides in the bulk. This adsorption barrier is also the reason for the reduced adsorption of the HEWL amyloid mix and the resultant weak foams at low pH. Below pH 4, the charge of the system is dominated by the repulsive forces between the different protonated basic amino acids (arginine, histidine and lysine). Negative charges are introduced with the deprotonation of the acidic amino acids, above their pK_a of around 4. Even though no drastic decrease in positive charge

can be observed in the pH-dependent ζ potential measurements (**Figure S2**), the negative charge from the acidic amino acids will cause local attraction and facilitate peptide adsorption. At pH 6, the acidic amino acids are fully deprotonated and therefore the double layer repulsion and the connected adsorption barrier are reduced, enabling more stable foams. The half-life of the foam at pH 8 was even higher. However, aggregates in the 2D foam film could be seen by eye due to too much attraction, which would also cause inhomogeneity in the foam film coating. Therefore, the optimized conditions for the coating were an amyloid concentration of 1 mg/mL and pH 6. Additional treatment of the amyloid mix, such as dialysis or ultrafiltration to reduce the relative amount of peptides in the system were omitted, to have the full surface activity provided by the peptides. Note that the results below were all generated with the crude amyloid system (without further purification) and referred to as amyloids or amyloid fibrils.

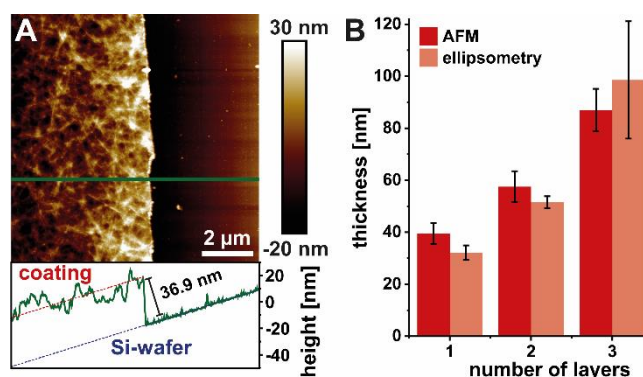


Figure 11: Thickness measurement of one amyloid fibril coating layer on Si-wafer by scratching off the coating on the right side of the image and measuring the step height using AFM (A). Comparison of thickness measurements using AFM and variable angle spectroscopic ellipsometry (VASE) (B).

Thickness measurements on HEWL amyloid coating on silicon wafers

Using the optimized conditions of the HEWL amyloid suspension, the stable 2D foam films were reproducibly coated onto Si-wafers and dried under ambient conditions. After the coating was completely dried, additional layers could be added to tune the thickness of the coating. The thickness of the coating after applying one, two, and three layers of HEWL amyloids was measured by AFM and ellipsometry (**Figure 3**). The AFM image in **Figure 3A** shows the coating on the left side, while the Si-wafer background exposed by scratching the coating with a syringe needle can be seen on the right side. The green line indicates the position at which the profile shown below the AFM image was measured. The coating thickness was measured by subtracting the average height of the background from the average height of the coating (including tilt correction). The measured thickness values as a function of number of coating layers determined by AFM and ellipsometry are summarized in **Figure 3B**. This demonstrates that layer-by-layer deposition with drying steps between the individual coating steps resulted in a discrete increase in layer thickness of around 30 nm with each additional layer. Notably, drying artifacts such as the coffee ring effect are reduced due to the amyloid fibril network present in the deposited wet films (**Figure S3**). The fibril network maintains its structure and densifies as the apparent amyloid fibril concentration increases upon evaporation of water.

Characterization of the HEWL amyloid fibril coating on TO-CNF nanopapers

To create a fully bio-based and bio-degradable material with antimicrobial properties, the foam film coating was successfully applied to dried TO-CNF nanopapers. The stress-strain curves from tensile testing of the nanopaper (**Figure S4**) and a summary of the derived mechanical properties (**Table S1**) are in good agreement with existing

literature for mechanically strong dry nanocellulose films.[110,172] The homogenous deposition of the foam film was confirmed with SEM and AFM imaging (**Figure 4**). The smooth surface of the TO-CNF nanopaper was clearly covered with amyloid fibrils after drying the deposited amyloid layer.

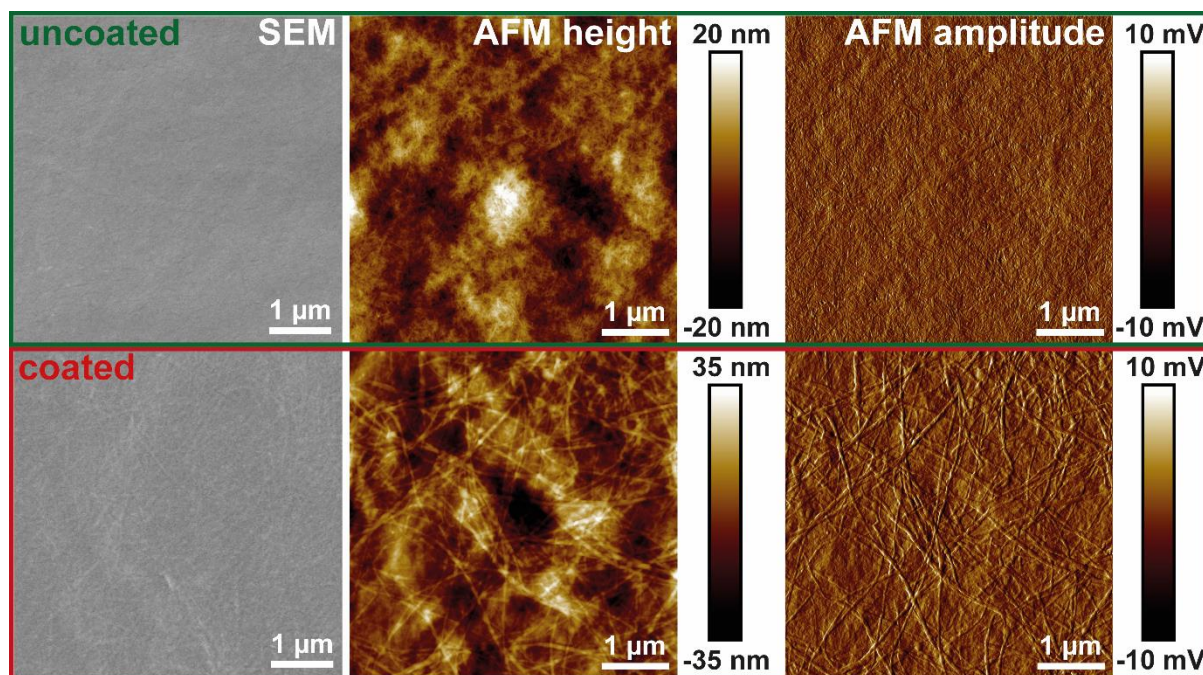


Figure 12: Morphology (SEM, AFM height and amplitude imaging) of TO-CNF nanopapers uncoated (upper panels) and coated (lower panels) with amyloid fibrils using the foam film coating method.

Thickness measurements of the coating could not be performed on the TO-CNF substrate, as scratching only the amyloid layer was not feasible and because the refractive indices of protein and cellulose are too similar to perform meaningful ellipsometry measurements. Instead, the surface chemistry of the coated nanopapers was characterized using FTIR spectroscopy, XPS, and surface ζ potential measurements. **Figure 5A** shows the IR spectrum of an uncoated TO-CNF nanopaper and after the deposition of the HEWL amyloid fibril coating in the region between 1450 and 1750 cm^{-1} (full spectra can be found in **Figure S5A** and **S5B**). The relevant peaks in this region are the C=O stretching vibration from deprotonated carboxyl groups of TO-CNF (1612 cm^{-1}

¹)[174] and the amide I (1650 cm^{-1}) and amide II (1550 cm^{-1}) contributions of the HEWL amyloid coating.[175] With the addition of the HEWL amyloid fibrils, a shoulder in the amide I region around 1650 cm^{-1} was observed, which can be attributed to the increase in protein content.[131,175] The uncoated side of the TO-CNF nanopaper shows a slight increase of absorbance in the amide II region, which might be due to the absorption of excess liquid containing peptides into the bulk of the TO-CNF nanopaper. Due to the absorption of peptides into the sample and the penetration depth of the infrared radiation in the order of micrometers,[176] protein was even detectable when measuring the uncoated side of the TO-CNF nanopaper. **Figure 5B** shows XPS spectra providing complementary information about the chemistry at the immediate surface (penetration depth $\sim 10\text{ nm}$).[177] As expected, the spectrum for the uncoated side TO-CNF side of the nanopaper was dominated by the C 1s (284 eV), and O 1s (532 eV) peaks, whereas the N 1s (398 eV) appeared after depositing the HEWL amyloid fibril coating. The elemental composition of the coating layer was 69 % carbon, 18 % oxygen and 13 % nitrogen, which are values typically found for protein layers.[178] The uncoated side contained around 1 % of nitrogen as well, which is likely due to the absorption of peptides mentioned above. Changes in the surface charge of the coated nanopapers were confirmed with surface ζ potential measurements (**Figure 5C**). The negative potential (-2 mV) of the uncoated TO-CNF nanopapers turned positive after the deposition of the amyloid coating layer ($+1\text{ mV}$). Importantly, the ζ potential values from surface measurements and suspension measurements at pH 7 (**Figure 5D**) are only comparable qualitatively and not in terms of absolute values. This is due to the reduced specific area of the measured surfaces as well as the different morphologies compared to the suspension and the fundamentally different measurement setup. Fur-

thermore, the high pressure during the rinsing step and the surface ζ potential measurement might shear off some of the adsorbed amyloids on the surface of the TO-CNF resulting in underestimation of the surface ζ -potential.

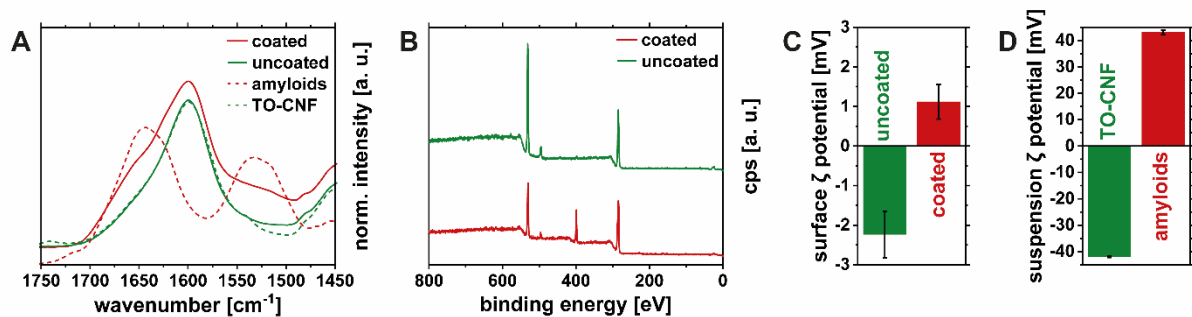


Figure 13: Surface characterization of TO-CNF nanopapers without (green) and with (red) the amyloid fibrils deposited with the foam film coating method. FTIR spectra of each side of the coated nanopaper (continuous lines) and reference spectra corresponding to pure TO-CNF and amyloids (dashed lines) (A). XPS spectra of uncoated and coated samples, with a nitrogen peak accounting for 13% of the elemental composition (B). Surface ζ potentials of uncoated and coated TO-CNF nanopapers (C) compared to ζ potentials of TO-CNF and amyloid suspensions at pH 7 (D).

The stability of the HEWL amyloid coating on the TO-CNF nanopapers was assessed by immersing a triplicate of samples in MilliQ water for 48 hours. Ultraviolet-visible (UV-vis) spectroscopy of the MilliQ water showed that the released material was mostly TO-CNF, which could also be seen by AFM imaging of the solution (**Figure S6**). Despite the lack of a pronounced protein signal in the UV-vis spectrum, some peptides could be seen in AFM as well, but no amyloid fibrils. These findings indicate that the TO-CNF nanopapers might not be stable enough for further use as wound dressing materials and require physical or chemical cross-linking to grant stability/integrity and improve the mechanical properties. However, AFM imaging of the amyloid-coated nanopapers after immersion in MilliQ water for 48 h confirmed the stability of the HEWL amyloid fibril coating (**Figure S7**). This can be explained by the good adhesion of the positively charged HEWL amyloids on the negatively charged TO-CNF,^[179] as well

as the entanglement of the fibril network, allowing only for the release of unreacted peptides but not the amyloid fibrils.

The hybrid HEWL amyloid coated TO-CNF nanopaper could potentially be used as a wound dressing, due to its high tensile strength, biocompatibility, transparency allowing to monitor the wound and its ability to control the moisture of the wound.[171] Another more cost-effective way to prepare a hybrid wound dressing using the HEWL-amyloid 2D foam coating could be its application onto other cellulose-based wound care materials like gauzes.[38]

Antimicrobial activity of the HEWL amyloid fibril coating

After confirming the successful and homogenous coating of TO-CNF nanopapers with the positively charged HEWL amyloid fibril layer, the antimicrobial activity of the hybrid material was investigated. The samples coated with HEWL amyloid fibrils were tested against *S. aureus* (Gram-positive bacteria), *E. coli* (Gram-negative bacteria) and *C. albicans* (pathogenic yeast). The TO-CNF nanopaper coated with HEWL amyloid fibrils showed a broad-spectrum antimicrobial effect against all the pathogens tested (**Figure 6A** and **6B**). The highest reduction of microbial growth, of almost 3 orders of magnitude compared to uncoated TO-CNF nanopaper (99.6% killing ratio), was observed against *S. aureus*. The reduction of *E. coli* and *C. albicans* was below 1 order of magnitude, corresponding to 82% and 72% killing efficiency, respectively. These results are qualitatively in good agreement with our previous study assessing antimicrobial potential of HEWL amyloid suspensions.[131] A similar broad-spectrum antimicrobial activity was found in both cases, with the best activity against *S. aureus* and higher concentrations needed to inhibit the growth of *E. coli* and *C. albicans*, which is in agreement

with other literature as well.[32,58] A direct quantitative comparison of the amyloid suspensions and the coating surface is difficult, since the experimental approaches for testing the antimicrobial activity differ fundamentally. Due to the substantially reduced surface area in the coating layer compared to amyloids in suspension, the exposure of the bacteria to positively charged groups is decreased, which is also supported by the ζ potential data. However, the broad-spectrum antimicrobial effect can still be linked to the interactions between the positively charged amyloid fibrils and the negatively charged cell wall and cell membrane of the microbial cells (**Figure 6C**). This antimicrobial mode of action based on positive charge has been proposed before for amyloid fibrils[32,58] and seems to be a common feature among cationic polymers[54,180] and also plays a role for the antimicrobial activity of cationic antimicrobial peptides.[181] In our previous publications we observed antimicrobial activity of the peptide fraction.[131] As discussed above, there is a release of peptides from the HEWL amyloid coating, which might also contribute to the antimicrobial effect through diffusion into the bulk medium.

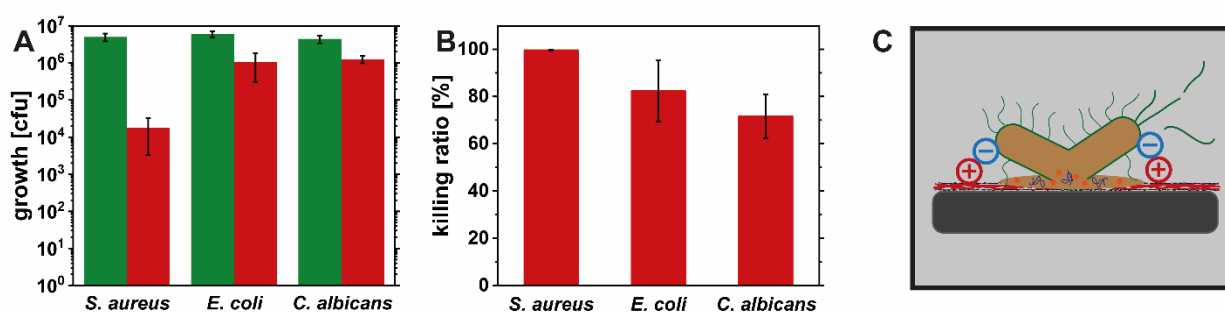


Figure 14: Antimicrobial activity of the uncoated TO-CNF nanopapers (green bars) and coated (red bars) with HEWL amyloid fibrils, expressed as microbial growth in CFU after 4 h of incubation (A). The same data expressed as killing ratio (B). Schematic illustrating the proposed mode of action based on electrostatic interactions between the positive charges of the coating and the negative cell walls and membranes of microorganisms leading to their rupture and the death of the microorganisms (C).

Conclusion

We report the successful use of 2D foam films based on HEWL amyloids as a coating method. The adsorption of HEWL amyloid fibrils at the air-water interface is concentration and pH dependent and actually dominated by the contribution of unconverted peptides present in the suspension. Therefore, the interfaces are effectively stabilized by the peptides, while the amyloid fibrils remain in the bulk of the foam lamella in the form of a network. The 2D foam film coating is a facile way of coating amyloid fibrils onto various substrates and offers tunability of the coating thickness by layer-by-layer deposition. The homogeneity of the coating was confirmed by SEM and AFM imaging, as well as spectroscopy techniques (FTIR and XPS). The 30 nm thick HEWL amyloid fibril coating is thick enough to shield the negative charge of the TO-CNFs as seen in surface ζ potential measurements of the coated nanopaper. Importantly, the HEWL amyloid coating resulted into functionalization of TO-CNF nanopaper, which showed broad-spectrum antimicrobial activity against *S. aureus* (Gram-positive), *E. coli* (Gram-negative) and *C. albicans* (pathogenic yeast) based on interactions between the positive charges of the HEWL amyloids and the negatively charged cell walls and membranes of the microbes leading to their disruption. The antimicrobial effect was strongest against *S. aureus* (3-log reduction of growth compared to uncoated TO-CNF nanopapers), while for *E. coli* and *C. albicans* the reduction was less than 1-log reduction. Our results indicate that for surface active proteins and protein aggregates the foam film coating potentially offers an alternative to other coating mechanisms, such as dip coating or spray coating, especially if it can be optimized to make the process continuous. The HEWL amyloid coated TO-CNF nanopapers are particularly attractive for their use as bio-based and, bio-compatible and bio-degradable wound dressing material, with an additional antimicrobial functionality. Overall, our findings offer a promising

alternative to traditional coating methods and contribute to the development of innovative biomedical materials.

Electronic Supporting Information (ESI)

pH-dependent ζ potential of the different amyloid species, stress-strain curves of the tensile tests of TO-CNF nanopapers, table with an overview of the derived mechanical properties, full FTIR spectra of coated and uncoated samples, control experiments on amyloid release from coating by UV-vis spectroscopy and AFM.

Author Contributions

Nico Kummer: Conceptualization; Data curation; Formal analysis; Investigation; Methodology; Project administration; Validation; Visualization; Writing - original draft

Luc Huguenin-Elie: Formal analysis; Investigation; Methodology; Validation; Writing - review & editing

Adrian Zeller: Formal analysis; Investigation; Methodology; Validation; Writing - review & editing

Yashoda Chandorkar: Formal analysis; Investigation; Methodology; Validation; Writing - review & editing

Jean Schoeller: Formal analysis; Investigation; Methodology; Validation; Writing - review & editing

Flavia Zuber: Formal analysis; Investigation; Methodology; Validation; Writing - review & editing

Qun Ren: Methodology; Supervision; Validation; Writing - review & editing

Ashutosh Sinha: Formal analysis; Investigation; Methodology; Validation; Writing - review & editing

Kevin De France: Formal analysis; Investigation; Methodology; Validation; Writing - review & editing

Peter Fischer: Conceptualization; Funding acquisition; Methodology; Supervision; Writing - review & editing

Silvia Campioni: Conceptualization; Funding acquisition; Project administration; Supervision; Writing - review & editing

Gustav Nyström: Conceptualization; Funding acquisition; Project administration; Supervision; Writing - review & editing

Conflicts of Interest

There are no conflicts to declare

Acknowledgements.

The authors would like to acknowledge Brian Sinnet for granting access to the Malvern Zetasizer at the Particle Laboratory of Eawag, Prof. Dr. René Rossi (Empa) for granting access to the Anton Paar Surpass 3, Dr. Gilberto Siqueira (Empa) for supplying the TO-CNF and Fabian Wiesemüller (Empa) for 3D-printing the loop used to deposit the amyloid fibrils. Prof. Dr. Katharina Maniura (Empa) and Dr. Pascal Bertsch (ETH Zürich) are acknowledged for valuable discussions. N. K., P. F., S. C. and G. N. would like to thank the Swiss National Science Foundation for financial support (Grant number: 200021_192225).

Supplementary information for:

2D foam film coating of antimicrobial lysozyme amyloid fibrils onto cellulose nanopapers

Nico Kummer^{1,2}, Luc Huguenin-Elie², Adrian Zeller², Yashoda Chandorkar³, Jean Schoeller^{4,5}, Flavia Zuber³, Qun Ren³, Ashutosh Sinha^{1,2}, Kevin De France^{1,#}, Peter Fischer², Silvia Campioni^{1,}, Gustav Nyström^{1,2,*}*

¹ Laboratory for Cellulose & Wood Materials, Empa – Swiss Federal Laboratories for Materials Science and Technology, Überlandstrasse 129, 8600 Dübendorf, Switzerland

² Institute of Food Nutrition and Health, Schmelzbergstrasse 9, ETH Zurich, 8092 Zurich, Switzerland

³ Laboratory for Biointerfaces, Empa – Swiss Federal Laboratories for Materials Science and Technology, Lerchenfeldstrasse 5, 9014 St. Gallen

⁴ Laboratory for Biomimetic Membranes and Textiles, Empa – Swiss Federal Laboratories for Materials Science and Technology, Lerchenfeldstrasse 5, 9014 St. Gallen

⁵ Institute for Biomechanics, Stefano-Franscini-Platz 5, ETH Zürich, 8093 Zürich, Switzerland

* To whom correspondence should be addressed

present address: Department of Chemical Engineering, Queen's University, Kingston, Ontario K7L 3N6, Canada

E-Mail Gustav Nyström.: gustav.nystroem@empa.ch

E-Mail Silvia Campioni.: silvia.campioni@empa.ch



Figure S1: Photography of the loop with a HEWL amyloid 2D foam film at pH 8, showing inhomogeneity due to aggregation.

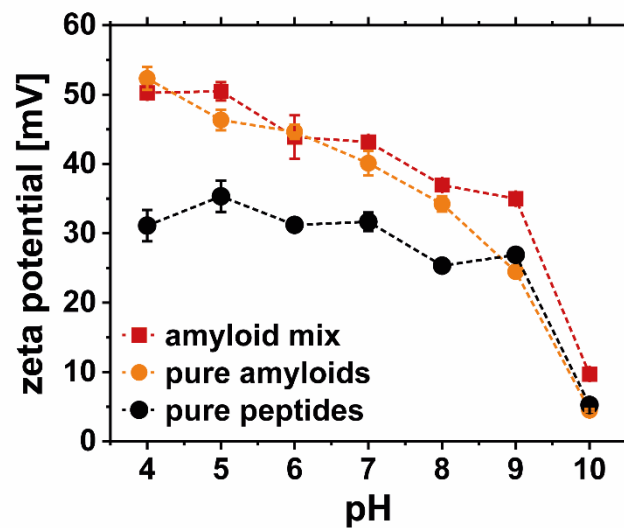


Figure S2: pH-dependent ζ potential of the amyloid mix and the pure amyloid fibrils and peptides separated by ultrafiltration.

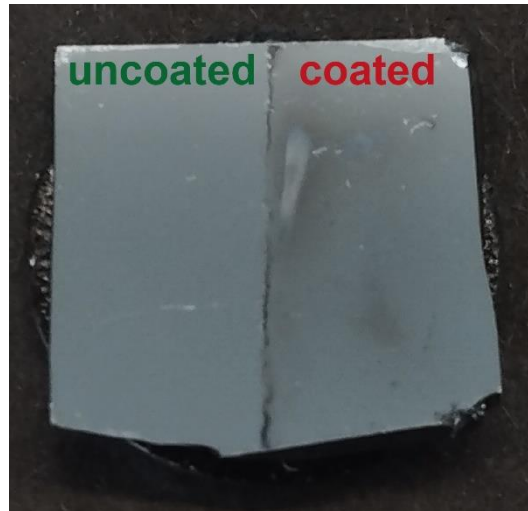


Figure S3: Photo of a silicon wafer that was covered with tape on the left side (uncoated) before depositing a layer of the 2D amyloid foam coating. After drying the tape was removed and the homogenous coating was visible on the right side (coated).

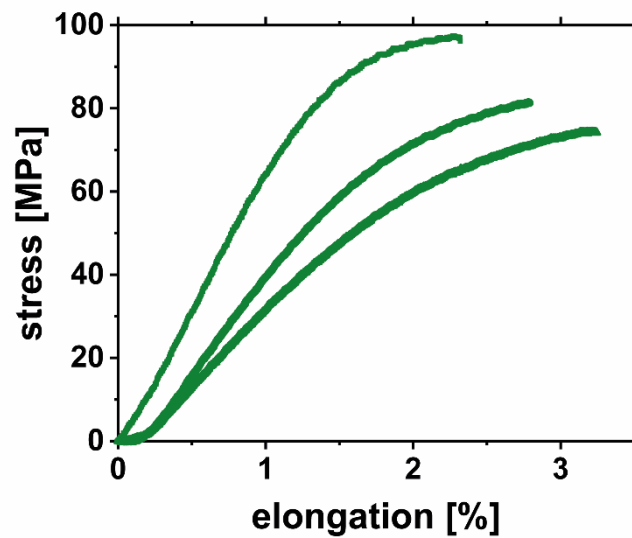


Figure S4: Stress-strain curves of the tensile tests performed on a triplicate of TO-CNF nanopaper.

Table S1: Summary of the result of the tensile tests including Elongation at break, modulus, tensile strength, and toughness, as well as water sorption behavior.

Elongation at Break	$2.27 \pm 0.24 \%$
Modulus	$6.66 \pm 2.21 \text{ GPa}$
Tensile Strength	$84.40 \pm 11.80 \text{ MPa}$
Toughness	$1.38 \pm 0.06 \text{ MJm}^{-3}$
Swelling	$2320 \pm 260 \%$

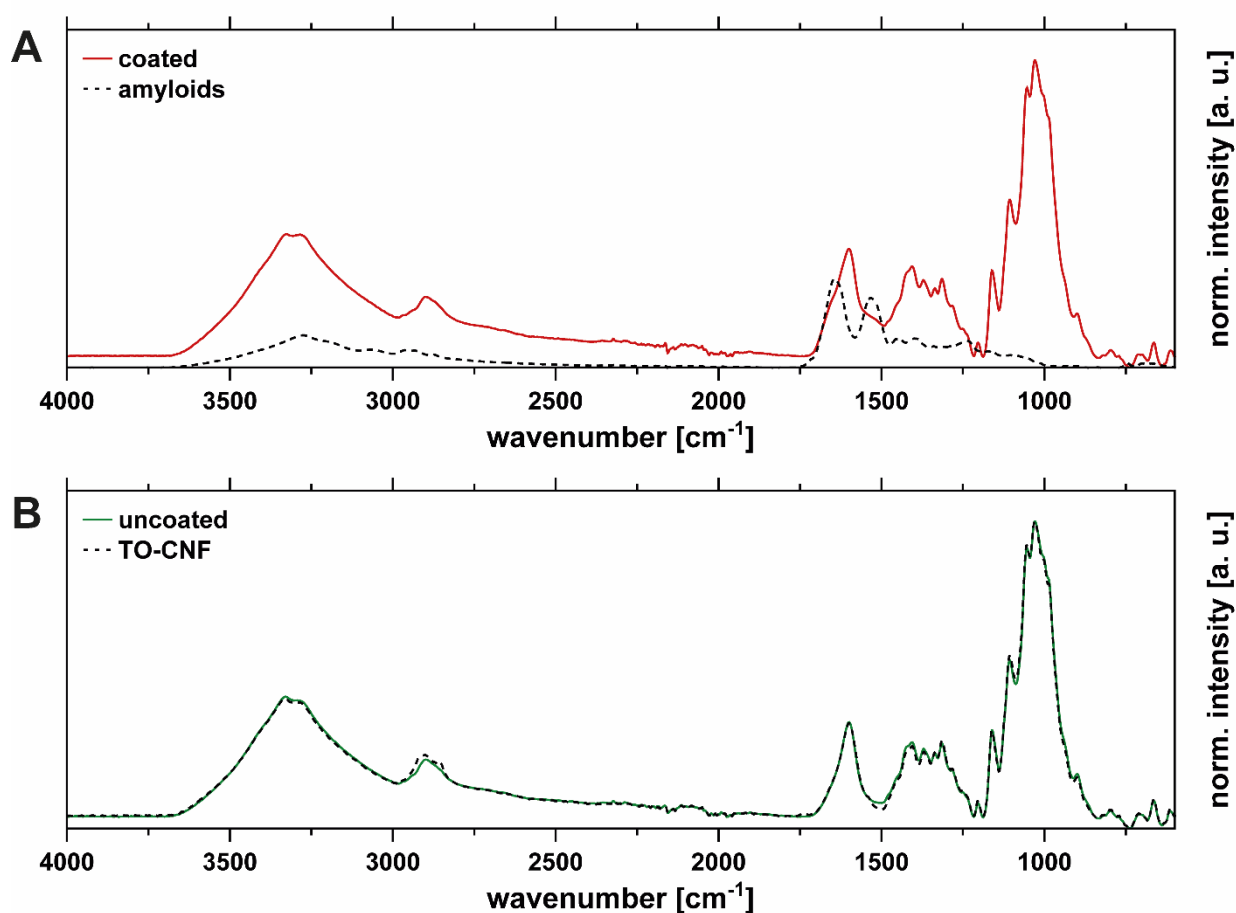


Figure S5: Full FTIR spectra of the side of the TO-CNF nanopaper coated with HEWL amyloid fibrils in red and reference dried HEWL amyloid fibril suspension in black (A). Full FTIR spectra of the uncoated side of the TO-CNF nanopaper in green and reference dried TO-CNF suspension in black (B).

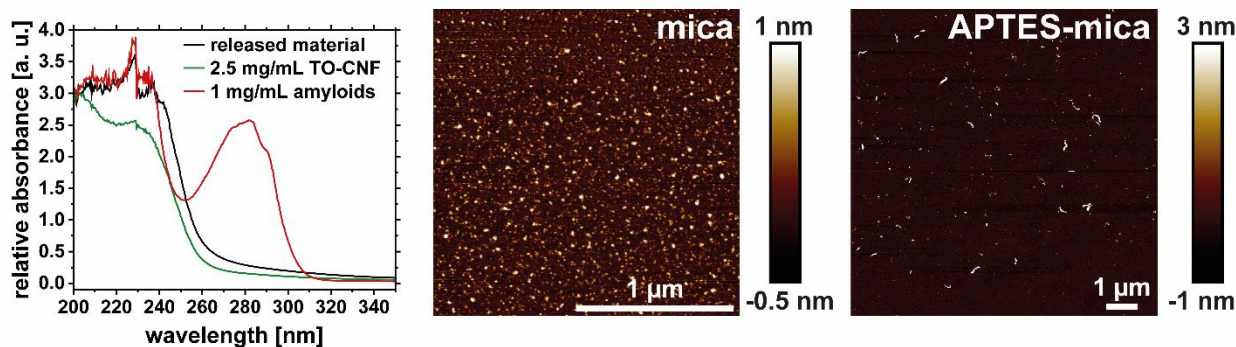


Figure S6: UV-vis spectrum of the material released from the TO-CNF nanopaper coated with HEWL amyloids (immersion of the film in MilliQ water for 48 h). For reference spectra of a 1 mg/mL amyloid fibril solution and a 2.5 mg/mL TO-CNF suspension are shown. The AFM images show the released material adsorbed onto freshly cleaved mica (negatively charged, adsorbing only positively charged peptides released from the coated nanopaper) and APTES-modified mica (positively charged, adsorbing negatively charged TO-CNFs released).

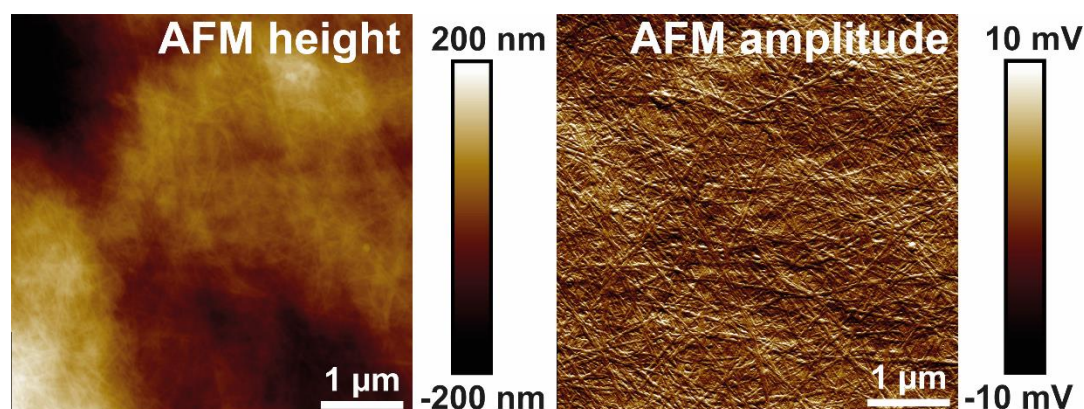


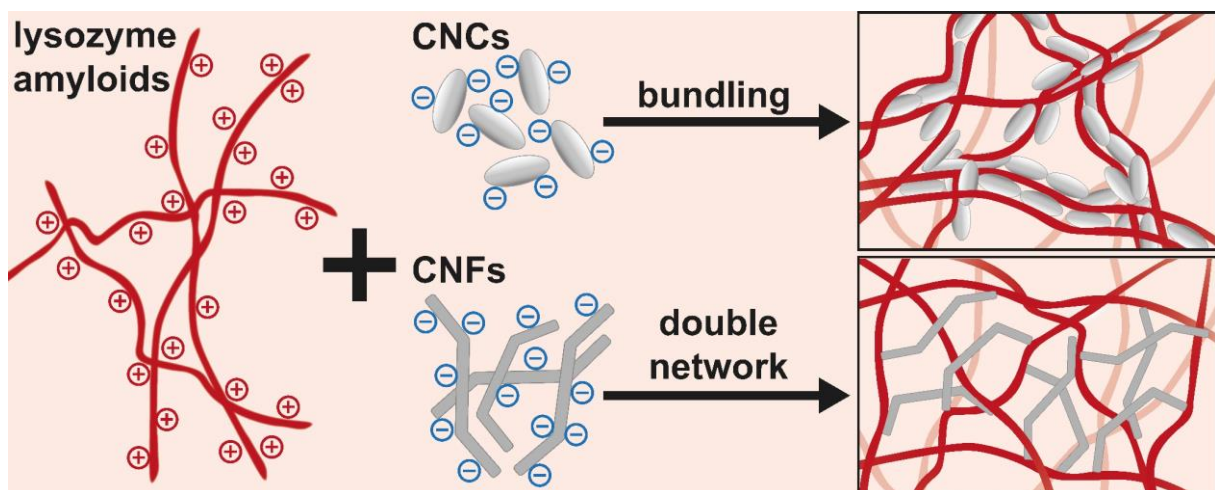
Figure S7: AFM height and amplitude images of a TO-CNF nanopaper coated with HEWL amyloids after immersion in MilliQ water and drying.

5 Amyloid fibril-nanocellulose interactions and self-assembly

Nico Kummer, Caroline E. Giacomini, Peter Fischer, Silvia Campioni and Gustav Nyström

Journal of Colloid and Interface Science, 2023, 641, 338-347

<https://doi.org/10.1016/j.jcis.2023.03.002>



Reproduced with permission from authors and publisher

© 2023, Elsevier

Amyloid fibril-nanocellulose interactions and self-assembly

Nico Kummer^{a,b}, Caroline E. Giacomini^b, Peter Fischer^b, Silvia Campioni^{a,}, Gustav Nyström^{a,b,*}*

^a Laboratory for Cellulose & Wood Materials, Empa – Swiss Federal Laboratories for Materials Science and Technology, Überlandstrasse 129, 8600 Dübendorf, Switzerland

^b Institute of Food Nutrition and Health, Schmelzbergstrasse 9, ETH Zurich, 8092 Zurich, Switzerland

* To whom correspondence should be addressed:

Gustav Nyström

Laboratory for Cellulose & Wood Materials, Empa – Swiss Federal Laboratories for Materials Science and Technology, Überlandstrasse 129, 8600 Dübendorf, Switzerland

Phone: +41587654583

E-mail: gustav.nystroem@empa.ch

Silvia Campioni

Laboratory for Cellulose & Wood Materials, Empa – Swiss Federal Laboratories for Materials Science and Technology, Überlandstrasse 129, 8600 Dübendorf, Switzerland

Phone: +41587654420

E-mail: silvia.campioni@empa.ch

Author E-mail addresses:

Nico Kummer: nico.kummer@empa.ch

Caroline E. Giacomini: caroline.giacomini@hest.ethz.ch

Peter Fischer: peter.fischer@hest.ethz.ch

KEYWORDS

amyloid fibrils, nanocellulose, colloidal interactions, self-assembly, gelation

ABSTRACT

Amyloid fibrils from inexpensive food proteins and nanocellulose are renewable and biodegradable materials with broad ranging applications, such as water purification, bioplastics and biomaterials. To improve the mechanical properties of hybrid amyloid-nanocellulose materials, their colloidal interactions need to be understood and tuned. A combination of turbidity and zeta potential measurements, rheology and atomic force microscopy point to the importance of electrostatic interactions. These interactions lead to entropy-driven polyelectrolyte complexation for positively charged hen egg white lysozyme (HEWL) amyloids with negatively charged nanocellulose. The complexation increased the elasticity of the amyloid network by cross-linking individual fibrils. Scaling laws suggest different contributions to elasticity depending on nanocellulose morphology: cellulose nanocrystals induce amyloid bundling and network formation, while cellulose nanofibrils contribute to a second network. The contribution of the amyloids to the elasticity of the entire network structure is independent of nanocellulose morphology and agrees with theoretical scaling laws. Finally, strong and almost transparent hybrid amyloid-nanocellulose gels were prepared in a slow self-assembly started from repulsive co-dispersions above the isoelectric point of the amyloids, followed by dialysis to decrease the pH and induce amyloid-nanocellulose attraction and cross-linking. In summary, the gained knowledge on colloidal interactions provides an important basis for the design of functional biohybrid materials based on these two biopolymers.

INTRODUCTION

Amyloids are fibrillar protein aggregates with a characteristic structure consisting of antiparallel β -sheets stacked perpendicular to the fibril axis [8]. Albeit amyloids are notorious for their role in many human diseases (e.g. Alzheimer's and Parkinson's), there are many known examples of functional amyloid fibrils, not only in microorganisms, but also in humans, where they are involved in hormone storage and release, and in the polymerization of melanin [9]. Some bacteria even exploit the rigidity and resistance to chemical or biological degradation of amyloid fibrils, which are a basic component of biofilms [9,182]. In addition to amyloid curli fibers, *Escherichia coli* biofilms also contain roughly 15% cellulose, resulting in a reinforced biocomposite, self-assembled into robust and elastic cage-like structures [125,183]. More generally, the rigidity and strength of amyloid fibrils makes them attractive for the design of renewable and biodegradable materials and simple aggregation protocols for the preparation of amyloids *in vitro* from inexpensive protein sources have been developed [6,9,11,184,185]. For instance, hen egg white lysozyme (HEWL) and milk β -lactoglobulin (BLG) are two food proteins that form amyloids after acid hydrolysis into peptide fragments, which in turn self-assemble into semi-flexible, high aspect ratio amyloid fibrils with the typical cross- β -sheet structure [25,27,147,149]. In recent years, amyloid fibrils made from HEWL and BLG in the form of hydrogels, aerogels, films and composites have found applications in biomaterials [9,35,163,185], membranes for water purification [166,186–188], bioplastics [167] and electronics [184].

To improve the mechanical properties of macroscopic amyloid materials, combinations of amyloid fibrils with polysaccharides [127] and with nanocelluloses [104,189] have been tested. Nanocelluloses are a class of bio-based and biodegradable materials with

excellent mechanical properties and an immensely broad range of applications in functional materials [79,80,107,108,111]. The term "nanocelluloses" encompasses cellulose nanofibrils (CNFs) containing disordered and crystalline regions and pure crystalline cellulose nanocrystals (CNCs) [81,82]. Colloidally stable dispersions of CNFs can be obtained from wood pulp by oxidation with 2,2,6,6-tetramethyl-1-piperidinyloxy (TEMPO) and mechanical grinding. The TEMPO-oxidized CNFs (TO-CNFs) are stabilized by negatively charged carboxyl groups [82]. CNCs are commonly prepared from wood pulp or cotton by a sulfuric acid hydrolysis treatment that shortens the CNCs and introduces negatively charged sulfate half-ester groups [81]. The negative charge of chemically modified nanocelluloses (or other polysaccharides) and the pH-dependent positive charge of proteins are the basis for polyelectrolyte complexation, a common type of interaction between oppositely charged polymers [80,115,116]. Polyelectrolytes are surrounded by an electrical double layer, a cloud of tightly packed counter-ions with reduced translational entropy. When complexes are formed through ionic bonds, the entropy of the polyelectrolytes is decreased, however the entropy of the system as a whole is increased due to the release of large amounts of counter-ions and bound water. Therefore, the driving force for complexation is the gain of entropy rather than short-ranged interactions between the polyelectrolytes [80,116–118]. In the specific case of positively charged, native lysozyme adsorbing onto mechanically disintegrated CNFs, isothermal titration calorimetry (ITC) proved that the adsorption is entropy-driven and influenced by the protonation state of hemicelluloses remaining on the CNF surface [119]. Similarly, the entropic gain from the release of water molecules and counter-ions and the strong effect of ionic interactions on the adsorption efficiency have been confirmed for negatively charged bovine serum albumin (BSA) mixed with positively charged pyridinium-grafted CNCs [120]. These purely physical interactions have been exploited to adsorb proteins onto nanocelluloses in order to prepare hybrid

materials. Depending on the functionality of the protein (enzyme) possible applications include biocatalysis [190,191], sensing [192], and the use as antimicrobial material [121,193]. Composites of oppositely charged nanocellulose and HEWL amyloid fibrils have been studied in recent years. Positive HEWL amyloids possess a broad-spectrum antimicrobial activity [131] and have been used to prepare antimicrobial films, in combination with TO-CNF [57] and CNCs [104]. Combinations of HEWL amyloids and TO-CNF have also shown their potential for water purification, efficiently removing proteins, emulsion droplets and heavy metals [194,195]. However, the mechanical performance of hybrid amyloid-nanocellulose films and aerogels has been poor, as no synergistic effect has been observed so far [57,104,189]. The complexation of the oppositely charged polyelectrolyte particles seems to lead to inhomogeneity and to defects in the network, which adversely affect the overall mechanical performance [104,121,189].

To understand the interplay of these biocolloidal systems, we investigated the basic colloidal interactions in suspensions of HEWL and BLG amyloids with CNCs using turbidity measurements, zeta potential measurements, rheology and atomic force microscopy (AFM). Rheological measurements of the HEWL amyloid-CNC complexes were compared to those obtained using the unconverted peptide fraction. The dependence of the amyloid network elasticity on both amyloid and CNC concentration was tested and described with power laws. Finally, the self-assembly of amyloids with CNCs as cross-linkers was studied by co-dispersing the two components at a high pH at which both polymers are negatively charged, followed by dialysis against a low pH solution to introduce positive charges on the protein fibrils and thus induce their interaction and physical cross-linking with CNCs. This approach led to the formation of strong, almost transparent hybrid gels. To study the effect of nanocellulose morphology on the rheological properties of the hybrid gels, TO-CNFs were also considered in addition to the

CNCs. Overall, the findings of this study contribute to an improved fundamental understanding of the colloidal interactions between amyloid fibrils and nanocellulose and provide important knowledge for the bottom-up self-assembly of functional biohybrid materials.

EXPERIMENTAL

Materials

HEWL (Mw = 14.3 kDa, purity >90%) was purchased from Sigma-Aldrich. Purified BLG was (Mw = 18.4 kDa, purity >97%) provided by the Food and Bioprocess Engineering group at the Technical University of Munich [196]. CNCs were purchased from CelluForce. TO-CNFs were prepared in-house according to a previously published protocol [121].

The 4-(2-hydroxyethyl)-1-piperazineethanesulfonic acid (HEPES, purity >99.5%), sodium hydroxide (NaOH, purity >99%) and hydrochloric acid (HCl, 37%) were obtained from VWR. The (3-aminopropyl)triethoxysilane (APTES, purity >98%) was purchased from Sigma-Aldrich. All chemicals were used as received without further purification.

Methods

Preparation of amyloid fractions

HEWL and BLG amyloid fibrils were prepared by acid hydrolysis and aggregation at pH 2, 90 °C and protein concentrations of 2 wt% as described before [131]. After 24 h and 5 h for HEWL and BLG, respectively, semi-flexible, high aspect ratio amyloid fibrils were formed. In both cases, roughly 38% of the protein was converted into amyloid fibrils, while the rest of the protein occurs as hydrolyzed peptides [131,150]. Stiff amyloid fibrils a few hundred nanometers long were prepared using a probe sonicator

[104,131,189]. The unconverted peptide fraction was separated from the amyloid fibrils using a centrifugal filter (Amicon) with a molecular weight cut-off (MWCO) of 100 kDa, and the exact concentration was measured by UV-Vis spectroscopy [131]. The suspensions of the different amyloid fractions, from now on called amyloids, sonicated amyloids and peptides, were stored in the refrigerator at 4 °C until further use.

Preparation of nanocellulose suspensions

A stock CNC suspension was prepared at a concentration of 2 wt% by mixing the CNCs with MilliQ water using stirring and tip sonication (Digital Sonifier 450, Branson Ultrasonics) [104]. The concentration of the original TO-CNF suspension was 1.4 wt%.

Mixing of amyloid fractions and nanocellulose

The amyloid fractions and the nanocellulose stocks were diluted with 10 mM HEPES buffer at pH 7 to a final concentration of 2 mg/mL. The pH of the suspension was measured and adjusted to 7 with 1 M HCl or NaOH. Subsequently, the amyloid fractions and the nanocellulose were mixed in different ratios, keeping one component at a constant final concentration of 1 mg/mL (denoted by the index 10) and adding the other component at a final concentration of 0.1, 0.2, 0.3, 0.5, 0.7, 1.0, and 2.0 mg/mL (denoted by indices 1 to 20). An amyloid to nanocellulose ratio of 1 to 0.1 mg/mL would be denoted by 10:1, while a sample containing 0.1 mg/mL amyloids and 1 mg/mL nanocellulose would be denoted by 1:10. It should be noted, that the total solid content varied throughout a series of amyloid-nanocellulose ratios. A detailed mixing plan can be found in Table S1.

Optical characterization

The optical density of the mixed amyloid-CNC samples was measured at a wavelength of 600 nm using a Cary 1E spectrophotometer. The measurements were performed in PMMA cuvettes with a path length of 1 cm and the baseline measurement of 10 mM HEPES buffer at pH 7 was subtracted. Additionally, photographs of the suspensions were taken to show the increase in turbidity due to complexation.

ζ potential measurements

The different amyloids and nanocellulose ratios were diluted by a factor of 10, using 10 mM HEPES buffer at pH 7. The ζ potential measurements were performed in triplicate using a Malvern Zetasizer nano ZS equipped with a folded capillary cell. The mean and the standard deviation of the three measurements are reported. However, since standard deviations were in general very small, they were not visible in some of the figures.

Atomic force microscopy

The complexation of the different amyloid fractions with the CNCs in the nanometer range was studied by AFM imaging in tapping mode using a Bruker Icon 3 AFM equipped with Bruker RTESPA-150 probes. The samples were diluted by a factor of 10, using 10 mM HEPES buffer at pH 7 (pure CNCs were diluted to 0.01 mg/mL). After vortexing, 100 μ L were dropped onto freshly cleaved mica, adsorbed for 1 min and then rinsed off with 1 mL MilliQ water. For the samples with positive zeta potentials, negatively charged unmodified mica was used, whereas for samples with negative zeta

potentials, the mica was modified with APTES to make it positively charged. The images were acquired at a scan rate of 0.5 Hz and a resolution of 1024x1024 lines. The raw data was flattened and processed with the Bruker Nanoscope software.

Rheological characterization

The rheological properties of the amyloid-nanocellulose mixtures were measured with an Anton Paar MCR 702 rheometer equipped with a double gap geometry DG26.7. During the measurement the temperature of the samples was kept constant at 20°C using a Peltier element. The linear viscoelastic regime was prescreened by amplitude sweeps at frequencies of 0.1, 1, and 10 rad/s. Finally, a frequency sweep from 0.1 to 100 rad/s at constant shear strain of 1 % and an amplitude sweep from 0.1 to 1000 % shear strain at a frequency of 1 rad/s were performed. Subsequently, the measuring cell was loaded with fresh sample and the shear viscosity was measured at shear rates ranging from 0.01 to 100 s⁻¹.

The dependence of the amyloid network elasticity on amyloid and nanocellulose concentration was characterized with the plateau storage modulus G_0 obtained from the storage modulus G' measured in the frequency sweeps at a fixed amplitude of 1 %. The mean of G_0 determined in triplicate, with error bars for the standard deviation was plotted against the amyloid and nanocellulose concentrations, respectively, in a double-logarithmic plot. The slope of the linear regression fitted with Origin 2022 (OriginLab Corporation, Northampton, MA, USA) including the standard deviation of the fit was taken as the exponent of the power law.

pH induced gelation

The HEWL and BLG amyloids were co-dispersed with the CNCs at a pH above the isoelectric point (pI) of the proteins, where both the amyloids and the CNCs are negatively charged. In order to immediately cross the pI during mixing, the 5 mL of 2 wt% HEWL amyloids at pH 2 were slowly mixed into 5 mL 2 wt% CNCs containing 75 μ L 4 M NaOH. In the case of co-dispersions of BLG amyloids with CNCs, both components were brought to pH 7 and then mixed. The gelation of the mixtures was induced by lowering the pH below the pI of the protein, where the amyloids are positively charged and complexation with the CNCs leads to physical cross-links. The pH change was achieved by using cut off 50 mL centrifuge tubes and covering the newly formed opening with a 1 kDa MWCO dialysis membrane (Repligen) attached with parafilm, similar to the setup described by Usuelli *et al.* [127]. For the rheological measurements, 2 mL of the CNC-amyloid co-dispersion were transferred into the custom-made dialysis tubes and then put into pH-adjusted (pH 3, 5, 7, 9) MilliQ baths overnight. The inner diameters of the dialysis tubes and the rough plate-plate geometry were both 25 mm, which enabled non-invasive (no cutting *et cetera*) analysis of the viscoelasticity of the gels. Frequency sweeps of the co-dispersions and the gels were measured at 1% deformation in the range of 0.1 to 1000 rad/s. Compression tests were performed using the Anton Paar MCR 702 multidrive rheometer equipped with linear motor and the rough plate-plate geometry.

Cryogenic scanning and transmission electron microscopy

Samples for cryo-SEM were prepared by placing 5 μ L of the liquid samples (pure amyloid fibrils and CNCs) on carbon coated TEM-grids (Quantifoil, Germany) previously

positively glow-discharged (Pelco easiGlow, TedPella, USA). For the hydrogel samples, the grid was placed onto the gel surface and then removed with material from inside the hydrogel exposed. After blotting and washing (for gel samples washing was omitted), the grids were plunge-frozen in a mix of liquid ethane/propane, freeze-dried up to $-80\text{ }^{\circ}\text{C}$ in a freeze-fracturing system BAF 060 (Bal-Tec/Leica, Vienna), then coated with tungsten (3 nm at an elevation angle of 45° and 3 nm at 90°) and imaged at $-120\text{ }^{\circ}\text{C}$ and 2 kV in a field emission SEM Leo Gemini 1530 (Zeiss, Germany) equipped with a cold stage (VCT Cryostage, Bal-Tec/Leica, Vienna). In-lens SE and Everhart-Thornley SE-signals at an acceleration voltage of 2 kV were used for image acquisition.

For cryo-TEM, aliquots of samples were applied onto lacey carbon-coated copper grids (EMS, USA), which were previously positively glow-discharged (Pelco easiGlow, TedPella, USA). Excess of sample was blotted away for two seconds and the grids were plunge frozen in a mixture of liquid ethane/propane (continuously cooled by liquid nitrogen) using a Vitrobot Mark IV (Thermo Fisher Scientific, USA) with the environmental chamber set to $22\text{ }^{\circ}\text{C}$ and 100% humidity. Vitrified grids were stored in liquid nitrogen until further processing. The cryo-EM grids were loaded into a Titan Krios microscope operating at 300 kV (Thermo Fisher Scientific, USA), equipped with a Gatan Quantum-LS Energy Filter (GIF) and a Gatan K2 Summit direct electron detector. The samples were imaged in EFTEM mode using the Thermo Fisher Scientific EPU software (81000x magnification, ca. 40 e/A² total electron dose, K2 in linear mode), with a defocus range of -2 to -4 μm . The diameters of the amyloids, CNCs and structures formed in the hybrid amyloid-CNC gels were measured using ImageJ software [197]. In total, the diameters of 30 individual objects from several images were analyzed and reported as mean and standard deviation.

RESULTS AND DISCUSSION

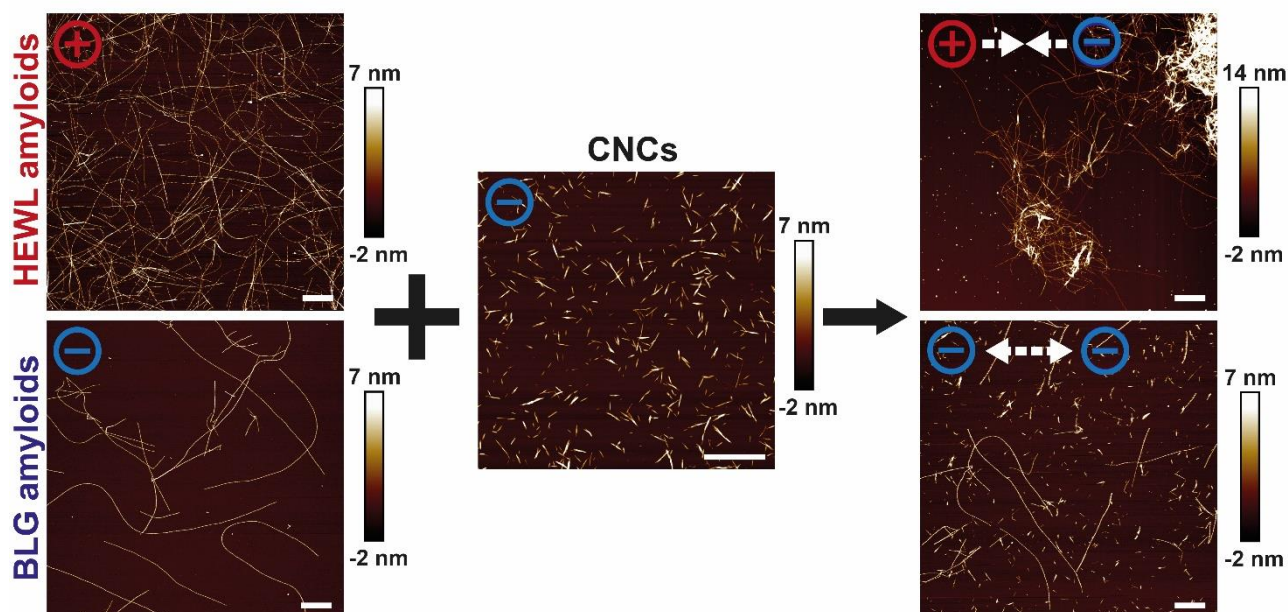


Figure 1: AFM images of HEWL and BLG amyloid fibrils and their mixtures with CNCs at an amyloids:CNC ratio of 10:3. The scale bars correspond to 1 μ m.

Effect of charge on the interactions between amyloids and CNCs

To probe the colloidal interactions between amyloids and CNCs, mixed suspensions at different ratios (index 10=1 mg/mL) were prepared (Table S1). HEPES buffer (10 mM) was used to keep the pH constant at 7, at which HEWL amyloids were positively charged and BLG amyloids were negatively charged, respectively. Upon aggregation, both HEWL and BLG form semi-flexible amyloid fibrils with diameters of few nanometers and lengths of several micrometers, as shown by AFM (images on the left in **Figure 1**). CNCs are stiff rod-like particles with diameters of a few nanometers and lengths of several hundred nanometers (image in the middle in Figure 1). Upon mixing HEWL amyloids with CNCs at a ratio of 10:3, complexation was observed, while CNCs and BLG amyloid mixtures were homogeneously co-dispersed (images on the right in Figure 1). Note that, the AFM images should be taken as qualitative snapshots of the

interactions (complexation vs. co-dispersion) occurring in the respective systems and cannot be compared in terms of amyloid or CNC concentrations. The complexation of HEWL amyloids with CNCs resulted in an increased turbidity, due to the increased scattering of light (turbidity measurements in **Figure 2A** and photographs in Figure S1). In contrast, BLG amyloid-CNC co-dispersions remained transparent. Moreover, the complexation led to a compensation of the positive charge of the HEWL amyloids by the CNCs, as observed with ζ potential measurements (**Figure 2B**). HEWL amyloids at pH 7 had a ζ potential of +30 mV, which was decreased with increasing amounts of added CNCs (ζ potential -40 mV). The charge was completely neutralized at a HEWL amyloid-CNC ratio of 6:10 (zero net charge). The ζ potential values of BLG amyloids (-37 mV) and CNCs were almost identical, which explained the nearly constant slope over all the measured ratios. It should be pointed out that the peak in turbidity was shifted to a ratio of 10:10 for the HEWL amyloid-CNC system and instead of the point of zero net charge (6:10). This can be attributed to the increased total solid content at the 10:10 ratio forming more complexes that scatter light and cause turbidity. Furthermore, the complexation of HEWL amyloids and CNCs led to an increase of the viscoelastic properties of the amyloid network, while the storage modulus G' and loss modulus G'' remained low for the CNC-BLG amyloid co-dispersions (**Figure 2C**). The same complexation behavior upon mixing with CNCs was found for shortened amyloid fibrils and unconverted peptides (Figure S2 and S3), with reduced rheological properties compared to full-length amyloids (Figure S4).

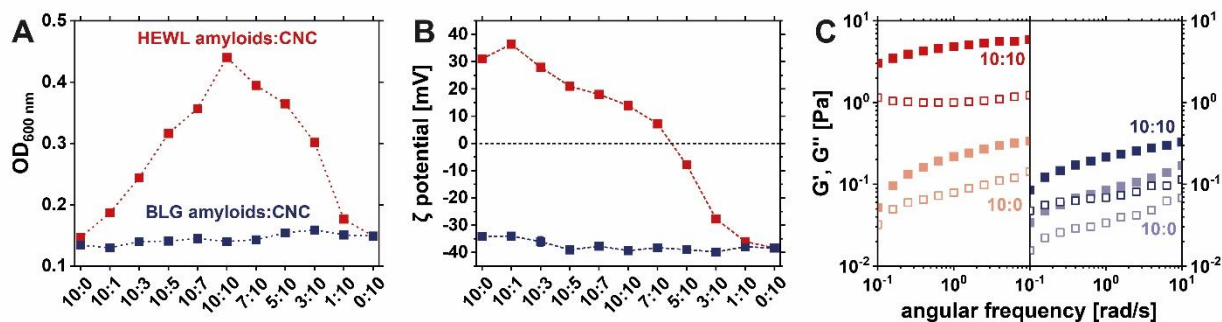


Figure 2: Turbidity (OD_{600}) (A) and ζ potential measurements (B) of amyloid-CNC mixtures at different ratios. Frequency sweeps at a fixed amplitude of 1% of pure HEWL and BLG amyloid fibrils (10:0) and amyloid-CNC mixtures at the 10:10 ratio, 10=1 mg/mL (C).

Overall the results in Figure 1 and Figure 2 demonstrate the importance of ionic interactions in promoting the complexation between protein amyloids and CNCs. As already pointed out by several studies of our group, polyelectrolyte complexation dominates the interactions of both native (i.e. monomeric) HEWL and HEWL amyloids with nanocelluloses [104,121,189]. The oppositely charged HEWL amyloids mixed with CNCs undergo complexation driven by the gain of entropy in the system, due to the release of counter-ions and bound water, rather than short-ranged ionic interactions [119,120]. Already the pure amyloid suspensions (10:0) formed a network of semi-flexible fibrils, as shown in the rheology measurements ($G' > G''$). The increase of G' upon the addition of CNCs, while keeping the HEWL amyloid concentration constant (10:10), suggested the formation of cross-links in the amyloid network.

Origin of the amyloid network elasticity

Rheology measurements also indicated that the viscoelastic properties of a network of HEWL amyloids and CNCs strongly depend on the ratio between these two particles, as this is related to the degree of complexation and cross-linking (**Figure 3**). The frequency sweeps of samples at a fixed amyloid concentration (10=1mg/mL) and

increasing amounts of CNCs indicated a progressive increase of G' values. Plotting the plateau modulus G_0 (G' at 1% amplitude and 1 rad/s frequency) against the concentration of CNCs/amyloids, in a double-logarithmic plot, while keeping the respective other component constant, allowed to determine power laws (Figure 3A and 3B). The scaling behaviours of $G_0 \sim c_{CNC}^{1.0 \pm 0.1}$ and $G_0 \sim c_{amyloids}^{2.3 \pm 0.1}$ were found. The power law for the amyloid concentration dependence was only valid for HEWL amyloid concentrations up to 0.6 mg/mL (white regime), while a plateau was reached at higher amounts of amyloids (grey regime). At this CNC-amyloid ratio of 6:10, all the CNCs (fixed concentration of 10=1 mg/mL) were assumed to be adsorbed onto the amyloid fibrils and their ability to further cross-link the amyloid network was exhausted. Therefore, higher additions of amyloids were not efficiently cross-linked and no further increase in elasticity was observed in the considered concentration window. This finding was supported by the zero net charge between the 5:10 and 7:10 ratio, as determined by ζ potential measurements (Figure 2B). This corresponds to an amyloid concentration of roughly 0.6 mg/mL, as shown also in Figure 3C, where the ζ potentials were replotted against the concentration of amyloids. The same set of experiments was also performed for BLG amyloids mixed with CNCs at pH 3, with similar results ($G_0 \sim c_{CNC}^{1.4 \pm 0.1}$ and $G_0 \sim c_{amyloids}^{2.3 \pm 0.4}$), however only four data points could be used for fitting, since the plateau was reached already at 0.3 mg/mL BLG amyloid concentration (Figure S5).

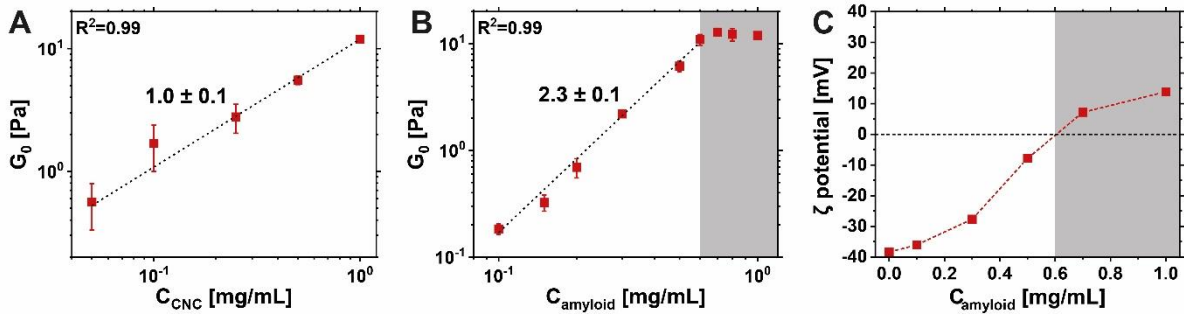


Figure 3: The plateau modulus G_0 at a fixed amyloid concentration of 1 mg/mL in dependence on the added CNCs, including the linear fit determining the exponent of the power law (A). The plateau modulus G_0 at a fixed CNC concentration of 1 mg/mL in dependence on the amyloid concentration, including the linear fit determining the exponent of the power law for concentrations up to 0.6 mg/mL (white regime) (B). At higher concentrations a plateau was reached (grey regime). The ζ potentials at a fixed CNC concentration of 1 mg/mL with increasing amyloid additions at pH 7 (C).

The determined power laws allow to draw certain conclusions about the structure of the network and the reason for its elasticity. The power law $G_0 \sim c_{CNC}^{1.0 \pm 0.1}$ reflects an almost proportional response of the elasticity when more CNCs are added. This lack of a synergistic effect on the mechanical properties of hybrid amyloid-nanocellulose films and aerogels has been observed before and was attributed to inhomogeneities causing defects in the network [104,189]. The exponent of the power law can provide information about the cross-linking mechanism. For instance, a much higher exponent of 4.4 was obtained for BLG and HEWL amyloid networks cross-linked with sodium chloride (NaCl), suggesting a cross-linking mechanism based on charge screening, which effectively increased the probability for physical cross-links to form at the entanglement points in the network [198]. Further examples for exponents larger than 1 are associated with the bundle formation (increase of the bending rigidity of the building blocks of the network) of actin filaments induced by the specific binding of scruin or fascin proteins (exponents of 2 and 1.5, respectively) [199,200]. Instead, a lower exponent of 0.6 has been reported for intermediate filaments, due to the cross-

linking with Ca^{2+} ions occurring via negatively charged side chains. Here, the cross-linking efficiency was reduced due to cross-links forming between side chains of the same filament, which then did not contribute to the elasticity of the intermediate filament network [201]. Based on these literature examples, we hypothesize that the cross-linking occurs through a mixed process of cross-linking at entanglement points, amyloid bundling and CNC aggregation with residual unconverted peptides (roughly 60% of the total protein mass [131]), effectively reducing the CNC surface available for cross-linking with amyloids and thus the contribution to the network elasticity.

The scaling of the elasticity with amyloid concentration to the power of 2.3 ± 0.1 is in good agreement with theoretical models and experimental data for semi-flexible polymers [202,203]. Mackintosh *et al.* [54] developed the affine thermal model to describe the elasticity of actin networks:

$$G_0 \sim \frac{\kappa^2}{k_B T} \xi^{-2} L_e^{-3}$$

where κ denotes the bending modulus, k_B the Boltzmann constant, T the absolute temperature, ξ the average mesh size of the network, and L_e the characteristic entanglement length. Since $\xi \sim c_{amyloid}^{-1/2}$ and $L_e \sim c_{amyloid}^{-2/5}$ the elasticity scales with the amyloid concentration to the power of 2.2 [202]:

$$G_0 \sim c_{amyloid}^{11/5}$$

Indeed, Cao *et al.* found exponents of 2.2 for semiflexible BLG and HEWL amyloids cross-linked with NaCl, fitting the affine thermal model [198]. Instead, van Dalen *et al.* used the non-affine floppy modes model on to describe their HEWL amyloid network elasticity, scaling with the amyloid concentration to the power of 2.4 [204].

Using pH-dependent charge of amyloids to induce gelation

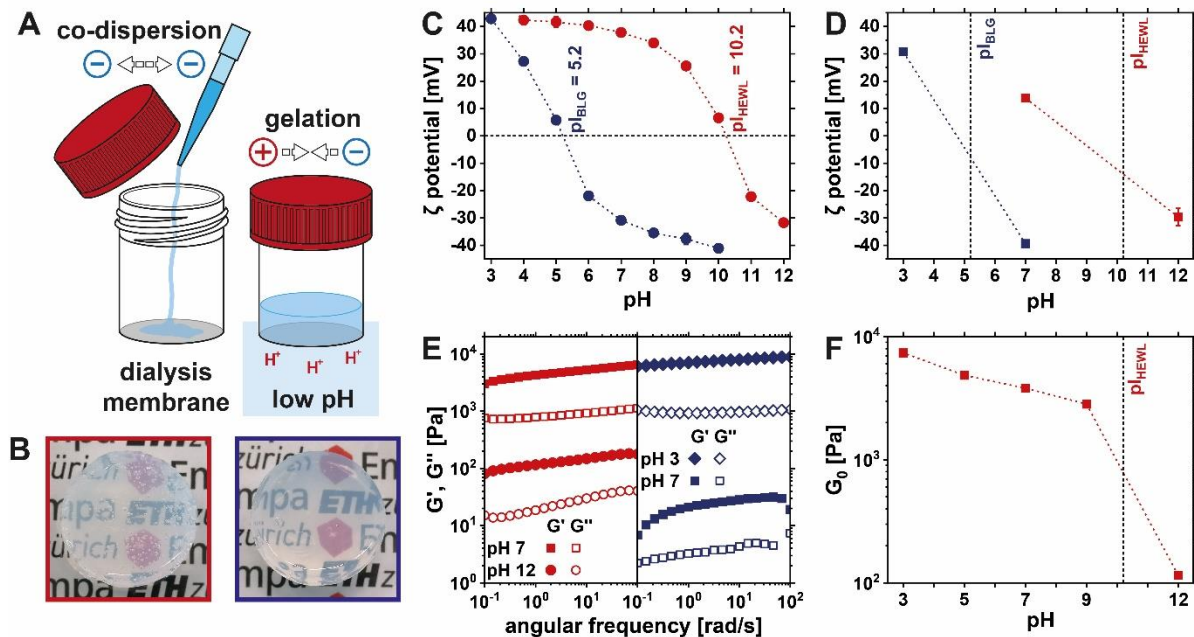


Figure 4: Illustration of the slow pH-mediated self-assembly of amyloids and CNCs (A). Photographs of hybrid amyloid-CNC gels (red: HEWL, blue: BLG) at a concentration of 10 mg/mL amyloids and CNCs each (B). pH-dependent ζ potentials of pure HEWL and BLG amyloids including isoelectric points (C). ζ potential measurements of the amyloid-CNC mixtures (10:10 ratio) at different pH. The data points were connected by a line to guide the eye (D). Frequency sweeps of the amyloid-CNC hybrid gels and the co-dispersions at the corresponding pH (E). pH-dependent plateau storage modulus G_0 (F).

With the gained knowledge on amyloid-CNC interactions, hybrid gels at a total solid content of 20 mg/mL were self-assembled exploiting the dependence of the charge of the amyloids on the pH (**Figure 4A** and **4B**). To have a purely repulsive system where both particles are co-dispersed in absence of complexation, amyloids and CNCs were homogeneously mixed at a pH higher than the isoelectric point (10.2 in the case of HEWL amyloids and 5.2 for BLG amyloids) (**Figure 4C**). The co-dispersions were pipetted into a custom-made dialysis tube, which was immersed into MilliQ water at pH 7 (for HEWL amyloid-CNC mixtures) or pH 3 (for BLG amyloid-CNC mixtures), respectively. This pH shift to a value lower than the isoelectric point of the amyloids introduced

positive charges on the protein colloids, enabling ionic interactions with the negatively charged CNCs (**Figure 4D**, data for dispersions at amyloid-CNC 10:10). After overnight dialysis, homogenous and almost transparent amyloid-CNC hybrid gels were formed with both HEWL amyloids (Figure 4B red frame) and BLG amyloids (Figure 4B blue frame). The HEWL amyloid-CNC gels trapped some air bubbles, which was the reason for the seemingly lower transparency. Overall, the slow self-assembly of the hybrid network led to homogenous gels and the formation of light-scattering features could be avoided. **Figure 4E** shows the increased storage modulus of the gels compared to the co-dispersions (1.5 and 2.5 orders of magnitude for HEWL amyloid-CNC and BLG amyloid-CNC gels, respectively). The higher storage modulus of the CNC-HEWL amyloid co-dispersion compared to the CNC-BLG amyloid co-dispersion was due to the addition of the sodium hydroxide needed to reach pH 12 (roughly 30 mM), which led to charge screening by Na⁺ and slight aggregation of the CNCs [205]. The storage moduli of both gels reached several kPa, which is slightly higher than previous values measured for amyloid gels at the same total solid content (20 mg/mL) cross-linked with 300 mM NaCl and reinforced with different polysaccharides [127]. **Figure 4F** shows the dependence of G_0 on the equilibrium pH after dialysis for HEWL amyloid-CNC gels. As seen before, the 1.5 order of magnitude increase in G_0 occurred after crossing the isoelectric point. The elasticity gradually increased when the pH was lowered, from ~3000 Pa at pH 9 to ~8000 Pa at pH 3. This can be associated to the increased linear charge density of the HEWL amyloids (ζ potential in Figure 4C) at lower pH, and to the ability to form more or stronger cross-links with CNCs.

Cryo-SEM imaging was performed on gels containing 10 mg/mL HEWL amyloids and 5 mg/mL CNCs to understand the structure of the self-assembled hybrid hydrogels (**Figure 5**). Predominantly, lateral aggregation of amyloid fibrils and CNCs into bundles was observed. Detailed analysis of the diameter of pure HEWL amyloids and CNCs,

as well as the formed bundles, proved that the bundles were on average three times as wide as the single components. To confirm that the bundles were not an artifact formed during the freeze-drying prior the cryo-SEM imaging, vitrified and still hydrated samples were imaged using cryo-TEM (Figure S6).

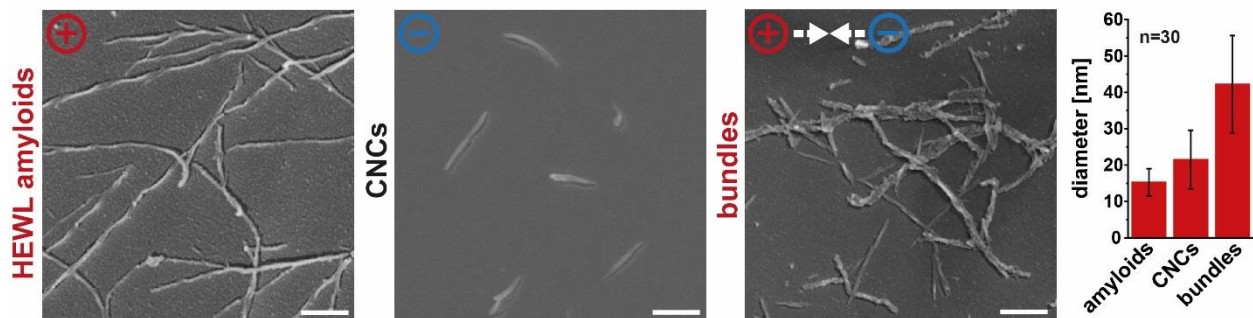


Figure 5: Cryo-SEM images of HEWL amyloid and CNC suspensions, as well as amyloid-CNC bundles found in hybrid gels. The diameter of the bundles increased by a factor of three compared to pure amyloids and CNCs. The scale bars correspond to 100 nm.

As already mentioned above, bundling is a common mechanisms in protein filament networks [199,200] and the exponents found in the scaling laws (Figure 3A and S5A) indicate that addition of CNCs induces cross-linking of amyloids through bundling. In the case of positive HEWL amyloids and oppositely charged CNCs the rules of entropy-driven polyelectrolyte complexation apply [115,116]. Therefore, lateral aggregation is favored since it leads to the minimization of free surface area of these rod-like particles, maximizing the release of hydration water and counter-ions and therefore the entropy in the system.

HEWL amyloid-TO-CNF system

With the knowledge on the interactions and self-assembly of amyloids with CNCs at hand, mixtures of HEWL amyloids and TO-CNF were also investigated by rheology to assess their complexation behavior. Scaling laws of the plateau modulus G_0 (G' at 1% amplitude and 1 rad/s frequency) with HEWL amyloids and TO-CNF concentrations were measured (**Figure 6A** and **6B**). Due to the robustness of the method demonstrated above, a single measurement series was sufficient to get reliable data. The scaling behaviours of $G_0 \sim c_{TO-CNF}^{4.0 \pm 0.2}$ and $G_0 \sim c_{amyloids}^{2.4 \pm 0.1}$ were found.

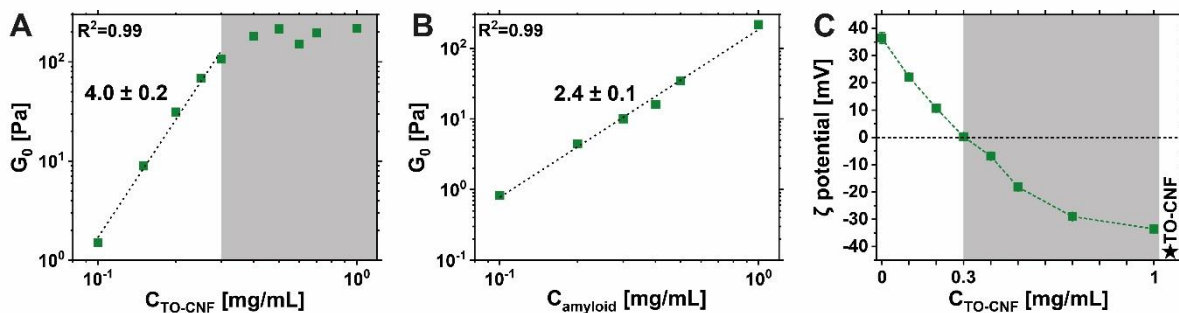


Figure 6: The plateau modulus G_0 at a fixed HEWL amyloid concentration of 1 mg/mL in dependence on the added TO-CNFs, including the linear fit determining the exponent of the power law for concentrations up to 0.3 mg/mL (white regime) (A). At higher concentrations a plateau was reached (grey regime). The plateau modulus G_0 at a fixed TO-CNF concentration of 1 mg/mL in dependence on the amyloid concentration, including the linear fit determining the exponent of the power (B). The ζ potentials at a fixed HEWL amyloid concentration of 1 mg/mL with increasing TO-CNF additions at pH 7 (C).

The power law for the TO-CNF concentration dependence was only valid for concentrations up to 0.3 mg/mL (white regime), while a plateau was reached at higher amounts of TO-CNF (grey regime). At this ratio of TO-CNF and HEWL amyloids of 10:3, the positive charge of the amyloids (fixed concentration of 10=1 mg/mL) in the system is fully compensated by TO-CNFs and any further addition of TO-CNFs would

not lead to more cross-linking and increased elasticity. Zeta potential measurements show that the net zero charge of the system is found at around this ratio (**Figure 6C**).

As for the amyloid-CNC system scaling laws were successfully fitted and linked to the charge-dependent cross-linking between amyloids and nanocellulose. The almost identical exponent of 2.4 for the scaling law with amyloid concentration agrees well with both theory and experimental data [198,202–204], describing the contribution of the amyloid fibrils to network elasticity. On the other hand, the elasticity scaling with TO-CNFs was fundamentally different to the scaling with CNCs. The much higher exponent of 4.0 can be explained by the fact that the TO-CNF efficiently contribute to the elasticity of the system by forming a network. While CNCs are not able to form a network at the concentrations added in the experiment, the overlap concentration of TO-CNFs is in a concentration window where the formation of TO-CNF networks has been previously reported [80,93]. The exponent of 4.0 ± 0.1 lies in between theoretical exponents of 3.67 for the relevant concentration range [206] and experimental scaling exponents for TO-CNFs of 4.1 and 4.5, respectively [207,208].

To test if the additional TO-CNF network improved the strength of the self-assembled hybrid gels made with the pH-switch method (Figure 4A), amyloid-CNC and amyloid-CNF gels containing 10 mg/mL amyloids and 7 mg/mL nanocellulose were prepared. The mechanical performance of the hybrid gels was tested with oscillatory shear rheology and oscillatory compression testing (**Figure 7**). The pH-mediated gelation increased the oscillatory shear moduli of the amyloid-nanocellulose mixtures by almost two orders of magnitude (Figure 7A). The nanocellulose morphology did not have an effect on the G' values, as no difference was seen between hybrid gels containing CNCs or TO-CNF. However, the strain of the dynamic yield point (indicated by arrows in Figure 7B) increased by almost an order of magnitude in hybrid gels containing TO-

CNF. Finally, compression testing (Figure 7C) showed no difference in elongational elastic modulus E' in the linear regime.

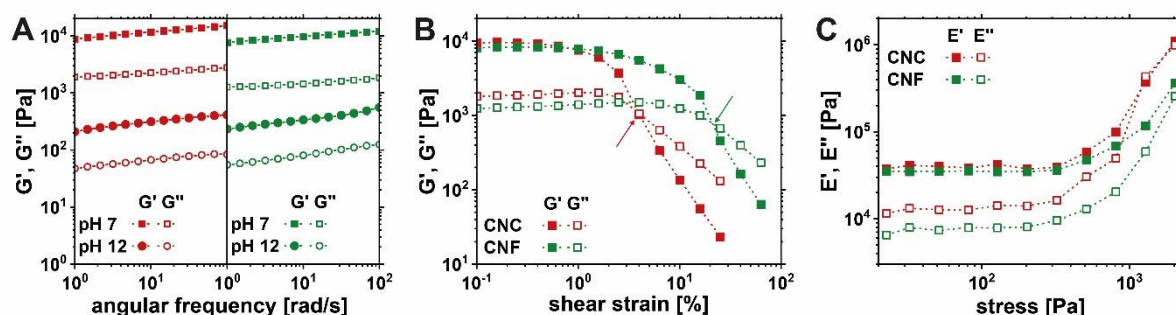


Figure 7: Frequency sweeps of the amyloid-nanocellulose (CNCs in red, TO-CNFs in green) hybrid gels and the co-dispersions at the corresponding pH (A), amplitude sweeps of the hybrid gels at a fixed frequency of 1 rad/s, with arrows indicating the dynamic yield points (B), and oscillatory compression testing of the hybrid gels (C).

The expected strengthening of the hybrid gels by switching from CNCs to TO-CNFs was rather challenging to observe in the mechanical experiments presented here. Although the gels amyloid-CNF gels were visibly more durable during sample handling, there was no difference in the linear regimes during frequency sweeps in shear rheology and in compression testing. Only the amplitude sweep data showed that the amyloid-CNF gels can withstand larger deformations. This can be attributed to the presence of two networks, increasing the overall toughness of the material. This set of experiments would be greatly improved with tensile measurements as shear and compression do not seem to be the ideal type of deformation to gain more knowledge on their mechanical properties. Unfortunately, these gels are not stable enough to be mounted into a tensile geometry.

CONCLUSION

The interactions between amyloid fibrils and nanocellulose were largely dependent on charge: AFM imaging, turbidity measurements, zeta potential measurements and rheology proved the attraction of positively charged HEWL amyloids and oppositely charged CNCs, while negatively charged BLG amyloids and CNCs repulsed each other and formed stable co-dispersions. The polyelectrolyte complexation of HEWL amyloids and nanocellulose is driven by the gain of entropy in the system due to the release of counter-ions and hydration water. The emerging complexes can be considered as HEWL amyloid networks cross-linked with nanocellulose. In-depth rheological characterization allowed description of the amyloid network elasticity as a function of amyloid and nanocellulose concentration. While the $G_0 \sim c_{CNC}^{1.0 \pm 0.1}$ relationship shows the proportional increase of elasticity with CNC addition, attributed to cross-link formation and bundling, the $G_0 \sim c_{CNF}^{4.0 \pm 0.1}$ scaling law indicates the formation of a double network of the added TO-CNFs [206–208]. On the other hand, the scaling of elasticity with amyloid concentration to the exponent of 2.3 ± 0.1 is in good agreement with the affine thermal model and experimental data for amyloid fibrils and other filamentous proteins [198,202–204]. Finally, homogenous, almost transparent hybrid HEWL and BLG amyloid-nanocellulose gels were made using a pH-mediated self-assembly method. In order to go from a repulsive co-dispersion of negative amyloids and nanocellulose, the pI was crossed, introducing positive charges on the amyloid and leading to a nanocellulose-amyloid network. The nanocellulose morphology did not affect the elastic modulus in shear and compression measurements, but the hybrid gels containing TO-CNF showed a higher dynamic yield point, and can therefore withstand larger deformations. Due to their higher aspect ratio and thus lower overlap concentration, the addition of TO-CNF will contribute an additional network and

therefore, amyloid-CNF hybrid materials have better mechanical properties compared to amyloid-CNC hybrids. In conclusion, these results contribute to the understanding of amyloid-nanocellulose interactions and self-assembly, and provide strategies for future work on the bottom-up assembly of sustainable hybrid functional materials.

Author contribution statement

Nico Kummer: Conceptualization; Data curation; Formal analysis; Investigation; Methodology; Project administration; Validation; Visualization; Writing - original draft

Caroline E. Giacomini: Formal analysis; Investigation; Methodology; Validation; Writing - review & editing

Peter Fischer: Conceptualization; Funding acquisition; Methodology; Supervision; Writing - review & editing

Silvia Campioni: Conceptualization; Funding acquisition; Project administration; Supervision; Writing - review & editing

Gustav Nyström: Conceptualization; Funding acquisition; Project administration; Supervision; Writing - review & editing

Declaration of Competing Interest

The authors declare that they have no known competing financial interests or personal relationships that could have influenced the work reported in this paper.

Acknowledgements

The authors would like to thank Brian Sinnet for providing access to the Zetasizer at the Particle Laboratory of Eawag, Gilberto Siqueira (Empa) for providing the TO-CNF

and Qiyao Sun for support with compression testing. Stephan Handschin and Miroslav Peterek from ScopEM at ETH are acknowledged for their support with cryo-EM. Kevin De France (Empa) and Mattia Uselli (ETH Zurich) are acknowledged for valuable discussions. N. Kummer, S. Campioni and G. Nyström would like to gratefully acknowledge financial support from the Swiss National Science Foundation (Grant number: 200021_192225). C.E. Giacomini and P. Fischer acknowledge financial support from the Swiss National Science Foundation (Grant number: CRSII5_189917).

Appendix A. Supplementary material

The amyloid-nanocellulose interactions were tested by mixing the two components at different ratios (Table S1). Changes in turbidity were observed by the naked eye (Figure S1) and also measured with UV-Vis spectroscopy and reported as OD₆₀₀.

Table S1: Mixing scheme for the different amyloid:CNC ratios at concentrations of 10=1 mg/mL. Note that the total solid content varies with the different ratios.

Amyloid:nanocellulose ratio	CNC 2 mg/mL (mL)	Amyloid 2 mg/mL (mL)	10 mM HEPES pH 7 (mL)
10:0	5	0	5
10:1	5	0.5	4.5
10:3	5	1.5	3.5
10:5	5	2.5	2.5
10:7	5	3.5	1.5
10:10	5	5	0
7:10	3.5	5	1.5
5:10	2.5	5	2.5
3:10	1.5	5	3.5
1:10	0.5	5	4.5
0:10	0	5	5

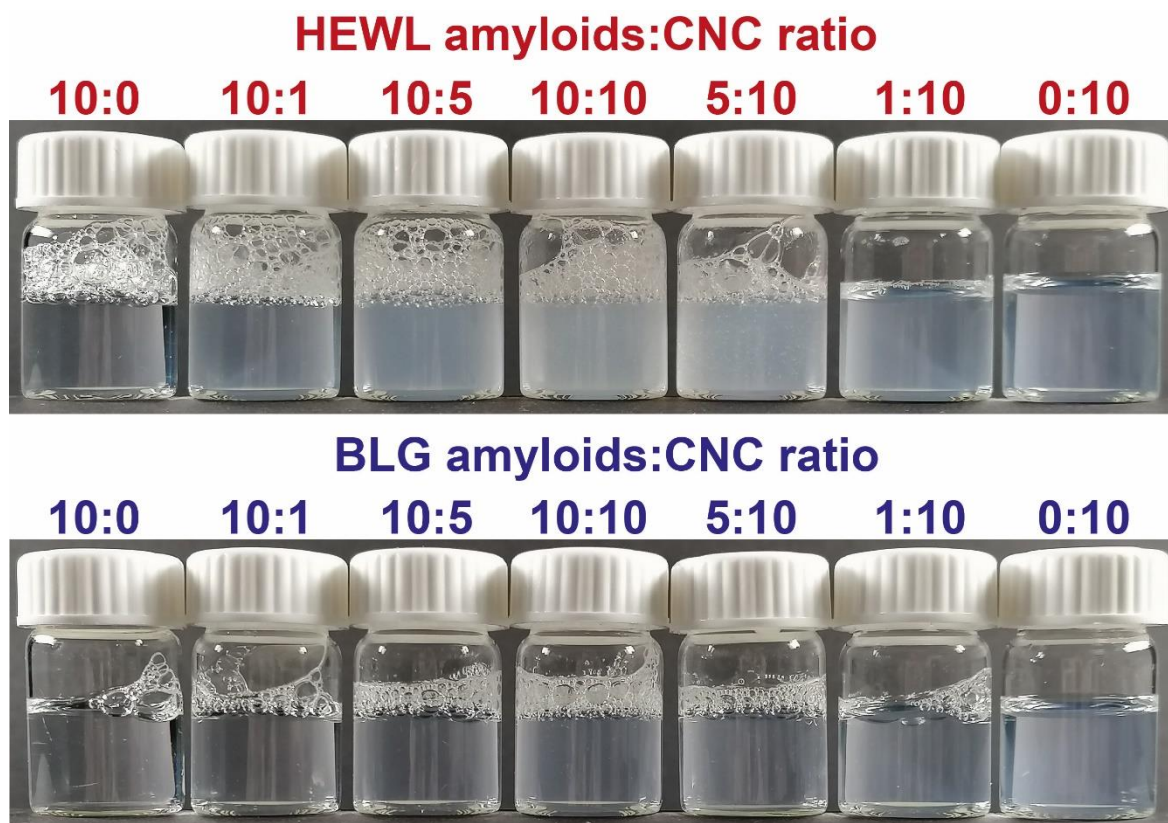


Figure S1: Photos of different amyloid:CNC ratios showing increased turbidity of the samples containing HEWL amyloids due to complexation. Samples with BLG amyloids instead did not turn turbid.

Complexation of different HEWL species with CNCs

In order to further characterize the HEWL amyloid-CNC complexes at pH 7, amplitude sweeps and viscosity measurements were performed. The results were compared to complexes of CNCs with amyloids shortened by sonication and with the residual unconverted peptide fraction, obtained by ultrafiltration of an aggregated sample using a 100 kDa MWCO centrifugal filter unit [131]. In all cases, complexation between the HEWL species and the CNCs occurred, as seen in the AFM images (**Figure S2**). In addition to the observation on the nanoscale, the complexation also resulted in visible changes in turbidity, which are similar to the ones seen in the amyloid-CNC mixtures (**Figure S3**). However, the complexes formed at a 10:10 ratio between the different HEWL species and CNCs differed in their rheological properties. The storage modulus

G' of the system containing the high aspect ratio amyloid fibrils was more than one order of magnitude higher than that of the systems containing sonicated amyloids or unconverted peptides (**Figure S4A**). Additionally, the dynamic yield point was shifted to shear strains on the order of 100% for the full-length amyloid-CNC mixture, compared to 10% observed for the mixtures with sonicated amyloids or peptides (Figure S4B). Viscosity measurements showed an increased viscosity at low shear rates for the amyloid-CNC system compared to the other mixtures (Figure S4C). The slope of the viscosity curve changed at a shear rate of around 1 s^{-1} and, additionally, strong hysteresis between the segments of increasing and decreasing shear rates within the cycle was observed. Hysteresis observed in linear viscosity measurements indicates a break-up of the network structure, which is not restored during the subsequent sweep of decreasing shear rate [209]. Due to their high aspect ratio and semiflexible nature, amyloid fibrils formed an elastic network, while the oppositely charged CNCs acted as counter charges introducing cross-linking points in the network. Overall, the complexes formed by mixing sonicated amyloids or unconverted peptides with CNCs were much weaker, due to their much lower aspect ratio and resulting poorer network formation. Possibly, these latter networks are actually dominated by the contribution of aggregated CNCs, which was also observed with AFM by De France *et al.* [104].

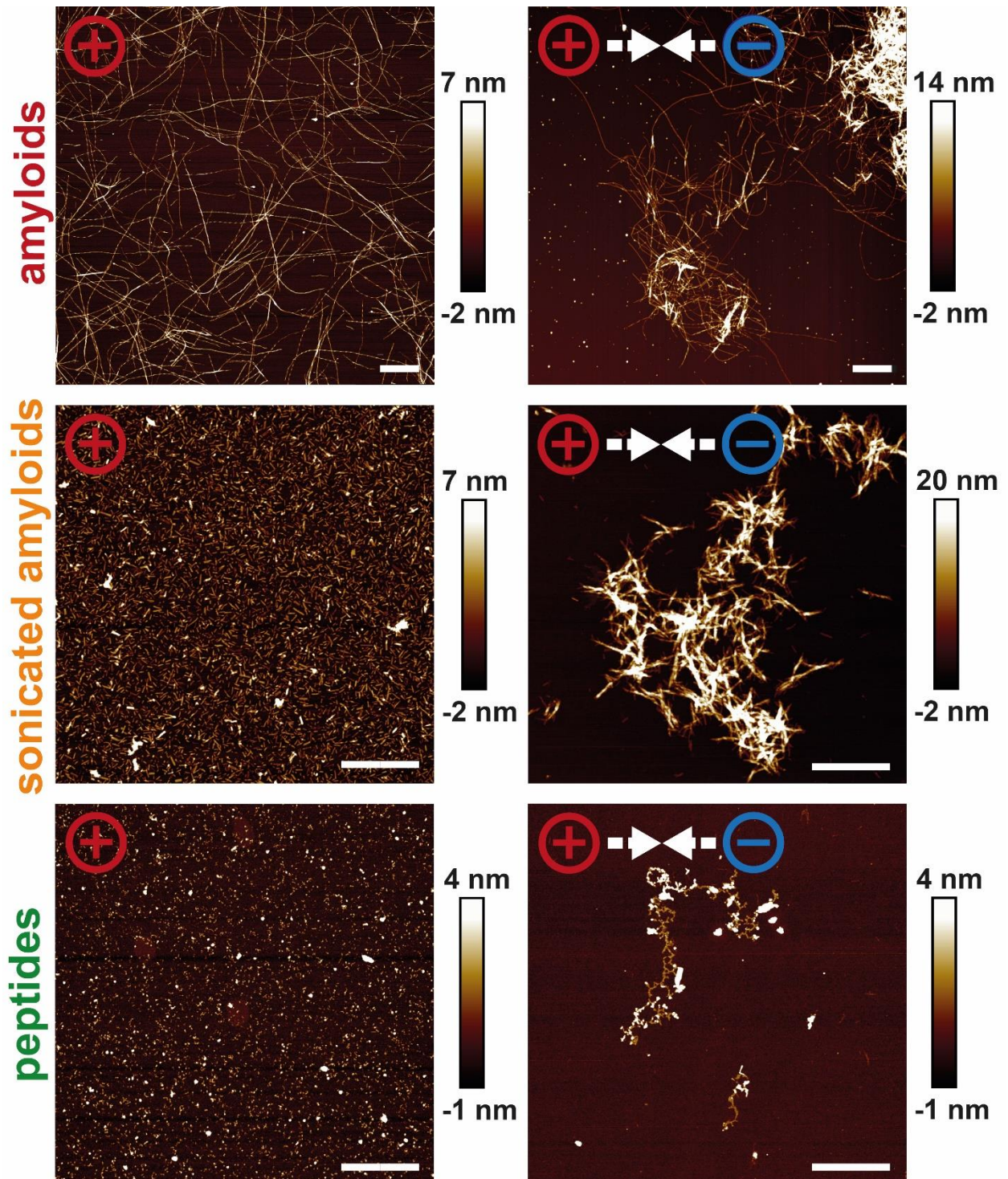


Figure S2: AFM images of pure amyloids, sonicated amyloids and unconverted peptides (left column) and their complexes with CNCs at a protein:CNC ratio of 10:3. The scale bars denote a distance of 1 μ m. The term unconverted peptides refers to the fraction in the amyloid fibril system, unable to self-assemble into amyloid fibrils, occurring as free peptide fragments.

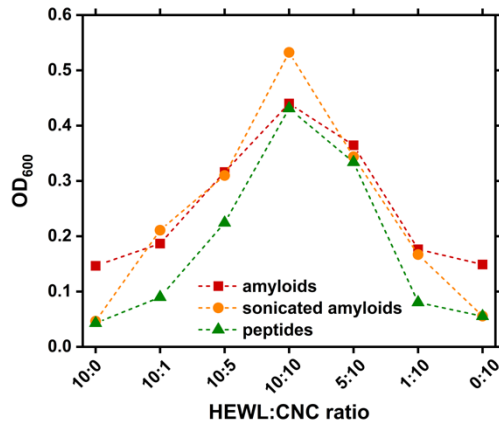


Figure S3: Turbidity measurements of mixtures at different ratios including CNCs and either full-length HEWL amyloids, sonicated HEWL amyloids and unconverted peptides.

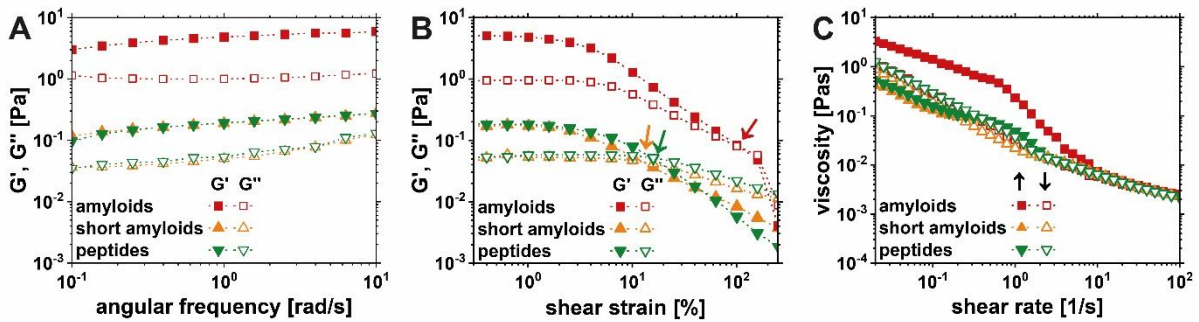


Figure S4: Rheological characterization of the mixtures of full-length amyloid fibrils, sonicated fibrils and unconverted peptides with CNCs at a 10:10 ratio (10=1 mg/mL). Frequency sweeps at a fixed amplitude of 1 % (A). Amplitude sweeps at a fixed frequency of 1 rad/s, with arrows indicating the dynamic yield points (B). Flow sweep cycles at increasing (full symbols) and decreasing (empty symbols) shear rates.

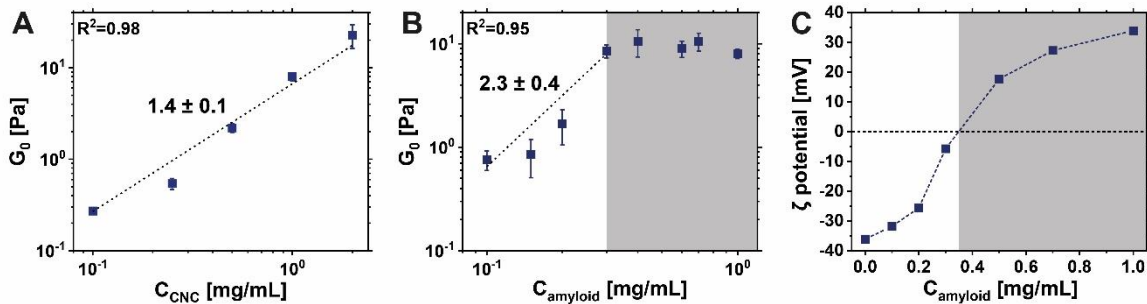


Figure S5: The plateau modulus G_0 (G' at 1% deformation and 1 rad/s frequency) at a fixed amyloid concentration of 1 mg/mL in dependence on the added CNC, including the linear fit determining the exponent of the power law (A). The plateau modulus

at a fixed CNC concentration of 1 mg/mL in dependence on the amyloid concentration, including the linear fit determining the exponent of the power law for concentrations up to 0.3 mg/mL (white regime) (B). At higher concentrations a plateau was reached (grey regime). ζ potentials at a fixed CNC concentration of 1 mg/mL with increasing amyloid additions at pH 3 (C).

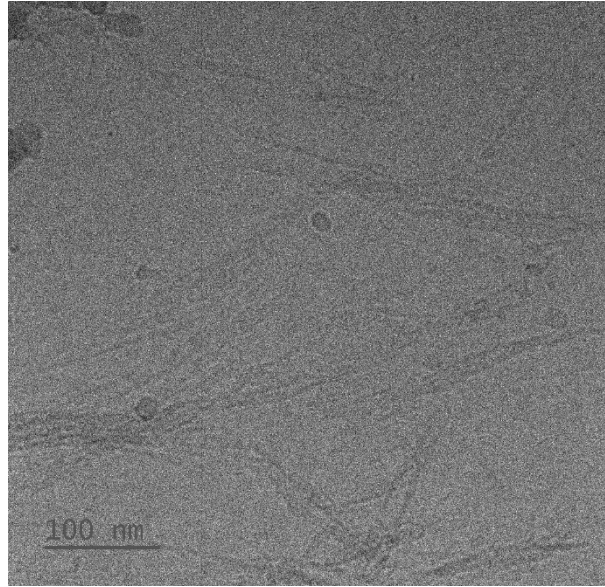


Figure S6: Cryo-TEM image of the vitrified but hydrated amyloid-CNC hybrid gels showing lateral aggregation into bundles. The cryo-TEM imaging was performed to confirm that the bundles observed in cryo-SEM were not an artifact due to freeze-drying of the samples.

6 Discussion

In this chapter, the main findings from the three first-author publications presented in chapter 3-5 are discussed and further developed. Certain aspects from the three second-author publications related to the topic of the thesis (chapters 9-11) will be taken up as well.

6.1 Self-assembly in 1D, 2D and 3D

This thesis includes results on the 1D self-assembly of HEWL into amyloid(-like) aggregates, the 2D self-assembly of HEWL amyloid fibrils at air-water interfaces (adsorption) for functional coatings and the 3D self-assembly of amyloid fibrils formed by HEWL and BLG with nanocellulose into hybrid gels (controlled polyelectrolyte complexation). The three self-assembly processes are summarized schematically in **Figure 1** focusing on the main parameters influencing self-assembly in each case, namely the building blocks, the interactions involved and the outer environment. Note that additional parameters such as mobility and adjustability have been left out, since the processes described in this thesis are all diffusion-dependent, and adjustability plays a minor role.

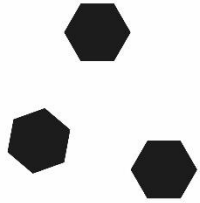
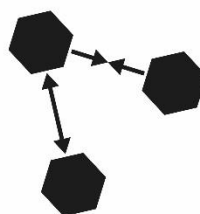
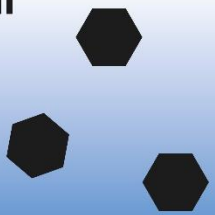
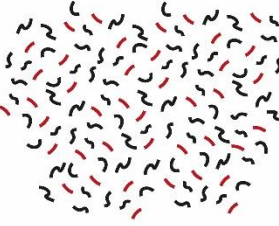
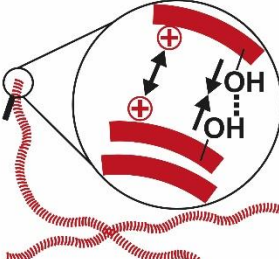
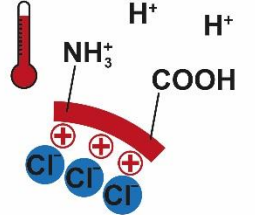
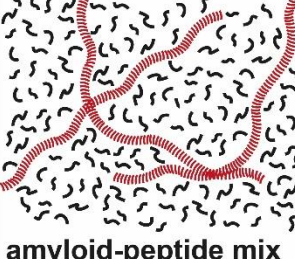
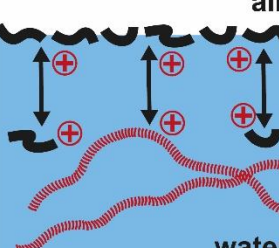
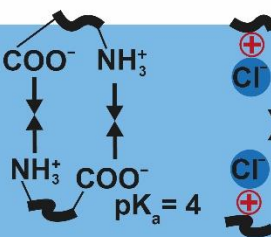
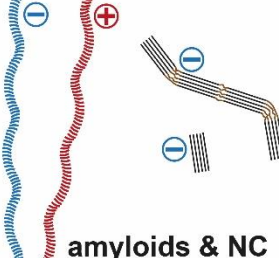
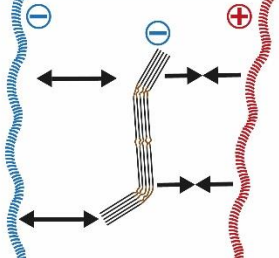
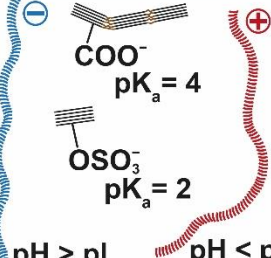
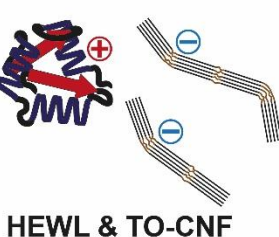
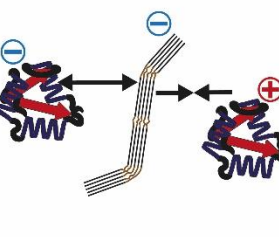
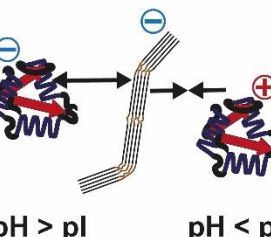
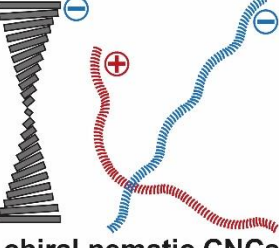
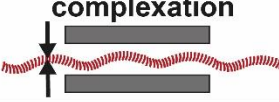
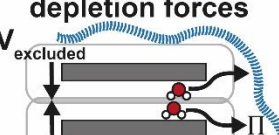
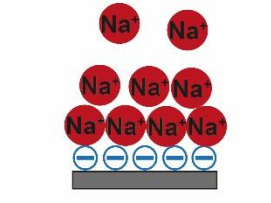
<div style="writing-mode: vertical-rl; transform: rotate(180deg);">parameter</div> self-assembly	I  building blocks	II  interactions	III  environment
1D amyloid aggregation chapter 3	 self-similar peptides	 	
2D amyloid adsorption chapter 4	 amyloid-peptide mix	 air water	 pK_a = 4
3D amyloid-CNF complexation chapter 5	 amyloids & NC	 	 COO⁻ pK_a = 4 OSO₃⁻ pK_a = 2 pH > pI pH < pI
CNF-HEWL complexation chapter 9	 HEWL & TO-CNF	 	 pH > pI pH < pI
CNC-amyloid liquid crystals chapters 10&11	 chiral nematic CNCs	complexation  depletion forces  V_{excluded} Π	 Na⁺ pH *not tested

Figure 1: Overview of the self-assembly pathways described in chapters 3-5 and 9-11 regarding building blocks, interactions and environmental control.

The 1D self-assembly of HEWL amyloid fibrils has been achieved using acid hydrolysis to cleave the native HEWL into short peptide fragments. The self-assembly of the peptide building blocks into semi-flexible fibrils is governed by the balance of attractive and repulsive forces. While the amyloid β -sheet structure is based mostly on H-bonding and hydrophobic interactions, the strong double layer repulsion between the highly charged building blocks is the main reason for the ordered 1D aggregation. Under conditions resulting in reduced double layer repulsion, such as neutral pH and increased salt concentrations, shorter and less ordered ("amorphous") aggregates form [11,12]. This demonstrates that by changing the environmental conditions, especially pH, ionic strength and temperature, the important balance of forces can be tuned. The complex amino acid composition of proteins with pH-responsive carboxylic and amino groups, makes pH an important parameter for protein self-assembly.

Another strategy to induce protein aggregation is the use of chaotropic substances to denature proteins. Reducing agents like TCEP and DTT fall in this category, but also guanidinium chloride and urea [11,34,64]. In contrast to acid hydrolysis, the disulfide bond reduction with TCEP maintains the primary structure of HEWL but leads to partial protein unfolding and reorganization of secondary and tertiary structure. As shown in Chapter 3, the self-assembly of amyloid-like HEWL aggregates is highly pH-sensitive. The decrease of the pH of the solution from pH 5.5 to pH 4.5, leads to a drastic increase in repulsion between the building blocks, resulting in colloiddally stable 1D amyloid-like worms. Similar worm-like structure has also been obtained with ethanol-induced aggregation of HEWL [210]. Ethanol and other organic solvents are known to cause protein aggregation based on the decrease of the dielectric constant of the solvent, which leads to the weakening of the hydrophobic effect stabilizing the structure of the protein, exposing non-polar amino acid resulting in structural rearrangements and aggregation [11,210]. According to literature, amyloids obtained via acid hydrolysis

aggregate into less ordered worm-like morphologies when the hydrolysis is reduced due to higher protein concentration or higher pH, leading to faster aggregation kinetics, less ordered cross- β -sheet structure and lower persistence lengths [14,21,22]. The reduced selectiveness of which part of the protein sequence is ending up in the aggregated state, might also affect the conversion yield of the aggregation reactions. Higher conversion were observed for flexible HEWL worms (65%) and BSA amyloids (90%) compared to semi-flexible HEWL and BLG amyloid fibrils (both 40%). The lower conversion of HEWL and BLG amyloids might be due to the hydrolysis resulting in peptides with a sequence unsuitable for the highly ordered amyloid self-assembly. Self-similarity is an important feature in self-assembly processes [2], which in this case means the physicochemical compatibility of the repeating peptide β -strands [8]. Another factor that contributes to the yield of the reaction is the equilibrium between non-aggregated and aggregated state, which is also a factor determining the stability of the aggregates [211]. Despite being an extreme minimum in the protein-folding landscape [15], the amyloid state seems to be prone to disassembly under certain conditions [151–153]. This instability can be explained by the loss of translational, rotational and conformational entropy a peptide building block experiences upon addition to a nucleus or amyloid fibril. Especially at low concentrations, the translational entropy loss cannot be offset by the non-covalent interactions (e.g. hydrogen bonds) holding together the amyloid backbone [211]. In the case of HEWL amyloids, fibril disassembly was observed upon the removal of unconverted peptides by extensive dialysis. In fact, the relative amyloid fraction could be increased to a maximum of 60%, which might be the equilibrium between peptides and amyloid species. However, the purification of the amyloids came at the expense of around 75% of the initial protein mass lost in the form of unconverted peptides or disassembled amyloids. The disassembly of amyloid fibrils can be classified under the reversibility/adjustability aspect of the self-assembly concept.

As the interactions between the peptides of the amyloids are non-covalent, they are more prone to be reversed by the constant bombardment of solvent molecules [2].

In practice, a total elimination of the peptide fraction was impossible (at least for HEWL amyloids), which was interfering with the interfacial adsorption experiments (Chapter 4). During attempted surface pressure and interfacial rheology measurements (not shown), the expected differences between full-length and shortened amyloids with regard to adsorption kinetics and elasticity of the self-assembled amyloid interfacial films formed could not be found. Measuring almost identical adsorption kinetics of the amyloid system (containing fibrils and peptides) and the pure peptide fraction revealed that the adsorption of the HEWL amyloid system at air-water interfaces was dominated by the unconverted peptides and not the amyloid fibrils, which is in agreement with the literature on adsorption of the soy glycinin amyloids system [76]. These findings indicate that for the 2D self-assembly of the amyloid system at the air-water interface, the building blocks are the peptides rather than the amyloids. Or, in other words, the peptides stabilize the air-water interface, while the amyloids are present in the "bulk" of the foam lamellae in the form of a network [76]. During the adsorption process, double layer repulsion between already adsorbed and adsorbing peptides determines the adsorption kinetics and stability of interfacial layers. In literature, this phenomenon is often called "electrostatic adsorption barrier" [76,212]. Of course, the double layer repulsion can be tuned by adjusting the ionic strength or the initial charge density of the adsorbing particles. Foam stability measurements confirmed a strong pH-dependence, with better foam stability for higher pH, where the peptides were less positively charged (due to the deprotonation of acidic amino acids). Zhang and co-workers used a similar soap film approach to coat different nanomaterials onto substrates [169]. They used surfactants to stabilize the air-water interface more efficiently, leading to highly elastic foams that even allowed to develop a continuous coating process. Despite already

having the surface activity of the peptides as a "surfactant" to deposit layers of amyloid fibrils (nanomaterial), a combination of the amyloid system with surfactants could be interesting for a further optimization of the foam stability.

In 3D hybrid systems made from amyloid fibrils and nanocellulose building blocks, the interactions were highly dependent on the charges of each component. Polyelectrolyte complexation dominated the self-assembly of oppositely charged amyloids (positive) and nanocellulose (negative) in the case of hybrid gels (Chapter 5 and Chapter 9), but also affected the chiral nematic self-assembly (Chapter 10). It is important to point out that polyelectrolyte complexation is an entropy-driven process, pushed by the release of counter-ions and hydration water gaining freedom [80,116,117]. Again, the easiest way to tune the self-assembly by environmental factors is the adjustment of pH, which influences the charge density of the protein components. By starting at high pH, above the isoelectric point of the protein, stable co-dispersions with nanocellulose can be prepared due to double layer repulsion. If the pH is then decreased below the isoelectric point, the charge of the protein is inverted and polyelectrolyte complexation kicks in. This procedure has been exploited for the controlled self-assembly of hybrid amyloid-nanocellulose hydrogels, which were transparent, indicating a high degree of homogeneity. The networks formed in this manner showed the characteristic elasticity scaling behavior of amyloid fibrils independent of the shape of the added nanocellulose (CNCs or CNFs) [198,202]. The scaling behavior observed with increasing nanocellulose additions was linked to amyloid fibril bundling in the case of CNC addition, or to the formation of a secondary CNF network [206–208]. Due to the higher dynamic yield point of the amyloid-CNF system, further improvements of the gel elasticity should be performed on this combination. Similar to the amyloid self-assembly in ethanol mentioned above, lowering the dielectric constant of the solvent inducing hydrophobic effects and probably more particle-particle hydrogen bonding could be another strategy

to induce the co-assembly of amyloids and nanocellulose. Gelation of the amyloids in ethanol has been reported for HEWL [213] and solvent exchange to ethanol is a common step in the preparation of nanocellulose aerogels by supercritical drying [214].

Finally, the self-assembly of CNCs into chiral nematic phases in the presence of BSA amyloids showed a special behavior, caused by depletion interactions. Due to the excluded volume between the CNCs, the BSA amyloids were hindered from their incorporation, resulting in higher osmotic pressure in the surrounding volume. This in turn caused the outflow of water from the space between CNC layers, compressing the chiral nematic pitch (blue-shift). Bast and co-workers infiltrated pre-formed chiral nematic films with BSA and PEG with molecular weights up to 400 kDa and observed a red-shift associated with the increase of the pitch due to the incorporation of the infiltrating species into the liquid crystals [130]. Despite being rather short for amyloids, the BSA aggregates are likely much bigger in size and molecular weight (probably hundreds of megadaltons [159], two orders of magnitude larger than the largest PEG tested) to intercalate the chiral nematic structure. However, it would be interesting to determine the critical size for the intercalation-depletion (red-blue shift) transition. BSA amyloids might not be the best candidates to determine this critical size, since their irregular morphology might also affect the depletion effect. Possibly, BLG amyloids shortened by sonication might be better suited, due to similar dimensions, charge density and stiffness of shortened BLG amyloids and CNCs favoring intercalation. Bast and co-workers also reported that the formation of the chiral nematic structure was prevented when CNCs and silk fibroin were pre-mixed and then left for EISA while infiltration of the pre-assembled CNC films preserved the chiral nematic structure [130]. Especially for proteins, like silk fibroin, interacting strongly with CNCs, the infiltration might prevent aggregation, which is detrimental for the formation of chiral nematic structure.

6.2 Antimicrobial activity of HEWL amyloids

As the overall goal was also to provide novel functionality to cellulose-based materials, the antimicrobial activities of the different HEWL particles were assessed. The colloiddally stable HEWL amyloid fibrils and worms were quantitatively assessed for their antimicrobial activity against Gram-positive *S. aureus*, Gram-negative *E. coli* and the yeast *C. albicans*. The expected non-catalytic, but charge-mediated antimicrobial activity was confirmed for the HEWL aggregate species, showing better and more broad-spectrum antimicrobial activity compared to native HEWL [32,37,58]. The more positively charged amyloid fibrils performed better than the worms. However, despite having a lower zeta potential than the amyloid fibrils, the unconverted peptides also showed considerable antimicrobial activity as the amyloid-peptide mixed systems, most probably due to a much higher number concentration. Therefore, a clear distinction between the antimicrobial activity of amyloid fibrils and peptides was not possible. The peptides might also cause an antimicrobial effect by a different mode of action, such as membrane permeabilization, as this phenomenon is also observed with antimicrobial peptides [181]. For HEWL amyloids the minimum inhibitory concentrations were 0.01 mg/mL against *S. aureus* and 0.1 mg/mL against *E. coli* and *C. albicans*, however 2-3 log reductions were already observed at 0.01 mg/mL. This antimicrobial effect at rather low concentrations in suspension might account for the successful killing of bacteria when the amyloids are used in a coating. On the one hand, the more compact structure of a 2-dimensional coated amyloid surface may lead to a drastic decrease of surface area and exposure of charged groups towards the targeted bacteria. However, on the other hand, the apparent concentration of amyloid fibrils in a coating is considerably increased which might compensate the loss of surface area. The 30 nm thick coating of amyloid fibrils coated on top of a dried film of TO-CNFs was

able to reduce the *S. aureus* cfu count by almost 3-log compared to uncoated TO-CNFs. However, the effect of the coating against *E. coli* and *C. albicans* was not even 1-log reduction. These results confirm the observations made in suspension, with *S. aureus* being the most susceptible to HEWL amyloids. In addition to that, the expected decrease of antimicrobial activity due to less available positively charged surface area was confirmed and directly linked to surface zeta potential measurements. Overall, HEWL aggregates (amyloid fibrils and amyloid-like worms) showed enhanced broad-spectrum antimicrobial activity compared to native HEWL. There was strong indication that the antimicrobial effect was stronger when the amyloids were more positively charged and exposing as much surface area as possible.

7 Conclusion

In this thesis amyloid-(like) aggregates of HEWL were produced using different pathways and characterized with regard to their structure and antimicrobial properties. Additionally, the self-assembly of sustainable biohybrid materials made from HEWL amyloids and nanocellulose was explored. The antimicrobial potential of HEWL amyloids was assessed quantitatively in suspension, as well as in the form of a coating.

The self-assembly of HEWL amyloids as well as the co-assembly of amyloids and nanocellulose were governed by the balance of attractive and repulsive intermolecular forces. Due to the strongly pH-dependent charge of amyloids originating in the protonation of functional groups, variations of the pH offer the tunability of electrical double layer interactions. In the case of HEWL self-assembly into amyloid-like worms induced by disulfide bond reduction, the increase in double layer repulsion by lowering the pH led to stable 1-dimensional aggregates, whereas higher pH resulted in flocculation and sedimentation of the HEWL.

The adsorption (2D self-assembly) at air-water interfaces of the amyloid fibrils system obtained by acid hydrolysis of HEWL was dominated by unconverted peptides.

Stable foams only foamed above pH 4, where the acidic amino acids were deprotonated, leading to a decreased adsorption barrier. The optimized 2D foams created inside a loop (similar to blowing soap bubbles) could be used to deposit homogenous layers of amyloid fibrils onto TO-CNF nanopapers to introduce antimicrobial functionality.

Lastly, polyelectrolyte complexation between oppositely charge amyloid fibrils and nanocellulose led to cross-linking and increased elasticity. An approach based on pH-

mediated self-assembly was applied to produce homogenous HEWL and BLG amyloid-nanocellulose hybrid hydrogels. The amyloids and nanocellulose were mixed above the isoelectric point of the proteins, so they were both negatively charged and formed stable co-dispersion. Using dialysis, the pH was decreased to cross the isoelectric point and introduce positive charges on the amyloids leading to polyelectrolyte complexation and gelation.

The positive charge of the HEWL amyloid fibrils at neutral pH also played an important role in their antimicrobial activity based on their interactions with the negatively charged cell walls and cell membranes of the microorganisms causing cell lysis. Suspensions of worms and amyloid fibrils had a dose-dependent, enhanced and broad-spectrum antimicrobial effect against Gram-positive *S. aureus*, Gram-negative *E. coli* and the yeast *C. albicans*. A similar charge-mediated antimicrobial effect was seen for the HEWL amyloid fibril layer deposited onto the TO-CNF nanopapers using the 2D foam film coating method. However, the loss of surface area of the amyloid fibrils compressed into a 2D coating layer led to decreased bacterial inactivation compared to the suspensions.

In summary, this thesis offers new perspectives regarding the self-assembly of HEWL aggregates and their co-assembly with nanocellulose. It suggests bottom-up approaches resulting in hybrid materials with improved mechanical properties and added functionalities (antimicrobial activity), that could be used to develop sustainable biomedical materials.

8 Outlook

Despite gaining important knowledge on the self-assembly of HEWL amyloids and on their co-assembly with nanocellulose, certain things remain unclear and open up new questions for the future. Especially, the amyloid fibril conversion, i.e. how much of the original protein will end up in the amyloid state, and the fragmentation and disassembly of amyloid fibrils are important topics underreported in the literature [211].

The acid hydrolysis mediated self-assembly of proteins is the most common pathway to obtain amyloid fibrils and the go-to method to test the ability to form amyloids from a new source of protein. However, due to the heterogeneity in peptide fragments, only a small fraction with suitable physicochemical properties and self-similarity will form amyloid fibrils, while the rest of the peptides remains in solution. In the future, the amyloid conversion should be a more important criterion in the development and optimization of amyloid self-assembly pathways. This would decrease the amount of material without a structural role in the system and make the amyloid formation process more sustainable. Moreover, a better conversion and a clear understanding of the composition of the amyloid system would most likely also influence co-assembly with other colloids, such as nanocellulose and allow for a more conclusive characterization of hybrid materials.

Although it is often assumed that the amyloid state is a highly stable energy-minimum in the protein folding landscape [15], fragmentation and disassembly seem to be common [211]. Extensive dialysis lead to the disassembly of the amyloid fibrils, most likely related to the removal of unconverted peptides, which were replaced by peptides released from amyloids to re-establish an amyloid-peptide equilibrium. This process should be examined in more detail, since it might influence the long-term stability of

amyloid based materials, especially if they are exposed to different solvent environments (pH, ionic strength). Gaining more knowledge on the equilibrium between amyloid fibrils and peptides/oligomers are of high interest with regard to disease-related amyloids, such as amyloid- β , since its oligomeric states are associated with cytotoxicity promoting neurodegeneration [6].

Furthermore, the use of HEWL amyloid fibrils for antimicrobial coatings of nanocellulose-based wound dressings needs to be explored in more detail. At the moment a hybrid hydrogel containing a base layer of TO-CNF for moisture control and mechanical stability coated with HEWL amyloid fibrils to introduce antimicrobial functionality is being developed. The biological assessment of the wound dressing hydrogel will be extended with antimicrobial tests under physiological conditions and with a cytotoxicity assessment. Approaches to further improve the mechanical properties of the hybrid amyloid-nanocellulose hydrogels include physical and chemical cross-linking between particles of the same species and between the species. Physical cross-linking by charge screening is common for amyloid fibrils and nanocellulose individually and could be applied to hybrid systems as well. Only recently, physical cross-linking of thin interfacial layers of BLG amyloid fibrils with phytic acid has resulted in high stability [215]. There seems to be a high affinity for interactions between phosphates and the guanidino groups of arginine residues [216]. Therefore, studying the combination of amyloid fibrils with phosphorylated nanocellulose could be of high interest. Covalent cross-linking of proteins using glutaraldehyde is well-known and has been recently used for the cross-linking of BLG amyloids [168]. Glutaraldehyde cross-linking potentially also offers the possibility to cross-link the amino groups of amyloid fibrils with amino groups of chitosan. Glutaraldehyde is also used for the immobilization of en-

zymes by covalent cross-linking to substrates [217] and could be applied to functionalize amyloid fibrils with cellulose-binding domains, which could introduce specific interactions between functionalized amyloids and nanocellulose [218].

In addition to the further research needed on the HEWL amyloid system, the work on functional laboratory-made amyloids needs to be broadened to other more sustainable sources of protein than animal proteins. In search of alternatives to lysozyme, plant proteins with high isoelectric points should be considered to obtain amyloid fibrils that are positively charged at a neutral pH in order to obtain a similar charge-mediated antimicrobial functionality. Candidates for such basic proteins include the rapeseed storage protein napin [219] and papain, a protease found in papaya latex [220].

Recently, the shift from animal proteins to plant proteins for amyloid fibril production has been pushed by several research groups [11,13,76]. In the future, proteins from single cell organisms such as autotrophic algae, that can be produced without arable land, as well as yeast, which is a side product from beer production. Both should also be considered as highly sustainable protein sources for amyloid formation with interesting functionalities that can open up new applications.

Overall, the research on the applications of amyloid fibrils should explore specific functionalities, such as filtration of heavy metals and antimicrobial healthcare materials, rather than the recently suggested use of valuable protein as bulk materials for single-use bioplastic packaging. The competition between proteins for materials and proteins for nutrition should be avoided at all costs. For packaging materials, nanocellulose could be an alternative if it is coming from sustainably managed forests or industrial side streams.

Selected co-authored publications

This chapter contains three related co-authored publications, which contributed to the understanding of the self-assembly and the interactions between proteins/amyloids and nanocellulose.

The publication by Wu and coworkers (Chapter 9) provided important knowledge about the interactions and complexation behavior of TO-CNF with native HEWL [121].

The work on chiral nematic assembly of CNCs in presence of amyloid fibrils, namely positively charged amyloid fibrils made from HEWL (Chapter 10) and negatively charged bovine serum albumin (BSA) (Chapter 11) [104,105].

9 Nanocellulose-lysozyme colloidal gels via electrostatic complexation

Tingting Wu, Nico Kummer, Kevin J. De France, Silvia Campioni, Zihui Zeng, Gilberto Siqueira, Jie Dong, Gustav Nyström

Volume 251, 1 January 2021, 117021

<https://doi.org/10.1016/j.carbpol.2020.117021>

Reproduced with permission from authors and publisher [121]

Copyright © 2020 Elsevier

Nanocellulose-Lysozyme Colloidal Gels via Electrostatic Complexation

*Tingting Wu^{1,2}, Nico Kummer^{1,3}, Kevin J. De France¹, Silvia Campioni¹, Zihui Zeng¹,
Gilberto Siqueira¹, Jie Dong², Gustav Nyström^{1,3,*}*

*¹ Laboratory for Cellulose & Wood Materials, Empa - Swiss Federal Laboratories for
Materials Science and Technology, Überlandstrasse 129, 8600 Dübendorf, Switzer-
land*

*² State Key Laboratory for Modification of Chemical Fibers and Polymer Materials, Col-
lege of Materials Science and Engineering, Donghua University, Shanghai 201620, P.
R. China*

*³ Department of Health Science and Technology, ETH Zürich, Schmelzbergstrasse 9,
CH-8092, Zürich, Switzerland*

* To whom correspondence should be addressed

E-mail: gustav.nystroem@empa.ch;

Abstract

Biohybrid colloids were fabricated based on electrostatic complexation between anionic TEMPO-oxidized cellulose nanofibrils (TO-CNF) and cationic hen egg white lysozyme (HEWL). By altering the loading of HEWL, physical colloidal complexes can be obtained at a relatively low concentration of TO-CNF (0.1 wt%). At neutral pH, increasing the HEWL loading induces an increase in charge screening, as probed by zeta-potential, resulting in enhanced TO-CNF aggregation and colloidal gel formation. Systematic rheological testing shows that mechanical reinforcement of the prepared biohybrid gels is easily achieved by increasing the loading of HEWL. However, due to the relatively weak nature of electrostatic complexation, the formed colloidal gels exhibit partial destruction when subjected to cyclic shear stresses. Still, they resist thermocycling up to 90 °C. Finally, the pH responsiveness of the colloidal complex gels was demonstrated by adjusting pH to above and below the isoelectric point of HEWL, representing a facile mechanism to tune the gelation of TO-CNF:HEWL complexes. This work highlights the potential of using electrostatic complexation between HEWL and TO-CNF to form hybrid colloids, and demonstrates the tunability of the colloidal morphology and rheology by adjusting the ratio between the two components and the pH.

Keywords: Cellulose nanofibrils; Lysozyme; Electrostatic complexation; Colloids; Rheology;

Introduction

Proteins and polysaccharides are commonly used to construct biohybrid food-grade colloids because they are both naturally biocompatible and biodegradable [221,222]. Cellulose nanofibrils (CNF) are a class of abundant, sustainable, biocompatible and renewable biomass with a large range of remarkable properties, such as biodegradability, biocompatibility and renewability, as well as ease of functionalization [108,223–227]. Among them, TEMPO-mediated oxidation of the hydroxyl groups on the surface of CNF is a widely reported method to introduce negatively charged carboxylate groups onto the CNF, here referred to as TO-CNF, resulting in new functionalities [82,190,228]. Several research efforts on TO-CNF have focused on its potential biomedical applications, such as drug delivery [229] and wound healing [230], or as rheological modifier in inks for 3D printing [231].

Lysozyme is a natural antimicrobial enzyme widely found in eggs and animal secretions; specifically lysozyme from hen egg whites (HEWL) has attracted significant research attention due to its low cost and widespread availability [232,233]. Moreover, the isoelectric point of HEWL is 10.7, bearing a net positive charge over a broad pH range making it an ideal candidate to form colloidal complexes with negatively charged biomolecules [234,235]. Furthermore, the intrinsic antimicrobial activity of lysozyme is often exploited in food packaging and wound healing applications, which demonstrates the multi-functionality of lysozyme [236–238].

The combination of cellulose and HEWL has been previously investigated for medical and food science applications [239,240]. In particular, many researchers have investigated the complexes and gels formed between sodium carboxymethyl cellulose (CMC) and HEWL based on electrostatic and hydrophobic interactions [221,241–243].

Composite networks have been successfully formed through a variety of different complexation mechanisms, including covalent cross-linking [244]. For instance, positively charged lysozyme was incorporated into a paper matrix containing CMC via non-covalent binding for food packaging applications [236]. In another example, a Ca^{2+} -cross-linked TO-CNF hydrogel was investigated to act as a carrier for positively charged lysozyme for topical drug delivery applications, where the electrostatic interactions between lysozyme and the TO-CNF hydrogel structure played a key role for the efficient loading of the hydrogels [245]. Moreover, lysozyme was immobilized to cellulose nanocrystals (CNC) by adsorption to carbodiimide-activated carboxylate groups in the surface of CNC, resulting in enhanced antibacterial activity [246]. Finally, the combination of nanocellulose and lysozyme was evaluated in paper filters for advanced separation applications [247]. All these works have shown a great potential of exploiting the electrostatic interaction between anionic cellulose and cationic lysozyme for the formulation of novel bio-complexes.

The interaction of lysozyme with charged polymers is pH-dependent. For example, the changes in pH greatly influenced the formation of electrostatic complexes between lysozyme and low methoxyl pectin [248]. Besides, the colloidal stability of pure TO-CNF gel networks is also controlled by pH [92,249,250], since under acidic conditions the carboxylic groups get protonated resulting in an aggregated CNF gel. The pH-responsiveness of TO-CNF hydrogels can be tuned by adjusting the negatively charged carboxyl density of the CNF during the TEMPO-mediated oxidation process [251] and is an attractive feature for the formulation of novel materials. Changes of pH can cause the dissociation or regeneration of hydrogel networks composed of phenylboronic acid-grafted alginate and PVA, due to the pH-responsiveness of phenylboronic acid-diol ester bonds, [252]. Interestingly, pH-dependent dimerization of an engineered spidroin

protein was exploited recently as a means to modulate the viscoelastic properties of protein-cellulose complexes [253]. Therefore, pH-responsiveness is a key point to investigate in the design of colloidal complexes between charged polymers.

To the best of our knowledge, there has been no report on the electrostatic complexation of TO-CNF and HEWL at low CNF concentrations (i.e. below the threshold to form a percolated gel network). Therefore, in this work a series of TO-CNF and HEWL complexes with different relative ratios were characterized. Effects of the loading of HEWL on the complexation process were evaluated in terms of zeta-potential, morphological and rheological properties. Moreover, the stability of the complexes was monitored under high shear stress, heating-cooling cycles, and changes in pH. Our results indicate that pH-dependent complexation of TO-CNF and HEWL can be used to formulate hybrid colloidal gels for possible applications in the food and medical industries, for instance as thickeners, stabilizers and gelling agents.

Experimental section

Materials. HEWL (hen egg white lysozyme, $M_w = 14.3$ kDa), sodium hydroxide (NaOH), and (3-Aminopropyl) triethoxysilane (APTES) were purchased from Sigma-Aldrich. HEPES (4-(2-hydroxyethyl)-1-piperazineethanesulfonic acid), 2,2,6,6-Tetramethyl-1-piperidinyloxy (TEMPO), and sodium hypochlorite (NaClO) solution (12-14% chlorine) were obtained from VWR. Never-dried elemental chlorine free (ECF) cellulose fibers from bleached softwood pulp (*Picea abies* and *Pinus* spp.) were obtained from Stendal GmbH (Berlin, Germany). Sodium bromide (NaBr $\geq 99\%$) was supplied by Carl Roth GmbH & Co. All chemicals were used as received without any further purification.

Preparation of TEMPO-oxidized cellulose nanofibrils (TO-CNF). TEMPO-mediated never dried cellulose fiber oxidation was performed following previously established protocols [82,190] with slight modifications. Briefly, the never dried cellulose pulp (33.3 wt%), with a chemical composition of 81.3% Cellulose, 12.6% hemicellulose, 0% lignin and 0.3% ash [254], was dispersed in distilled water to a final concentration of 2 wt%. TEMPO and NaBr were dissolved in water at ratios of 0.1 and 1.0 mmol/g of cellulose pulp respectively, and were then mixed with the cellulose pulp dispersion. The pH of the suspension was then adjusted to 10-10.5 using 2 wt% NaOH. 10 mmol NaClO was then added per gram of cellulose. The reaction was allowed to proceed at room temperature for 4-5 h, after which the TEMPO-oxidized cellulose fibers were washed several times with distilled water until the conductivity was close to that of distilled water, and subsequently ground using a Supermass Colloider (MKZA10-20J CE Masuko Sangyo, Japan) at an applied energy of 9 kWh/kg. The ground CNF was further fibrillated using a high shear homogenizer (M-110EF, Microfluidics Ind., Newton, MA-USA) for a total of 10 passes at a pressure of 8 bar. After homogenization, a uniform and transparent TO-CNF dispersion (Figure S1) with a concentration of 0.5 ± 0.1 wt% was obtained.

Preparation of TO-CNF and HEWL complexes. A stock solution of HEWL was dissolved in 10 mM HEPES buffer (final concentration ~ 2.2 mg/mL) and the pH was adjusted to 7.4-7.5 using 1M NaOH. The HEWL solution in HEPES buffer was then passed through a 0.2 μ m cellulose acetate syringe filter to remove any aggregates. Subsequently, 0.5 wt% TO-CNF in water was mixed with a specified amount of HEWL, yielding a final concentration of TO-CNF of 0.1 wt% (1 mg/mL) and a final concentration of HEWL between 0 and 0.1 wt% (10:1 – 10:10 weight ratio of TO-CNF:HEWL). 0.1

wt% TO-CNF only (denoted 10:0) and 0.1 wt% HEWL only (denoted 0:10) samples were also prepared as controls. Specifically, a volume of 30 mL of TO-CNF and HEWL was obtained by mixing 6 mL of 0.5 wt% TO-CNF in MilliQ, 9 mL of MilliQ, and the required amount of HEWL stock solution in 15 mL of HEPES buffer, ensuring the same ionic strength in each biohybrid mixture. Similarly, for pure HEWL suspensions, 6 mL 0.5 wt% TO-CNF was replaced by 6 mL of MilliQ, such that the final concentration of HEWL was kept at 1 mg/mL. For pure TO-CNF suspensions, 15 mL HEPES buffer was added without any HEWL. Samples were allowed to equilibrate for 1 week under ambient conditions before further characterization.

Characterization. Attenuated Total Reflection-Fourier Transform Infra-Red (ATR-FTIR) measurements were performed on a Tensor 27 spectrometer (Bruker Switzerland AG) over the wavenumber range from 500 to 4000 cm^{-1} . Circular Dichroism (CD) testing was performed on a JASCO J-815 CD spectrometer, using a 1 mm cuvette. Here, the selected mixtures were diluted by a factor of 3 prior to CD measurements. Morphology of TO-CNF and HEWL biohybrid complexes were characterized by high-resolution transmission electron microscopy (HRTEM, JEOL, JEM 2200fS), atomic force microscopy (AFM, Bruker ICON3) and field-emission scanning electron microscopy (FESEM, Fei Nova Nanosem 230). For AFM measured in tapping mode, note that all samples contain the same concentration of TO-CNF and were deposited onto a freshly cleaved mica substrate, modified with 0.05% APTES prior to imaging (note that due to their positive charge, pure HEWL samples were deposited onto an unmodified substrate). TEM images were obtained after the complexes (0.001 wt%) were deposited, stained by 1 wt% uranyl acetate and dried on copper grids coated with car-

bon. Zeta-potential measurements were performed at 25 °C using a suspension concentration of 0.005 wt% (Malvern, zetasizer nano series). pH values were measured at room temperature (METTLER TOLEDO, SevenEasy). Rheological testing was performed with an Anton Paar MCR302 rheometer using a double gap cylinder geometry (STANDARD MEASURING SYSTEM DG26.7/T200/SS) at 25 °C for both oscillatory and rotational measurements. For the double gap cylinder, the internal and external diameter are 23.830 mm and 27.593 mm, respectively. Turbidity measurements were acquired from the Transmittance at 600 nm by using a Cary UV-Vis spectrophotometer. Optical microscopy images were obtained from a Leica DFC420 Microscope.

Results and Discussion

TO-CNF and HEWL biohybrid colloids were formed on the basis of electrostatic complexation between negatively charged TO-CNF and positively charged HEWL. This is analogous to previous studies where negatively charged nanocellulose-based matrices have been shown to act as an efficient adsorbent for positively charged proteins such as lysozyme [255,256]. In **Figure 1(a)**, the electrostatic interaction process is illustrated for increasing concentrations of HEWL. With no added HEWL, a stable and homogenous TO-CNF suspension is formed, due to the existence of repulsive forces between the negatively charged carboxylate groups arising from the TEMPO-mediated oxidation. The addition of positively charged HEWL leads to adsorption directly to the negatively charged TO-CNF surfaces via electrostatic complexation, thus reducing the CNF colloidal stability via charge screening. However, at relatively low HEWL concentrations (up to ca. 10:4 of CNF to HEWL mass ratio) the degree of complexation is not yet sufficient to form a stable gel-like network. After the addition of a sufficiently high concentration of HEWL (above ca. 10:5 mass ratio), enhanced charge screening leads

to the aggregation of TO-CNF into clusters in the size range of a few hundreds of microns (Figure 1(d)). Herein, we focus on understanding the fundamentals of the interactions between TO-CNF and HEWL, while simultaneously investigating the effects of the ratio between positively charged HEWL and negatively charged TO-CNF on the characteristics of the resulting biohybrid colloids.

Scanning electron microscopy (SEM) (Figure 1(b and c)) and optical microscopy (Figure 1(d)) were used to visualize the association between TO-CNF and HEWL. Note that in the case of pure TO-CNF suspensions, a relatively uniform fibrillar network is apparent, whereby upon the addition of HEWL, this network largely collapses. However, due to the relatively small hydrodynamic radius of HEWL (ca. 2.0 nm) [257], it is challenging to visualize its distribution within the final complexes via SEM. The complexes obtained at mass ratio values higher than 10:5 are on the order of hundreds of micrometers, and relatively irregular in shape.

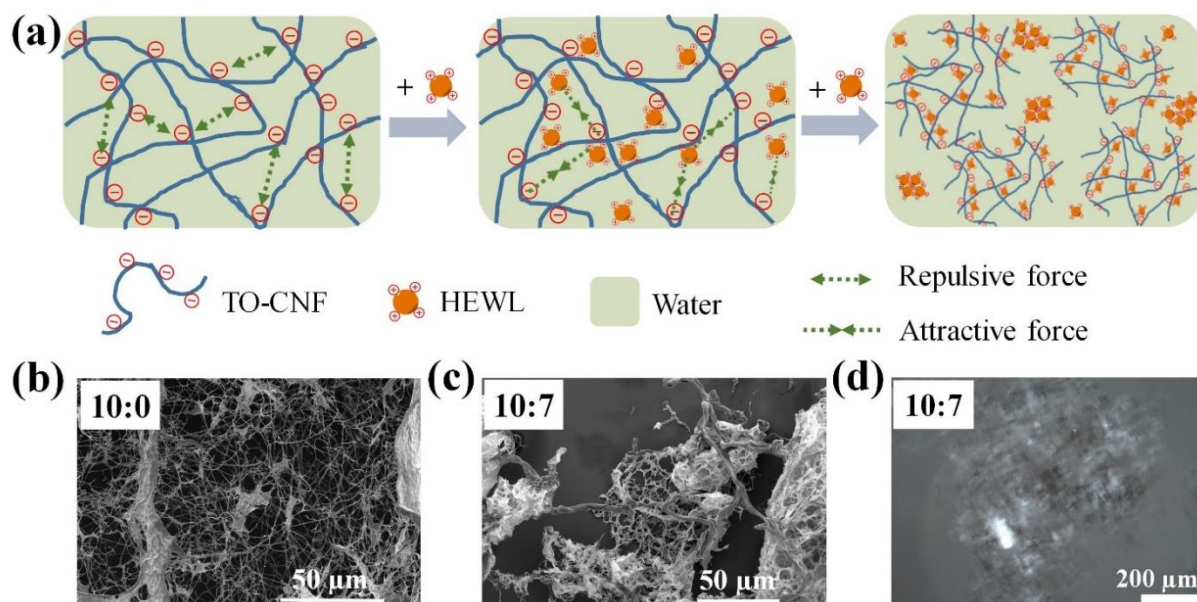


Figure 1. (a) Schematic illustration of the interaction mechanism between TO-CNF and HEWL upon increasing the HEWL loading; (b and c) SEM images of pure TO-CNF and TO-CNF and HEWL colloidal complexes (10:7 relative mass ratio); (d) Optical microscope image of TO-CNF and HEWL colloids (10:7 relative mass ratio).

As surface charge chemistry and density are largely responsible for the formation of stable colloidal systems [258], the zeta potential of the TO-CNF:HEWL complexes was measured (**Figure 2**). HEWL, with an isoelectric point of 10.7, is positively charged under physiological pH (zeta potential of +13.9 mV), while TO-CNF is negatively charged (zeta potential of -57.0 mV), demonstrating a strong potential for electrostatic complexation. At lower concentrations of HEWL (10:0 to 10:3), there is little change in the overall zeta potential due to the strongly negative nature of TO-CNF and limited charge screening (Figure 2). As the concentration of HEWL is further increased (from 10:3 to 10:10), the zeta potential begins to increase accordingly, indicative of increased charge screening. Correspondingly, an increase in suspension turbidity and aggregation becomes apparent from a TO-CNF:HEWL ratio of 10:4, whereby with further increasing HEWL concentration, the aggregation becomes more pronounced. By comparison, pure TO-CNF and HEWL suspensions with the same concentration (1 mg/mL) are transparent (Figure S1), implying that any observed turbidity/aggregation arises solely due to electrostatic complexation between the two oppositely charged biomolecules. Notably, the interaction between various positively charged biomolecules and negatively charged TO-CNF has shown a strong dependency on the ionic strength and pH value of the suspension mixture [190,214,221,256]. Since the pH of the solution remained relatively constant across all ratios of TO-CNF:HEWL (Figure 2b), we can conclude that the electrostatic interactions between TO-CNF and HEWL are the cause of the appearance of these aggregates/flocs, without the requirement of any chemical or heat treatments. Further turbidity analysis is shown in Figure S2, demonstrating that turbidity increases as HEWL loading is also increased (the same trend seen in the photographs).

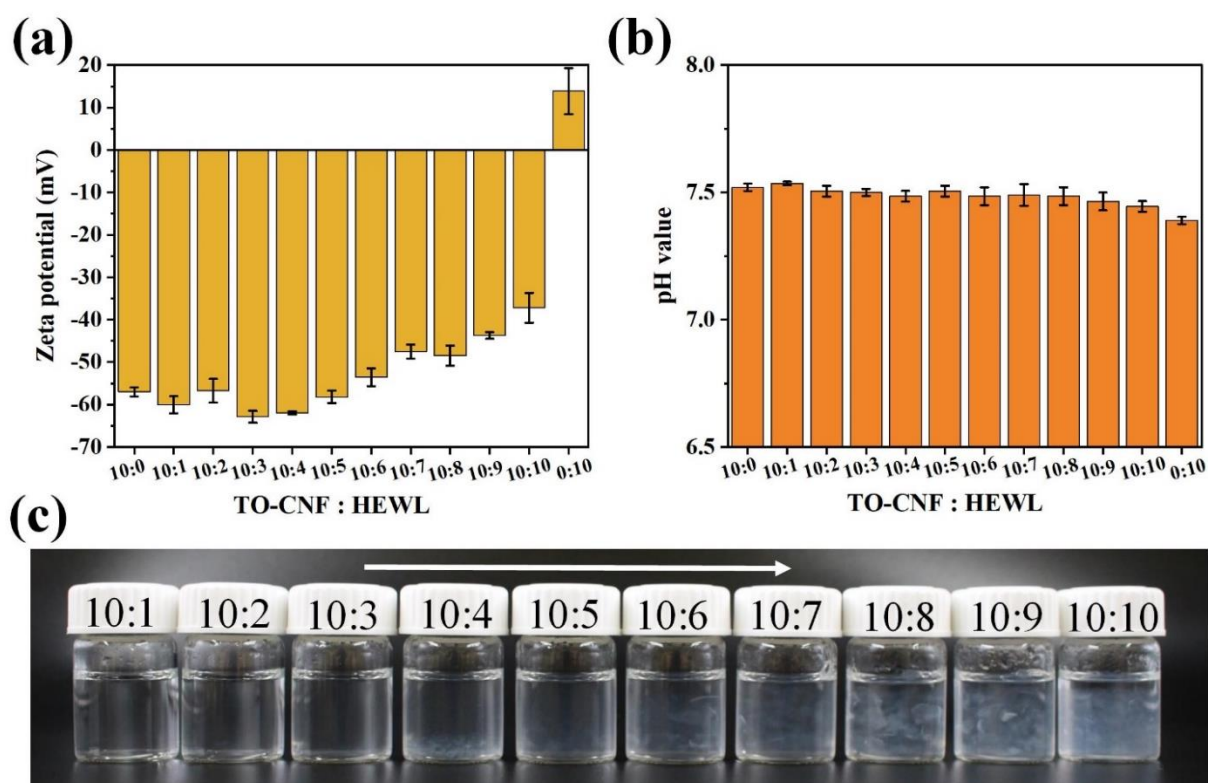


Figure 2. (a) Zeta-potential, (b) pH value and (c) photographs of TO-CNF and HEWL colloidal complexes with different ratios between TO-CNF and HEWL (10:0 to 0:10).

FTIR spectroscopy is a conventional method to investigate the conformational changes in secondary structure of proteins [259,260]. The binding of HEWL to negatively charged lipid vesicles leads to conformational changes and subsequent aggregation of the protein [261]. Herein, the effect of TO-CNF on the secondary structure of HEWL was investigated by means of ATR-FTIR. Pure HEWL shows two strong peaks, one at 1650 cm^{-1} , attributed to α -helices, and one at 1534 cm^{-1} , due to N-H bending of the peptide chains (**Figure 3**). In pure TO-CNF, the peak at 1600 cm^{-1} is attributed to the COONa group on the TO-CNF surface after TEMPO oxidation. For 10:5 and 10:10 formulations, the two peaks at ~ 1650 and 1534 cm^{-1} are still apparent, and with a little shift, indicating the successful incorporation of HEWL into TO-CNF and that the secondary structure of HEWL is stable and not significantly affected by the interaction with

TO-CNF. In addition, CD measurements (Figure S3) supported the presence of α -helices in the TO-CNF and HEWL colloidal systems. Of note, the signal of α -helices from HEWL in the colloidal systems is significantly decreased upon gel formation, indicating the presence of less 'free' HEWL in the suspensions, especially for 10:7 and 10:10 ratios.

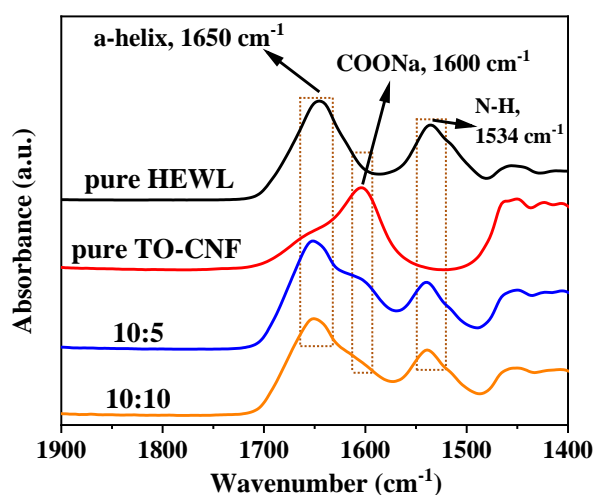


Figure 3. ATR-FTIR spectra of TO-CNF and HEWL casted films with different ratios.

TEM was performed to confirm the microstructure of the TO-CNF:HEWL colloids at various HEWL loadings (**Figure 4** and Figure S4). Generally, the TEM images are in good agreement with the results seen via AFM. For pure TO-CNF suspensions, the individual cellulose nanofibers show uniform diameters of 3-4 nm with a length on the order of hundreds of nm. Upon the addition of HEWL (starting from a ratio of 10:3), no obvious differences between pure TO-CNF (10:0) are noticed. Increasing the HEWL concentration further, starting from 10:5, the TO-CNF tends to aggregate into nanofiber clusters, with similar structures also observed at 10:7.

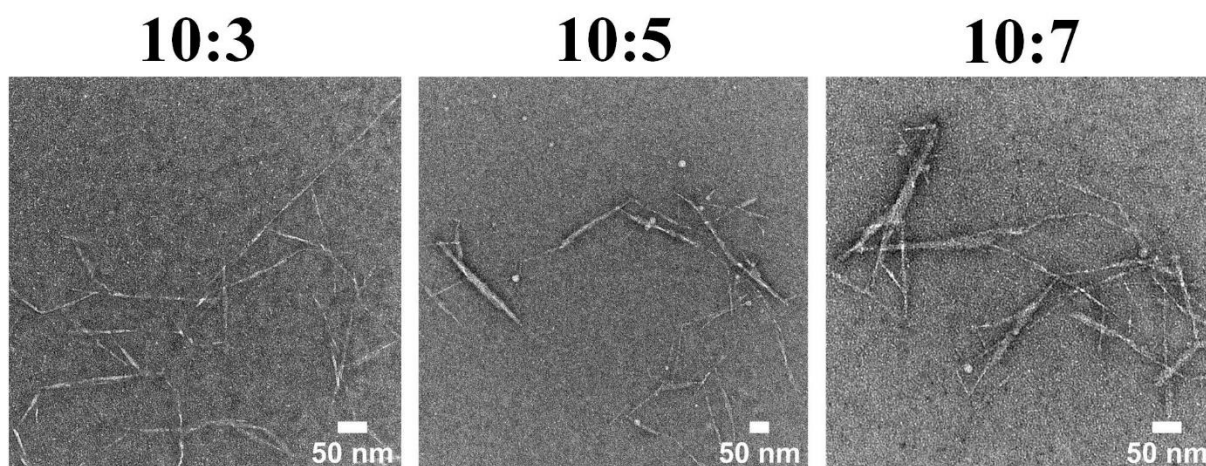


Figure 4. TEM images of TO-CNF and HEWL colloidal complexes with different relative mass ratios (10:3, 10:5 and 10:7).

AFM images were acquired at selected TO-CNF:HEWL ratios (10:0, 10:3, 10:5, 10:7 and 10:10), in order to gain an understanding of the evolution of the microstructure within these biohybrid colloids with increasing HEWL concentration (**Figure 5**, Figure S5 and S6). Individual nanofibers are readily observed in the pure TO-CNF (10:0) sample, as expected (Figure S5). Individual filaments are also evident at low HEWL concentrations (10:3), again suggesting that the extent of charge screening caused by HEWL/TO-CNF electrostatic interaction is not enough to form colloids below a certain threshold concentration (Figure 5). However, as the HEWL concentration is further increased, starting from 10:5, the TO-CNF start to entangle and aggregate together, indicative of significant charge screening (link to figure). At even higher HEWL loadings (10:7), the size of TO-CNF clusters begins to increase drastically (link). We hypothesize that at these high loadings, the biohybrid colloidal complexes become so big that most of the material precipitates out of suspension (Figure 2(c)), and is thus not observable via AFM.

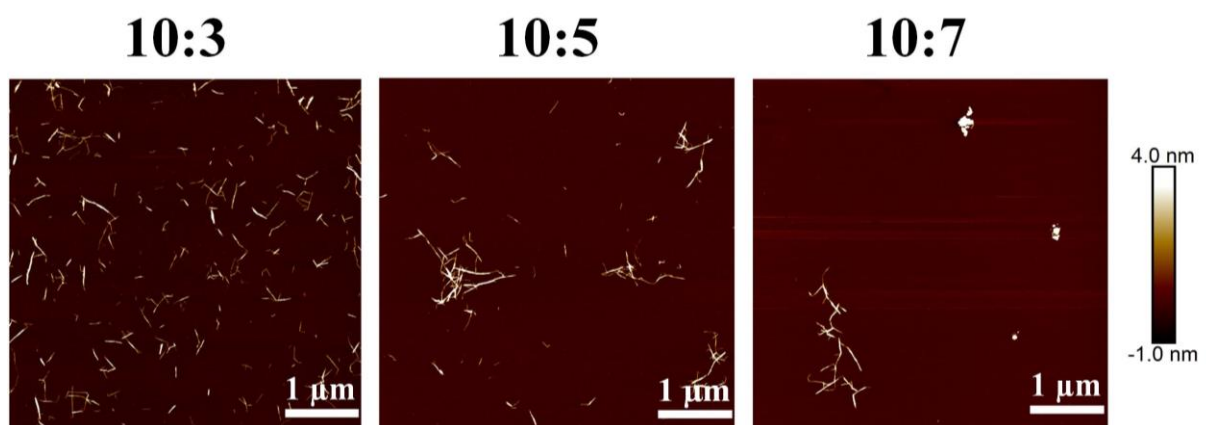


Figure 5. AFM images of TO-CNF and HEWL colloidal complexes with different relative mass ratios (10:3, 10:5 and 10:7).

It is well known that the morphological properties of CNF suspensions affect their rheological behavior [262]. Therefore, the rheological properties of the prepared biohybrid colloidal dispersions were studied in detail to gain an understanding of the stability of these colloids as well as their possibility to undergo a sol-gel transition. As with previous experiments, here we focus on the effects of HEWL loading on the rheological properties of the formed complexes at a fixed concentration of TO-CNF (0.1 wt%). Generally, during strain sweep measurements the crossover point of G' and G'' can be defined as the apparent yield point, where G' represents the storage modulus and G'' represents the loss modulus, which give a measure of the elasticity and viscosity of a material, respectively [249,250]. All strain sweep measurements were performed from a strain of 0.01% to 100 % at a constant angular frequency of 10 rad/s (**Figure 6(a)**). For biohybrid colloidal dispersions with high HEWL loadings (starting from 10:5), there is a crossover of the G' and G'' curves, indicating that with increasing the concentration of positively charged HEWL, the electrostatic interactions are enhanced, promoting the formation of a gelled network. Further increasing the HEWL concentration results in an increase in G' and in complex viscosity (**Figure 6(b)**), suggesting the formation of a

stronger viscoelastic network and gel-like structure due to enhanced electrostatic interaction throughout the system. Note that for all formulations, a linear viscoelastic region exists up to $\sim 10\%$ strain, after which further increasing the strain results in a significant decrease of both G' and G'' , until an eventual crossover point is reached, indicating the destruction/yield of the gel networks and a gel-sol transition. Note that for complexes from 10:1 to 10:4, pure TO-CNF and HEWL, no gelation point is observed via rheology (Supporting Information, Figures S7 and S8).

Frequency sweep tests are widely used to obtain information about the stability of 3D entangled networks in gel and colloidal systems [263]. Herein, frequency sweeps were performed from 0.01 to 100 rad/s under a constant strain of 1 % (within the linear viscoelastic region identified via strain sweep, Figure 6(c)). Above TO-CNF:HEWL ratios of 10:5, all formulations show a single plateau region in the dynamic modulus (G' and G''), with G' dominating over G'' , indicative of a gelled/solid-like behavior. For the 10:5 complex, in the low frequency range the rheological behavior is similar to that of the other formulations, however at increased frequencies G' suddenly drops dramatically, representing liquid-like behavior and partial destruction of the entangled networks.

Additionally, cyclic rotation tests were performed to investigate the stability of these colloidal gels under cyclic shear force (Figure 6(d)). Notably, the apparent viscosity decreases with increasing shear rate, depicting shear-thinning behavior, which is typical for CNF systems [250]. Within the first cycle, there is already a large decrease in apparent viscosity, indicating partial destruction of the TO-CNF:HEWL gel networks (data shown for 10:7). The apparent viscosity appears to be relatively stable for up to 3 cycles however. Similar trends were observed for 10:10 (Figure S9). Notably, for pure TO-CNF suspensions, this significant decrease in viscosity is not evident (Figure S10), which is expected due to the lack of any gelled colloidal network. Importantly,

the apparent viscosity for both 10:7 and 10:10 is still far higher than the apparent viscosity of pure TO-CNF after cyclic shearing, indicating only a partial (and not full) destruction of the gelled networks. Shear viscosity prior to cyclic testing for 10:10, 10:7, and 10:0 can be seen in Figure 6(f).

Previous work has shown that proteins like HEWL are sensitive to heat treatments and generally show a heat-induced gelation behavior [264]. Therefore, the thermo-stability of the colloids was inspected by cyclic heating and cooling from 25 to 90 °C at a heating rate of 3 °C/min (Figure 6(e)), where the G' and G'' were recorded under fixed frequency (10 rad/s) and strain (1 %). Notably, upon increasing the temperature to 90 °C, both G' and G'' decrease dramatically; conversely upon decreasing the temperature from 90 to 25 °C, both G' and G'' increase dramatically. However, during the whole cycle, the G' values are always higher than the G'' values, implying that the networks still exist in a gel-like state during the imposed heat treatment. The thermal-stability of pure HEWL was also characterized (Figure S11) and the measured G' was always lower than G'' , suggesting a more liquid-like behavior. Furthermore, only a minor change in both G' and G'' is observed as a result of thermal cycling, which is different from the change occurring in the complex systems, likely indicating that the changes observed within the TO-CNF:HEWL complexes are primarily due to varied electrostatic interactions attributed to the increased mobility of TO-CNF and HEWL with increased temperature and not due to protein denaturation.

Moreover, the time-dependency of gel complexation was investigated visually and by rheological characterization for 10:7 (Figure S12). Immediately after mixing, the gel complexes appear more homogeneous, and then after 1 week bigger flocs are readily observed, indicating increased aggregation/charge screening. In this state, the

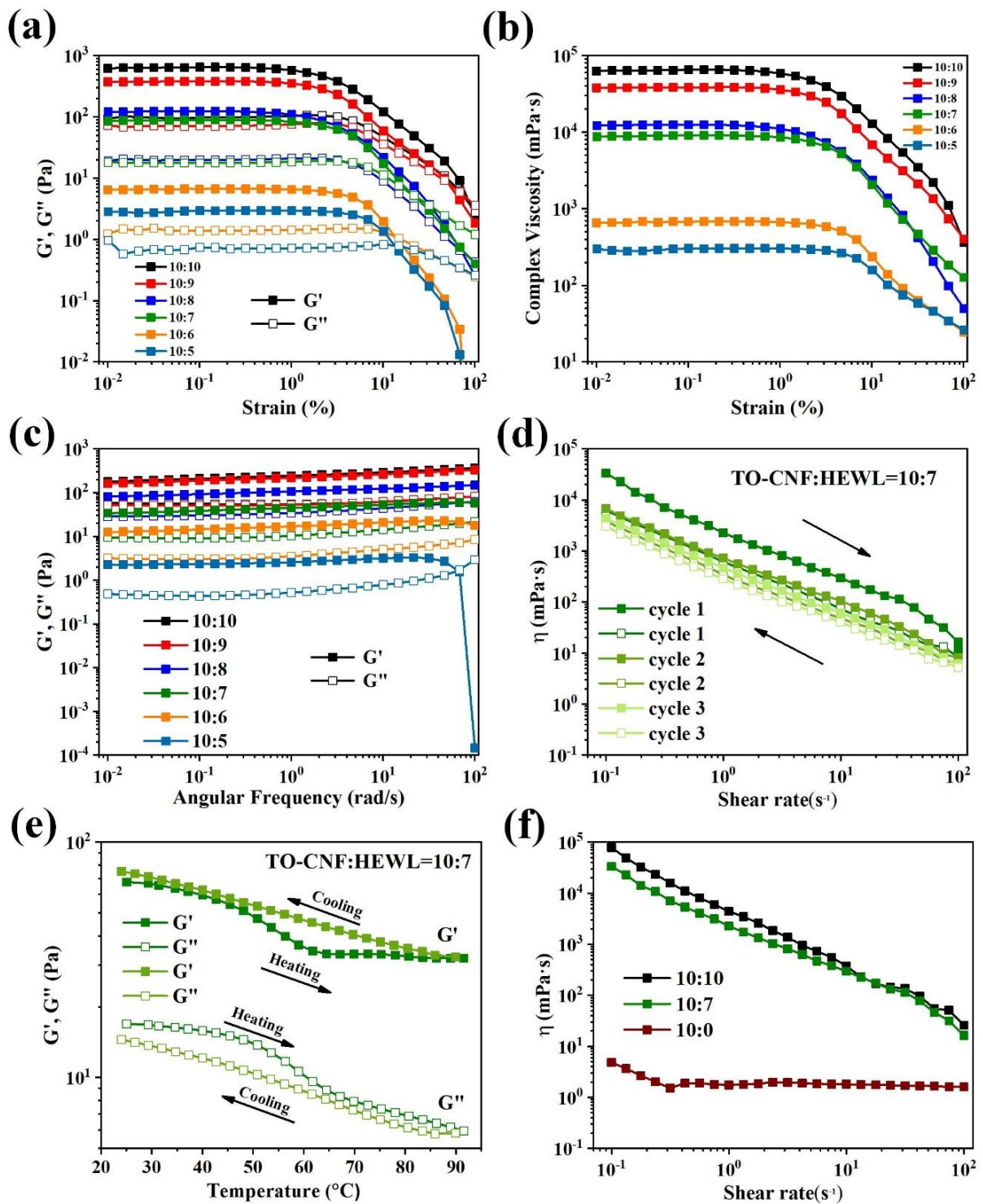


Figure 6. Rheological properties of TO-CNF and HEWL colloidal systems at 25 °C with different ratios from 10:5 to 10:10, (a) storage modulus G' (solid) and loss modulus G'' (open) on strain sweep at 10 rad/s, (b) complex viscosity at 10 rad/s, (c) dynamic frequency sweep ($\gamma = 1\%$). (d) Shear viscosity loop of TO-CNF and HEWL colloids (TO-CNF:HEWL=10:7), the increase and decrease of the shear rate (s^{-1}) is indicated by the arrows. (e) The values of both modulus of TO-CNF and HEWL complex (TO-CNF:HEWL=10:7) during heating (dark green) and cooling (light green) cycles are displayed, storage modulus G' (solid) and loss modulus G'' (open). (f) Shear viscosity of TO-CNF and HEWL colloids with different ratios (10:0, 10:7 and 10:10).

colloidal gels are then relatively stable, after which no significant visual changes are observed. In addition, although 10:7 demonstrates a gel-like behavior (with $G' > G''$) both instantaneously and after 1 week in suspension, the modulus does increase over time, supporting the formation of a stronger/more prominent gel network with increased aggregation.

Previous studies have demonstrated that the electrostatic complexation between charged colloids depends on the pH of the solution [249,250,265]. Therefore, we analyzed the effects of changing the pH of the TO-CNF:HEWL mixtures at a fixed mass ratio of 10:7. The strain sweep curves measured at pH 12 (above the isoelectric point of HEWL) indicate that the complex shows a predominantly liquid-like behavior, due lack of binding between negatively charged HEWL and equally charged TO-CNF (**Figure 7(a)**). Lowering the pH to 7.5 results in a significant increase in G' , attributed to renewed complexation between oppositely charged TO-CNF and HEWL. Further lowering the pH to 3 results in an even higher increase in G' , due to higher density of positive charges on HEWL, and increased TO-CNF aggregation due to protonation of carboxylic groups; similar observations have been seen in other systems with TO-CNF and polyacrylic acid derivatives [250,266].

The photographs in Figure 7(b) demonstrate that as the pH is decreased from 12 to 3, the turbidity of the TO-CNF and HEWL complexes increases, indicative of increased aggregation. Moreover, this phenomenon is completely reversible, as demonstrated in Figure 7(c), whereby turbidity is decreased upon sequential increase in pH to 12. We envision that these pH-switchable complexes could be useful for several potential applications, such as in cosmetic gels, and rheological modifiers for the food industry, where the colloidal properties can be easily controlled by adjusting the overall pH of

the system. In particular, the ability to readily control suspension aggregation and rheological properties gives a level of flexibility which would be beneficial for matching targeted material properties.

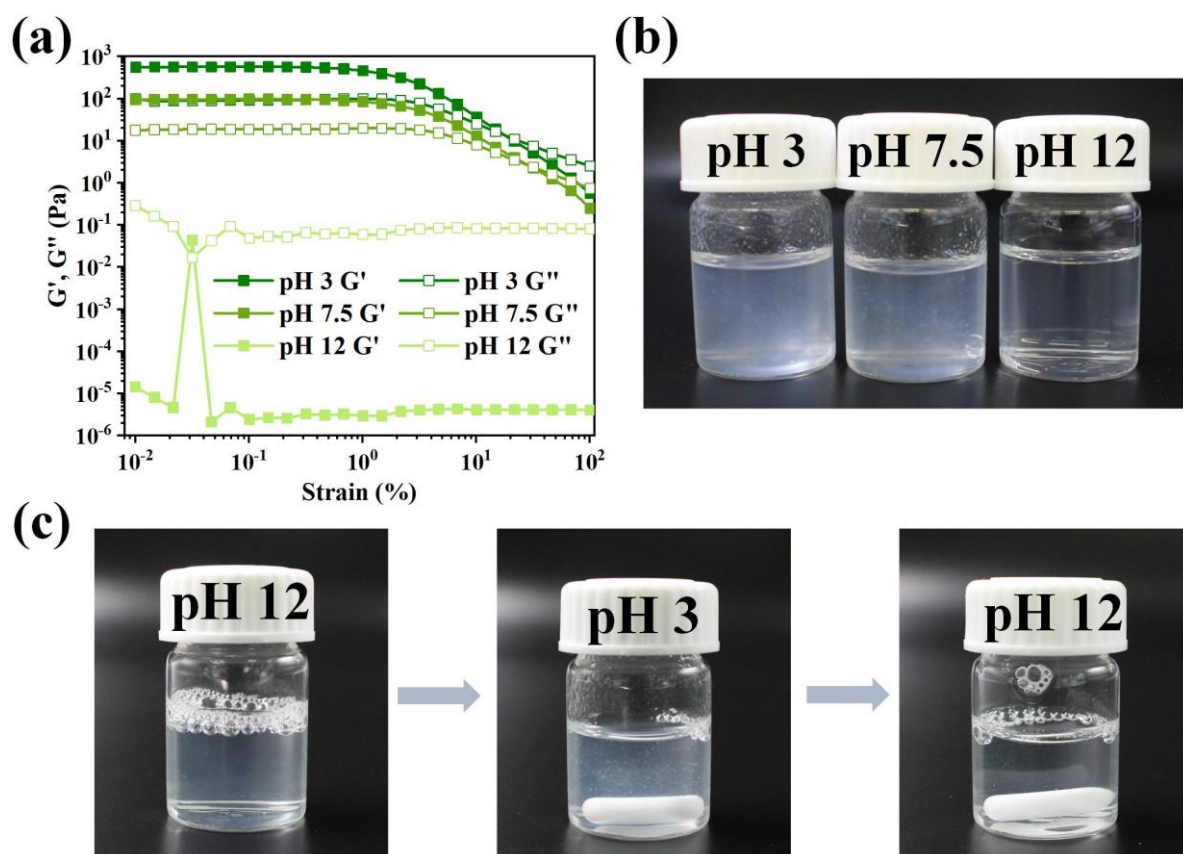


Figure 7. Rheological properties of TO-CNF and HEWL colloids (TO-CNF:HEWL=10:7) at 25 °C with different pH 3, 7.5 and 12 (a) storage modulus G' (solid) and loss modulus G'' (open) on strain sweep at 10 rad/s; (b) photographs of the colloidal systems at different pH; (c) the colloidal complexes with changed pH, first from 12 to 3, then from 3 back to 12.

Conclusion

In conclusion, a series of TO-CNF and HEWL colloids with different ratios were fabricated via simple electrostatic complexation between positively charged HEWL and negatively charged TO-CNF. Increasing the overall HEWL concentration within the colloidal complexes resulted in an increase in zeta potential (absolute value closer to 0) due to enhanced charge screening. Above HEWL concentrations of 10:5, TO-CNF and

HEWL were prone to aggregation, attributed to the electrostatic attraction between opposite charges, evidenced via AFM and TEM. This aggregation resulted in noticeable differences in rheological properties, whereby complexes above HEWL loadings of 10:5 demonstrated gel-like properties, with G' values greater than G'' values. The obtained colloids show a shear-thinning behavior and are relatively stable upon heating up to 90 °C. Importantly, this electrostatic complexation between HEWL and TO-CNF is pH-dependent; at a pH above the isoelectric point of HEWL whereby HEWL is not positively charged, there is no interaction and therefore no colloidal formation. Decreasing the pH to below the isoelectric point of HEWL triggers complexation between the positively charged HEWL and negatively charged TO-CNF, resulting in flocculation and gelation. Importantly, the pH of the solution can be used to drive reversible formation and the dissolution of the colloids as in stimulus responsive gel systems. Overall, this work provides insights for understanding and utilizing the charge interactions between TO-CNF and HEWL and their responsiveness to changes in environmental conditions such as pH for a variety of potential applications ranging from drug delivery, 3D printing, packaging films to wound dressing.

Conflicts of interest

There are no conflicts to declare.

Acknowledgements

T.W. is supported by the China Scholarship Council (CSC) Fellowship. K.D. acknowledges funding from the Natural Sciences and Engineering Research Council of Canada (NSERC) Postdoctoral Fellowship program. We thank Anja Huch for help with TEM and SEM imaging. We thank Tutu Sebastian and Frank Clemens for help with rheological testing.

Supporting Information for:

Nanocellulose-Lysozyme Colloidal Gels via Electrostatic Complexation

*Tingting Wu^{1,2}, Nico Kummer^{1,3}, Kevin J. De France¹, Silvia Campioni¹, Zhihui Zeng¹,
Gilberto Siqueira¹, Jie Dong², Gustav Nyström^{1,3,*}*

- 1. Laboratory for Cellulose & Wood Materials, Empa - Swiss Federal Laboratories for Materials Science and Technology, Überlandstrasse 129, 8600 Dübendorf, Switzerland*
- 2. State Key Laboratory for Modification of Chemical Fibers and Polymer Materials, College of Materials Science and Engineering, Donghua University, Shanghai 201620, P. R. China*
- 3. Department of Health Science and Technology, ETH Zürich, Schmelzbergstrasse 9, CH-8092, Zürich, Switzerland*

* To whom correspondence should be addressed

E-mail: gustav.nystroem@empa.ch



Figure S1. Photographs of pure TO-CNF 0.1 wt% dispersion (left) and pure HEWL 0.1 wt% suspension (right).

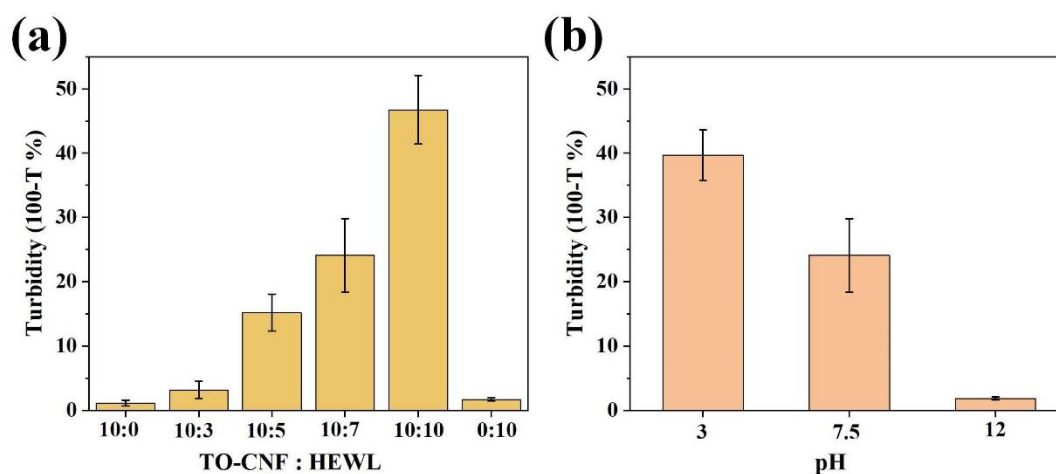


Figure S2. (a) Turbidity of TO-CNF and HEWL colloidal complexes with different ratios between TO-CNF and HEWL (10:0, 10:3, 10:5, 10:7, 10:10 and 0:10). (b) Turbidity of 10:7 colloidal complexes at different pH (3, 7.5 and 12).

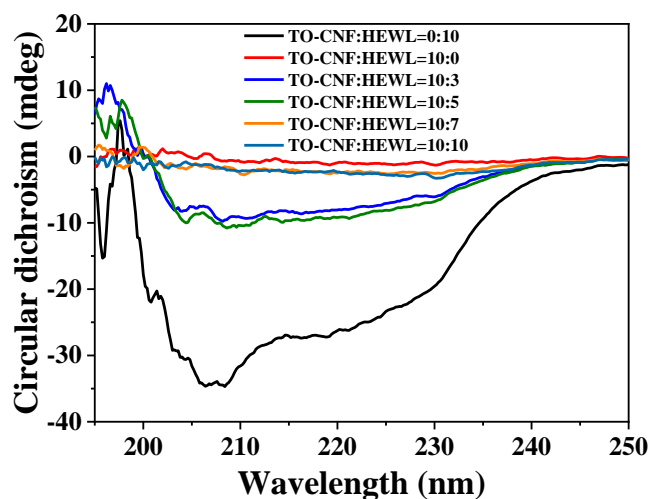


Figure S3. CD spectra of TO-CNF and HEWL colloidal complexes with different ratios between TO-CNF and HEWL (0:10, 10:0, 10:3, 10:5, 10:7 and 10:10).

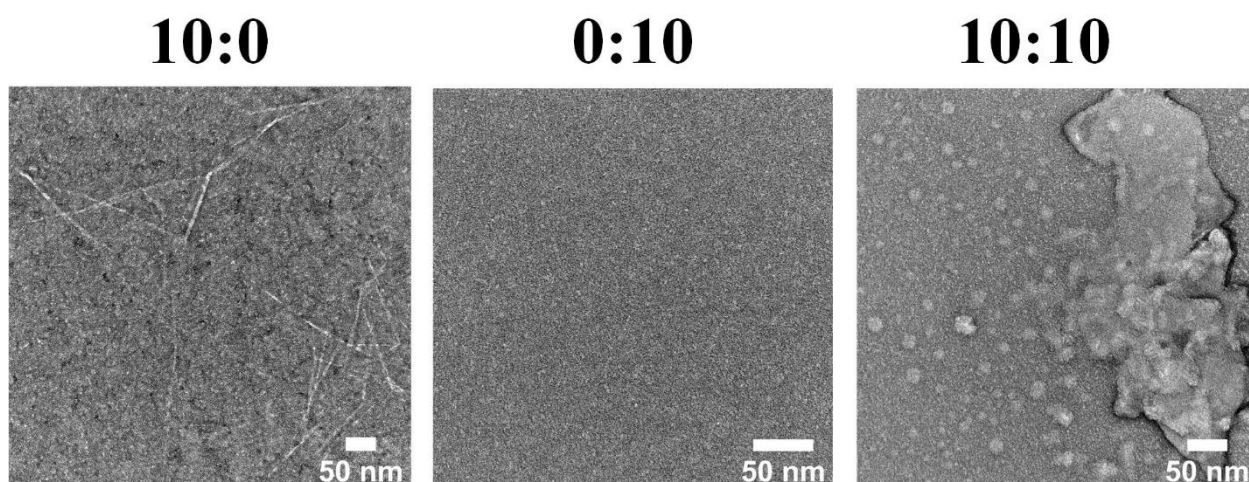


Figure S4. TEM images of pure TO-CNF (10:0) and HEWL (0:10) as well as TO-CNF-HEWL at a 10:10 relative mass ratio.

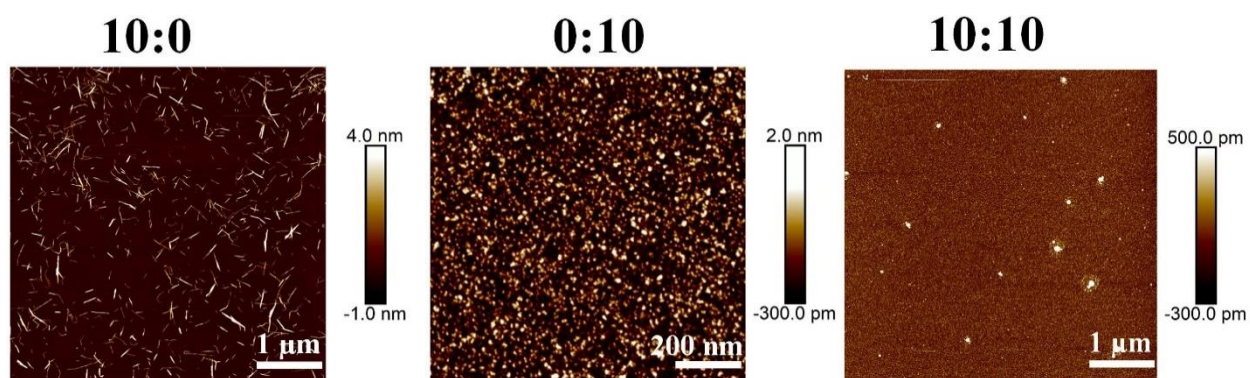


Figure S5. AFM images of pure TO-CNF (10:0) and HEWL (0:10) as well as TO-CNF-HEWL at a 10:10 relative mass ratio.

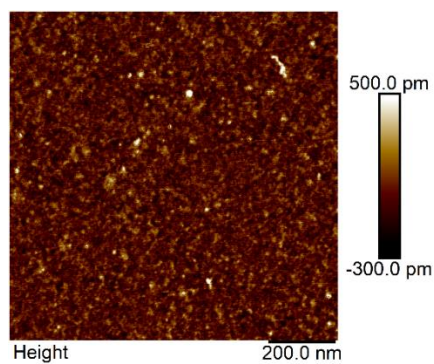


Figure S6. AFM image of 0.001 wt% pure HEWL solution on APTES coated mica.

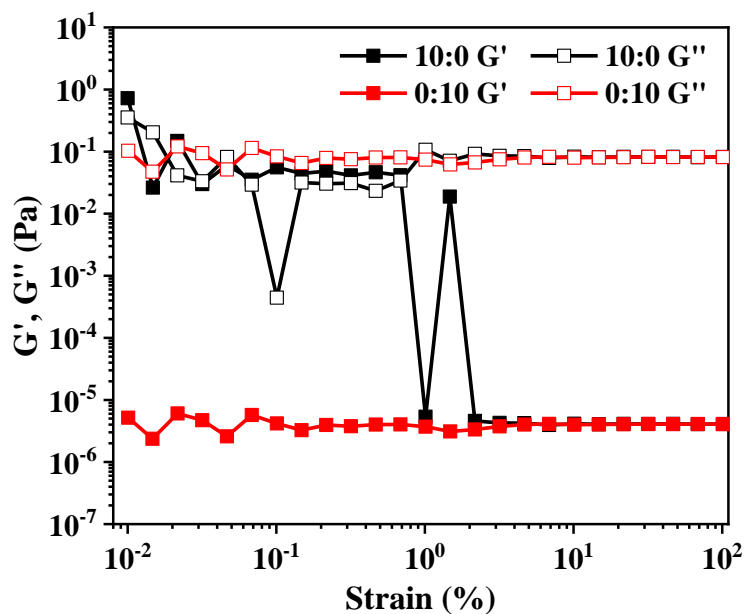


Figure S7. Rheological properties of pure TO-CNF 0.1 wt% dispersion (black, 10:0) and pure HEWL 0.1 wt% solution (red, 0:10), storage modulus G' (solid) and loss modulus G'' (open).

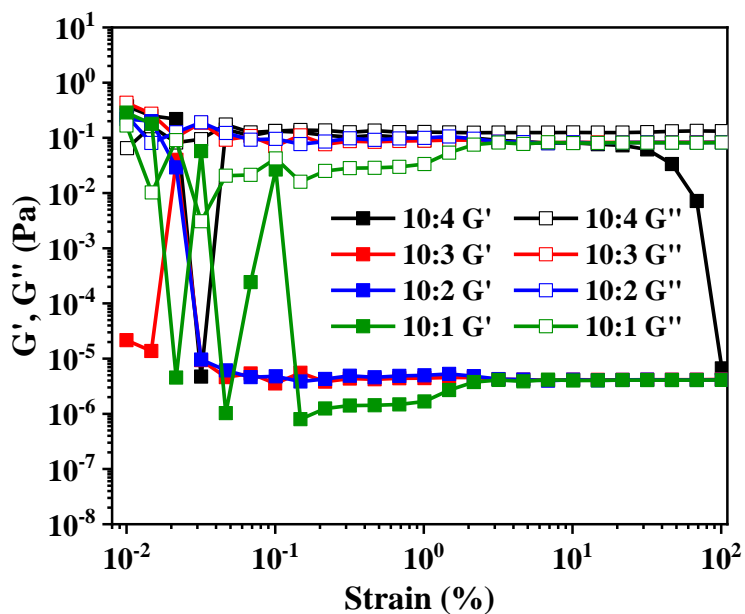


Figure S8. Rheological properties of TO-CNF and HEWL complexes with different ratios (from 10:1 to 10:4), storage modulus G' (solid) and loss modulus G'' (open).

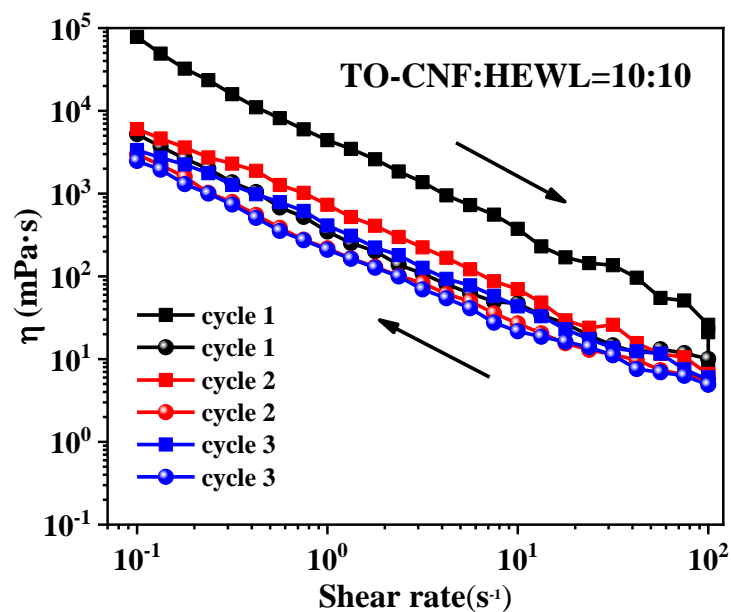


Figure S9. Shear viscosity loop of TO-CNF and HEWL complexes (TO-CNF:HEWL=10:10), the increase and decrease of the shear rate (s^{-1}) is indicated by the arrows.

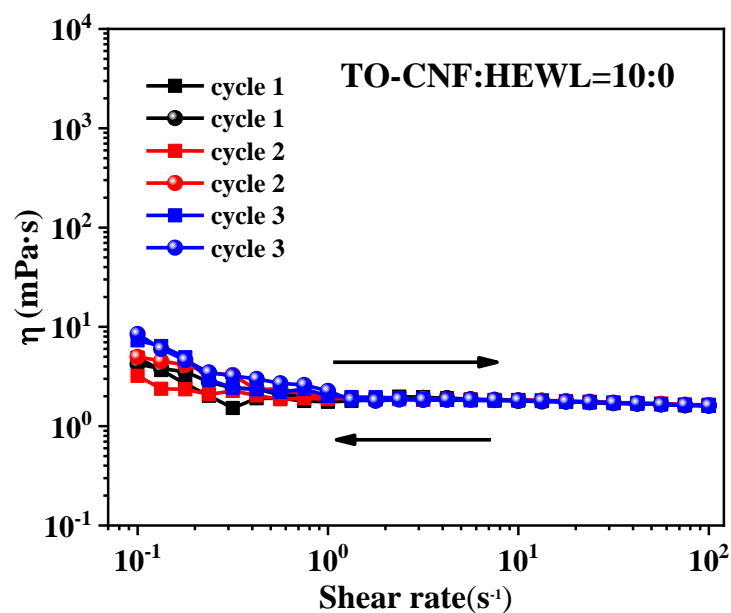


Figure S10. Shear viscosity loop of pure TO-CNF dispersion (TO-CNF:HEWL=10:0), the increase and decrease of the shear rate (s^{-1}) is indicated by the arrows.

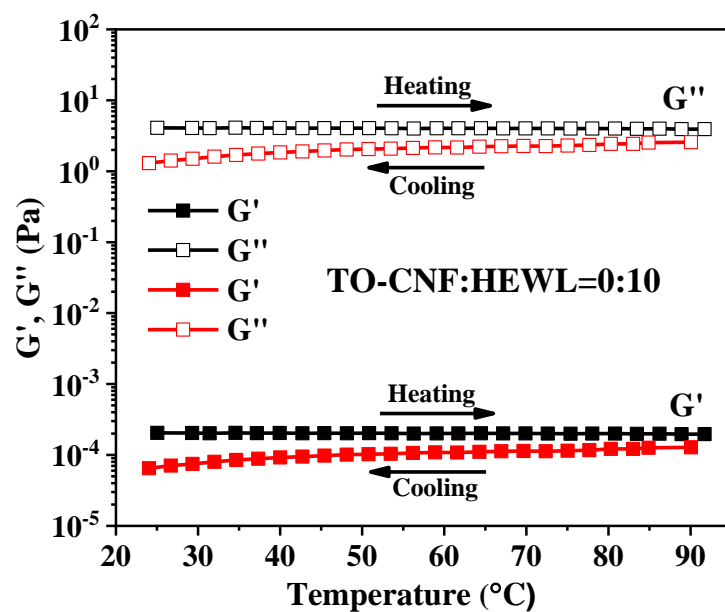


Figure S11. Temperature ramp test of pure HEWL solution (TO-CNF:HEWL=0:10), storage modulus G' (solid) and loss modulus G'' (open).

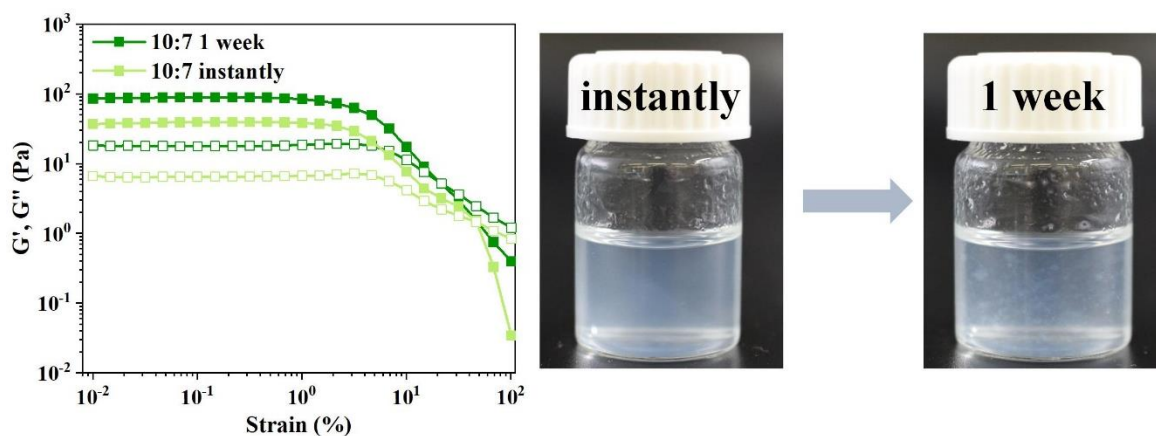


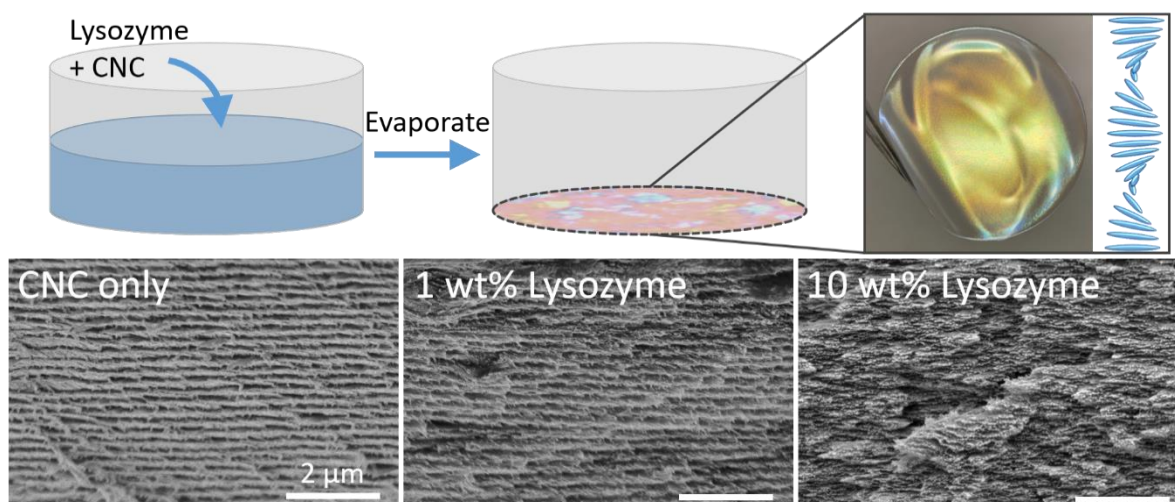
Figure S12. Strain sweep and photographs of selected colloidal gels (TO-CNF:HEWL=10:7), after mixing instantly and 1 week storage modulus G' (solid) and loss modulus G'' (open).

10 Assembly of Cellulose Nanocrystal–Lysozyme Composite Films with Varied Lysozyme Morphology

Kevin J. De France, Nico Kummer, Qun Ren, Silvia Campioni, Gustav Nyström

Biomacromolecules 2020, 21, 5139–5147

<https://doi.org/10.1021/acs.biomac.0c01267>



Reproduced with permission from authors and publisher [104]

Copyright © 2020 American Chemical Society

Assembly of Cellulose Nanocrystal – Lysozyme Composite Films with Varied Lysozyme Morphology

Kevin J. De France¹, Nico Kummer^{1,2}, Qun Ren³, Silvia Campioni¹, Gustav Nyström^{1,2,}*

¹ Laboratory for Cellulose & Wood Materials, Empa – Swiss Federal Laboratories for Materials Science and Technology, Überlandstrasse 129, 8600 Dübendorf, Switzerland

² Institute of Food Nutrition and Health, Schmelzbergstrasse 7, ETH Zurich, 8092 Zurich, Switzerland

³ Laboratory for Biointerfaces, Empa – Swiss Federal Laboratories for Materials Science and Technology, Lerchenfeldstrasse 5, 9014 St. Gallen

* To whom correspondence should be addressed

E-mail: gustav.nystroem@empa.ch

ABSTRACT

In modern society, there is a constant need for developing reliable, sustainable and cost-effective antibacterial materials. Here, we investigate the preparation of cellulose nanocrystal – lysozyme composite films via the well-established method of evaporation-induced self-assembly. We consider the effects of lysozyme concentration and aggregation state (native lysozyme, lysozyme amyloid fibers, and sonicated lysozyme amyloid fibers) on suspension aggregation and film-forming ability. Although at higher lysozyme loading levels (ca. 10 wt%), composite films lost their characteristic chiral nematic structuring, these films demonstrated improved mechanical properties and antibacterial activity with respect to CNC-only films, regardless of lysozyme aggregation state. We anticipate that the results presented herein could also contribute to the preparation of other CNC/protein-based materials, including films, hydrogels and aerogels, with improved mechanical performance and antibacterial activity.

INTRODUCTION

It is estimated that between 1 and 2% of the total population in developed countries will experience a chronic wound in their lifetime; and in the United States, chronic wounds reportedly affect 6.5 million people annually.[267,268] Critically, a combination of an aging population and an increase in diabetes prevalence will likely further increase the number of individuals affected by chronic wounds. Moreover, in a recent clinical study of chronic wounds, 60% of the wounds analyzed were characterized as severely infected.[269] This growing global burden of chronic wounds imposes a significant cost to both the afflicted individual, and to the healthcare system. In Europe, an estimated 2 – 5.5% of the annual healthcare expenditure is related to wound care;[270] while in the United States treatment costs are similar, corresponding to annual healthcare expenditure estimates as high as \$96.8 billion.[271] As a result, it is estimated that the annual global market for wound care products will reach \$22 billion by 2024.[272] Therefore, it is critical to address this need for investigating, developing, and thoroughly characterizing innovative wound dressings with improved antimicrobial action.

Cellulose nanocrystals (CNCs) are rigid, high aspect ratio nanoparticles derived from cellulose, the most abundant natural polymer on Earth.[77,273] Recently, CNCs have gained significant interest for use in biomedical applications due to their renewable nature, low cost, commercial availability, excellent mechanical properties, good biocompatibility, and low cytotoxicity.[108,225,282,274–281] Furthermore, because of their strongly interacting hydroxyl groups and anisotropic rod-like shape, CNCs undergo a concentration-dependent chiral nematic self-assembly, giving rise to iridescent films with structural colour through evaporation-induced self-assembly (EISA).[91,283–287] Due to their impressive mechanical and optical properties, these

structured films have since found application as responsive hydrogels, optical filters, soft actuators, and flexible electronic components.[288–290] However, cellulosic materials such as CNCs are not intrinsically antibacterial/antimicrobial, and therefore there is vast potential to develop composites whereby the CNCs provide the structural component with which to embed an antibacterial agent.

Lysozyme is a cheap, abundant natural protein, which is an essential component of our innate immune system. Lysozyme in its native form has well-documented antimicrobial properties and has been combined with several different materials to impart bacterial resistance; however lysozyme in this form is largely only effective against gram-positive bacteria.[291] Interestingly, lysozyme can assemble into highly compact amyloid fibrils/aggregates which display reduced enzymatic antimicrobial activity versus native lysozyme due to inaccessibility of the active site;[55] yet display increased broad spectrum antimicrobial properties due to contact-mediated bacterial agglomeration and membrane disintegration.[32] Currently, only few published works have combined CNC and lysozyme, all of which focused on immobilizing/conjugating lysozyme in its native form to the surface of CNC.[244,246,292,293] Notably, Abouhmad et al. investigated the immobilization of lysozyme onto CNC through various mechanisms, finding that after immobilization enzymatic stability is increased over time, while total antimicrobial activity can be largely retained (albeit with some decrease compared to free lysozyme).[292] Interestingly, covalent immobilization to CNCs with a net cationic charge resulted in antimicrobial activity against model Gram negative bacteria, which was not observed with free lysozyme and was attributed to the combination of positive charge of the CNC and lytic activity of the lysozyme.[292] Uddin et al. observed similar results, where enzymatic activity was largely retained and antibacterial activity against Gram positive and Gram negative bacteria was increased for lysozyme conjugated to cationic cellulose nanofibers (CNF), versus lysozyme conjugated to negatively charged

CNF.[294] However, despite these findings, the effects of lysozyme aggregation state has not yet been investigated, demonstrating a prominent knowledge gap in understanding the detailed structure-function relationship of lysozyme composite materials, particularly in the context of antimicrobial efficacy.

Herein, we demonstrate composite films prepared from cellulose nanocrystals and lysozyme in various aggregation states via simple EISA. Notably, the use of cationic species in combination with CNCs has generally been avoided for preparing EISA-based films due to concerns over agglomeration and inhibiting effects on self-assembly.[129] However, here we aim to investigate the detailed morphological effects of the incorporation of positively charged lysozyme in different aggregation states on the suspension behaviour and self-assembly of composite films. Film properties including chiral nematic structuring, optical characteristics, mechanical strength, and antibacterial activity are systematically evaluated.

EXPERIMENTAL

Materials.

Cellulose nanocrystals (CNC, prepared *via* sulfuric acid hydrolysis of bleached softwood kraft pulp, characterized elsewhere[279,295]), were purchased in freeze-dried form from CelluForce (Montreal, Canada). CNC (120 ± 61 nm length by 4.0 ± 1.3 nm height, determined via AFM, Bruker ICON3, Supporting Information Figure S1, using FiberApp tracking[296]) were dispersed in distilled water at 2 wt%, probe sonicated in an ice bath (3×10 minute cycles, 60% amplitude, Digital Sonifier 450, Branson Ultrasonics) and stored at 4 °C prior to use. Lysozyme from Hen Egg White (HEWL, >90%) was purchased from Sigma Aldrich. Hydrochloric acid and sodium chloride were purchased from VWR Chemicals and used as received.

Preparation of lysozyme amyloids (full-length and sonicated).

Lysozyme amyloid fibrils were prepared via incubation at pH 2 and elevated temperature, as previously reported.[25,27,297] Briefly, HEWL was dissolved in a falcon tube at 2 wt% in distilled water, and the pH was adjusted to 2.0 using 1.0 M HCl. The falcon tube was then placed in a thermomixer (Eppendorf AG) set to 90 °C, and mixed at 400 rpm for 24 hours. Amyloid fibrils were then optionally sonicated for a total of 20 minutes using 2 second pulses at 20% amplitude to generate shorter fibers (75 ± 34 nm by 5.5 ± 1.3 nm, determined via AFM). Fibril suspensions were subsequently dialyzed using 100 kDa MWCO membranes for ten 12 h cycles to remove any small native/oligomeric species. The suspensions of lysozyme fibrils (sonicated and unsonicated, imaged using AFM, Supporting Information, Figure S1) were stored at 4 °C until further use.

Preparation of CNC-lysozyme composite films.

CNC was mixed with either native lysozyme monomer, lysozyme amyloid fibers, or sonicated amyloid fibers to a final concentration of 1 wt% CNC and between 0 and 1 wt% lysozyme (0 to 50 wt% with respect to total solids). Suspensions were characterized via DLS (0.025 wt% in water), Zeta potential, (0.25 wt% in 10 mM NaCl) using a ZetaSizer Nano ZS (Malvern), and AFM (~ 2g/L of CNC, using APTES coated Mica substrates). 10 mL of the mixed suspension was deposited into a polystyrene petri dish, and films were formed via evaporation under ambient conditions (~ 1 – 2 days). Note that films above 10 wt% lysozyme with respect to total solids were extremely brittle, and could therefore only be characterized via FTIR. The remaining films (between 0 and 10 wt% lysozyme) all showed thicknesses of ~ 20 – 25 μ m, as determined via ImageJ analysis of SEM images (10 measurements per image, 3 images per sample;

no significant differences were evidenced between samples, therefore an average of 22 μm was taken for determination of the mechanical properties of all films). For all characterizations performed, care was taken to use sections of film from the center of each sample, in order to avoid any inhomogeneous areas which may arise from edge/other effects during drying. Also note that lysozyme-only films for any lysozyme morphology were unable to be prepared due to extensive brittleness/cracking upon drying. Film composition was analyzed via FTIR (Bruker Tensor 27 FT-IR spectrometer in attenuated total reflectance (ATR) mode). Spectra were recorded between 4000 and 600 cm^{-1} with a resolution of 4 cm^{-1} and 32 scans per sample. Film transparency and optical properties were investigated via UV/Vis (UV3600 UV-vis NIR Spectrophotometer, Shimadzu) and polarized optical microscopy (POM, Zeiss Axioplan microscope equipped with cross-polarizing filters and retardation plate). Film morphology was investigated via SEM, whereby individual samples were fractured by bending, and loaded in sample holders to view the fracture cross-section. Samples were coated with a thin layer of platinum (~ 2 nm) before imaging (5.0mm working distance, 5.0 kV accelerating voltage, Fei Nova NanoSEM 230 Instrument, Fei, Hillsboro, OR, USA).

Mechanical testing.

Films were cut into 4 \times 25 mm strips using a laser cutter (Nova24 60W, Thunderlasers) to avoid creating microfractures within the samples. Tensile testing of the prepared film strips was performed using a micromechanical testing device equipped with a 5N load cell.[298] Samples were clamped (initial length ~ 15 mm) and strained at 1 $\mu\text{m/s}$ until breakage. Video extensometry was used to precisely determine sample displacement/elongation at break. Stress-strain curves were generated, whereby the Young's modulus was calculated from the initial linear portion of the curves, tensile strength

was determined as the maximum stress achieved during testing, and toughness was calculated from the area under the stress-strain curve. All samples were tested in at least quintuplicate, with results presented as the average \pm standard deviation. A two-tailed t-test was used to determine any significant differences between the samples.

Antibacterial activity.

Films were cut into 10 mm diameter discs using a laser cutter as described above, and were then sterilized via exposure to UV light in a sterile bench for 30 minutes under ambient conditions. Bacteria (*Escherichia coli* DSMZ 1103, and *Staphylococcus aureus* ATCC 6538) were pre-cultured in 5 mL of 30% Tryptic Soy Broth (TSB) + 0.25% Glucose, and incubated overnight at 37 °C at a stir speed of 160 rpm. Bacterial pre-cultures were then diluted to OD_{600nm} 0.1 and allowed to grow for 2 h (exponential growth phase). 1000 μ L of exponential growing cells with a final concentration of OD_{600nm} 0.001 in PBS were then pipetted into a well-plate containing the CNC-lysozyme discs (1 disc per well), ensuring each disc was fully covered. The plate was incubated for 2 h at 37 °C and 40 rpm, at which point the discs were removed, placed onto PC-Agar plates (Sigma Aldrich 70152), and incubated overnight prior to imaging. Note that due to the highly hydrophilic nature of these CNC-based films, partial redispersion of the films was evidenced following bacterial incubation; although this may have an effect on the results presented, the relative differences between samples are taken to be significant due to the identical handling of each sample. Additional diffusion assays were performed by spreading 100 μ L of exponentially growing bacteria (OD_{600nm} 0.1) on PC-Agar plates, at which point CNC-lysozyme discs were added, and the plates were incubated overnight at 37 °C prior to imaging. All samples were tested in at least triplicate for each condition.

RESULTS AND DISCUSSION

CNC-lysozyme suspensions were prepared by simple mixing of negatively charged CNCs and positively charged lysozyme in various forms (native, amyloid fibers, or sonicated amyloid fibers). The addition of a relatively low concentration of native lysozyme (1 wt% with respect to CNC weight) did not result in any significant aggregation, as evidenced via AFM imaging (Figure 1). However, some aggregation was apparent upon the addition of 1 wt% amyloid fibers and sonicated amyloid fibers, potentially due to the increased zeta potential (and thus enhanced charge screening) of the (sonicated) lysozyme amyloid as compared to the native lysozyme (Supporting Information, Figure S2). We attribute this increased zeta potential of lysozyme amyloid versus native lysozyme to two main factors: (1) the compact structure of highly organized β -sheets present in lysozyme amyloids, acting to increase the overall surface charge density compared to native lysozyme, and (2) the different amino acid composition of native lysozyme and lysozyme amyloid fibers. Hydrolysis at pH 2 fragments native lysozyme into short peptide chains, only some of which are eventually incorporated into amyloid fibers. Of note, this hydrolysis also leads to the formation of succinimide derivatives (and the loss of a negative charge due to the isomerization of Asp peptide bonds).[25] Nevertheless, the addition of 1 wt% lysozyme did not lead to any significant changes to the overall apparent size or surface charge of the suspension mixtures, regardless of lysozyme morphology (Supporting Information, Figure S2). Increasing the lysozyme loading to 10 wt% resulted in enhanced aggregation for all samples, evidenced via both AFM and DLS. However, at this loading no significant changes in zeta potential were evidenced, potentially due to the precipitation of large charge-screened aggregates. Note that the zeta potential switched to positive values at ~ 33 wt% lysozyme

loading, indicative of complete charge screening of the CNCs and ubiquitous suspension aggregation (apparent size exceeded the maximum measurement capacity via DLS).

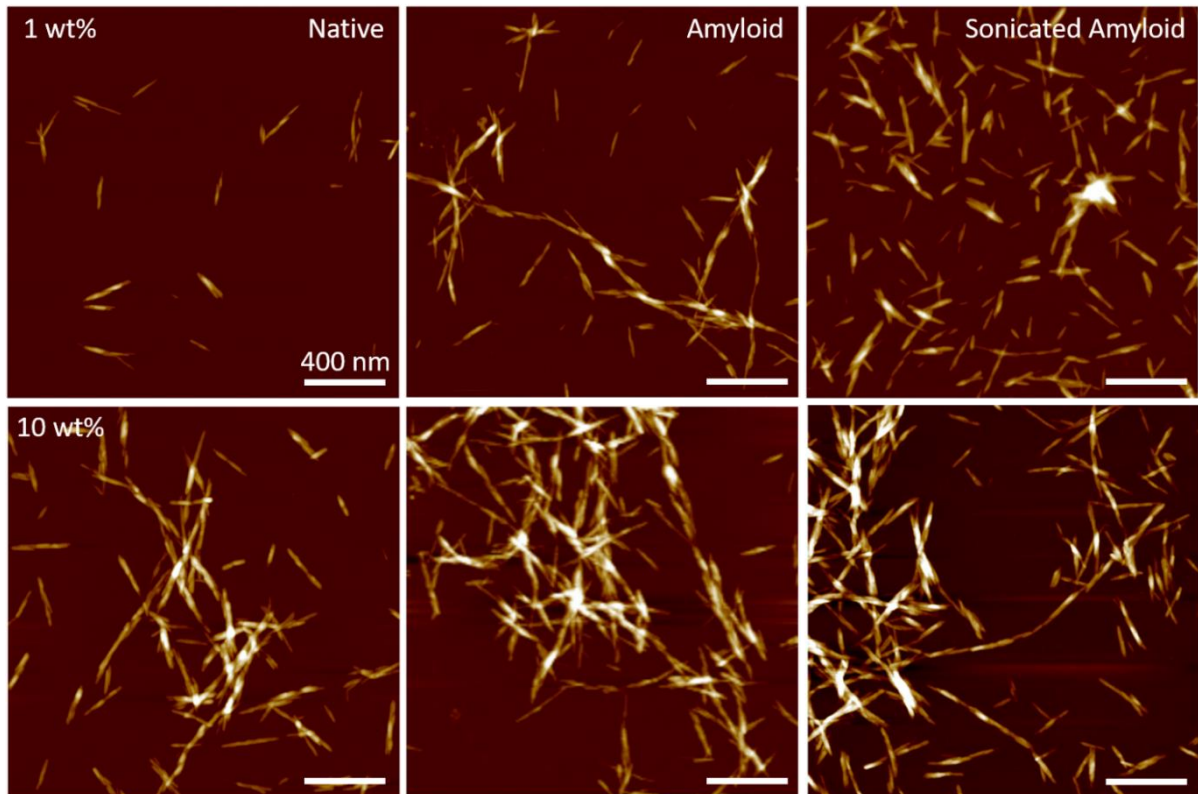


Figure 15: AFM height images of CNC-lysozyme suspensions (~ 2 g/L) at lysozyme loadings of 1.0 wt% and 10 wt% lysozyme (with respect to CNC weight). All scale bars are 400 nm. Large area scans can be seen in the Supporting Information (Figure S3).

Regardless of lysozyme loading concentration, composite films were prepared via the well-established method of evaporation-induced self-assembly (EISA, depicted in Figure 2).^[283,287,289,299–301] Here, 10 mL of suspension containing 1 wt% CNC and between 0 and 1 wt% lysozyme (both with respect to total weight) were deposited into polystyrene petri dishes and allowed to dry fully under ambient conditions. Lysozyme incorporation within the films was monitored via FTIR, and as expected, increasing the lysozyme concentration resulted in an increase in the amide I absorbance region ($1580 - 1720$ cm^{-1}).^[302] This region is also sensitive to protein secondary structure, and can

be used to evaluate the predominant structural features of the incorporated lysozyme.[303] Composite films with native lysozyme show a strong peak centered around 1650 cm^{-1} , attributed to native α -helices and random coils, whereas films with lysozyme amyloids show a second peak around 1620 cm^{-1} , attributed to aggregation-specific β -sheets (Figure 3).[155,302,303] Importantly, these results indicate that the secondary structure of the lysozyme proteins is maintained within the composite films following the EISA process. Note that films prepared from sonicated lysozyme fibrils showed an identical secondary structure to that of films prepared from non-sonicated lysozyme amyloids, indicating that the sonication process does not significantly affect the lysozyme secondary structure, but simply breaks the fibers into shorter fragments (Supporting Information, Figure S4).

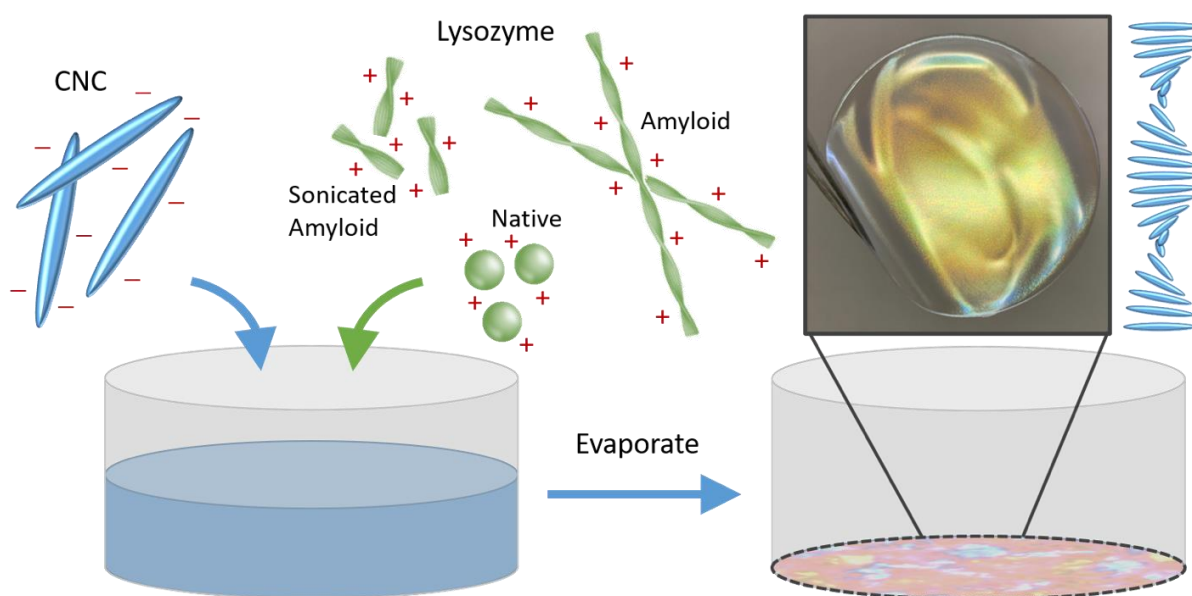


Figure 2: Schematic representation of the EISA process used to prepare CNC-lysozyme composite films. 100 mg of negatively charged CNC are added in combination with varying amounts of positively charged lysozyme in different aggregation states (either native, amyloid, or sonicated amyloid) to form structured films. In all cases, film thickness is $\sim 20 - 25\ \mu\text{m}$.

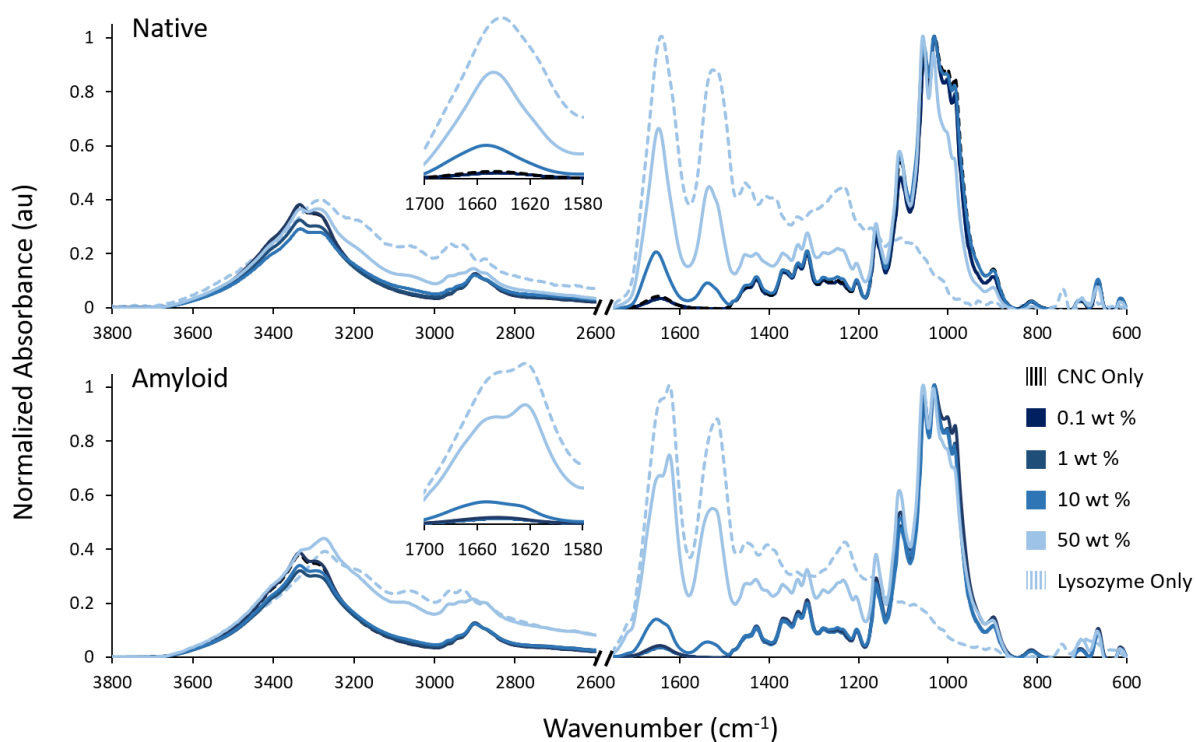


Figure 3: Baseline-corrected, normalized FTIR spectra for CNC only, lysozyme only, and CNC-lysozyme composite films at varying lysozyme concentrations for lysozyme in aggregated (amyloid) and non-aggregated (native) states.

Composite film structure is highly dependent on both lysozyme loading concentration, and aggregation state. Up to 1.0 wt% lysozyme, a characteristic chiral nematic structure can be seen in all films, regardless of lysozyme aggregation state, evidenced via SEM (Figure 4) and POM (Supporting Information, Figure S5). Furthermore, the addition of less than 1.0 wt % lysozyme (regardless of aggregation state) does not appear to have a significant effect on the chiral nematic pitch, characterized via UV/Vis (Figure 5). However, increasing the lysozyme concentration to 1.0 wt % (and further) does significantly broaden the width of the reflection peak (as shown by an increase in the reflection $\frac{1}{2}$ band, Figure 5), indicative of a decrease in film uniformity and a disturbance within the chiral nematic structure. Notably, this trend has also been observed in other EISA CNC films upon the addition of various polymers/plasticiz-

ers.[288,290,304,305] For lysozyme amyloid and sonicated amyloid fibers, this decrease in chiral nematic structure at concentrations above 1.0 wt% is likely due to enhanced charge screening/aggregation, as evidenced via AFM (Figure 1 and Supporting Information, Figure S3). This is also evidenced as a loss in fingerprint texture observed via POM (Supporting Information, Figure S6).

In the case of composite films with native lysozyme, a chiral nematic structure is evidenced up to 10 wt% lysozyme loading (additional images in Supporting Information, Figure S7), indicating a weaker aggregation potential between CNC and native lysozyme. Here as well however, increasing the lysozyme concentration results in increased heterogeneity within the chiral nematic pitch (i.e. an increase in the number of defect regions, observed by SEM) and general broadening of the reflection peak (observed by UV/Vis). Interestingly, increasing the native lysozyme concentration also results in a blue-shifting of the reflection peak (from ~ 620 nm to ~ 500 nm), representing a decrease in the chiral nematic pitch. Typically, the incorporation of polymers results in a red-shifting of the chiral nematic pitch due to the intercalation of polymers between the CNCs.[129,288,304–306] Therefore, it is likely that the native lysozyme does not uniformly intercalate between CNC rods, but interacts in different ways to cause the observed blue-shift. We hypothesize that this is largely caused by a combination of (1) charge screening, (2) local/irregular aggregation, and (3) hygroscopic effects: (1) It is known that decreasing the surface charge of a CNC suspension will lead to a blue-shift of the reflection peak (reduction in chiral nematic pitch) due to reduced electrostatic repulsion allowing closer CNC packing.[91] (2) From AFM imaging, the presence of irregular aggregates are observed at higher lysozyme loading; these aggregates should not participate in cholesteric ordering, but nonetheless take up space, and likely compress adjacent ordered domains. This is oppositely analogous to what is seen

when sonicating CNC suspensions prior to forming chiral nematic films; local aggregates are broken, causing a red-shifting in the final films.[91,307,308] (3) The removal of water from CNC films is known to cause a blue-shift due to decreased free water between adjacent CNCs; as lysozyme is highly hygroscopic, it is likely that free water is selectively adsorbed by the local lysozyme-rich aggregates during the EISA process.[309] Similar phenomenon was noticed by the Walther group,[304,310] where at relatively low polymer concentrations (< 20 wt%), the polymers tend to preferentially fill voids between the cholesteric domains rather than intercalate between CNCs, attributed to the unfavorable change in entropy associated with polymer stretching to fill the interstitial space between CNCs.

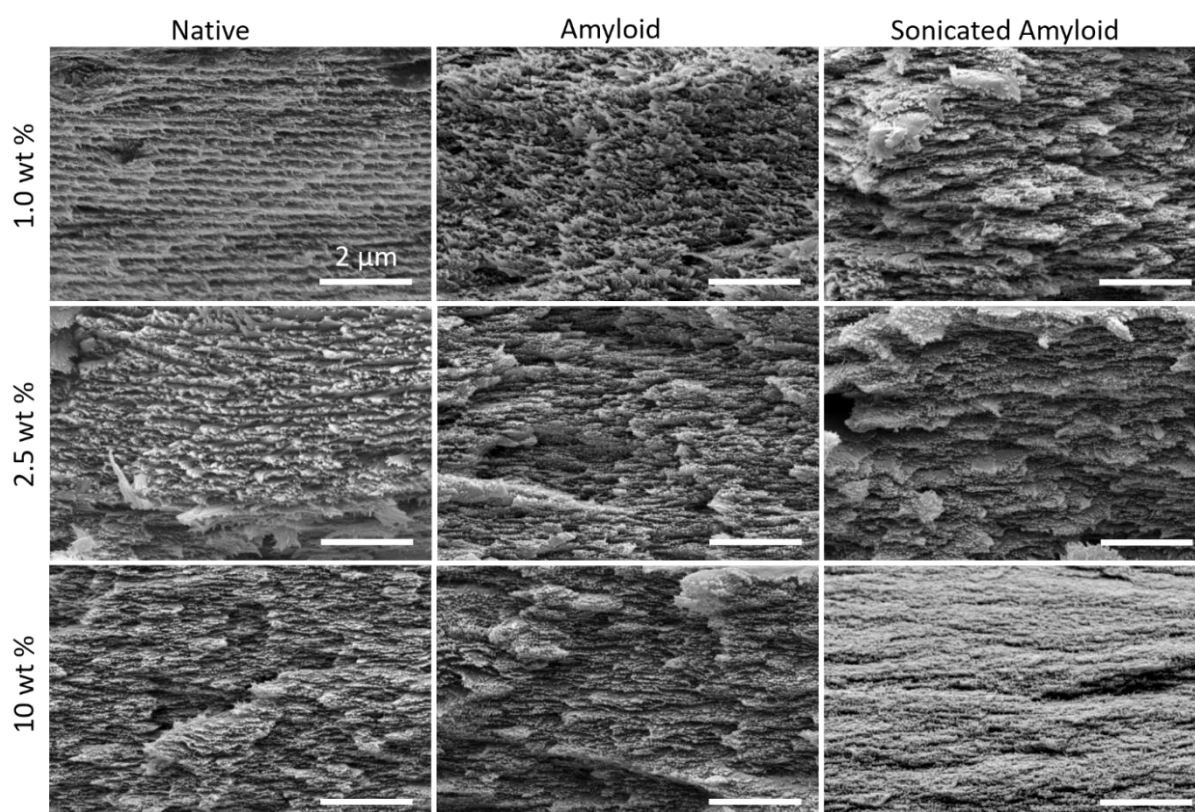


Figure 4: SEM images of the cross section of CNC-lysozyme composite films at varying lysozyme concentrations and aggregation states. All scale bars are 2 μm.

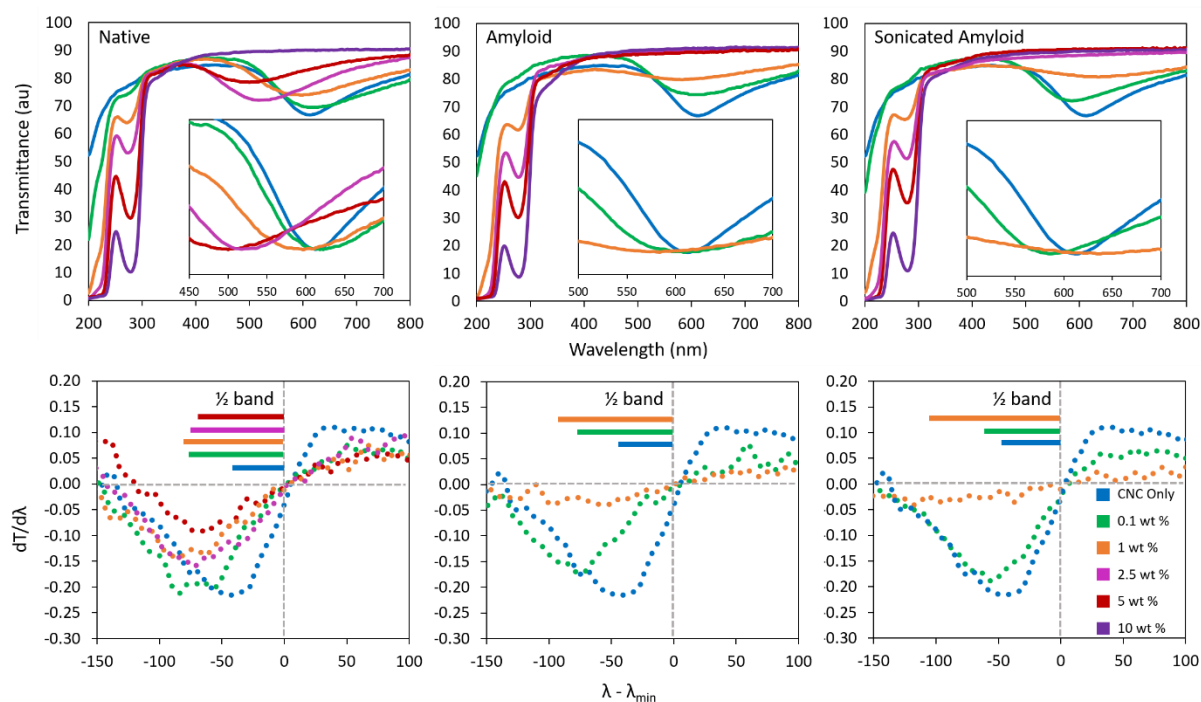


Figure 5: Evaluation of the optical properties of CNC-lysozyme composite films via UV/Vis. The top row shows representative transmittance spectra for all samples (with insets displaying normalized transmittance of the minimum peak reflectance wavelength), and the bottom row shows the derivative around this minimum peak reflectance wavelength. The “half-bandwidth” ($\frac{1}{2}$ band), giving a measure between the peak reflection wavelength and closest half-maxima, is also indicated.

The effects of lysozyme loading on the mechanical properties of the resulting CNC-lysozyme films are summarized in Figure 6. Note that in all samples, a relatively linear increase in stress with increasing strain occurred, (i.e. no inelastic deformation) indicative of good interfacial adhesion and stress transfer throughout the composites. The mechanical properties of the CNC only films assembled here are similar to previous reports on self-assembled CNC films.[290,305,311] These films are quite brittle (strain to break $\sim 0.73 \pm 0.08$ %), attributed to the relatively short overlap length of wood-based CNCs (investigated in detail elsewhere by molecular dynamics)[290] and limited soft-phase dynamics.[304] The addition of 1.0 wt% lysozyme (regardless of morphology) results in a qualitative (albeit largely statistically insignificant) reduction in the modulus, strain at break, tensile strength, and toughness. This systemic decrease in

mechanical performance is attributed to the increased heterogeneity in the chiral nematic structure, as observed via SEM and UV/Vis; the introduction of defects is known to weaken the mechanical properties of CNC-based films, resulting in increased probability of premature fracture.[311]

Interestingly, increasing the lysozyme loading to 10 wt% (again, regardless of morphology) results in a relatively systematic and significant increase in mechanical properties (notably tensile strength, toughness, and elongation at break, albeit these films remain relatively brittle with elongation at break still < 1%). Notably, this increase is evidenced simultaneously for elongation at break and tensile strength, which are typically inversely related.[311] However, Natarajan et al. also demonstrated a simultaneous increase in elongation at break (still up to only ~ 1 wt%) and tensile strength for chiral nematic CNC films by incorporating longer tunicate CNCs into a suspension of wood-based CNCs.[290] They attribute this simultaneous increase to effectively increasing the overlap length between CNC rods; as the film is strained, load is primarily transferred through non-bonded CNC-CNC interfaces (hydrogen bonding, van der Waals interactions), the number of which is directly related to CNC overlap length.[290] Although in our case the chiral nematic structuring is largely lost at 10 wt% lysozyme loading, a similar argument about overlap can be made; the addition of a relatively high concentration of lysozyme induces significant aggregation/attractive forces between CNCs, effectively increasing the strength of non-bonded interfaces. Supporting this point, it has previously been demonstrated that non-ordered CNC films show increased elongation at break and tensile stress versus chiral nematic CNC films of similar composition.[129] Our previous work has also demonstrated similar results for hydrogels with aligned and randomly distributed CNCs, whereby hydrogels with randomly distributed CNCs show increased shear strength due to the presence of out-of-plane CNCs providing increased entanglement and resistance to shear.[312]

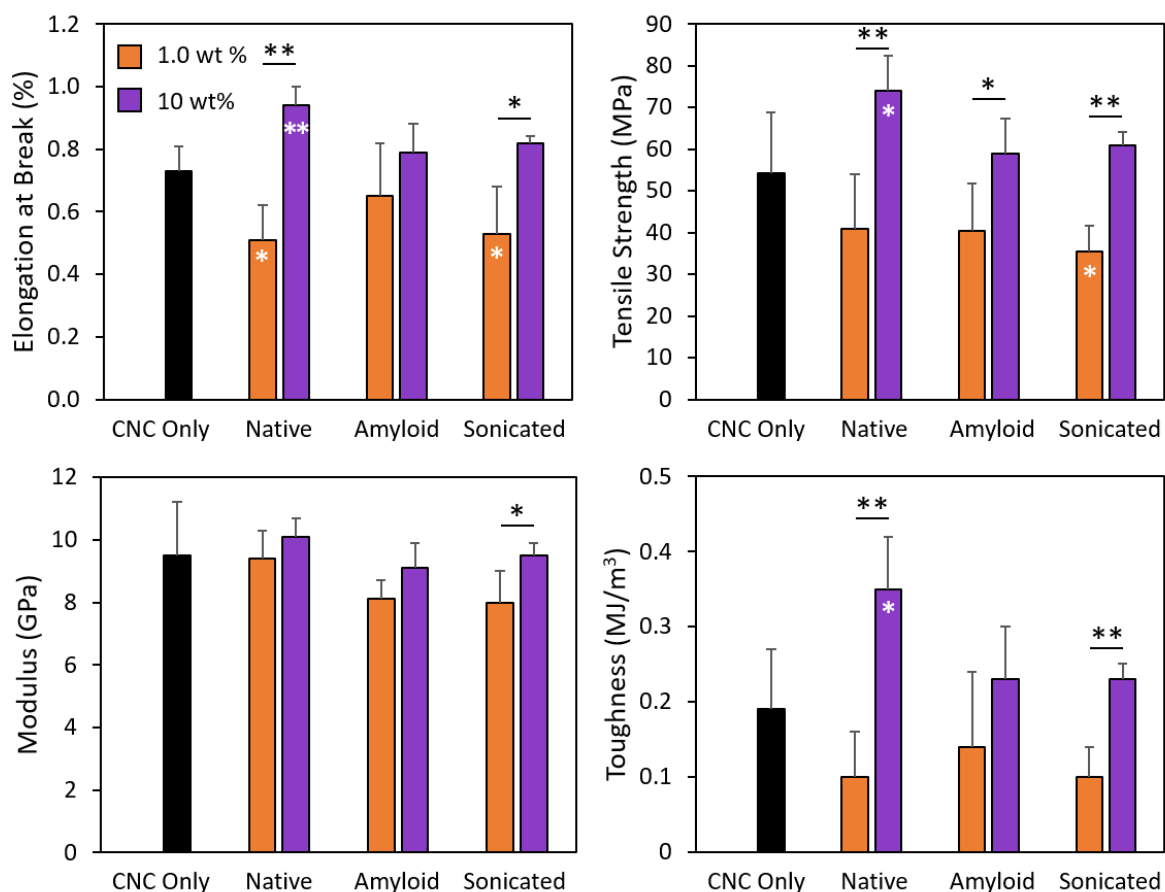


Figure 6: Mechanical properties for CNC-Lysozyme films with varying lysozyme content. * = $p < 0.05$, ** = $p < 0.01$; symbols placed directly in the bar are as compared to CNC only films. Representative stress-strain curves and a table of exact values can be seen in the Supporting Information (Figure S8, Table S1).

Finally, the antibacterial efficacy of CNC-lysozyme composite films was determined against both Gram-positive *S. aureus* and Gram-negative *E. coli*. Minimal contact-mediated antibacterial efficacy was evidenced for CNC only and CNC-lysozyme composite films with 1.0 wt% lysozyme loading (regardless of lysozyme morphology) against both *S. aureus* (Figure 7) and *E. coli* (Supporting Information, Figure S9). However, when the lysozyme concentration was increased to 10 wt%, some qualitative improvements in antibacterial activity against Gram-positive *S. aureus* are apparent, also regardless of lysozyme morphology. This improved antibacterial efficacy was not evi-

denced against Gram-negative *E. coli*. This is largely intuitive, as the antibacterial efficacy of native lysozyme is predominantly due to the hydrolysis of peptidoglycan, which comprises roughly 90% and 10% of the cell envelope in Gram-positive and Gram-negative bacteria, respectively.[313] Although there have been some reports of lysozyme amyloids displaying increased broad spectrum antimicrobial activity (hypothesized due to contact-mediated bacterial agglomeration and membrane disintegration via positive charges binding negatively charged cell wall components),[32,313] this was not evidenced here. We hypothesize that this may be due both to the hindered accessibility of lysozyme, and to the overall negative charge of the CNC-lysozyme composite films, even at 10 wt% lysozyme, reducing this propensity to bind to the bacterial cell walls. In support of this hypothesis, previous research has shown that lysozyme antibacterial activity against Gram-positive *S. epidermidis* for both native lysozyme and lysozyme amyloid fibers decreased when it was adsorbed to surfaces, likely due to the hindered accessibility of active sites.[55] Furthermore, nanocellulose surface charge has also been shown to affect the antibacterial activity of lysozyme, whereby aerogels prepared from cationic CNF showed significantly improved antibacterial efficacy than aerogels prepared from TEMPO-oxidized (anionic) CNF against both Gram-positive and Gram-negative bacteria.[294] It should also be noted that in all cases there was no evidence for diffusion-mediated antibacterial activity, indicating that the lysozyme, regardless of aggregation state, is strongly bound to the CNC within the composite films, and is not readily released (Supporting Information, Figure S10).

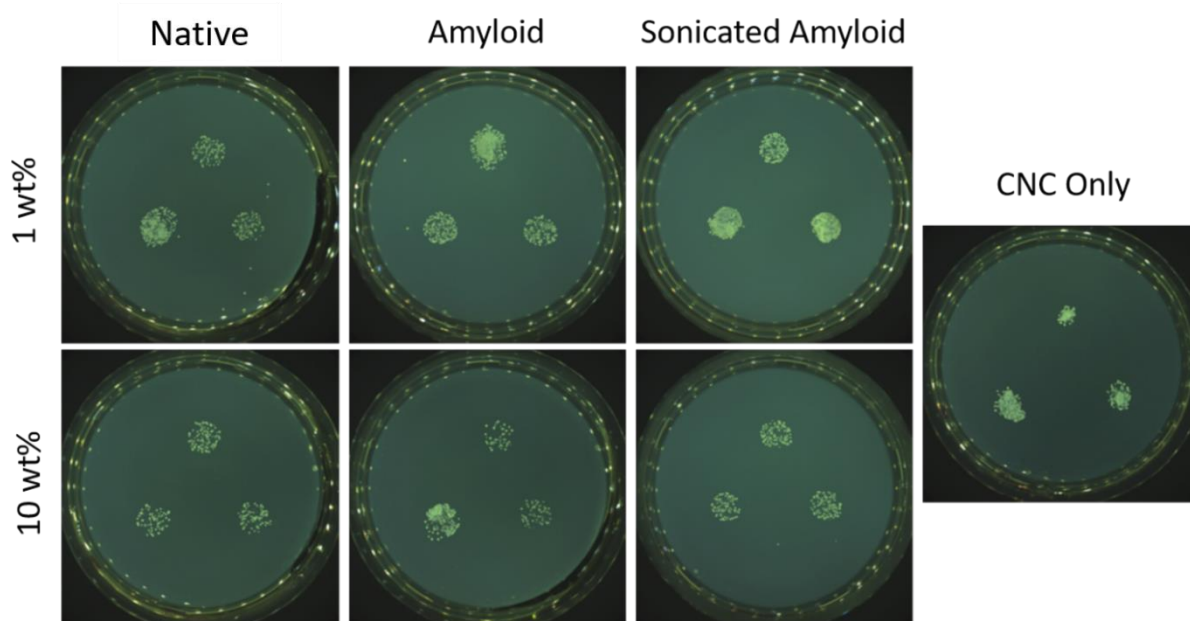


Figure 7: Antibacterial activity of CNC-lysozyme composite films with varying lysozyme content against Gram-positive *S. aureus*. Activity against Gram-negative *E. coli* and diffusion-based antibacterial activity can be seen in the Supporting Information (Figure S9 and Figure S10, respectively)

CONCLUSION

In summary, composite films were successfully prepared from CNCs and lysozyme in different aggregation states (native, amyloid fibers, or sonicated amyloid fibers) via EISA. Both lysozyme amyloids and sonicated lysozyme amyloids resulted in enhanced CNC aggregation versus native lysozyme, attributed to the increased positive surface charge density of amyloid fibers. The resulting composite films showed a more heterogeneous chiral nematic structure with a higher density of defects, attributed to local CNC-lysozyme aggregates. For films with lysozyme amyloids, there was no discernible effect of lysozyme concentration on the chiral nematic pitch, whereby the chiral nematic structure was no longer evident at concentrations above 1.0 wt%. For films with native lysozyme, increasing the concentration up to 10 wt% lysozyme results in a blue-shift to the chiral nematic pitch, before the structure is largely lost. Regardless of lysozyme aggregation state, films with 10 wt% lysozyme showed improved tensile strength, toughness, and elongation at break, attributed to increased overlap between CNCs.

Finally, antibacterial activity against Gram-positive *S. aureus* was improved for films with 10 wt% lysozyme, although little efficacy was evidenced against Gram-negative *E. coli*, attributed to the overall negative charge of the films reducing contact-mediated antibacterial activity. We see an opportunity to extend the knowledge gained here surrounding CNC-lysozyme (and CNC-protein, in general) aggregation and assembly into films and other materials (such as hydrogels and aerogels) with improved mechanical properties and antibacterial activity.

Supporting Information Available. This material is available free of charge via the Internet at <http://pubs.acs.org>. AFM height images of CNC and lysozyme, DLS and Zeta Potential measurements of CNC-lysozyme suspensions, large area AFM scans of CNC-lysozyme suspensions, additional FTIR spectra of CNC-lysozyme films, Polarized Optical Microscopy images of CNC-lysozyme films, additional SEM images of CNC-lysozyme film cross-sections, representative stress-strain curves, table of mechanical properties from tensile testing of CNC-lysozyme films, antibacterial activity of CNC-lysozyme composite films against gram positive *E. coli*, diffusion-based antibacterial activity of CNC-lysozyme composite films.

Acknowledgements.

The authors thank Anja Huch for help with scanning electron microscopy sample prep and imaging, Dr. Alexandre Poulin and Patrick Zumsteg for help with laser cutting, Dr. Ingo Burgert, Dr. Markus Rüggeberg, and Dr. Marion Frey at ETH Zurich for access to and help with micromechanical testing, and Flavia Zuber for antibacterial testing. KD gratefully acknowledges funding from the Natural Sciences and Engineering Research Council of Canada (NSERC) Postdoctoral Fellowship program. NK and GN also acknowledge funding from the Swiss National Science Foundation (Grant No. 200021_192225 / 1).

Supporting Information for:

Assembly of Cellulose Nanocrystal – Lysozyme

Composite Films with Varied Lysozyme

Morphology

Kevin J. De France¹, Nico Kummer^{1,2}, Qun Ren³, Silvia Campioni¹, Gustav Nyström^{1,2,}*

¹ Laboratory for Cellulose & Wood Materials, Empa – Swiss Federal Laboratories for Materials Science and Technology, Überlandstrasse 129, 8600 Dübendorf, Switzerland

² Institute of Food Nutrition and Health, Schmelzbergstrasse 7, ETH Zurich, 8092 Zurich, Switzerland

³ Laboratory for Biointerfaces, Empa – Swiss Federal Laboratories for Materials Science and Technology, Lerchenfeldstrasse 5, 9014 St. Gallen

* To whom correspondence should be addressed

E-mail: gustav.nystroem@empa.ch

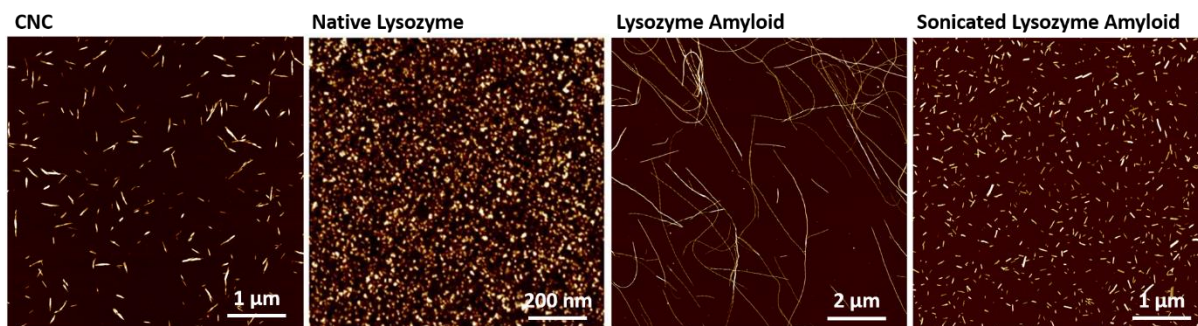


Figure S1: AFM images of CNC, native lysozyme, lysozyme amyloid, and sonicated lysozyme amyloid. Suspensions were drop-cast onto APTES-coated mica substrates at a concentration of ~ 2 g/L prior to imaging.

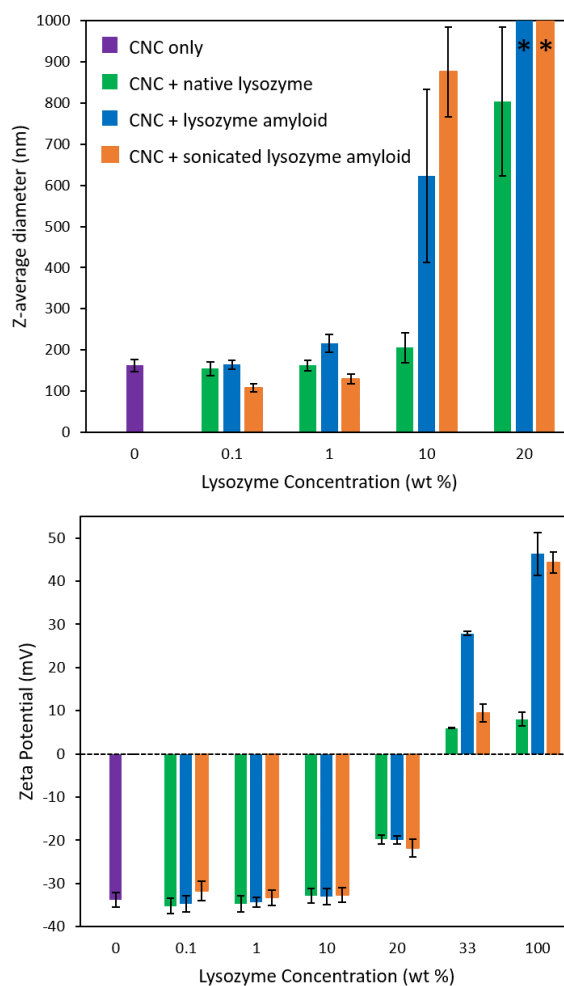


Figure S2: DLS (top) and zeta potential (bottom) measurements for CNC-lysozyme suspensions at varying lysozyme concentrations for lysozyme in aggregated and non-aggregated states. * Apparent size larger than the maximum measurable value for the instrument ($10 \mu\text{m}$). Mean count rates for all samples were between 50 and 5000 kcps for both DLS and Zeta Potential measurements.

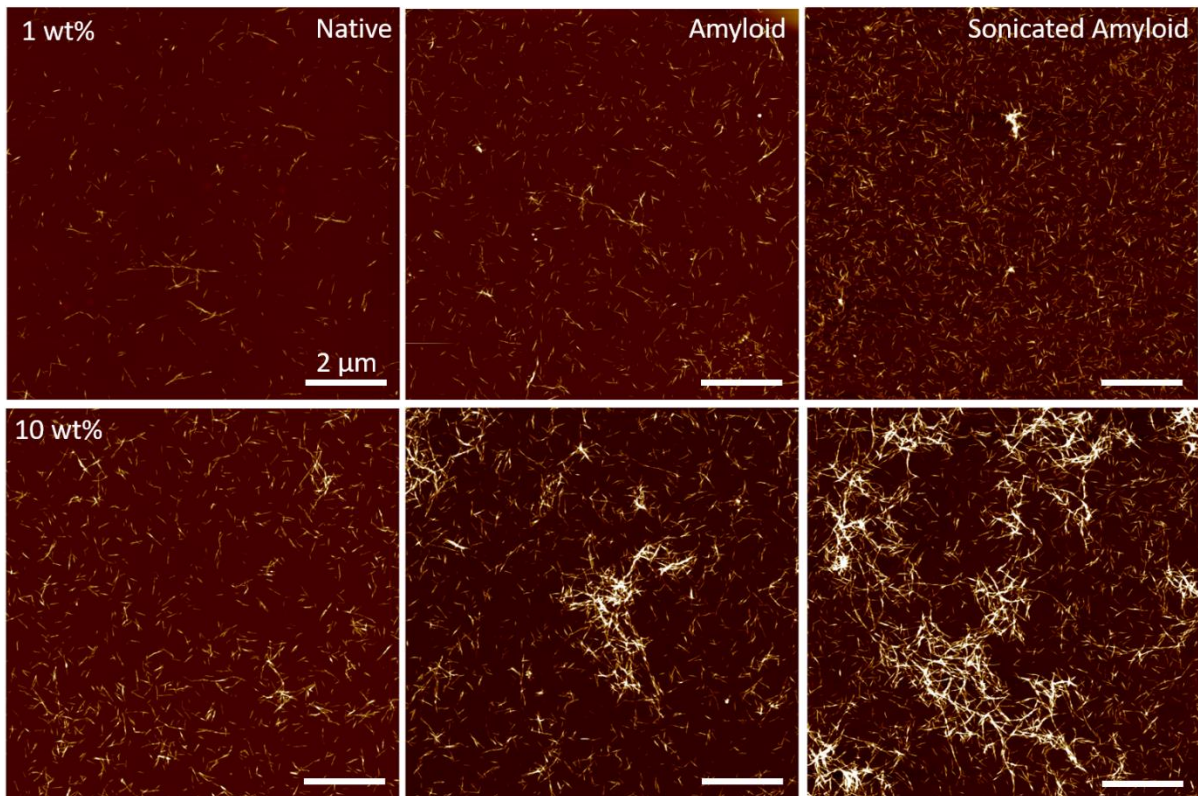


Figure S3: AFM height images (large area scans) of CNC-lysozyme mixtures at 100:1 and 10:1 CNC:lysozyme weight ratios.

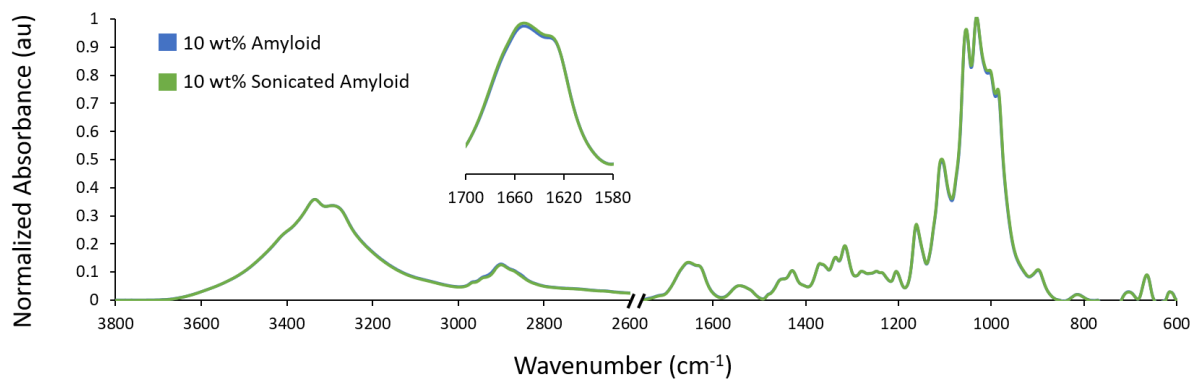


Figure S4: Baseline-corrected, normalized FTIR spectra for CNC-lysozyme composite films at 10 wt% for sonicated and unsonicated lysozyme amyloids.

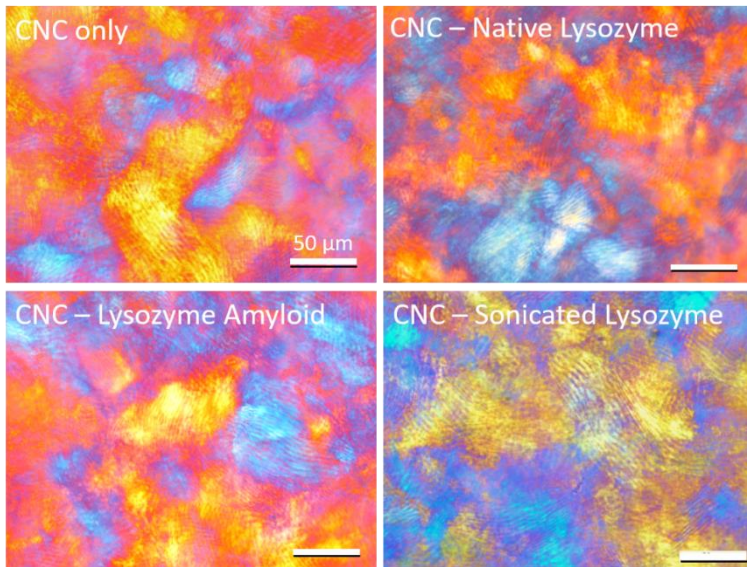


Figure S5: POM images of the surface of CNC-only CNC-lysozyme composite films at a loading of 1.0 wt% lysozyme. All scale bars are 50 μm .

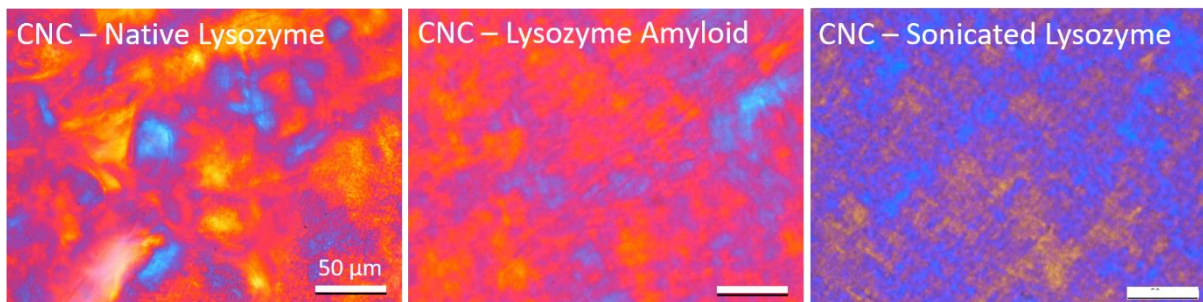


Figure S6: POM images of the surface of CNC-lysozyme composite films at a loading of 10 wt% lysozyme. All scale bars are 50 μm .

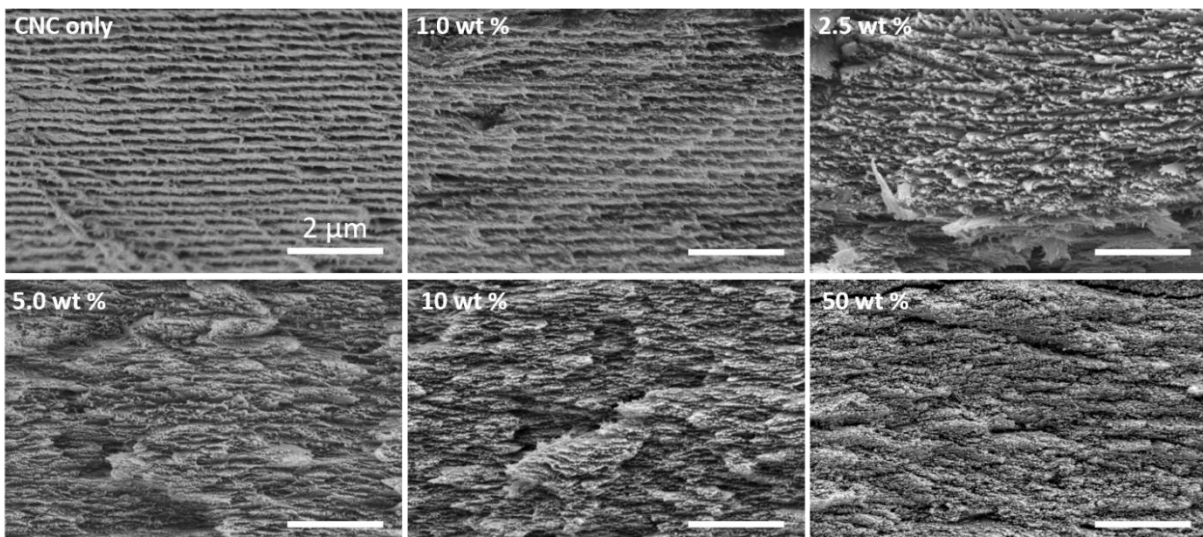


Figure S7: Additional SEM images of the cross section of CNC-native lysozyme composite films at varying concentrations. All scale bars are 2 μm .

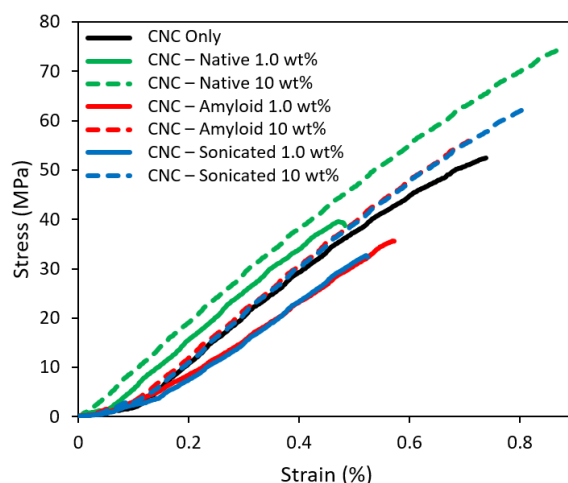


Figure S8: Representative stress-strain curves for tensile testing of CNC only and CNC-lysozyme composite films at a loading of 1.0 wt% and 10 wt% lysozyme. All samples were tested in at least quintuplicate.

Table S1: CNC-Lysozyme film mechanical properties for films containing native lysozyme (N), lysozyme amyloids (A), or sonicated lysozyme amyloids (SA) at 1 and 10 wt %.

Sample	Strain at Break (%)	Modulus (GPa)	Tensile Strength (MPa)	Toughness (MJ/m ³)
CNC Only	0.73 ± 0.08	9.5 ± 1.7	54.3 ± 14.6	0.19 ± 0.08
CNC-N-1	0.51 ± 0.11	9.4 ± 0.9	40.9 ± 13.0	0.10 ± 0.06
CNC-N-10	0.94 ± 0.06	10.1 ± 0.6	74.1 ± 8.4	0.35 ± 0.07
CNC-A-1	0.65 ± 0.17	8.1 ± 0.6	40.5 ± 11.3	0.14 ± 0.10
CNC-A-10	0.79 ± 0.09	9.1 ± 0.8	59.0 ± 8.4	0.23 ± 0.07
CNC-SA-1	0.53 ± 0.15	8.0 ± 1.0	35.4 ± 6.3	0.10 ± 0.04
CNC-SA-10	0.82 ± 0.02	9.5 ± 0.4	60.8 ± 3.4	0.23 ± 0.02

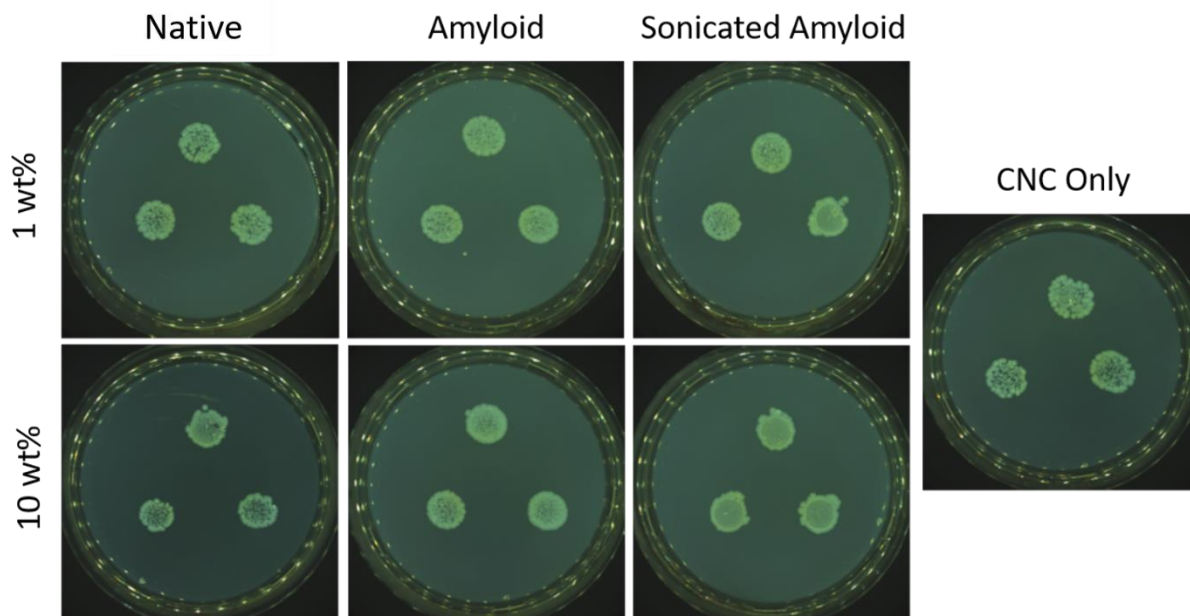


Figure S9: Antibacterial activity of CNC-lysozyme composite films with varying lysozyme content against Gram-negative *E. coli*.

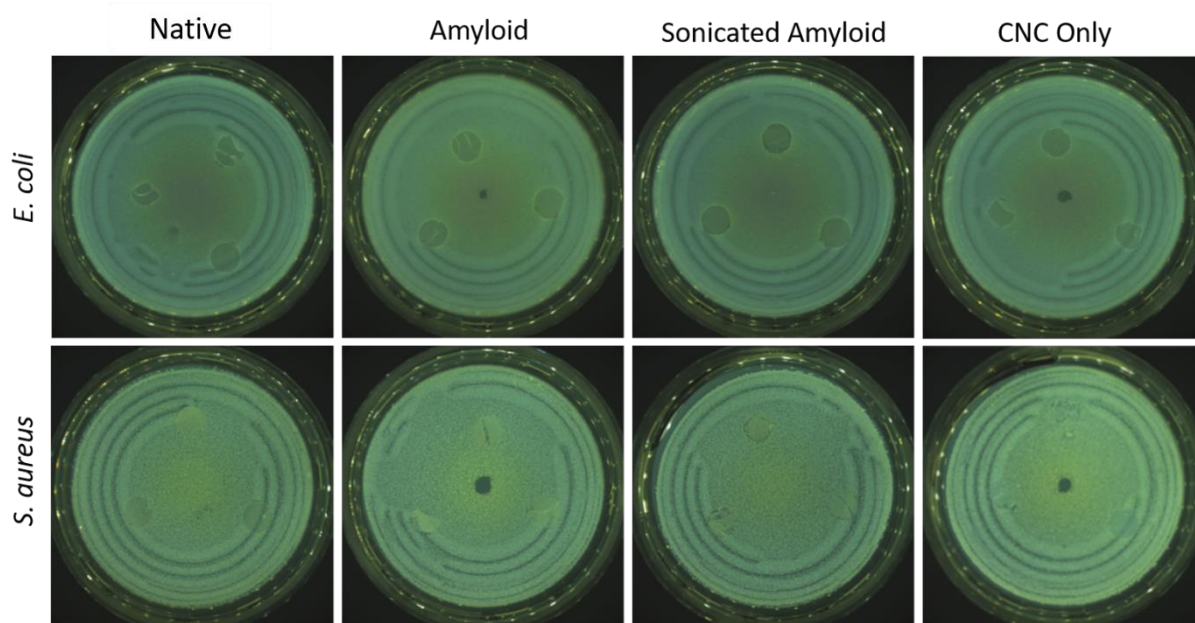


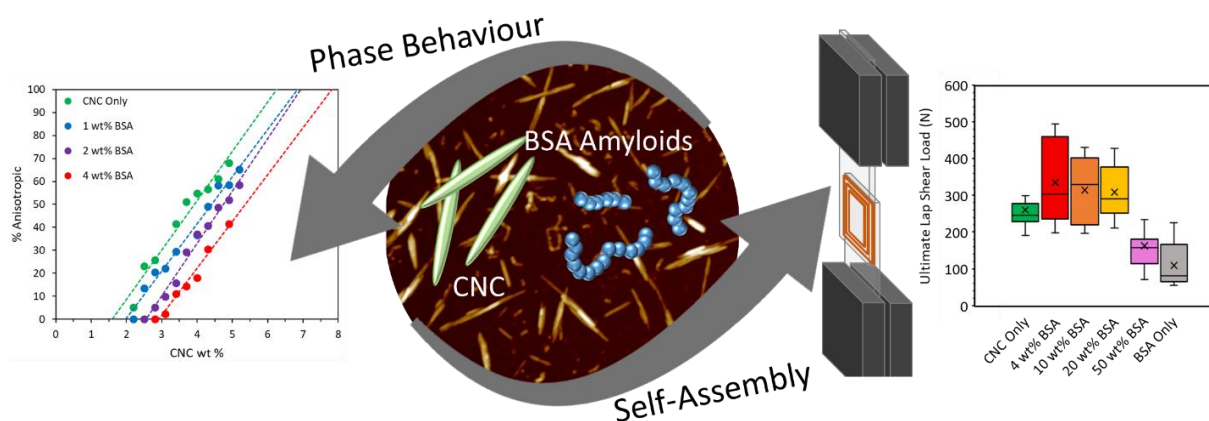
Figure S10: Diffusion-based antibacterial activity of CNC-only and CNC-lysozyme composite films containing 10 wt% lysozyme.

11 Phase Behavior, Self-Assembly, and Adhesive Potential of Cellulose Nanocrystal–Bovine Serum Albumin Amyloid Composites

Kevin J. De France, Nico Kummer, Silvia Campioni, Gustav Nyström

ACS Appl. Mater. Interfaces 2023, 15, 1, 1958–1968

<https://doi.org/10.1021/acsami.2c14406>



Reproduced with permission from authors and publisher [105]

Copyright © 2022 American Chemical Society

Phase Behaviour, Self-Assembly, and Adhesive Potential of Cellulose Nanocrystal – BSA Amyloid Composites

Kevin J. De France^{1,2}, Nico Kummer^{1,3}, Silvia Campioni¹, Gustav Nyström^{1,3*}*

¹ Laboratory for Cellulose & Wood Materials, Empa – Swiss Federal Laboratories for Materials Science and Technology, Überlandstrasse 129, 8600 Dübendorf, Switzerland

² Department of Chemical Engineering, Queen's University, 19 Division St., Kingston, Ontario K7L 3N6, Canada

³ Department of Health Sciences and Technology, ETH Zürich, Schmelzbergstrasse 9, 8092 Zürich, Switzerland

KEYWORDS

Cellulose nanocrystals, protein amyloids, chiral nematic self-assembly, structural adhesives, biohybrid materials

ABSTRACT

Structural organization is ubiquitous throughout nature and contributes to the outstanding mechanical/adhesive performance of organisms including geckoes, barnacles, and crustaceans. Typically, these types of structures are composed of polysaccharide and protein-based building blocks, and therefore there is significant research interest in using similar building blocks in the fabrication of high-performance synthetic materials. Via evaporation-induced self-assembly, the organization of cellulose nanocrystals (CNC) into a chiral nematic regime results in the formation of structured CNC films with prominent mechanical, optical, and photonic properties. However, there remains an important knowledge gap in relating equilibrium suspension behavior to dry film structuring and other functional properties of CNC-based composite materials. Herein, we systematically investigate the phase behavior of composite suspensions of rigid CNCs and flexible bovine serum albumin (BSA) amyloids in relation to their self-assembly into ordered films and structural adhesives. Increasing the concentration of BSA amyloids in the CNC suspensions results in a clear decrease in the anisotropic fraction volume percent via the preferential accumulation of BSA amyloids in the isotropic regime (as a result of depletion interactions). This translates to a blue-shifting or compression of the chiral nematic pitch in dried films. Finally, we also demonstrate the synergistic adhesive potential of CNC – BSA amyloid composites, with ultimate lap shear strengths in excess of 500 N/mg. We anticipate that through understanding the systematic relationships between material interactions and self-assembly in suspension such as investigated here will pave the way for a new generation of structured composite materials with a variety of enhanced functionalities.

INTRODUCTION

Nature excels in the production of composite materials with impressive optical, mechanical, and adhesive properties via the evolution of sophisticated hierarchical organization and optimized interactions between constituent building blocks.[314,315] These phenomena are starkly apparent in lobster cuticle for example, the high strength of which is attributed to both the helicoidal arrangement of rigid chitin nanofibrils at the micron scale, and their interactions with flexible proteins at the nanoscale.[314] This type of structural architecture – long-range organization of a majority rigid component with a flexible biomacromolecular binder – is also responsible for the mechanical functionality of bone, nacre, and ivory, and as such has motivated the engineering of nanocomposite analogues to emulate these multifunctional natural structures.[316] Furthermore, given the increased attention towards the development of sustainable materials in modern society, natural building blocks based on polysaccharides such as cellulose or chitin, and protein nanofibers have attracted significant interest in this area.

Cellulose nanocrystals (CNCs) are rigid, high aspect ratio nanoparticles derived from cellulose, the most abundant natural polymer on Earth.[77,273] CNCs have gained significant interest for use as structural building blocks in a variety of applications due to their renewable nature, commercial availability, excellent mechanical properties, thermal stability, potential for functionalization, and biocompatibility.[84,108,279,317,318] Furthermore, CNCs undergo a concentration-dependent chiral nematic self-assembly, giving rise to hierarchically structured thin films upon solvent evaporation (evaporation-induced self-assembly; EISA).[91,227,283–286,319] Yet, these assemblies tend to be extremely brittle, due to limited shear transfer between the short, rigid, still well-organized CNCs, which limits their translation to practical ap-

plications.[290] As in nature, here the use of a softer, flexible biomacromolecular/polymeric binder has demonstrated success in improving film mechanics such as toughness and ductility.[320,321] However, detailed investigations relating the effects of soft biomacromolecular binders on CNC equilibrium dispersion behavior and self-assembly in an aqueous regime to resulting film structuring and other functional properties such as adhesive potential remains largely unexplored.

To this end, we hypothesize that understanding the detailed interactions between CNCs and biomacromolecular binders will enable the preparation of structural adhesives with significantly improved performance. We demonstrate that rigid CNC and flexible protein amyloids interact through depletion effects in suspension to form well-organized films and structural adhesives with specific lap shear strengths in excess of 500 N/mg, which is among the highest demonstrated for bio-based materials.[322–326] Protein amyloids are a class of fibrillar and highly stable protein aggregates which form via a self-assembly process.[6,9,184,185] Originally gaining interest because of their implication in several pathological disorders, protein amyloids have also recently been discovered in a diverse array of biologically functional roles. Of particular note, protein amyloids have been identified as a major component in adhesive marine species including barnacles, mussels, and algae.[327–330] The adhesive properties of other amyloids have also been documented, with amyloids from bovine serum albumen (BSA) demonstrating cell adhesiveness, in stark contrast to the cell-repulsive nature of BSA in its native form.[331] Herein, we investigate the preparation of protein amyloids from BSA,[332–336] and probe their interactions with CNCs in both aqueous and dried regimes, presenting a detailed understanding of self-assembly mechanisms towards the development of next-generation bio-based structural adhesives.

RESULTS AND DISCUSSION

Preparation of BSA Amyloids

Proteinaceous amyloids ("amyloid") were prepared via the high temperature acid-mediated hydrolysis of native BSA ("monomer") at pH 2 and 90 °C for 4 days. As evidenced via AFM imaging (Figure 1 A, B), globular BSA monomer aggregated to yield flexible worm-like fibers with lengths of up several hundreds of nanometers (average length = 60 ± 68 nm). The worm-like fibers exhibited multiple amyloidogenic hallmarks, including increased ThT emission (Figure 1 C),^[337,338] and a shift in the amide I absorbance region from 1650 cm^{-1} towards 1620 cm^{-1} , indicating the increased presence of intermolecular β -sheets typical of amyloids (Figure 1 D; full Fourier-transform infrared (FTIR) spectra available in the Supporting Information, Figure S1).^[155,303] Aggregation was also apparent via dynamic light scattering (DLS), whereby the z-average apparent diameter increased to 88 ± 5 nm for amyloids, from 11.2 ± 0.5 nm for monomer (Supporting Information Figure S2). Due to the acid-mediated hydrolysis, BSA amyloids (isoelectric point of BSA ~ 4.7)^[339] were also demonstrated to have a negative surface charge density (zeta potential -30.2 ± 0.9 mV at pH 7, Supporting Information Figure S2), which increased in absolute value as compared to BSA monomer. Amyloid aggregate-to-monomer ratio was analyzed via UV-vis absorbance, whereby amyloids were passed through a 100 kDa MWCO centrifuge filter, and the protein absorbance peak at 280 nm was compared for as-prepared amyloids and the protein filtrate therein.^[131] The protein concentration in each sample was then estimated using the Beer-Lambert Law, whereby it was determined that 9.3% by weight of the BSA amyloid suspension was composed of unaggregated species/monomers or low molecular weight oligomers, indicating a high level of aggregation/conversion from the native state.

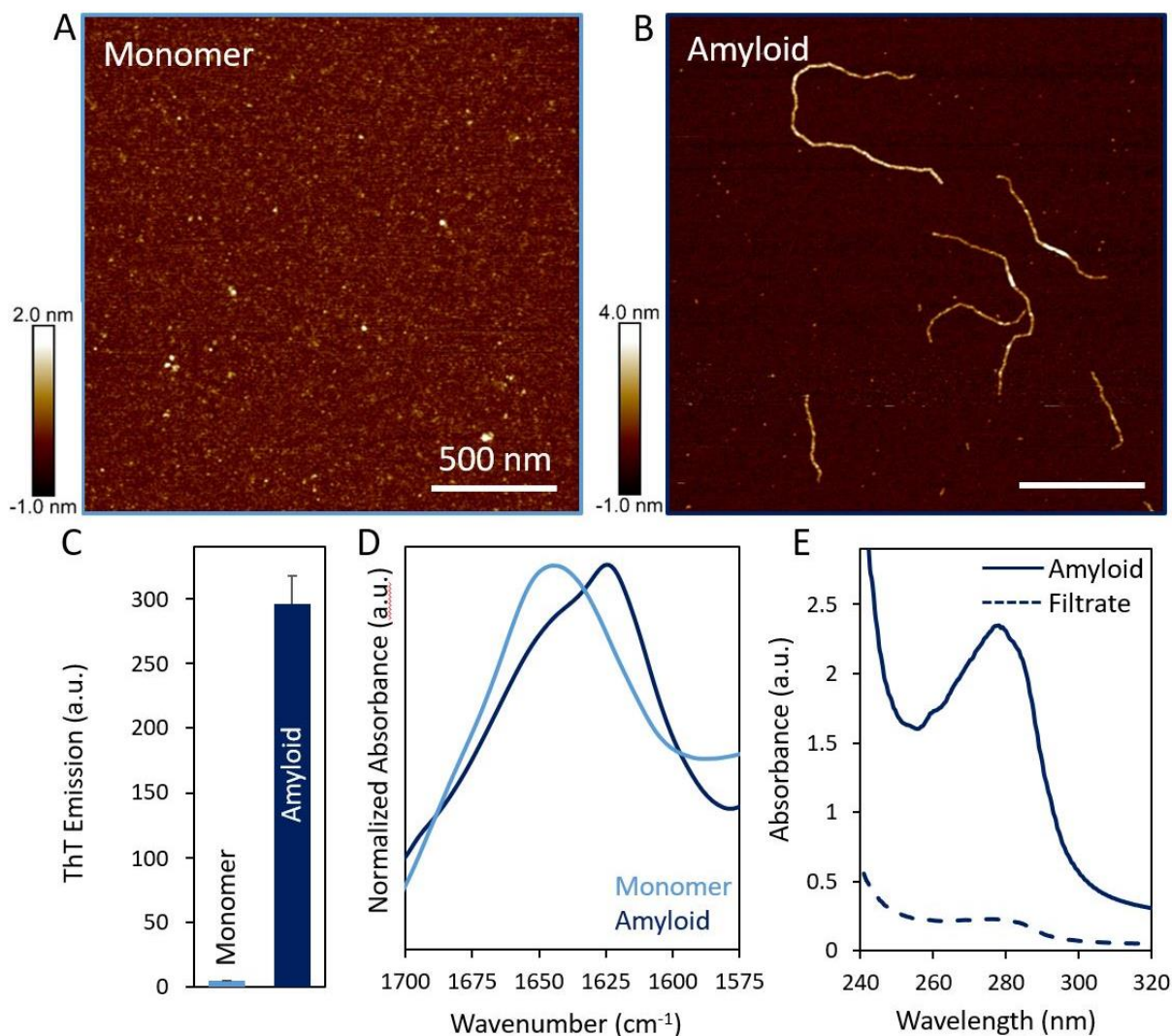


Figure 16: Preparation and characterization of BSA amyloids prepared via acid-mediated hydrolysis (pH 2) of BSA at 90 °C for 96 h. AFM images of (A) BSA monomer and (B) BSA amyloids. Both scale bars are 500 nm. (C) ThT emission of BSA monomer and amyloids. (D) Normalized FTIR absorbance of BSA monomer and amyloids. (E) UV-vis absorbance of BSA amyloids and the filtrate therein.

Aqueous Interactions & Phase Behaviour of CNC – BSA Amyloid Composites

Negatively charged sulfuric-acid hydrolyzed CNCs (purchased from CelluForce, average length = 117 ± 64 nm) were added to as-prepared BSA amyloid suspensions via simple mixing of the two components in defined ratios. As expected, due to the negative surface charge of both components (zeta potential ~ -30 mV, Figure 2), no aggregation was apparent in any of the mixed suspensions via AFM, DLS, or zeta potential measurements (50% BSA shown in Figure 2, all other ratios shown in the Supporting

Information, Figure S3 for AFM and Figure S4 for DLS and zeta potential). CNC – BSA amyloid suspensions were then concentrated in order to investigate the effects of BSA amyloid addition on the phase behaviour of CNCs; CNCs are known to undergo a smooth transition from a fully isotropic regime, through a biphasic regime, and finally towards a fully chiral nematic/anisotropic liquid crystalline regime as their concentration is increased.[340] This chiral nematic regime is formed in order to maximize translational entropy between individual CNC rods as they pack closer together, and can be severely hindered by interacting particles which limit CNC reorganization.[284] Due to the lack of aggregation between CNCs and BSA amyloids evidenced here, we anticipate that BSA amyloids will not hinder the formation of a CNC chiral nematic regime.

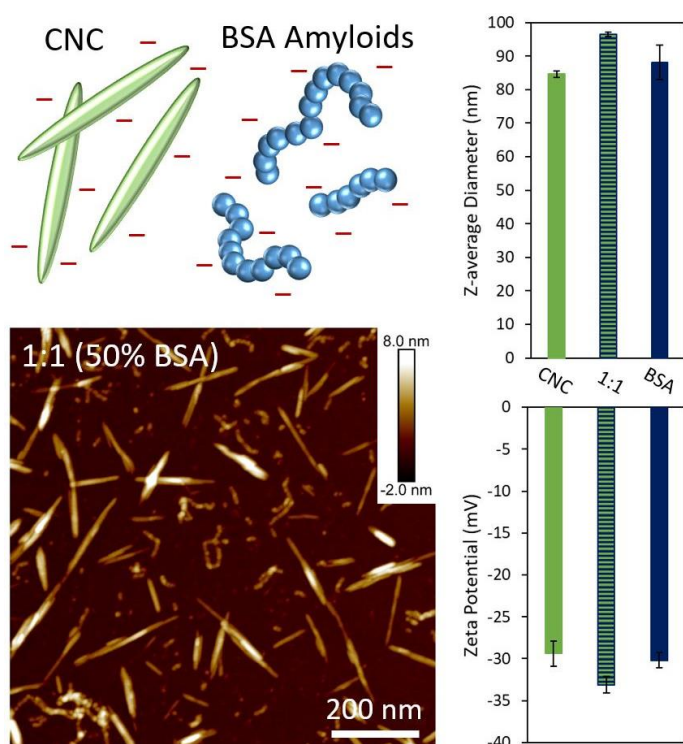


Figure 2: Schematic representation of negatively charged CNC (green) and BSA amyloid (blue) mixtures. A 1:1 mixture of the two components (50% BSA amyloid, mixed horizontal bars) yields no significant aggregation or domain formation of either constituent, as demonstrated by AFM, DLS, and Zeta potential measurements.

Concentrated CNC suspensions containing varying amounts of BSA amyloids (0 – 4% with respect to CNC content) were prepared in order to investigate their phase behaviour (Figure 3). Although the effects of CNC rod length (c.f. Onsager Theory),^[99,341] surface charge,^[342] and ionic strength have been investigated in relation to CNC phase behaviour,^[284,343] to date fundamental research in this area has overwhelmingly focused on CNCs in pure suspension. There is however a large knowledge gap related to the phase behaviour of composite CNC suspensions, which is especially striking considering the significant amount of research interest in the preparation of structured composite CNC films with various functional polymers, particles, or other additives.^[129,283,304,321,344,345] To this end, here we demonstrate that the addition of increasing concentrations of BSA amyloids results in a systematic shift in the CNC phase diagram, whereby the onset of the biphasic region is delayed. In other words, at similar CNC concentrations the addition of BSA amyloids leads to a lower chiral nematic volume fraction, and hence an overall compression of the chiral nematic pitch.^[307] This same phenomenon is also evidenced upon increasing CNC concentration in pure suspensions, whereby the chiral nematic pitch is progressively compressed in the biphasic regime.^[295,346]

For each suspension mixture, the biphasic regime was modeled by linear regression (Supporting Information, Table S1) following Onsager Theory,^[99] to assess the CNC weight fraction required for the onset of chiral nematic phase formation (ϕ_i) and complete anisotropic/chiral nematic organization (ϕ_a). Although it has been demonstrated for CNC-based systems that the absolute concentration for onset and saturation of the biphasic regime deviate slightly from theory,^[284] the relative differences observed here are still deemed physically significant.

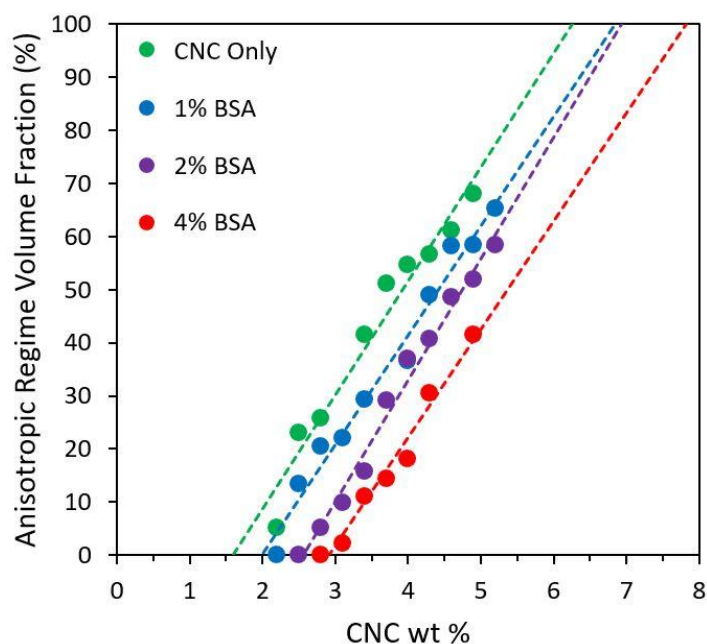


Figure 3: Equilibrium phase behaviour of aqueous CNC suspensions containing varying amounts of BSA amyloids. Note that it was challenging to determine the exact anisotropic fraction at CNC loadings higher than ca. 5.0 wt% due to increased light scattering throughout the sample (and as such, some measurement points have been omitted), as discussed in detail in a previous publication.[347] Lines are linear regressions to be used as guides for the eye.

The addition of increasing amounts of BSA amyloids led to a suppression of ϕ_i to higher CNC wt%, delaying the formation of the chiral nematic phase. In this low CNC concentration regime where spacing between individual CNC rods is large (below ϕ_i), likely the presence of BSA amyloids disturbs CNC – CNC interactions, thus hindering organization. Note that in this concentration regime, the distance between individual CNC rods (> 50 nm[346]) is on the same length scale as the hydrodynamic diameter of the BSA amyloids, supporting this hypothesis. Furthermore, following Lekkerkerker[348] this leads to increased repulsion between individual CNCs, and hence increased colloidal stability delaying the onset of chiral nematic phase formation.

Once the overall CNC concentration is increased above ϕ_i , chiral nematic organization occurs and the average spacing between rods decreases progressively throughout this

biphasic regime.⁵⁶ For a given CNC concentration within the biphasic regime, the addition of BSA amyloids causes a decrease in the CNC anisotropic regime volume fraction, and thus a compression of the chiral nematic pitch (decreased spacing between individual CNC rods).[307] According to Flory,[349] decreased separation between individual rod-like particles in suspension (i.e. increased attraction between the rods) is predicted to lead to a widening co-existence window (biphasic regime). Correspondingly, here, upon the addition of 4% BSA amyloids, a broadening of the overall biphasic regime ($\phi_a - \phi_i$) by roughly 20 % (Table S1) is evidenced based on linear regression analysis.

In order to further rationalize the effects of BSA amyloid addition on CNC phase behaviour, equilibrated 4 wt% CNC suspensions containing varying amounts of BSA amyloids were carefully fractionated into isotropic and anisotropic portions. Samples were then investigated via UV-vis absorbance, FTIR, and AFM to determine the specific partitioning of BSA amyloids into the isotropic and anisotropic CNC regimes (4% BSA shown in Figure 4, CNC only and 2% BSA shown in the Supporting Information, Figures S5 and S6). For suspensions containing 4% BSA, UV-vis analysis showed the presence of a stronger absorbance band at 280 nm for the isotropic fraction compared to the anisotropic fraction, suggesting a larger concentration of protein within the isotropic regime. This was also supported by FTIR analysis, whereby increased absorbance peaks were observed in the amide I (1600 – 1700 cm^{-1} , C=O stretching) and amide II (~ 1515 – 1555 cm^{-1} , N-H bending) regions for the isotropic fraction.[303,334] Note that CNC only samples also show an absorbance band centered in the amide I region (around 1631 cm^{-1}), attributed to -OH bending of adsorbed water:[344] this band is stronger in the isotropic fraction due to decreased CNC-CNC interactions versus the highly organized anisotropic fraction. Finally, AFM imaging demonstrated a higher quantity of flexible aggregates in the isotropic fraction than in the anisotropic fraction;

208

in both regimes, these aggregates were absent from the CNC only samples (Supporting Information, Figure S6), and can therefore be confidently attributed to BSA amyloids. Thus, we can conclude that although BSA is present in both fractions, it appears to selectively partition to the upper isotropic regime in a much higher concentration, resulting in a compression of CNCs within the lower anisotropic phase. Similar behaviour has previously been observed for CNC suspensions with blue dextran, which like the BSA amyloids herein is also non-adsorbing, whereby the blue dextran preferentially separated into the isotropic phase and resulted in a broadening of the biphasic regime.[350,351]

Taken together, these results indicate that mechanistically, BSA amyloids interact with CNCs through depletion interactions, which is typical for non-adsorbing polymer additives to colloidal systems.[348,352] In a binary mixture of large colloids and non-adsorbing polymers/particles, the large-sized colloids (here, the CNCs) are 'depleted' by the non-adsorbing particles (here, the BSA amyloids) due to an imbalance in osmotic pressure.[352–355] This imbalance induces a net attractive force between the large colloids, pulling them together and increasing the free volume for the non-adsorbing component, and resulting in an overall increase in the entropy of the mixture and corresponding lowering of the free energy of the system. Here, this is seen as a compression of the chiral nematic pitch and an overall decrease in the chiral nematic volume fraction upon increasing BSA amyloid addition due to its preferential exclusion to the isotropic regime.

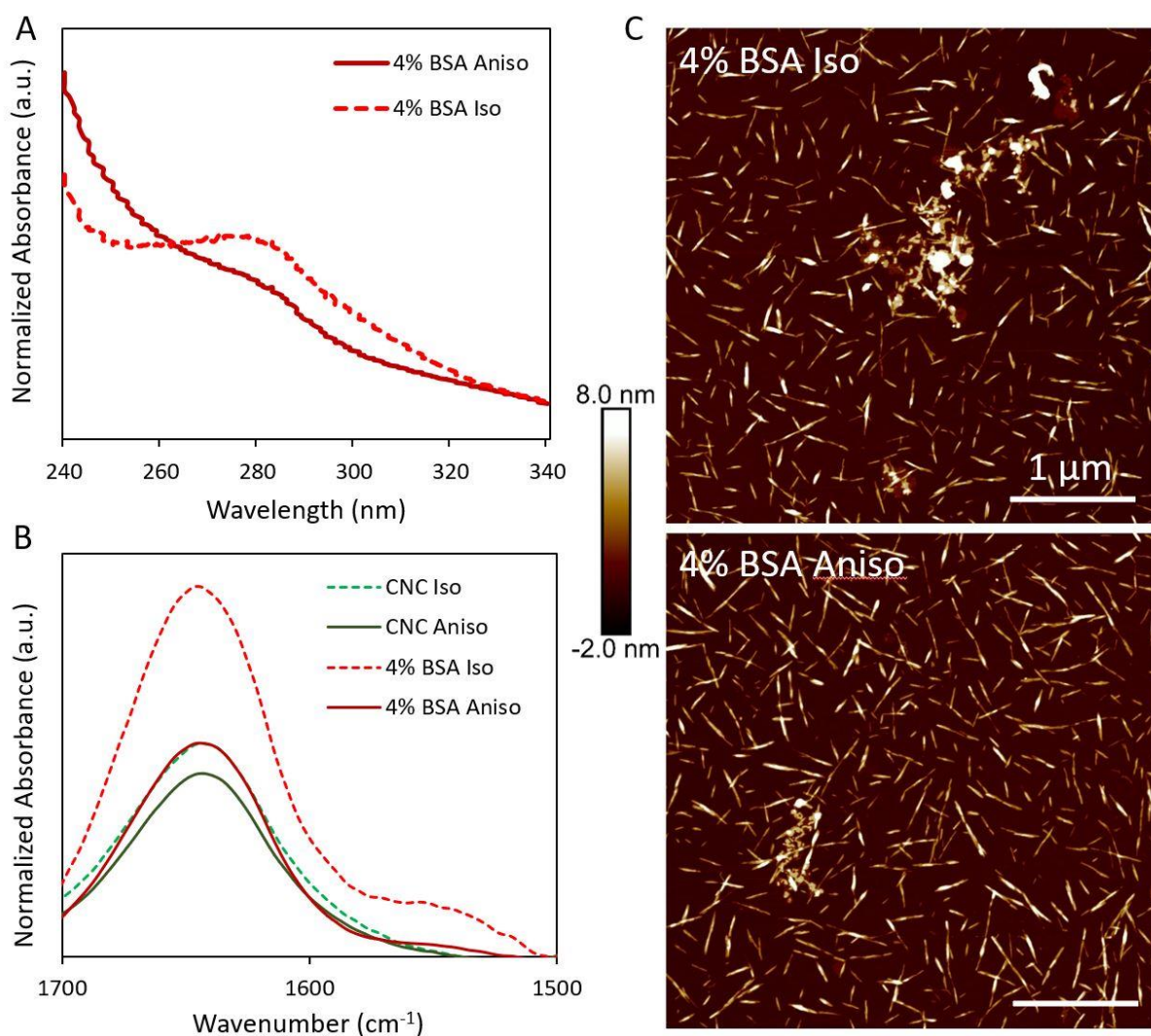


Figure 4: Partitioning of BSA amyloids into the isotropic and chiral nematic/anisotropic regimes at equilibrium. (A) Baseline-normalized UV-vis absorbance spectra (CNC suspension used as baseline), (B) normalized absorbance via FTIR and (C) AFM images of the isotropic and anisotropic regimes of CNC suspensions containing 4% BSA amyloids. Scale bars are both 1 μm .

One of the additional hallmarks of depletion interactions is the increased attraction between self-assembling colloids resulting in faster kinetics of phase separation.[352,356] To this end, CNC phase separation was recorded on a roughly weekly basis for 42 weeks in order to determine the kinetics of phase separation (Supporting Information Figure S7); three distinct CNC concentrations were chosen within the biphasic region and the change in the anisotropic fraction volume percent was investigated over time (Supporting Information Figure S8). In general, samples reached equilibrium quicker

(smaller percent change) at the lower end of the biphasic region, due to the lower suspension viscosity enabling quicker particle motion/reorganization.[307] Regardless of CNC concentration, samples containing 1 and 2% BSA amyloids reached equilibrium progressively quicker than CNC only samples. Although samples containing 4% BSA amyloids also reached equilibrium quicker than CNC only samples, they did not reach equilibrium as fast as the 1 and 2% BSA amyloid samples, perhaps due to an increase in suspension viscosity/overall solids content. Albeit, for all BSA amyloid concentrations tested, faster kinetics of phase separation were evidenced versus CNC only samples, again indicative of depletion interactions.

Evaporation-Induced Self-Assembly and Film Structuring of CNC – BSA Amyloid Composites

CNC – BSA amyloid composite films with varying concentration of BSA were prepared via evaporation-induced self-assembly (EISA, Figure 5). The incorporation of BSA amyloids into the structured films was monitored by FTIR, whereby as expected, increasing BSA loading resulted in an increase in the amide I and amide II absorbance regions (Figure 5 A; full spectra are shown in the Supporting Information, Figure S9). Detailed film structure was investigated via UV-vis absorbance, with CNC only films demonstrating a characteristic reflectance peak related to the chiral nematic pitch therein. Upon increasing addition of BSA amyloids, this characteristic reflectance peak was systematically blue-shifted to lower wavelengths, representing a compression of the chiral nematic pitch. SEM imaging of film cross-sections qualitatively supplemented this analysis, whereby the chiral nematic pitch appears to progressively decrease with increasing loading of BSA amyloids (Supporting Information, Figures S11 and S12).

Moreover, this trend agrees well with data observed in concentrated suspensions (discussed above, where the addition of increasing amounts of BSA amyloids resulted in a decrease in the anisotropic fraction volume percent and a compression of the equilibrium pitch), and also agrees well with data observed previously in CNC films upon the addition of non-adsorbing sodium polyacrylate or L-histidine.[129,357] Note that the results observed here are contrasting to what is observed upon the addition of adsorbing polymers to CNC films,[304,344] whereby the adsorbed polymers increase the effective diameter of CNC rods, leading to a red-shifting or expansion of the chiral nematic pitch.

The addition of up to 10% BSA amyloids did not result in any significant broadening of the reflectance peak (Supporting Information, Figure S10), indicating good preservation of the chiral nematic structure (albeit, the broad protein absorbance peak centered around 280 nm interferes with the chiral nematic peak at higher BSA amyloid concentrations). Although no clear peak could be evidenced for films with 20% BSA amyloids, a clear lamellar organization was present via SEM; this structure disappeared completely for films with 50% BSA amyloids (Supporting Information, Figures S11 and S12). This is significantly different from our previous results upon positively-charged lysozyme amyloid addition to self-assembling CNC suspensions, whereby a clear broadening of the reflectance peak was observed, indicating an overall disruption in chiral nematic structuring.[104]

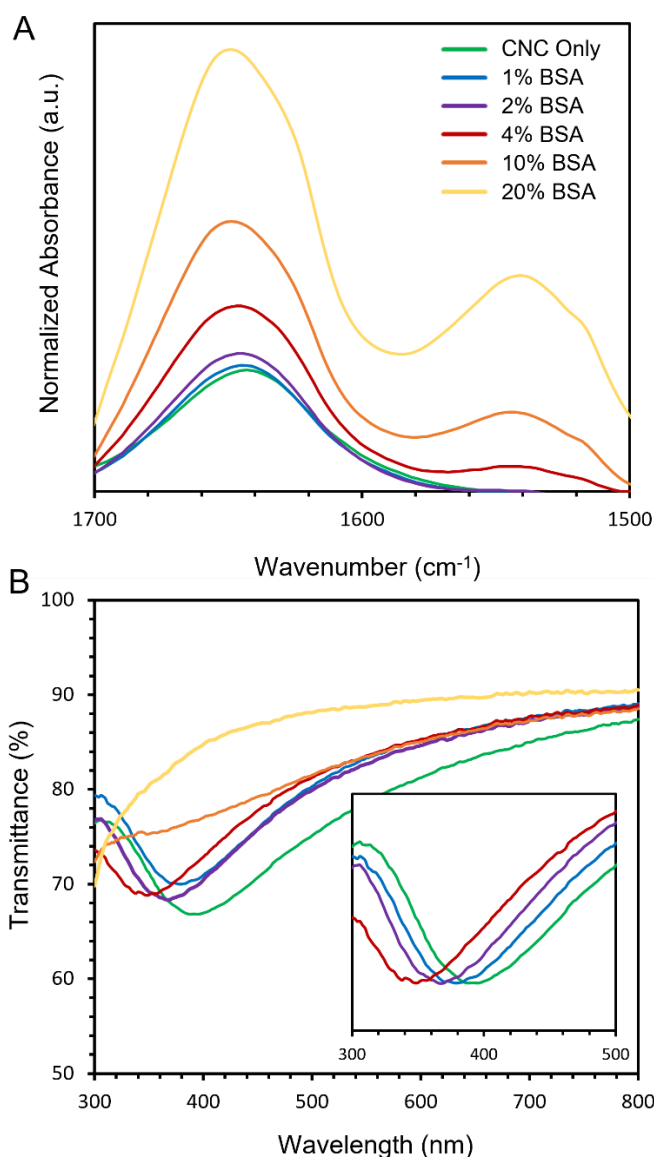


Figure 5: Characterization of CNC – BSA amyloid composite films with varying BSA amyloid concentrations prepared via EISA. (A) Baseline-corrected, normalized FTIR spectra in the amide I and II absorbance region, (B) representative transmittance spectra via UV-vis (with inset displaying individually normalized transmittance of the minimum peak reflectance wavelength to help visualize the peak shift upon BSA amyloid addition).

Evaporation-Induced Self Assembly Under Confined Conditions and Lap Shear

Adhesion of CNC – BSA Amyloid Composites

Finally, CNC – BSA amyloid structural adhesives were prepared via EISA under confined conditions (c-EISA). Here, 40 μ L of a 1.6 wt % suspension (0.64 mg total solids content) was allowed to dry under ambient conditions between 2 glass slides in order

to obtain a final areal density of ca. 0.09 mg/cm^2 (shown schematically in Figure 6, A – C). The bonded glass slides were then loaded into a uniaxial tensile tester to determine the ultimate lap shear load before bond failure (Figure 6 D, numerical values shown in the Supporting Information, Table S2). In all cases, the controlled c-EISA process induced the formation of strong cohesive and adhesive supramolecular interactions between the biomacromolecule building blocks and the glass substrates. This was evidenced by the high lap shear loads of both pure BSA amyloid assemblies ($112 \pm 59 \text{ N}$) and pure CNC assemblies ($267 \pm 63 \text{ N}$). Interestingly, synergistic improvements in lap shear loads were evidenced for CNC – BSA amyloid mixed assemblies up to 20% BSA, with a 3-fold improvement vs pure BSA amyloid assemblies and 1.25-fold improvement vs pure CNC assemblies for 4% BSA samples ($336 \pm 114 \text{ N}$).

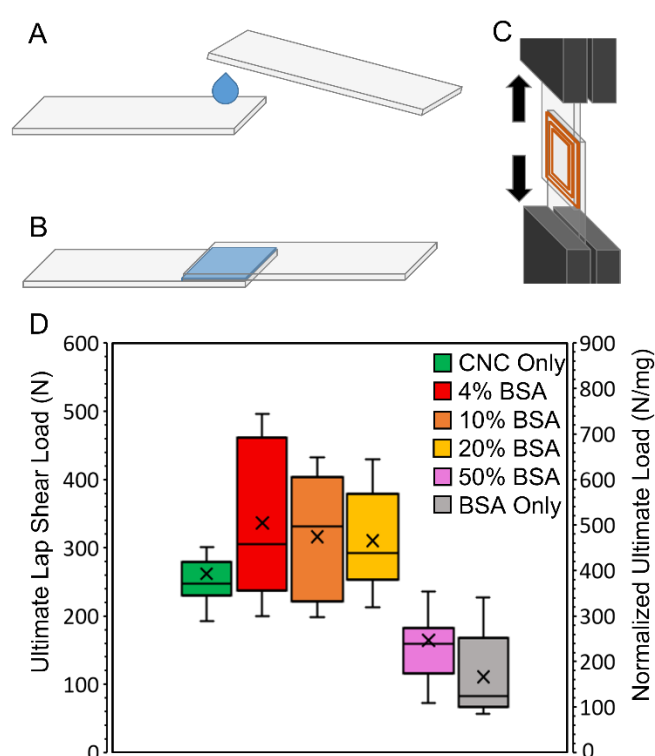


Figure 6: Schematic representation of the c-EISA process, whereby (A) suspensions are dropped on a glass slide, (B) covered with a second glass slide and allowed to dry overnight under ambient conditions, and (C) loaded into a uniaxial tensile tester to determine lap shear adhesion. (D) Box plot showing the ultimate lap shear load (N)

normalized ultimate load per adhesive mass (N/mg) for CNC – BSA amyloid structural adhesives with varying BSA amyloid content. In each box, \times represents the mean, the midline represents the median, the box represents the interquartile range, and the error bars represent the statistical maximum and minimum values based on the interquartile ranges. In each case, between 8 and 12 samples were analyzed.

In order to further investigate these synergistic improvements in lap shear adhesion, we observed the morphology of the formed assemblies via optical, polarized optical, and scanning electron microscopy (OM, POM, and SEM respectively; Figure 7 and Supporting Information, Figure S13). CNC only assemblies demonstrated a strong accumulation of material around the edges of the overlapping glass substrates, due to the well-established coffee-ring effect (capillary flow),^[358,359] whereby solvent evaporation from the glass slide edges induces an outward flow of material. This is particularly noticeable under polarized light, with little birefringence evidenced in the middle of the glass slides (Figure 7 B), and well-organized birefringent lamellae evidenced around the edges (Figure 7 C). Note that the formation and long-range ordering of these lamellae are discussed in detail elsewhere, but involves fracture initiation and propagation during drying between regions of chiral nematically organized CNCs.^[322] These well-organized lamellae lead to greatly enhanced molecular contact between the CNCs and the glass substrate, which magnifies relatively weak van der Waals interactions yielding large overall attractive forces, mechanistically similar to the periodic arrays of micro- and nano-structured lamellae and setae in gecko feet.^[316]

Upon the addition of small amounts of BSA amyloids (4 – 20%), material still strongly accumulated around the edges of the laps, with little remaining in the middle, as evidenced via OM and POM. Although well-organized lamellae were still apparent around the very edges of the laps, the formation of multibranched lamellar patterns emerged, indicative of increased depinning and a transition towards Marangoni flow.^[360,361]

These multibranching lamellar patterns became more evident as the BSA amyloid concentration was progressively increased from 4 to 20% (Figure 7 and Supporting Information Figure S13), supporting the proposed mechanism. As the BSA amyloid concentration is further increased beyond 20%, Marangoni flow dominates and a more uniform deposition of material is evidenced (Figure 7 for 50% BSA amyloids and Figure S13 for pure BSA amyloids), whereby the lamellar structures disappear (although some material accumulation around the edges is still apparent due to the outward flux of water). This is likely caused by the increased surface activity of the BSA amyloids lowering the overall surface tension of the suspensions and facilitating depinning during water evaporation; a similar phenomenon has previously been described for increasing concentrations of small ionic surfactants.[360]

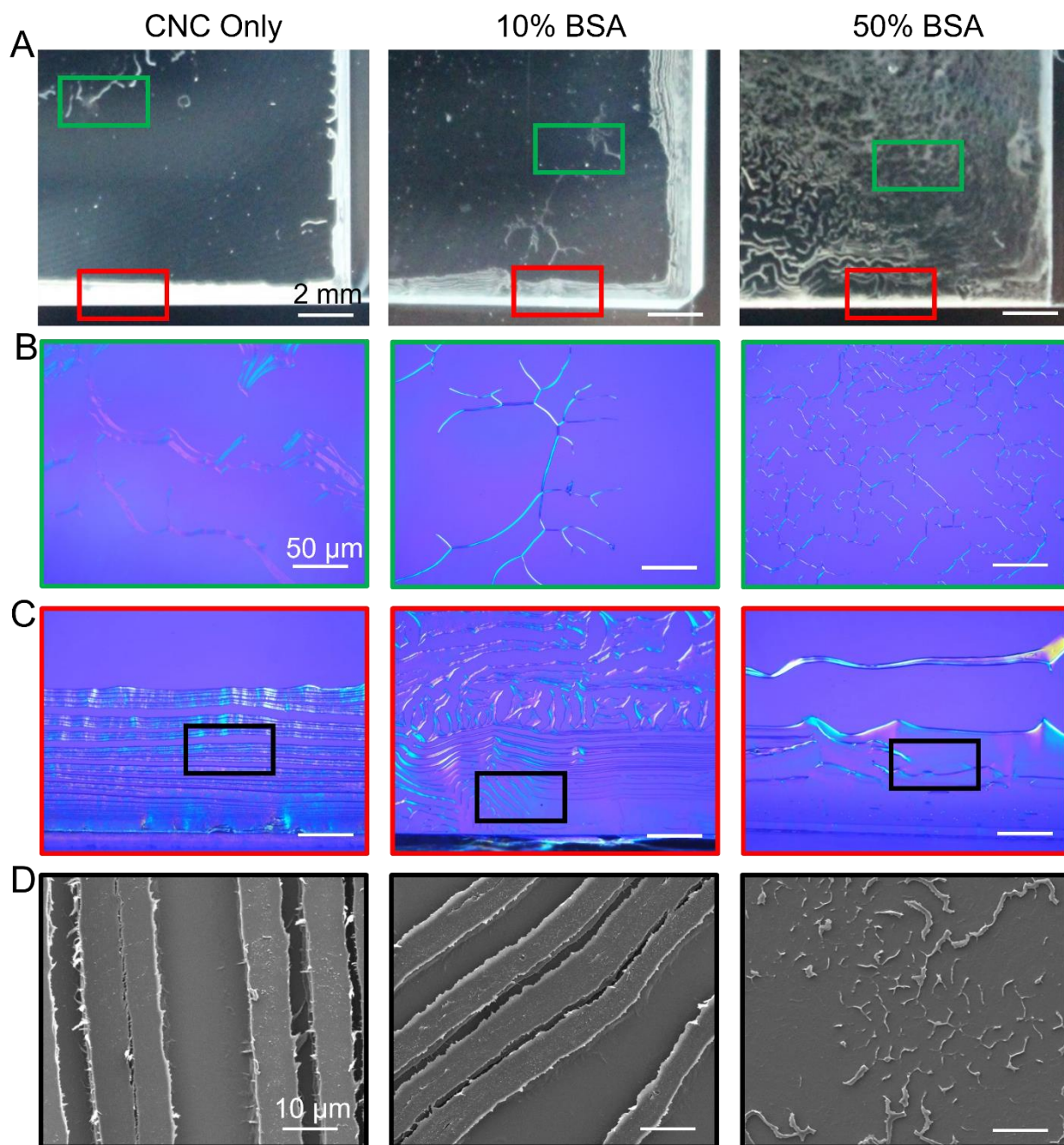


Figure 7: Structural morphology of CNC – BSA amyloid lap adhesives formed via c-EISA. (A) Optical images of the formed laps between glass slides, (B) polarized optical microscopy images of representative areas in the middle, and (C) near the edges of the laps, and (D) SEM images of representative areas near the edges of the laps. All scale bars in (A) are 2 mm, in (B) and (C) are 50 μm, and in (D) are 10 μm.

Previous work has demonstrated that organized lamellae facilitate intimate contact between biopolymers and substrates in structural adhesives,[323] leading to increased

adhesive strength. Here, adhesive laps with small amounts of BSA amyloids show increased lamellar area (the organization extends inwards from the edges of the laps, evidenced via POM and optical images), versus CNC only laps, which we anticipate is the main reason for the increased ultimate lap shear adhesion. Although the interplay between (mainly) capillary and (nominally) Marangoni flows during drying is likely a leading contributor to the increased lamellar area,[323] we hypothesize that the interactions between BSA amyloids and CNCs during self-assembly also affects the formation of lamellae themselves. As mentioned previously, for CNC only lap shear adhesives, lamellae formation is generated through a fracture initiation process, whereby the formed lamellae are composed of organized assemblies of CNCs in a chiral nematic regime.[322] Here, due to the depletion interactions between BSA amyloids and CNCs investigated above, CNCs are compressed within the self-assembling chiral nematic regime while BSA amyloids are preferentially excluded. We hypothesize that these BSA amyloid-rich regions, which are more likely to undergo Marangoni flow, enable increased opportunity for fracture initiation as the evaporation process proceeds from the edges of the lap inwards. This likely leads to an increased number of lamellae and thus increased lamellar area and increased overall lap shear adhesion. Further supporting this hypothesis, as seen in free-standing films, the addition of over 50% BSA amyloids completely disrupts CNC chiral nematic ordering; consequentially, the adhesive laps with similar BSA amyloid concentration lack well organized lamellar structures, and show a much weaker ultimate lap shear load.

Contextually, the synergistic improvements in lap shear adhesion demonstrated here represent some of the strongest values ever reported for bio-colloidal structural adhesives with glass substrates.[322,323,326,362,363] It should however be mentioned that an in-depth comparison across different literature examples is challenging for sev-

eral reasons, including suspension viscosity, substrate physical and chemical properties, and other differences in experimental set-up and conditions. This is especially apparent when comparing the mass-normalized lap shear load for BSA in its native form and CNCs across various literature examples (Figure 8 A). Although the mass-normalized lap shear load is correlated with areal density, stark differences nevertheless exist between samples prepared at similar areal densities. Furthermore, mass-normalized lap shear load is in itself a flawed comparison metric, due to differences in adhesive organization greatly affecting the actual load-bearing area of the adhesive.[323] For example, in this work the adhesive area was fixed at 26 × 26 mm, yet the organized lamellae which are primarily responsible for the adhesive performance do not cover this entire area; this results in an underestimate of true adhesive performance. With these caveats being said, several bio-based structural adhesives prepared at a similar areal density (ca. 0.1 – 0.2 mg/cm²) were compared, as shown in Figure 8 B. With the curious exception of native BSA,[326,363] the CNC-based structural adhesives developed in this work demonstrated normalized lap shear loads at the higher end of all bio-based structural adhesives. Note that several other bio-based structural adhesives prepared at larger areal densities are summarized in the Supporting Information, Table S3. Importantly, regardless of absolute adhesive performance, the mechanistic advantage of combining BSA amyloids with CNCs to improve adhesive performance is clear, as the 4% BSA hybrid performs better than both pure CNC (1.25 fold improvement in normalized lap shear load) and pure BSA amyloid (3 fold improvement in normalized lap shear load) adhesives. Similar synergistic improvements are evidenced for other protein-polysaccharide hybrid adhesives,[323,326] suggesting that the nature-inspired combination of protein and polysaccharide building blocks can enable the next generation of high-performance bio-based materials for a variety of applications.

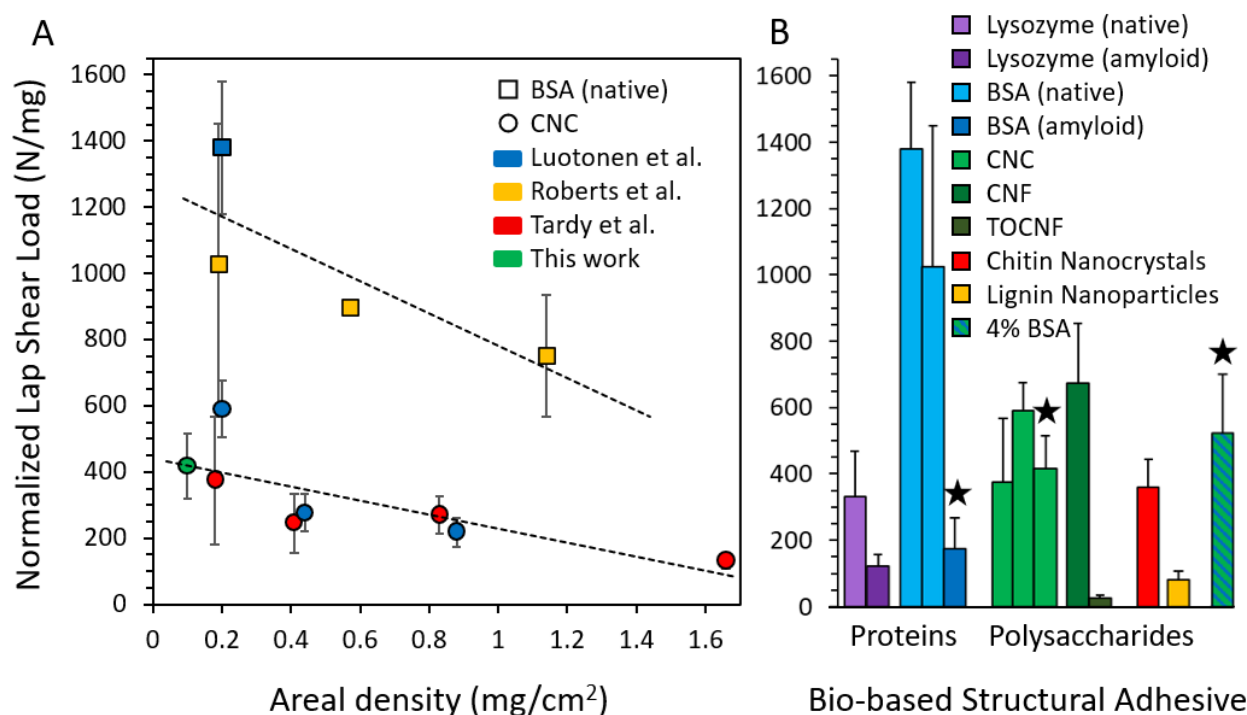


Figure 8: Comparison of bio-based structural adhesives with glass substrates. (a) Effects of areal density on mass-normalized adhesion for CNC and BSA from different literature investigations. Lines are linear regressions. (b) Mass-normalized lap shear load for various protein and polysaccharide-based structural adhesives. Measurements performed in this work are designated with a star. A summary of mass-normalized lap shear load and areal density for these bio-based structural adhesives can be seen in the Supporting Information, Table S3. Literature values are from references.[322,323,326,362,363]

CONCLUSION

In conclusion, the self-assembly of synergistically adhesive polysaccharide-protein composite structures were enabled by a thorough understanding of the mechanistic interactions therein. The phase behaviour of negatively charged and non-interacting CNCs and BSA amyloids was investigated, whereby increasing the BSA amyloid concentration resulted in a systematic decrease in the anisotropic regime volume fraction, an overall broadening of the biphasic regime, and improved the kinetics of self-assembly. We observed a specific partitioning of BSA amyloids into the isotropic fraction, suggesting that mechanistically, depletion interactions are mainly responsible for the

observed phase behaviour. Correspondingly, the preparation of structured films via EISA demonstrated a compression of the chiral nematic pitch and blue-shifting of the absorbance peak upon increasing BSA amyloid addition; importantly the overall chiral nematic structure was well-preserved as evidenced by no significant broadening of the absorbance peak. Finally, CNC – BSA amyloid composite structural adhesives were demonstrated with adhesive strengths in excess of 500 N/mg, representing some of the highest ever reported values for biocolloidal adhesives. The synergistic improvements in adhesive strength were attributed to a balance between capillary and Marangoni flows within the laps during drying, and depletion of the BSA amyloids resulting in improved self-assembly of CNCs into lamellar structures, increased fracture generation and thus increased lamellar area. We anticipate that the knowledge generated herein will enable significant progress in the development of next-generation sustainable structural adhesives for a wide range of practical applications.

EXPERIMENTAL

Materials

Cellulose nanocrystals (CNC, prepared *via* sulfuric acid hydrolysis of bleached softwood kraft pulp, characterized elsewhere[279,295]), were purchased in freeze-dried form from CelluForce (Montreal, Canada). CNC were dispersed in distilled water at 2 wt%, probe sonicated in an ice bath (3 × 10 min cycles, 60% amplitude, Digital Sonifier 450, Branson Ultrasonics) and stored at 4 °C prior to further characterization/use. CNC were concentrated as necessary via ambient evaporation. Bovine serum albumin (BSA, ≥ 98%) was purchased from Sigma Aldrich as a lyophilized powder and used as received. Hydrochloric acid and sodium chloride were purchased from VWR Chemicals

and used as received. Thioflavin T (ThT) was purchased from Acros Organics and used as received.

Preparation of BSA amyloids

BSA amyloids were prepared via incubation at pH 2 and elevated temperature following an established protocol with minor modifications.[27] Briefly, BSA (monomer) was dissolved in a falcon tube at 2 wt% in distilled water, and the pH was adjusted to 2 using 1 M HCl. The falcon tube was then placed in a thermomixer (Eppendorf AG), and mixed at 90 °C and 400 rpm for 96 h. The formed BSA amyloids were then dialyzed against distilled water (100 kDa MWCO membranes, 6 × 12 h cycles) and stored at 4 °C until further use (final concentrations determined gravimetrically). BSA monomer and as-prepared BSA amyloids were imaged via atomic force microscopy (AFM, Bruker ICON3) whereby 100 µL of 0.01 mg/mL sample was dropped onto a freshly-cleaved mica substrate, adsorbed for 1 min, rinsed with 1 mL MilliQ water at pH 2 and then dried with pressurized air prior to imaging. The average amyloid fiber length was measured using FiberApp[296] open-source software, whereby 200 individual particles were analyzed from AFM images (CNC length was also measured using this technique). Note that branched or overlapping fibers were excluded from the analysis, which may lead to a slight underestimate in fiber length. The secondary structure changes during the BSA amyloid conversion were analyzed via FTIR (Bruker Tensor 27 FT-IR spectrometer in attenuated total reflectance mode, spectra recorded between 4000 and 600 cm^{-1} with a resolution of 4 cm^{-1} and 32 scans per sample), and ThT absorbance measurements (TECAN Spark Multimode Reader operating at 450/488 nm excitation/emission with a Greiner 96-well plate, samples tested in quintuplicate

and 30 accumulations per well). BSA amyloid aggregate-to-monomer ratio was determined by measuring the UV-absorbance at 280 nm (Cary 1E spectrophotometer) of dialyzed suspensions versus their filtrate after centrifuge filtration (10 min, 4,000 g) through a 100 kDa MWCO centrifuge filter. The Beer-Lambert Law (equation 1) was then used to estimate and compare protein concentration in both the as-prepared amyloid and filtrate suspensions:

Equation 1: $A = \epsilon LC$

Where A is the measured UV-vis absorbance at 280 nm, ϵ is the molar extinction coefficient for BSA at 280 nm ($\sim 43,824 \text{ M}^{-1} \text{ cm}^{-1}$), L is the optical path length (thickness of the cuvette), and C is the calculated protein concentration.

Preparation and characterization of dilute CNC-BSA amyloid suspensions

CNC were mixed with BSA amyloids to a final concentration of 1 wt% CNC and up to 1 wt% BSA (i.e., 50% with respect to total solids content, or 1:1 with respect to CNC). Suspensions (including pure BSA monomer, pure BSA amyloid, and pure CNC) were characterized via dynamic light scattering (DLS, 0.025 wt% in water) and Zeta potential, (0.25 wt% in 10 mM NaCl; 2.5 wt% in 10 mM NaCl for BSA monomer) using a Malvern ZetaSizer Nano ZS. For all mixed suspensions, AFM images were captured using 0.01 mg/mL of CNC deposited onto freshly cleaved (3-Aminopropyl)triethoxysilane (APTES) coated mica substrates.

Investigation of phase behaviour and BSA partitioning

CNC suspensions were slowly up-concentrated via ambient evaporation in order to avoid any significant particle aggregation. Concentrated CNC suspensions (8 wt%)

were then mixed with BSA amyloids to a final concentration of 5.5 wt% CNC and between 0 and 4% BSA amyloids with respect to CNC content. These mixed suspensions were then serially diluted down to 2.2 wt% and loaded into glass capillary tubes sealed with parafilm. Optical photographs were taken of the suspensions between cross polarizers over time (up to 42 weeks post-preparation) in order to investigate the kinetics of formation of the isotropic and anisotropic regimes; the height of these regimes were measured in ImageJ in order to build phase diagrams. Linear regression analysis was performed on each sample after 42 weeks in order to determine theoretical CNC wt% at the end of the biphasic regime (100% anisotropic phase). To further investigate regime formation kinetics, three CNC concentrations in the middle of the biphasic regime for all samples were chosen (4.0 wt%, 4.3 wt%, and 4.9 wt%) and the rate of change in the anisotropic regime percent was calculated up to 42 weeks of storage. To investigate BSA partitioning, 4.0 wt% CNC suspensions with varying concentration of BSA amyloids were allowed to phase separate over a period of 2 months. The top isotropic phase was then carefully decanted to isolate the two regimes. FTIR, AFM, and UV-absorbance measurements (all as described above) were then performed separately on the isolated isotropic and anisotropic regimes.

Preparation and characterization of CNC-BSA amyloid self-assembled films

Films were prepared by depositing 10 mL of the above-described dilute suspensions (1 wt% CNC and between 0 and 1 wt% BSA) into a polystyrene petri dish, which were then allowed to evaporate under ambient conditions. Note that pure BSA amyloid films were too delicate to handle, and thus could not be fully characterized. Film composition was analyzed via FTIR as described above. Optical properties were investigated via UV/Vis (UV3600 UV-vis NIR Spectrophotometer, Shimadzu). The “half-bandwidth” ($1/2$

band) was calculated by plotting the derivative around the minimum peak reflectance wavelength ($dT/d\lambda$) against $\lambda - \lambda_{\min}$ for each film. Film morphology was investigated via scanning electron microscopy (SEM),[364] whereby individual films were freeze-fractured by bending after submersion in liquid nitrogen, and loaded in sample holders to view the fracture cross-section. Samples were coated with a thin layer of platinum (~ 2 nm) before imaging (5.0mm working distance, 5.0 kV accelerating voltage, Fei Nova NanoSEM 230). For all characterizations performed, care was taken to use sections of film from the center of each sample in order to avoid inhomogeneous areas, which may arise from edge/other effects during drying.

Preparation and characterization of CNC-BSA amyloid structural adhesives

Suspensions of CNC and BSA amyloids were used at 1.6 wt % for preparing adhesive laps. All suspensions were thoroughly vortex mixed for ca. 1 min prior to deposition on standard glass microscope slides (76 x 26 x 1 mm; VWR), whereby 40 μ L of suspension was deposited onto the end of one slide and subsequently covered with a second slide such that an overlap area of ca. 26 x 26 mm was formed. The upper glass slides were supported on the free end by another glass slide so as to ensure uniform drying/evaporation and contact between the two slides. All laps were dried under ambient conditions, remaining untouched for ca. 60 h prior to handling/testing. Masking tape was then wrapped around the free ends of the formed laps to increase the friction with the clamps used for tensile testing (Zwick Z005 AllroundLine equipped with a 5 kN load cell and using a strain rate of 1 mm min⁻¹). Tensile testing was repeated on between 8 and 12 samples for each condition, and the maximum force achieved prior to shear breakage was recorded. Laps were imaged using a digital camera and via

polarized optical microscopy (Zeiss Axioplan microscope equipped with cross-polarizing filters and first order retardation plate), with the illumination, exposure and gain settings held constant for all samples. Scanning electron microscopy images of adhesive bond areas were gathered using a Fei Nova NanoSEM 230 Instrument operating at 5.0 mm working distance and 5.0 kV accelerating voltage. Samples were coated with a thin layer of platinum (~2 nm) before imaging.

ASSOCIATED CONTENT

Supporting Information. Full-spectra FTIR, DLS, and Zeta Potential measurements for BSA amyloid and monomer, AFM images of CNC – BSA amyloid mixed suspensions, DLS and Zeta Potential measurements of CNC – BSA amyloid suspensions, linear regression analysis and detailed kinetics of phase separation of CNC – BSA amyloid suspension biphasic regimes, additional FTIR spectra and AFM images of isotropic and anisotropic fractions, FTIR spectra and SEM images of self-assembled films, UV-vis $\frac{1}{2}$ band analysis of self-assembled films, ultimate lap shear load and load per adhesive mass values for CNC – BSA amyloid laps, additional microscopy images of laps, and a summary of recent bio-based structural adhesives.

AUTHOR INFORMATION

Corresponding Author

* Kevin De France, kevin.defrance@queensu.ca

* Gustav Nyström, gustav.nystroem@empa.ch

Author Contributions

The manuscript was written through contributions of all authors. All authors have given approval to the final version of the manuscript.

Funding Sources

Natural Sciences and Engineering Research Council of Canada (NSERC) Postdoctoral Fellowship program (to KD), Swiss National Science Foundation (SNF) Grant (No. 200021_192225 / 1, to GN).

ACKNOWLEDGEMENT

The authors thank Anja Huch (Empa) for help with SEM sample prep and imaging, Brian Sinnet (Eawag) for access to DLS equipment, and Luiz Greca (Aalto University) for helpful discussions regarding lap shear testing. KD gratefully acknowledges funding from the NSERC Postdoctoral Fellowship program. NK, SC and GN also acknowledge funding from the SNF.

Supporting Information for:

Phase Behaviour, Self-Assembly, and Adhesive
Potential of Cellulose Nanocrystal – BSA Amyloid
Composites

Kevin J. De France^{1,2}, Nico Kummer^{1,3}, Silvia Campioni¹, Gustav Nyström^{1,3*}*

¹ Laboratory for Cellulose & Wood Materials, Empa – Swiss Federal Laboratories for Materials Science and Technology, Überlandstrasse 129, 8600 Dübendorf, Switzerland

² Department of Chemical Engineering, Queen's University, 19 Division St., Kingston, Ontario K7L 3N6, Canada

³ Department of Health Sciences and Technology, ETH Zürich, Schmelzbergstrasse 9, 8092 Zürich, Switzerland

KEYWORDS

Cellulose nanocrystals, protein amyloids, chiral nematic self-assembly, structural adhesives, biohybrid materials

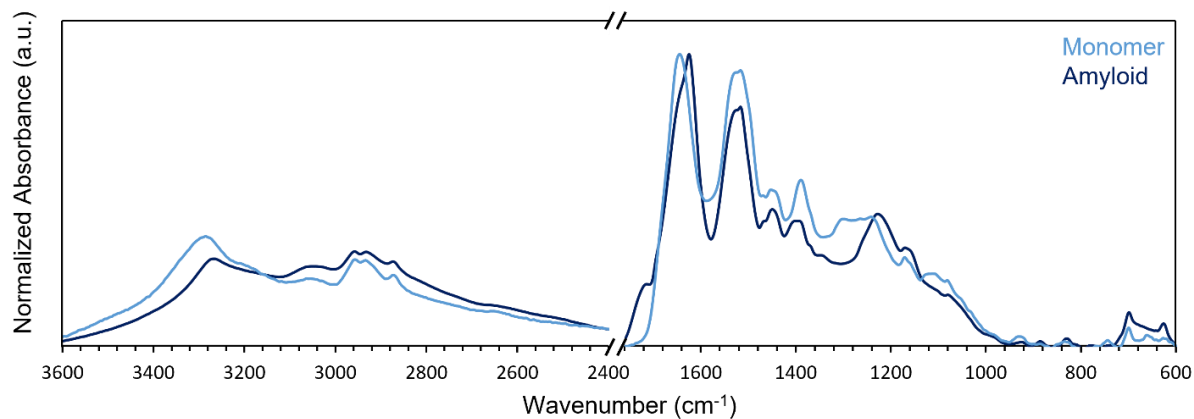


Figure S1. Normalized FTIR absorbance of BSA monomer and amyloid fibers.

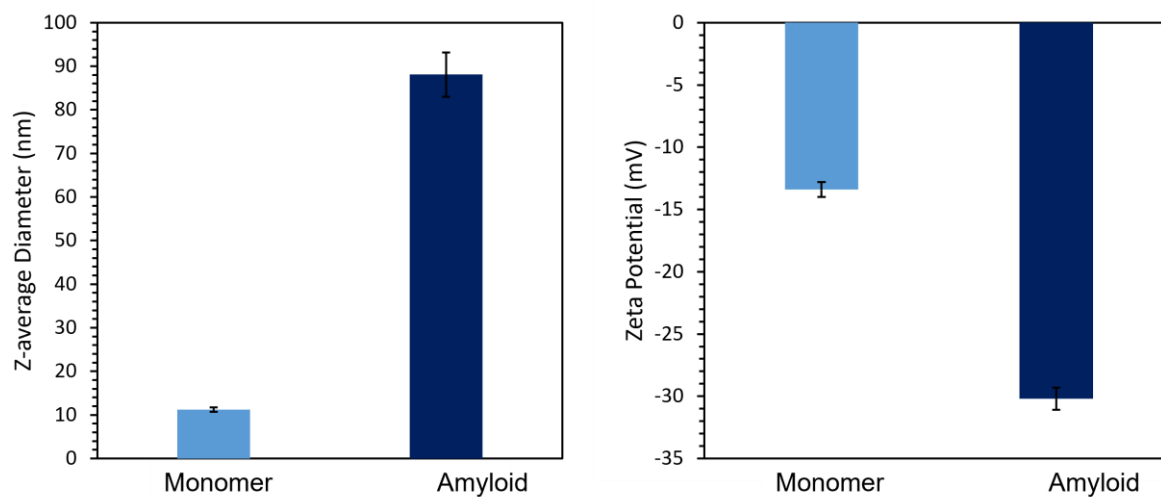


Figure S2. Z-average diameter (nm) and Zeta potential (mV) of BSA monomer and amyloid fibers.

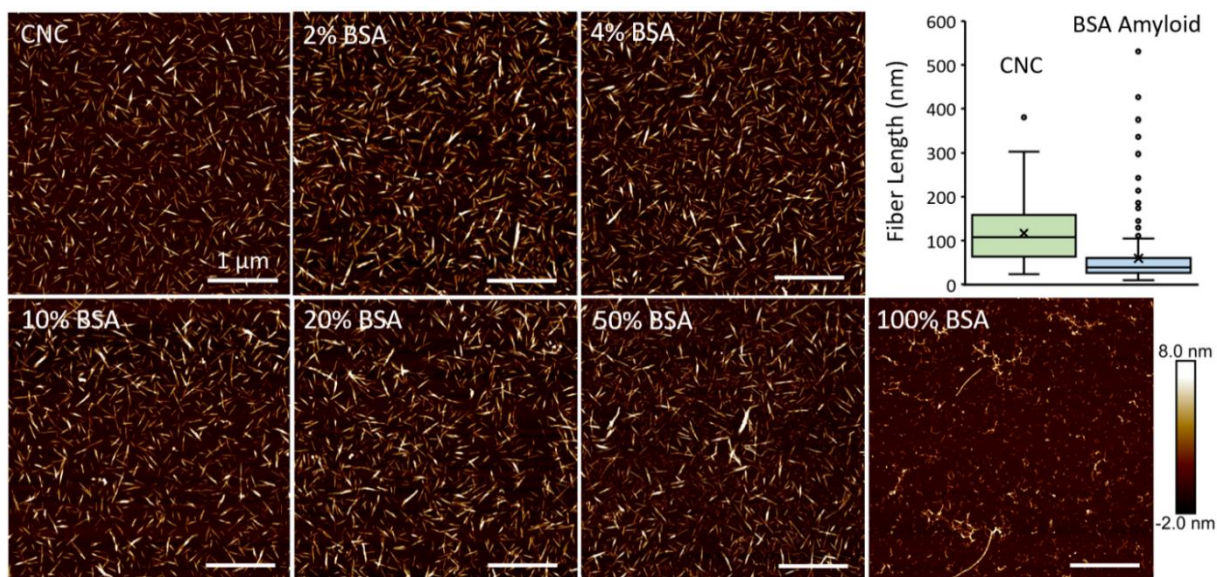


Figure S3. AFM images of CNC – BSA amyloid fiber mixed suspensions containing varying percent BSA. All scale bars are 1 μm . Suspensions were drop-cast onto APTES-coated mica substrates at a CNC concentration of ~ 10 g/L prior to imaging. The pure BSA amyloid suspension was cast at a similar concentration. Box plots of fiber length are shown for pure CNC and pure BSA amyloid, whereby 200 particles were analyzed per sample using FiberApp open-source software.

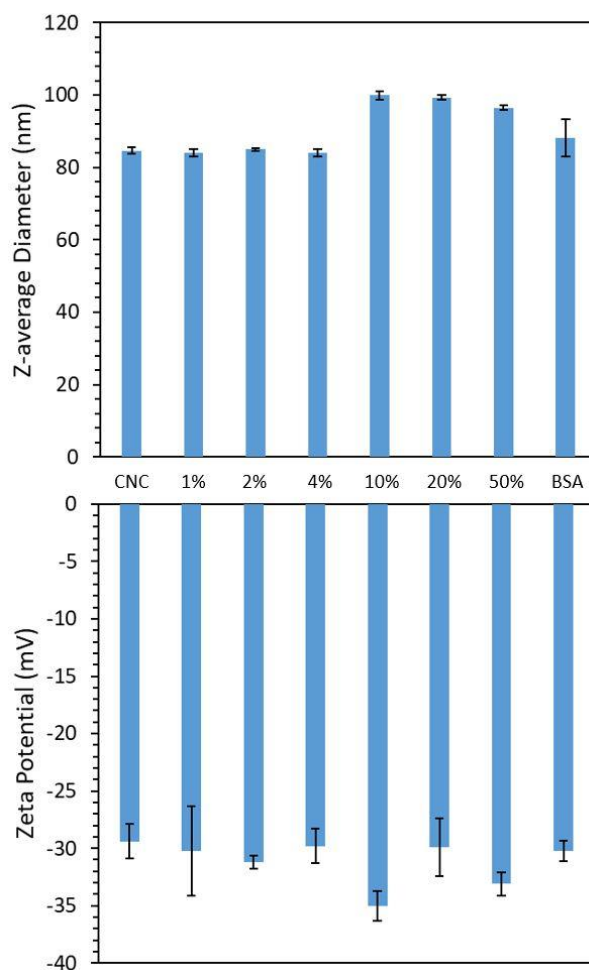


Figure S4. Z-average diameter (nm) and Zeta potential (mV) of CNC – BSA amyloid fiber mixed suspensions containing varying percent BSA.

Table S1. Linear regression analysis of the biphasic regime, where ϕ_i corresponds to the CNC wt% at the onset on of chiral nematic phase formation, and ϕ_a corresponds to the CNC wt% at total anisotropic/chiral nematic organization.

Sample	Linear Regression	R ²	ϕ_a	$\phi_a - \phi_i$
CNC Only	$y = 22.29x - 36.72$	0.951	6.13	4.01
1% BSA	$y = 20.60x - 40.92$	0.979	6.84	4.85
2% BSA	$y = 22.84x - 58.26$	0.986	6.93	4.38
4% BSA	$y = 20.40x - 59.51$	0.974	7.82	4.90

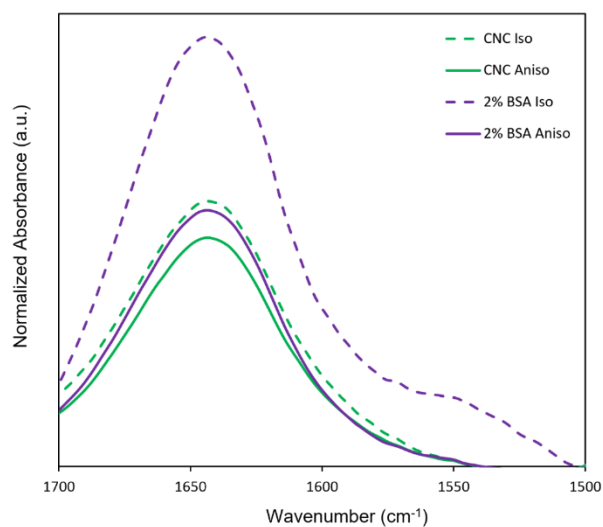


Figure S5. FTIR Spectra of isotropic and anisotropic fractions for CNC suspensions containing 0 and 2 wt% BSA amyloids.

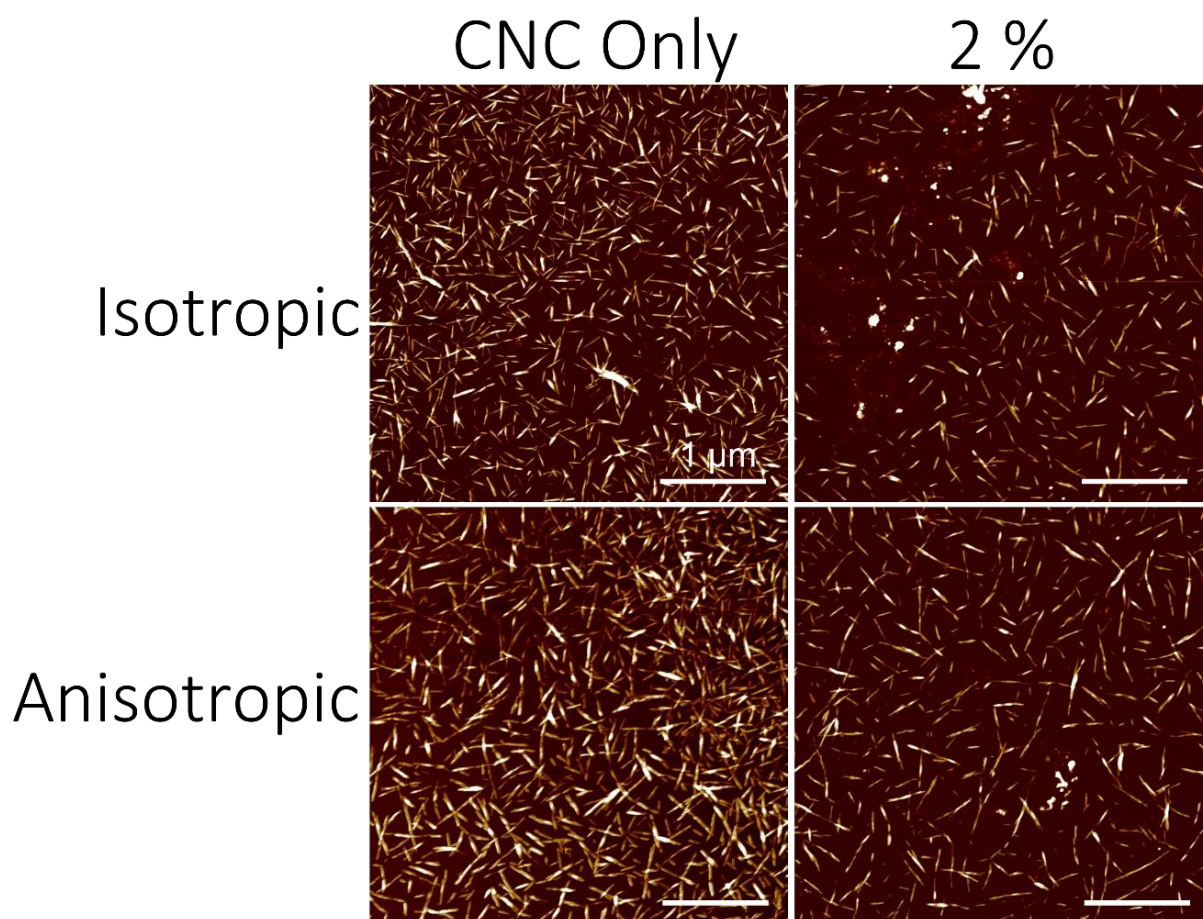


Figure S6. AFM images of isotropic and anisotropic fractions for CNC suspensions containing 0 and 2 wt% BSA amyloids.

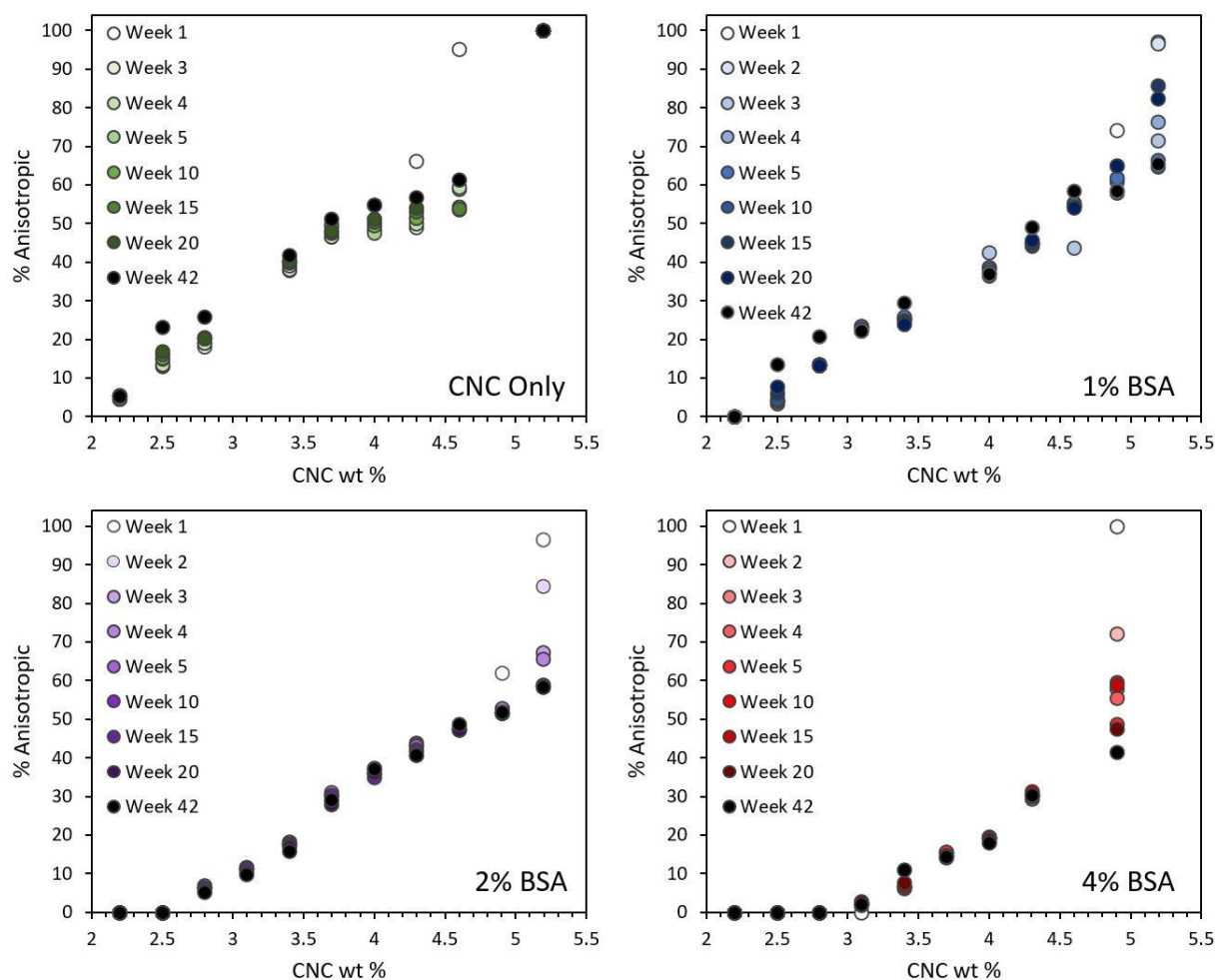


Figure S7. Phase behaviour kinetics of aqueous CNC suspensions containing varying amounts of BSA amyloid fibers.

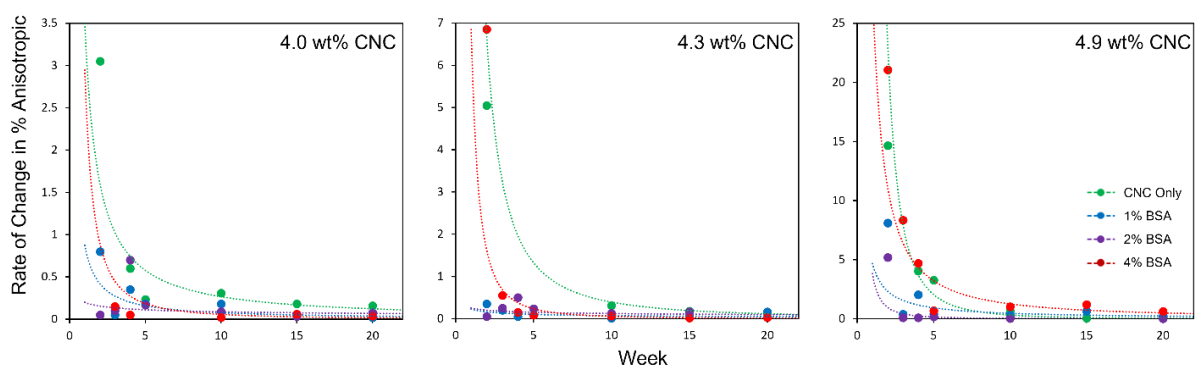


Figure S8. Percent change over time in the anisotropic volume fraction of aqueous CNC suspensions (4.0, 4.3, and 4.9 wt% CNC) containing varying amounts of BSA amyloid fibers. Lines are Power-law fits generated via Excel (to be used as guides for the eye).

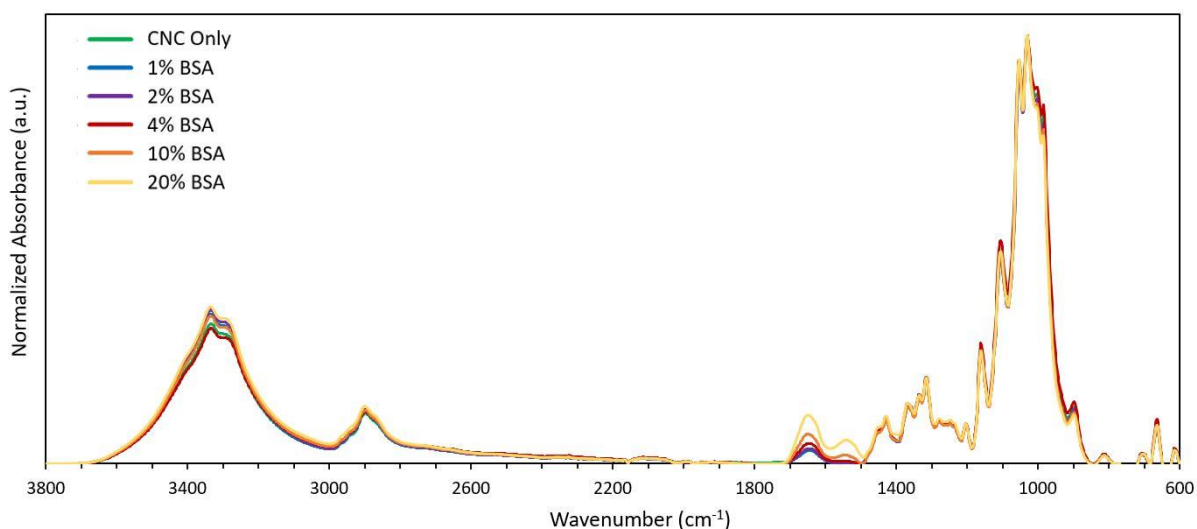


Figure S9. Baseline-corrected, normalized FTIR spectra for self-assembled CNC films containing varying amounts of BSA amyloids.

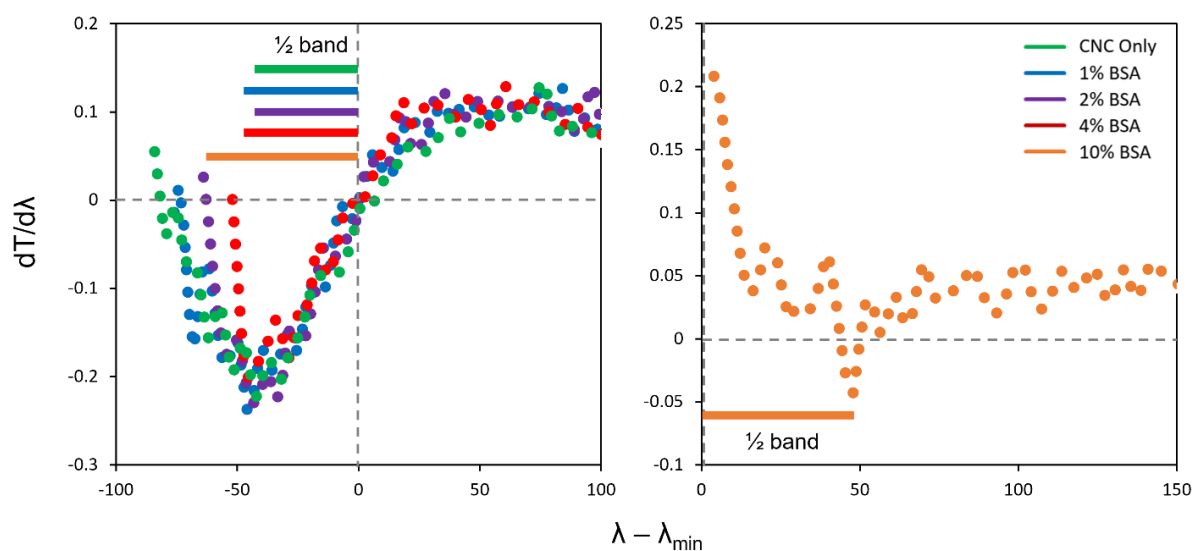


Figure S10. Analysis of the minimum peak reflectance wavelength via UV-vis for self-assembled CNC films containing BSA amyloids, showing the derivative around this minimum peak reflectance wavelength. The “half-bandwidth” ($\frac{1}{2}$ band), giving a measure between the peak reflection wavelength and closest half-maxima, is also indicated.

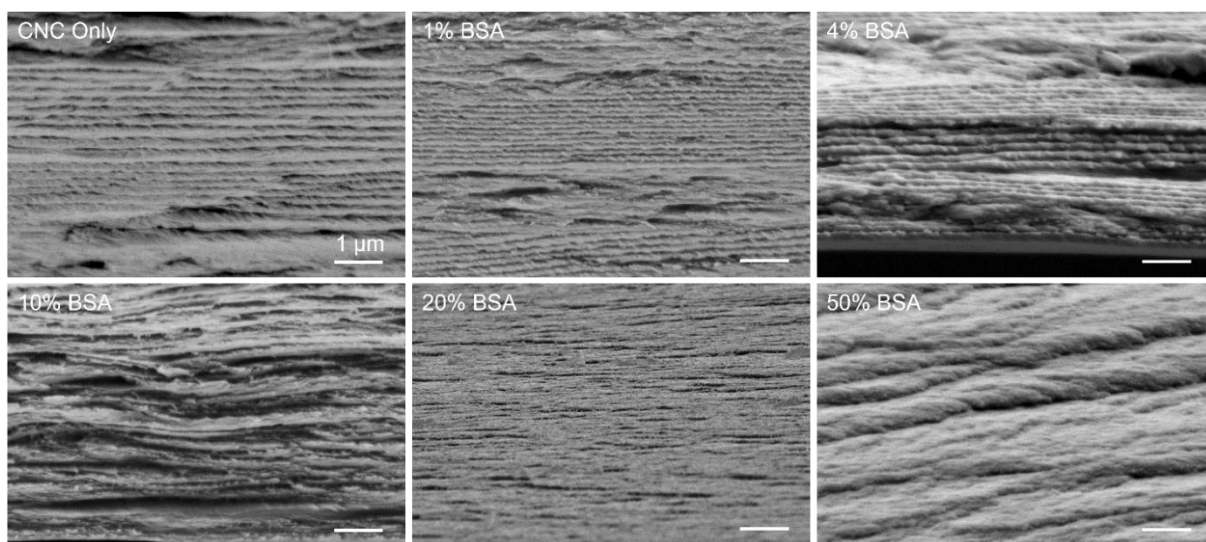


Figure S11. Cross-sectional SEM images of self-assembled CNC films containing BSA amyloids. All scale bars are 1 μm .

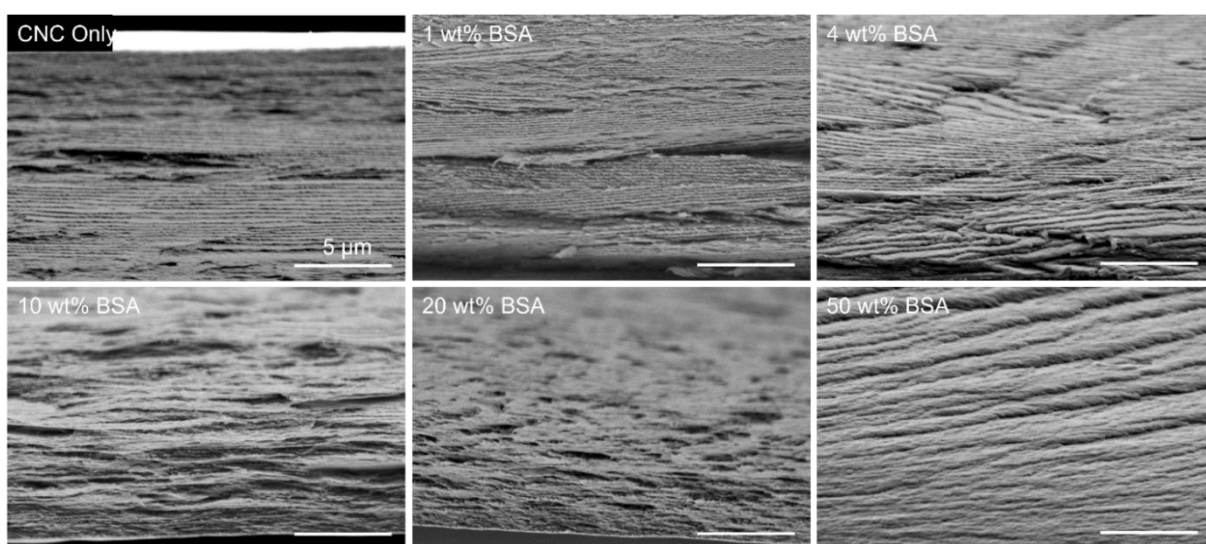


Figure S12. Lower magnification cross-sectional SEM images of self-assembled CNC films containing BSA amyloids. All scale bars are 5 μm .

Table S2. Ultimate lap shear load and load per adesive mass for CNC – BSA amyloid composite assemblies with varying BSA amyloid content. Data shows the average \pm standard deviation for between 8 and 12 samples per condition.

Sample	Ultimate Lap Shear Load (N)	Load per Adhesive Mass (N/mg)
CNC Only	267 \pm 63	417 \pm 99
4% BSA	336 \pm 114	525 \pm 177
10% BSA	316 \pm 94	493 \pm 147
20% BSA	312 \pm 93	488 \pm 145
50% BSA	163 \pm 65	255 \pm 102
100% BSA	112 \pm 59	175 \pm 92

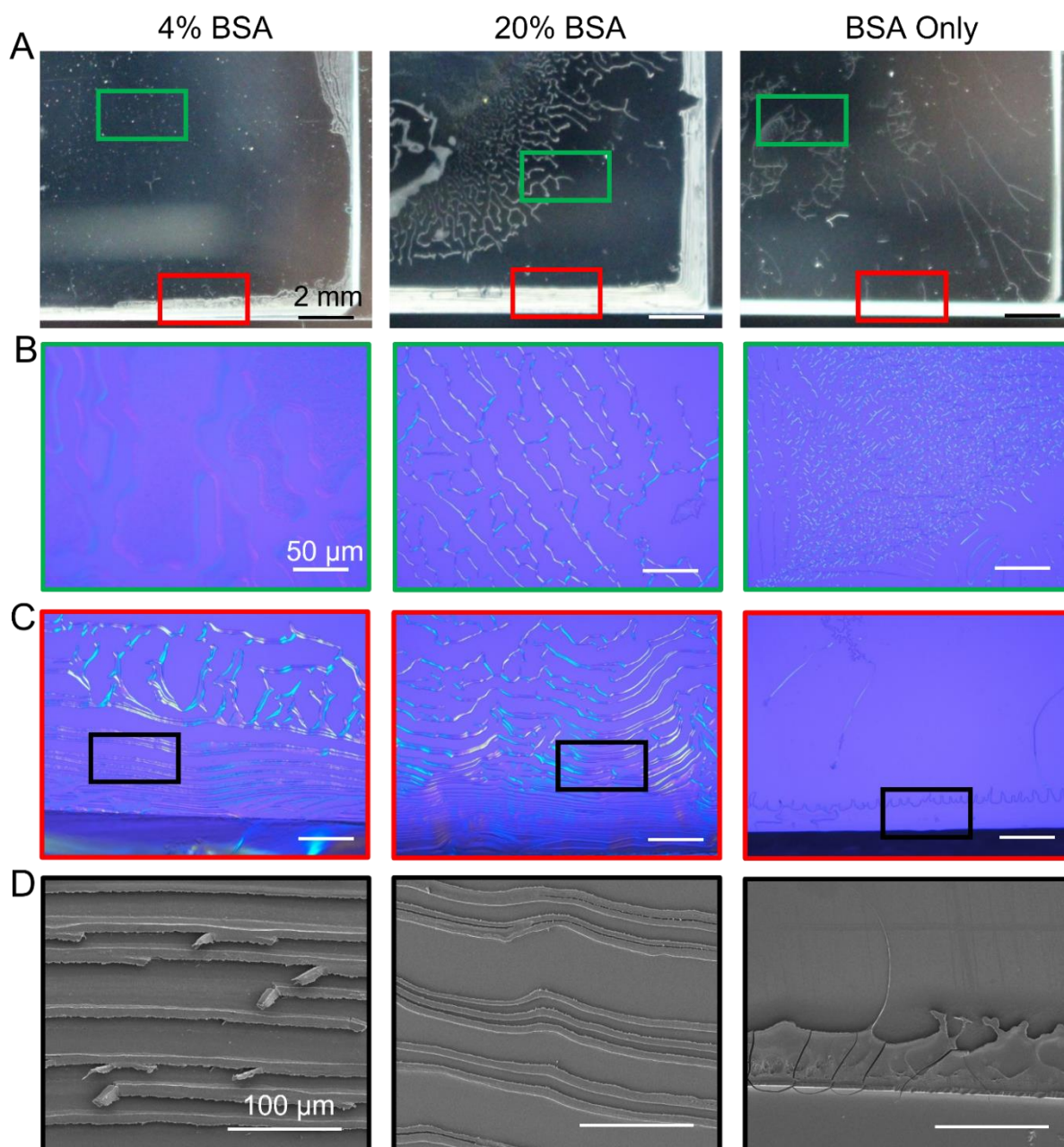


Figure S13. Structural morphology of CNC – BSA amyloid lap adhesives formed via c-EISA. (A) Optical images of the formed laps between glass slides, (B) polarized optical microscopy images of representative areas in the middle, and (C) near the edges of the laps, and (D) SEM images of representative areas near the edges of the laps. All scale bars in (A) are 2 mm, in (B) and (C) are 50 μm , and in (D) are 100 μm .

Table S3. Mass-normalized ultimate lap shear load and areal density for a variety of bio-based structural adhesives from this work and from the recent literature.

	Sample	Normalized Ultimate Lap Shear Load (N/mg)	Areal density (mg/cm ²)	Reference
Proteins	BSA (Native)	749 ± 184	1.14	Roberts et al. ¹
	BSA (Native)	895 ± 7	0.57	Roberts et al. ¹
	BSA (Native)	1026 ± 425	0.19	Roberts et al. ¹
	BSA (Native)	1380 ± 200	0.20	Luotonen et al. ²
	BSA (Amyloid)	175 ± 92	0.09	This work
	Lysozyme (Native)	136 ± 110	0.44	Luotonen et al. ²
	Lysozyme (Native)	333 ± 135	0.13	Greca et al. ³
	Lysozyme (Amyloid)	123 ± 35	0.13	Greca et al. ³
	Spider Silk (pH 8)	552 ± 103	1.14	Roberts et al. ¹
	Spider Silk (pH 5.5)	317 ± 108	1.14	Roberts et al. ¹
	Polysaccharides	Chitin Nanocrystals	361 ± 84	0.13
CNC		131 ± 23	1.66	Tardy et al. ⁴
CNC		270 ± 55	0.83	Tardy et al. ⁴
CNC		245 ± 90	0.41	Tardy et al. ⁴
CNC		375 ± 193	0.18	Tardy et al. ⁴
CNC		218 ± 44	0.88	Luotonen et al. ²
CNC		277 ± 56	0.44	Luotonen et al. ²
CNC		590 ± 85	0.20	Luotonen et al. ²
CNC		417 ± 99	0.09	This work
CNF		675 ± 180	0.16	Luotonen et al. ²
TOCNF		25 ± 10	0.16	Luotonen et al. ²
HPC		773 ± 98	0.44	Luotonen et al. ²

	CMC	331 ± 149	0.44	Luotonen et al. ²
	Lignin Nanoparticles	81 ± 27	0.15	Beisl et al. ⁵
Hybrids with CNC	10% HPC	450 ± 24	0.44	Luotonen et al. ²
	10% CMC	391 ± 29	0.44	Luotonen et al. ²
	10% CNF	273 ± 38	0.44	Luotonen et al. ²
	10% TOCNF	282 ± 43	0.44	Luotonen et al. ²
	10% Lysozyme (Native)	359 ± 40	0.44	Luotonen et al. ²
	10% Lysozyme (Native)**	333 ± 75	0.13	Greca et al. ³
	10% Lysozyme (Amyloid)**	441 ± 98	0.13	Greca et al. ³
	10% BSA (Native)	630 ± 61	0.20	Luotonen et al. ²
	10% BSA (Amyloid)	493 ± 147	0.09	This work

** Hybrid is with Chitin Nanocrystals, not CNC

CNF = cellulose nanofibers, TOCNF = tempo-oxidized CNF, HPC = hydroxypropyl cellulose, CMC = carboxymethyl cellulose

Bibliography

- [1] G. Whitesides, B. Grzybowski, Self-Assembly at All Scales, *Science*. 295 (2002) 2418–2421. <https://doi.org/https://doi.org/10.1126/science.1070821>.
- [2] G.M. Whitesides, M. Boncheva, Beyond molecules: Self-assembly of mesoscopic and macroscopic components, *Proc. Natl. Acad. Sci.* 99 (2002) 4769–4774. <https://doi.org/10.1073/pnas.082065899>.
- [3] D.J. Kushner, Self-assembly of biological structures., *Bacteriol. Rev.* 33 (1969) 302–345. <https://doi.org/10.1128/membr.33.2.302-345.1969>.
- [4] P.A. Monnard, D.W. Deamer, Membrane self-assembly processes: Steps toward the first cellular life, *Anat. Rec.* 268 (2002) 196–207. <https://doi.org/10.1002/ar.10154>.
- [5] C.M. Dobson, Protein folding and misfolding, *Nature*. 426 (2003) 884–890. <https://doi.org/doi:10.1038/nature02261>.
- [6] P.C. Ke, R. Zhou, L.C. Serpell, R. Riek, T.P.J. Knowles, H.A. Lashuel, E. Gazit, I.W. Hamley, T.P. Davis, M. Fändrich, D.E. Otzen, M.R. Chapman, C.M. Dobson, D.S. Eisenberg, R. Mezzenga, Half a century of amyloids: Past, present and future, *Chem. Soc. Rev.* 49 (2020) 5473–5509. <https://doi.org/10.1039/c9cs00199a>.
- [7] T.P.J. Knowles, M. Vendruscolo, C.M. Dobson, The amyloid state and its association with protein misfolding diseases, *Nat. Rev. Mol. Cell Biol.* 15 (2014) 384–396. <https://doi.org/10.1038/nrm3810>.
- [8] D.S. Eisenberg, M.R. Sawaya, Structural Studies of Amyloid Proteins at the Molecular Level, *Annu. Rev. Biochem.* 86 (2017) 69–95. <https://doi.org/10.1146/annurev-biochem-061516-045104>.
- [9] T.P.J. Knowles, R. Mezzenga, Amyloid Fibrils as Building Blocks for Natural and Artificial Functional Materials, *Adv. Mater.* 28 (2016) 6546–6561. <https://doi.org/10.1002/adma.201505961>.
- [10] L.M.C. Sagis, C. Veerman, E. Van Der Linden, Mesoscopic properties of semiflexible amyloid fibrils, *Langmuir*. 20 (2004) 924–927. <https://doi.org/10.1021/la035390s>.
- [11] Y. Cao, R. Mezzenga, Food protein amyloid fibrils: Origin, structure, formation, characterization, applications and health implications, *Adv. Colloid Interface Sci.* 269 (2019) 334–356. <https://doi.org/10.1016/j.cis.2019.05.002>.
- [12] S.M. Loveday, S.G. Anema, H. Singh, β -Lactoglobulin nanofibrils: The long and the short of it, *Int. Dairy J.* 67 (2017) 35–45. <https://doi.org/10.1016/j.idairyj.2016.09.011>.
- [13] T. Li, J. Zhou, M. Peydayesh, Y. Yao, M. Bagnani, I. Kutzli, Z. Chen, L. Wang, R. Mezzenga, Plant Protein Amyloid Fibrils for Multifunctional Sustainable Materials, *Adv. Sustain. Syst.* 7 (2023) 2200414. <https://doi.org/10.1002/adsu.202200414>.
- [14] S.M. Loveday, X.L. Wang, M.A. Rao, S.G. Anema, L.K. Creamer, H. Singh, Tuning the properties of β -lactoglobulin nanofibrils with pH, NaCl and CaCl₂, *Int. Dairy J.* 20 (2010) 571–579. <https://doi.org/10.1016/j.idairyj.2010.02.014>.
- [15] J. Adamcik, R. Mezzenga, Amyloid Polymorphism in the Protein Folding and Aggregation Energy Landscape, *Angew. Chemie - Int. Ed.* 57 (2018) 8370–8382. <https://doi.org/10.1002/anie.201713416>.

- [16] S.I.A. Cohen, M. Vendruscolo, C.M. Dobson, T.P.J. Knowles, From macroscopic measurements to microscopic mechanisms of protein aggregation, *J. Mol. Biol.* 421 (2012) 160–171. <https://doi.org/10.1016/j.jmb.2012.02.031>.
- [17] P. Arosio, T.P.J. Knowles, S. Linse, On the lag phase in amyloid fibril formation, *Phys. Chem. Chem. Phys.* 17 (2015) 7606–7618. <https://doi.org/10.1039/c4cp05563b>.
- [18] M. Törnquist, T.C.T. Michaels, K. Sanagavarapu, X. Yang, G. Meisl, S.I.A. Cohen, T.P.J. Knowles, S. Linse, Secondary nucleation in amyloid formation, *Chem. Commun.* 54 (2018) 8667–8684. <https://doi.org/10.1039/c8cc02204f>.
- [19] T.P.J. Knowles, C.A. Waudby, G.L. Devlin, S.I.A. Cohen, A. Aguzzi, M. Vendruscolo, E.M. Terentjev, M.E. Welland, C.M. Dobson, An Analytical Solution to the Kinetics of Breakable Filament Assembly, *Science*. 326 (2009) 1533–1537. <https://doi.org/https://doi.org/10.1126/science.1178250>.
- [20] P. Azzari, R. Mezzenga, Liquid-liquid crystalline phase separation of evolving amyloid fibrils, *Phys. Rev. Res.* 5 (2023) 13137. <https://doi.org/10.1103/PhysRevResearch.5.013137>.
- [21] C.C. VandenAkker, M.F.M. Engel, K.P. Velikov, M. Bonn, G.H. Koenderink, Morphology and persistence length of amyloid fibrils are correlated to peptide molecular structure, *J. Am. Chem. Soc.* 133 (2011) 18030–18033. <https://doi.org/10.1021/ja206513r>.
- [22] X. Ye, M.S. Hedenqvist, M. Langton, C. Lendel, On the role of peptide hydrolysis for fibrillation kinetics and amyloid fibril morphology, *RSC Adv.* 8 (2018) 6915–6924. <https://doi.org/10.1039/c7ra10981d>.
- [23] M.B. Pepys, P.N. Hawkins, D.R. Booth, D.M. Vigushin, G.A. Tennent, A.K. Soutar, N. Totty, O. Nguyen, C.C.F. Blake, C.J. Terry, T.G. Feest, A.M. Zalin, J.J. Hsuan, Human lysozyme gene mutations cause hereditary systemic amyloidosis, *Nature*. 362 (1993) 553–557. <https://doi.org/10.1038/362553a0>.
- [24] L.N. Arnaudov, R. De Vries, Thermally induced fibrillar aggregation of hen egg white lysozyme, *Biophys. J.* 88 (2005) 515–526. <https://doi.org/10.1529/biophysj.104.048819>.
- [25] E. Frare, P. Poverino De Laureto, J. Zurdo, C.M. Dobson, A. Fontana, A highly amyloidogenic region of hen lysozyme, *J. Mol. Biol.* 340 (2004) 1153–1165. <https://doi.org/10.1016/j.jmb.2004.05.056>.
- [26] M.R.H. Krebs, D.K. Wilkins, E.W. Chung, M.C. Pitkeathly, A.K. Chamberlain, J. Zurdo, C. V. Robinson, C.M. Dobson, Formation and seeding of amyloid fibrils from wild-type hen lysozyme and a peptide fragment from the β -domain, *J. Mol. Biol.* 300 (2000) 541–549. <https://doi.org/10.1006/jmbi.2000.3862>.
- [27] C. Lara, J. Adamcik, S. Jordens, R. Mezzenga, General self-assembly mechanism converting hydrolyzed globular proteins into giant multistranded amyloid ribbons, *Biomacromolecules*. 12 (2011) 1868–1875. <https://doi.org/10.1021/bm200216u>.
- [28] J. Adamcik, J.M. Jung, J. Flakowski, P. De Los Rios, G. Dietler, R. Mezzenga, Understanding amyloid aggregation by statistical analysis of atomic force microscopy images, *Nat. Nanotechnol.* 5 (2010) 423–428. <https://doi.org/10.1038/nnano.2010.59>.
- [29] J. Adamcik, R. Mezzenga, Adjustable twisting periodic pitch of amyloid fibrils, *Soft Matter*. 7 (2011) 5437–5443. <https://doi.org/10.1039/c1sm05382e>.

- [30] C. Lara, S. Handschin, R. Mezzenga, Towards lysozyme nanotube and 3D hybrid self-assembly, *Nanoscale*. 5 (2013) 7197–7201. <https://doi.org/10.1039/c3nr02194g>.
- [31] N.P. Reynolds, M. Charnley, R. Mezzenga, P.G. Hartley, Engineered lysozyme amyloid fibril networks support cellular growth and spreading, *Biomacromolecules*. 15 (2014) 599–608. <https://doi.org/10.1021/bm401646x>.
- [32] B. Hu, Y. Shen, J. Adamcik, P. Fischer, M. Schneider, M.J. Loessner, R. Mezzenga, Polyphenol-Binding Amyloid Fibrils Self-Assemble into Reversible Hydrogels with Antibacterial Activity, *ACS Nano*. 12 (2018) 3385–3396. <https://doi.org/10.1021/acsnano.7b08969>.
- [33] Y. Chen, Q. Liu, F. Yang, H. Yu, Y. Xie, W. Yao, Lysozyme amyloid fibril: Regulation, application, hazard analysis, and future perspectives, *Int. J. Biol. Macromol.* 200 (2022) 151–161. <https://doi.org/10.1016/j.ijbiomac.2021.12.163>.
- [34] P. Yang, Direct Biomolecule Binding on Nonfouling Surfaces via Newly Discovered Supramolecular Self-Assembly of Lysozyme under Physiological Conditions, *Macromol. Biosci.* 12 (2012) 1053–1059. <https://doi.org/10.1002/mabi.201200092>.
- [35] C. Li, R. Qin, R. Liu, S. Miao, P. Yang, Functional amyloid materials at surfaces/interfaces, *Biomater. Sci.* 6 (2018) 462–472. <https://doi.org/10.1039/c7bm01124e>.
- [36] D. Wang, Y. Ha, J. Gu, Q. Li, L. Zhang, P. Yang, Nanofilms: 2D Protein Supramolecular Nanofilm with Exceptionally Large Area and Emergent Functions, *Adv. Mater.* 28 (2016) 7414–7423. <https://doi.org/10.1002/adma.201670239>.
- [37] J. Gu, Y. Su, P. Liu, P. Li, P. Yang, An Environmentally Benign Antimicrobial Coating Based on a Protein Supramolecular Assembly, *ACS Appl. Mater. Interfaces*. 9 (2017) 198–210. <https://doi.org/10.1021/acsmi.6b13552>.
- [38] J. Zhao, Y. Qu, H. Chen, R. Xu, Q. Yu, P. Yang, Self-assembled proteinaceous wound dressings attenuate secondary trauma and improve wound healing in vivo, *J. Mater. Chem. B*. 6 (2018) 4645–4655. <https://doi.org/10.1039/c8tb01100a>.
- [39] Y. Qu, T. Wei, J. Zhao, S. Jiang, P. Yang, Q. Yu, H. Chen, Regenerable smart antibacterial surfaces: Full removal of killed bacteria: Via a sequential degradable layer, *J. Mater. Chem. B*. 6 (2018) 3946–3955. <https://doi.org/10.1039/c8tb01122b>.
- [40] P. Laschtschenko, Über die keimtötende und entwicklungshemmende Wirkung von Hühnereiweiß, *Zeitschrift Für Hyg. Und Infekt.* 64 (1909) 419–427. <https://doi.org/10.1007/BF02216170>.
- [41] A. Fleming, On a Remarkable Bacteriolytic Element found, *Proc. R. Soc. B*. 93 (1922) 306–317.
- [42] C. Blake, D. Koenig, G. Mair, A. North, D. Phillips, V. Sarma, The three-dimensional structure of hen eggwhite lysozyme, *Nature*. 206 (1965) 757–761.
- [43] C.M. Dobson, P.A. Evans, S.E. Radford, Understanding how proteins fold: the lysozyme story so far, *Trends Biochem. Sci.* 19 (1994) 31–37. [https://doi.org/10.1016/0968-0004\(94\)90171-6](https://doi.org/10.1016/0968-0004(94)90171-6).
- [44] S.A. Ragland, A.K. Criss, From bacterial killing to immune modulation: Recent insights into the functions of lysozyme, *PLoS Pathog.* 13 (2017) e1006512. <https://doi.org/10.1371/journal.ppat.1006512>.

- [45] J.A. Rupley, The binding and cleavage by lysozyme of N-acetylglucosamine oligosaccharides., *Proc. R. Soc. London. Ser. B. Biol. Sci.* 167 (1967) 416–428. <https://doi.org/10.1098/rspb.1967.0038>.
- [46] D.J. Vocadlo, G.J. Davies, R. Laine, S.G. Withers, Catalysis by hen egg-white lysozyme proceeds via a covalent intermediate, *Nature*. 412 (2001) 835–838. <https://doi.org/10.1038/35090602>.
- [47] H.R. Ibrahim, S. Higashiguchi, L.R. Juneja, M. Kim, T. Yamamoto, A structural phase of heat-denatured lysozyme with novel antimicrobial action, *J. Agric. Food Chem.* 44 (1996) 1416–1423. <https://doi.org/10.1021/jf9507147>.
- [48] K. Düring, P. Porsch, A. Mahn, O. Brinkmann, W. Gieffers, The non-enzymatic microbicidal activity of lysozymes, *FEBS Lett.* 449 (1999) 93–100. [https://doi.org/10.1016/S0014-5793\(99\)00405-6](https://doi.org/10.1016/S0014-5793(99)00405-6).
- [49] H.R. Ibrahim, T. Matsuzaki, T. Aoki, Genetic evidence that antibacterial activity of lysozyme is independent of its catalytic function, *FEBS Lett.* 506 (2001) 27–32. [https://doi.org/10.1016/S0014-5793\(01\)02872-1](https://doi.org/10.1016/S0014-5793(01)02872-1).
- [50] R. Vilcacundo, P. Méndez, W. Reyes, H. Romero, A. Pinto, W. Carrillo, Antibacterial activity of hen egg white lysozyme denatured by thermal and chemical treatments, *Sci. Pharm.* 86 (2018) 48. <https://doi.org/10.3390/scipharm86040048>.
- [51] R. Cegielska-Radziejewska, G. Lesnierowski, J. Kijowski, Antibacterial activity of hen egg white lysozyme modified by thermochemical technique, *Eur. Food Res. Technol.* 228 (2009) 841–845. <https://doi.org/10.1007/s00217-008-0997-5>.
- [52] H.K. Kang, C. Kim, C.H. Seo, Y. Park, The therapeutic applications of antimicrobial peptides (AMPs): a patent review, *J. Microbiol.* 55 (2017) 1–12. <https://doi.org/10.1007/s12275-017-6452-1>.
- [53] H.B. Koo, J. Seo, Antimicrobial peptides under clinical investigation, *Pept. Sci.* 111 (2019) e24122. <https://doi.org/10.1002/pep2.24122>.
- [54] Y. Yang, Z. Cai, Z. Huang, X. Tang, X. Zhang, Antimicrobial cationic polymers: From structural design to functional control, *Polym. J.* 50 (2018) 33–44. <https://doi.org/10.1038/pj.2017.72>.
- [55] Z. Bouaziz, L. Soussan, J.M. Janot, M. Lepoitevin, M. Bechelany, M.A. Djebbi, A.B.H. Amara, S. Balme, Structure and antibacterial activity relationships of native and amyloid fibril lysozyme loaded on layered double hydroxide, *Colloids Surfaces B Biointerfaces.* 157 (2017) 10–17. <https://doi.org/10.1016/j.colsurfb.2017.05.050>.
- [56] N.H.C.S. Silva, C. Vilela, A. Almeida, I.M. Marrucho, C.S.R. Freire, Pullulan-based nanocomposite films for functional food packaging: Exploiting lysozyme nanofibers as antibacterial and antioxidant reinforcing additives, *Food Hydrocoll.* 77 (2018) 921–930. <https://doi.org/10.1016/j.foodhyd.2017.11.039>.
- [57] N.H.C.S. Silva, P. Garrido-Pascual, C. Moreirinha, A. Almeida, T. Palomares, A. Alonso-Varona, C. Vilela, C.S.R. Freire, Multifunctional nanofibrous patches composed of nanocellulose and lysozyme nanofibers for cutaneous wound healing, *Int. J. Biol. Macromol.* 165 (2020) 1198–1210. <https://doi.org/10.1016/j.ijbiomac.2020.09.249>.
- [58] Z. Wei, S. Wu, J. Xia, P. Shao, P. Sun, N. Xiang, Enhanced Antibacterial Activity of Hen Egg-White Lysozyme against *Staphylococcus aureus* and *Escherichia coli* due to Protein Fibrillation, *Biomacromolecules.* 22 (2021) 890–

897. <https://doi.org/10.1021/acs.biomac.0c01599>.
- [59] T. Chen, Y. Wang, J. Xie, X. Qu, C. Liu, Lysozyme Amyloid Fibril-Integrated PEG Injectable Hydrogel Adhesive with Improved Antiswelling and Antibacterial Capabilities, *Biomacromolecules*. 23 (2022) 1376–1391. <https://doi.org/10.1021/acs.biomac.1c01597>.
- [60] N. Zhang, Z. Deng, Q. Wang, M. Zhou, P. Wang, Y. Yu, Phase-transited lysozyme with secondary reactivity for moisture-permeable antibacterial wool fabric, *Chem. Eng. J.* 432 (2022) 134198. <https://doi.org/10.1016/j.cej.2021.134198>.
- [61] J. Chen, M. Xu, L. Wang, T. Li, Z. Li, T. Wang, P. Li, Converting lysozyme to hydrogel: A multifunctional wound dressing that is more than antibacterial, *Colloids Surfaces B Biointerfaces*. 219 (2022) 112854. <https://doi.org/10.1016/j.colsurfb.2022.112854>.
- [62] E. Dickinson, Adsorbed protein layers at fluid interfaces: Interactions, structure and surface rheology, *Colloids Surfaces B Biointerfaces*. 15 (1999) 161–176. [https://doi.org/10.1016/S0927-7765\(99\)00042-9](https://doi.org/10.1016/S0927-7765(99)00042-9).
- [63] R. Mezzenga, P. Fischer, The self-assembly, aggregation and phase transitions of food protein systems in one, two and three dimensions, *Reports Prog. Phys.* 76 (2013) 046601. <https://doi.org/10.1088/0034-4885/76/4/046601>.
- [64] J. Bergfreund, M. Diener, T. Geue, N. Nussbaum, N. Kummer, P. Bertsch, G. Nyström, P. Fischer, Globular protein assembly and network formation at fluid interfaces: effect of oil, *Soft Matter*. 17 (2021) 1692–1700. <https://doi.org/10.1039/d0sm01870h>.
- [65] R.M. Murphy, Kinetics of amyloid formation and membrane interaction with amyloidogenic proteins, *Biochim. Biophys. Acta - Biomembr.* 1768 (2007) 1923–1934. <https://doi.org/10.1016/j.bbamem.2006.12.014>.
- [66] F. Grigolato, P. Arosio, The role of surfaces on amyloid formation, *Biophys. Chem.* 270 (2021) 106533. <https://doi.org/10.1016/j.bpc.2020.106533>.
- [67] J. Pronchik, X. He, J.T. Giurleo, D.S. Talaga, In vitro formation of amyloid from α -synuclein is dominated by reactions at hydrophobic interfaces, *J. Am. Chem. Soc.* 132 (2010) 9797–9803. <https://doi.org/10.1021/ja102896h>.
- [68] L. Jean, C.F. Lee, C. Lee, M. Shaw, D.J. Vaux, Competing discrete interfacial effects are critical for amyloidogenesis, *FASEB J.* 24 (2010) 309–317. <https://doi.org/10.1096/fj.09-137653>.
- [69] X. Han, X. Wu, L. Lv, C. Li, Inhibiting and catalysing amyloid fibrillation at dynamic lipid interfaces, *J. Colloid Interface Sci.* 543 (2019) 256–262. <https://doi.org/10.1016/j.jcis.2019.02.072>.
- [70] C. Schladitz, E.P. Vieira, H. Hermel, H. Möhwald, Amyloid- β -sheet formation at the air-water interface, *Biophys. J.* 77 (1999) 3305–3310. [https://doi.org/10.1016/S0006-3495\(99\)77161-4](https://doi.org/10.1016/S0006-3495(99)77161-4).
- [71] S. Campioni, G. Carret, S. Jordens, L. Nicoud, R. Mezzenga, R. Riek, The presence of an air-water interface affects formation and elongation of α -synuclein fibrils, *J. Am. Chem. Soc.* 136 (2014) 2866–2875. <https://doi.org/10.1021/ja412105t>.
- [72] S. Campioni, M. Bagnani, D. Pinotsi, S. Lecinski, S. Rodighiero, J. Adamcik, R. Mezzenga, Interfaces Determine the Fate of Seeded α -Synuclein Aggregation, *Adv. Mater. Interfaces*. 7 (2020) 200446. <https://doi.org/10.1002/admi.202000446>.

- [73] L. Isa, J.M. Jung, R. Mezzenga, Unravelling adsorption and alignment of amyloid fibrils at interfaces by probe particle tracking, *Soft Matter*. 7 (2011) 8127–8134. <https://doi.org/10.1039/c1sm05602f>.
- [74] S. Jordens, L. Isa, I. Usov, R. Mezzenga, Non-equilibrium nature of two-dimensional isotropic and nematic coexistence in amyloid fibrils at liquid interfaces, *Nat. Commun.* 4 (2013) 1917. <https://doi.org/10.1038/ncomms2911>.
- [75] S. Jordens, P.A. Rühls, C. Sieber, L. Isa, P. Fischer, R. Mezzenga, Bridging the gap between the nanostructural organization and macroscopic interfacial rheology of amyloid fibrils at liquid interfaces, *Langmuir*. 30 (2014) 10090–10097. <https://doi.org/10.1021/la5020658>.
- [76] Z. Wan, X. Yang, L.M.C. Sagis, Contribution of Long Fibrils and Peptides to Surface and Foaming Behavior of Soy Protein Fibril System, *Langmuir*. 32 (2016) 8092–8101. <https://doi.org/10.1021/acs.langmuir.6b01511>.
- [77] R.J. Moon, A. Martini, J. Nairn, J. Simonsen, J. Youngblood, Cellulose nanomaterials review: Structure, properties and nanocomposites, *Chem. Soc. Rev.* 40 (2011) 3941–3994. <https://doi.org/10.1039/c0cs00108b>.
- [78] T. Abitbol, A. Rivkin, Y. Cao, Y. Nevo, E. Abraham, T. Ben-Shalom, S. Lapidot, O. Shoseyov, Nanocellulose, a tiny fiber with huge applications, *Curr. Opin. Biotechnol.* 39 (2016) 76–88. <https://doi.org/10.1016/j.copbio.2016.01.002>.
- [79] E. Kontturi, P. Laaksonen, M.B. Linder, Nonappa, A.H. Gröschel, O.J. Rojas, O. Ikkala, Advanced Materials through Assembly of Nanocelluloses, *Adv. Mater.* 30 (2018) 1703779. <https://doi.org/10.1002/adma.201703779>.
- [80] T. Benselfelt, N. Kummer, M. Nordenström, A.B. Fall, G. Nyström, L. Wågberg, The Colloidal Properties of Nanocellulose, *ChemSusChem*. 16 (2023) e202201955. <https://doi.org/10.1002/cssc.202201955>.
- [81] S. Beck-Candanedo, M. Roman, D.G. Gray, Effect of reaction conditions on the properties and behavior of wood cellulose nanocrystal suspensions, *Biomacromolecules*. 6 (2005) 1048–1054. <https://doi.org/10.1021/bm049300p>.
- [82] T. Saito, S. Kimura, Y. Nishiyama, A. Isogai, Cellulose nanofibers prepared by TEMPO-mediated oxidation of native cellulose, *Biomacromolecules*. 8 (2007) 2485–2491. <https://doi.org/10.1021/bm0703970>.
- [83] L. Wågberg, L. Winter, L. Ödberg, T. Lindström, On the charge stoichiometry upon adsorption of a cationic polyelectrolyte on cellulosic materials, *Colloids and Surfaces*. 27 (1987) 163–173. [https://doi.org/10.1016/0166-6622\(87\)80335-9](https://doi.org/10.1016/0166-6622(87)80335-9).
- [84] Y. Habibi, Key advances in the chemical modification of nanocelluloses, *Chem. Soc. Rev.* 43 (2014) 1519–1542. <https://doi.org/10.1039/c3cs60204d>.
- [85] H. Sehaqui, U. Perez De Larraya, P. Tingaut, T. Zimmermann, Humic acid adsorption onto cationic cellulose nanofibers for bioinspired removal of copper(ii) and a positively charged dye, *Soft Matter*. 11 (2015) 5294–5300. <https://doi.org/10.1039/c5sm00566c>.
- [86] S. Eyley, W. Thielemans, Surface modification of cellulose nanocrystals, *Nanoscale*. 6 (2014) 7764–7779. <https://doi.org/10.1039/c4nr01756k>.
- [87] J.N. Israelachvili, *Intermolecular and Surface Forces* (3rd Edition), Academic Press, 2011.
- [88] H.C. Hamaker, The London-van der Waals attraction between spherical particles, *Physica*. 4 (1937) 1058–1072. [https://doi.org/10.1016/S0031-8914\(37\)80203-7](https://doi.org/10.1016/S0031-8914(37)80203-7).

- [89] A.M. Smith, M. Borkovec, G. Trefalt, Forces between solid surfaces in aqueous electrolyte solutions, *Adv. Colloid Interface Sci.* 275 (2020) 102078. <https://doi.org/10.1016/j.cis.2019.102078>.
- [90] M. Nordenström, A. Fall, G. Nyström, L. Wågberg, Formation of Colloidal Nanocellulose Glasses and Gels, *Langmuir.* 33 (2017) 9772–9780. <https://doi.org/10.1021/acs.langmuir.7b01832>.
- [91] R.M. Parker, G. Guidetti, C.A. Williams, T. Zhao, A. Narkevicius, S. Vignolini, B. Frka-Petescic, The Self-Assembly of Cellulose Nanocrystals: Hierarchical Design of Visual Appearance, *Adv. Mater.* 30 (2018) 1704477. <https://doi.org/10.1002/adma.201704477>.
- [92] A.B. Fall, S.B. Lindström, O. Sundman, L. Ödberg, L. Wågberg, Colloidal stability of aqueous nanofibrillated cellulose dispersions, *Langmuir.* 27 (2011) 11332–11338. <https://doi.org/10.1021/la201947x>.
- [93] L. Geng, N. Mittal, C. Zhan, F. Ansari, P.R. Sharma, X. Peng, B.S. Hsiao, L.D. Söderberg, Understanding the Mechanistic Behavior of Highly Charged Cellulose Nanofibers in Aqueous Systems, *Macromolecules.* 51 (2018) 1498–1506. <https://doi.org/10.1021/acs.macromol.7b02642>.
- [94] R.J. Kerekes, C.J. Schell, Characterization of fibre flocculation regimes by a crowding factor, *J. Pulp Pap. Sci.* 18 (1992) 32–38.
- [95] Q. Ying, B. Chu, Overlap Concentration of Macromolecules in Solution, *Macromolecules.* 20 (1987) 362–366. <https://doi.org/10.1021/ma00168a023>.
- [96] A. Celzard, V. Fierro, R. Kerekes, Flocculation of cellulose fibres: New comparison of crowding factor with percolation and effective-medium theories, *Cellulose.* 16 (2009) 983–987. <https://doi.org/10.1007/s10570-009-9314-0>.
- [97] H. Tanaka, J. Meunier, D. Bonn, Nonergodic states of charged colloidal suspensions: Repulsive and attractive glasses and gels, *Phys. Rev. E.* 69 (2004) 031404. <https://doi.org/10.1103/PhysRevE.69.031404>.
- [98] G. Nyström, R. Mezzenga, Liquid crystalline filamentous biological colloids: Analogies and differences, *Curr. Opin. Colloid Interface Sci.* 38 (2018) 30–44. <https://doi.org/10.1016/j.cocis.2018.08.004>.
- [99] L. Onsager, The Effects of Shape on the Interaction of Colloidal Particles, *Ann. N. Y. Acad. Sci.* 51 (1949) 627–659. <https://doi.org/10.1111/j.1749-6632.1949.tb27296.x>.
- [100] A. Stroobants, H.N.W. Lekkerkerker, T. Odjik, Effect of electrostatic interaction on the liquid crystal phase transition in solutions of rodlike polyelectrolytes, *Macromolecules.* 19 (1986) 2232–2238. <https://doi.org/https://doi.org/10.1021/ma00162a020>.
- [101] J.M. Jung, R. Mezzenga, Liquid crystalline phase behavior of protein fibers in water: Experiments versus theory, *Langmuir.* 26 (2010) 504–514. <https://doi.org/10.1021/la9021432>.
- [102] I. Usov, G. Nyström, J. Adamcik, S. Handschin, C. Schütz, A. Fall, L. Bergström, R. Mezzenga, Understanding nanocellulose chirality and structure-properties relationship at the single fibril level, *Nat. Commun.* 6 (2015) 7564. <https://doi.org/10.1038/ncomms8564>.
- [103] G. Nyström, M. Arcari, J. Adamcik, I. Usov, R. Mezzenga, Nanocellulose Fragmentation Mechanisms and Inversion of Chirality from the Single Particle to the Cholesteric Phase, *ACS Nano.* 12 (2018) 5141–5148. <https://doi.org/10.1021/acsnano.8b00512>.

- [104] K.J. De France, N. Kummer, Q. Ren, S. Campioni, G. Nyström, Assembly of Cellulose Nanocrystal-Lysozyme Composite Films with Varied Lysozyme Morphology, *Biomacromolecules*. 21 (2020) 5139–5147. <https://doi.org/10.1021/acs.biomac.0c01267>.
- [105] K.J. De France, N. Kummer, S. Campioni, G. Nyström, Phase Behavior, Self-Assembly, and Adhesive Potential of Cellulose Nanocrystal-Bovine Serum Albumin Amyloid Composites, *ACS Appl. Mater. Interfaces*. 15 (2023) 1958–1968. <https://doi.org/10.1021/acsami.2c14406>.
- [106] T. Saito, R. Kuramae, J. Wohler, L.A. Berglund, A. Isogai, An ultrastrong nanofibrillar biomaterial: The strength of single cellulose nanofibrils revealed via sonication-induced fragmentation, *Biomacromolecules*. 14 (2013) 248–253. <https://doi.org/10.1021/bm301674e>.
- [107] E. Niinivaara, E.D. Cranston, Bottom-up assembly of nanocellulose structures, *Carbohydr. Polym.* 247 (2020) 116664. <https://doi.org/10.1016/j.carbpol.2020.116664>.
- [108] K.J. De France, T. Hoare, E.D. Cranston, Review of Hydrogels and Aerogels Containing Nanocellulose, *Chem. Mater.* 29 (2017) 4609–4631. <https://doi.org/10.1021/acs.chemmater.7b00531>.
- [109] S. Zhao, W.J. Malfait, N. Guerrero Albuquerque, M.M. Koebel, G. Nyström, Biopolymer Aerogels: Chemistry, Properties and Applications, *Angew. Chemie Int. Ed.* 57 (2018) 7580–7608. <https://doi.org/10.1002/anie.201709014>.
- [110] Z. Fang, G. Hou, C. Chen, L. Hu, Nanocellulose-based films and their emerging applications, *Curr. Opin. Solid State Mater. Sci.* 23 (2019) 100764. <https://doi.org/10.1016/j.cossms.2019.07.003>.
- [111] P. Bertsch, P. Fischer, Adsorption and interfacial structure of nanocelluloses at fluid interfaces, *Adv. Colloid Interface Sci.* 276 (2020) 102089. <https://doi.org/10.1016/j.cis.2019.102089>.
- [112] I. Capron, O.J. Rojas, R. Bordes, Behavior of nanocelluloses at interfaces, *Curr. Opin. Colloid Interface Sci.* 29 (2017) 83–95. <https://doi.org/10.1016/j.cocis.2017.04.001>.
- [113] S. Parajuli, E.E. Ureña-Benavides, Fundamental aspects of nanocellulose stabilized Pickering emulsions and foams, *Adv. Colloid Interface Sci.* 299 (2022) 102530. <https://doi.org/10.1016/j.cis.2021.102530>.
- [114] E. Buxbaum, *Fundamentals of Protein Structure and Function*, Springer, Cham, 2015. <https://doi.org/10.1007/978-3-319-19920-7>.
- [115] S.L. Turgeon, C. Schmitt, C. Sanchez, Protein-polysaccharide complexes and coacervates, *Curr. Opin. Colloid Interface Sci.* 12 (2007) 166–178. <https://doi.org/10.1016/j.cocis.2007.07.007>.
- [116] J. van der Gucht, E. Spruijt, M. Lemmers, M.A. Cohen Stuart, Polyelectrolyte complexes: Bulk phases and colloidal systems, *J. Colloid Interface Sci.* 361 (2011) 407–422. <https://doi.org/10.1016/j.jcis.2011.05.080>.
- [117] J. Gummel, F. Cousin, F. Boué, Counterions release from electrostatic complexes of polyelectrolytes and proteins of opposite charge: A direct measurement, *J. Am. Chem. Soc.* 129 (2007) 5806–5807. <https://doi.org/10.1021/ja070414t>.
- [118] S. Lombardo, W. Thielemans, Thermodynamics of adsorption on nanocellulose surfaces, *Cellulose*. 26 (2019) 249–279. <https://doi.org/10.1007/s10570-018-02239-2>.

- [119] R. Kolakovic, L. Peltonen, A. Laukkanen, M. Hellman, P. Laaksonen, M.B. Linder, J. Hirvonen, T. Laaksonen, Evaluation of drug interactions with nanofibrillar cellulose, *Eur. J. Pharm. Biopharm.* 85 (2013) 1238–1244. <https://doi.org/10.1016/j.ejpb.2013.05.015>.
- [120] S. Lombardo, S. Eyley, C. Schütz, H. Van Gorp, S. Rosenfeldt, G. Van Den Mooter, W. Thielemans, Thermodynamic Study of the Interaction of Bovine Serum Albumin and Amino Acids with Cellulose Nanocrystals, *Langmuir.* 33 (2017) 5473–5481. <https://doi.org/10.1021/acs.langmuir.7b00710>.
- [121] T. Wu, N. Kummer, K.J. De France, S. Campioni, Z. Zeng, G. Siqueira, J. Dong, G. Nyström, Nanocellulose-lysozyme colloidal gels via electrostatic complexation, *Carbohydr. Polym.* 251 (2021) 117021. <https://doi.org/10.1016/j.carbpol.2020.117021>.
- [122] J. Li, Y. Wang, L. Zhang, Z. Xu, H. Dai, W. Wu, Nanocellulose/Gelatin Composite Cryogels for Controlled Drug Release, *ACS Sustain. Chem. Eng.* 7 (2019) 6381–6389. <https://doi.org/10.1021/acssuschemeng.9b00161>.
- [123] P. Dorishetty, R. Balu, S.S. Athukoralalage, T.L. Greaves, J. Mata, L. De Campo, N. Saha, A.C.W. Zannettino, N.K. Dutta, N.R. Choudhury, Tunable Biomimetic Hydrogels from Silk Fibroin and Nanocellulose, *ACS Sustain. Chem. Eng.* 8 (2020) 2375–2389. <https://doi.org/10.1021/acssuschemeng.9b05317>.
- [124] K. Heise, E. Kontturi, Y. Allahverdiyeva, T. Tammelin, M.B. Linder, Nonappa, O. Ikkala, Nanocellulose: Recent Fundamental Advances and Emerging Biological and Biomimicking Applications, *Adv. Mater.* 33 (2021) 2004349. <https://doi.org/10.1002/adma.202004349>.
- [125] O.A. McCrate, X. Zhou, C. Reichhardt, L. Cegelski, Sum of the parts: Composition and architecture of the bacterial extracellular matrix, *J. Mol. Biol.* 425 (2013) 4286–4294. <https://doi.org/10.1016/j.jmb.2013.06.022>.
- [126] S. Wei, Y. Li, K. Li, C. Zhong, Biofilm-inspired Amyloid-Polysaccharide Composite Materials, *Appl. Mater. Today.* 27 (2022) 101497. <https://doi.org/10.1016/j.apmt.2022.101497>.
- [127] M. Usuelli, T. Germerdonk, Y. Cao, M. Peydayesh, M. Bagnani, S. Handschin, G. Nyström, R. Mezzenga, Polysaccharide-reinforced amyloid fibril hydrogels and aerogels, *Nanoscale.* 13 (2021) 12534–12545. <https://doi.org/10.1039/d1nr03133c>.
- [128] M. Chen, F. Yang, X. Chen, R. Qin, H. Pi, G. Zhou, P. Yang, Crack Suppression in Conductive Film by Amyloid-Like Protein Aggregation toward Flexible Device, *Adv. Mater.* 33 (2021) 2104187. <https://doi.org/10.1002/adma.202104187>.
- [129] R. Bardet, N. Belgacem, J. Bras, Flexibility and color monitoring of cellulose nanocrystal iridescent solid films using anionic or neutral polymers, *ACS Appl. Mater. Interfaces.* 7 (2015) 4010–4018. <https://doi.org/10.1021/am506786t>.
- [130] L.K. Bast, K.W. Klockars, L.G. Greca, O.J. Rojas, B.L. Tardy, N. Bruns, Infiltration of proteins in cholesteric cellulose structures, *Biomacromolecules.* 22 (2021) 2067–2080. <https://doi.org/10.1021/acs.biomac.1c00183>.
- [131] N. Kummer, T. Wu, K.J. De France, F. Zuber, Q. Ren, P. Fischer, S. Campioni, G. Nyström, Self-Assembly Pathways and Antimicrobial Properties of Lysozyme in Different Aggregation States, *Biomacromolecules.* 22 (2021) 4327–4336. <https://doi.org/10.1021/acs.biomac.1c00870>.

- [132] P. Dadgostar, Antimicrobial resistance: implications and costs, *Infect. Drug Resist.* 12 (2019) 3903–3910. <https://doi.org/10.2147/IDR.S234610>.
- [133] D.M.P. De Oliveira, B.M. Forde, T.J. Kidd, P.N.A. Harris, M.A. Schembri, S.A. Beatson, D.L. Paterson, M.J. Walker, Antimicrobial resistance in ESKAPE pathogens, *Clin. Microbiol. Rev.* 33 (2020) e00181-19. <https://doi.org/10.1128/CMR.00181-19>.
- [134] L.S.J. Roope, R.D. Smith, K.B. Pouwels, J. Buchanan, L. Abel, P. Eibich, C.C. Butler, P.S. Tan, A. Sarah Walker, J. V. Robotham, S. Wordsworth, The challenge of antimicrobial resistance: What economics can contribute, *Science*. 364 (2019) eaau4679. <https://doi.org/10.1126/science.aau4679>.
- [135] N. Beyth, Y. Hourri-Haddad, A. Domb, W. Khan, R. Hazan, Alternative antimicrobial approach: Nano-antimicrobial materials, *Evidence-Based Complement. Altern. Med.* 2015 (2015) 246012. <https://doi.org/10.1155/2015/246012>.
- [136] A. León-Buitimea, C.R. Garza-Cárdenas, J.A. Garza-Cervantes, J.A. Lerma-Escalera, J.R. Morones-Ramírez, The Demand for New Antibiotics: Antimicrobial Peptides, Nanoparticles, and Combinatorial Therapies as Future Strategies in Antibacterial Agent Design, *Front. Microbiol.* 11 (2020) 1669. <https://doi.org/10.3389/fmicb.2020.01669>.
- [137] C. Li, L. Xu, Y.Y. Zuo, P. Yang, Tuning protein assembly pathways through superfast amyloid-like aggregation, *Biomater. Sci.* 6 (2018) 836–841. <https://doi.org/10.1039/c8bm00066b>.
- [138] S.C. Gill, P.H. von Hippel, Calculation of protein extinction coefficients from amino acid sequence data, *Anal Biochem.* 182 (1989) 319–326.
- [139] A. Micsonai, F. Wien, L. Kernya, Y.H. Lee, Y. Goto, M. Réfrégiers, J. Kardos, Accurate secondary structure prediction and fold recognition for circular dichroism spectroscopy, *Proc. Natl. Acad. Sci.* 112 (2015) E3095–E3103. <https://doi.org/10.1073/pnas.1500851112>.
- [140] N. Sreerama, R.W. Woody, Estimation of protein secondary structure from circular dichroism spectra: Comparison of CONTIN, SELCON, and CDSSTR methods with an expanded reference set, *Anal. Biochem.* 287 (2000) 252–260. <https://doi.org/10.1006/abio.2000.4880>.
- [141] S. Wu, F. Zuber, J. Brugger, K. Maniura-Weber, Q. Ren, Antibacterial Au nanostructured surfaces, *Nanoscale*. 8 (2016) 2620–2625. <https://doi.org/10.1039/c5nr06157a>.
- [142] H. Levine, Thioflavine T interaction with synthetic Alzheimer's disease β -amyloid peptides: Detection of amyloid aggregation in solution, *Protein Sci.* 2 (1993) 404–410. <https://doi.org/10.1002/pro.5560020312>.
- [143] C. Xue, D. Chang, Thioflavin T as an amyloid dye : fibril quantification, optimal concentration and effect on aggregation, *R. Soc. Open Sci.* 4 (2017) 160696. <https://doi.org/10.1098/rsos.160696>.
- [144] C. Perez, T. Miti, F. Hasecke, G. Meisl, W. Hoyer, M. Muschol, G. Ullah, Mechanism of Fibril and Soluble Oligomer Formation in Amyloid Beta and Hen Egg White Lysozyme Proteins, *J. Phys. Chem. B.* 123 (2019) 5678–5689. <https://doi.org/10.1021/acs.jpccb.9b02338>.
- [145] A. Kamada, N. Mittal, L.D. Söderberg, T. Ingverud, W. Ohm, S. V. Roth, F. Lundell, C. Lendel, Flow-Assisted assembly of nanostructured protein microfibers, *Proc. Natl. Acad. Sci. U. S. A.* 114 (2017) 1232–1237.

<https://doi.org/10.1073/pnas.1617260114>.

- [146] G. Guérin, H. Wang, I. Manners, M.A. Winnik, Fragmentation of fiberlike structures: Sonication studies of cylindrical block copolymer micelles and behavioral comparisons to biological fibrils, *J. Am. Chem. Soc.* 130 (2008) 14763–14771. <https://doi.org/10.1021/ja805262v>.
- [147] J.-M. Jung, D.Z. Gunes, R. Mezzenga, Interfacial Activity and Interfacial Shear Rheology of Native β -Lactoglobulin Monomers and Their Heat-Induced Fibers, *Langmuir*. 26 (2010) 15366–15375. <https://doi.org/10.1021/la102721m>.
- [148] M. Bagnani, G. Nyström, C. De Michele, R. Mezzenga, Amyloid Fibrils Length Controls Shape and Structure of Nematic and Cholesteric Tactoids, *ACS Nano*. 13 (2019) 591–600. <https://doi.org/10.1021/acsnano.8b07557>.
- [149] C. Veerman, H. Ruis, L.M.C. Sagis, E. van der Linden, Effect of electrostatic interactions on the percolation concentration of fibrillar β -lactoglobulin gels, *Biomacromolecules*. 3 (2002) 869–873. <https://doi.org/10.1021/bm025533+>.
- [150] M. Usuelli, Y. Cao, M. Bagnani, S. Handschin, G. Nyström, R. Mezzenga, Probing the Structure of Filamentous Nonergodic Gels by Dynamic Light Scattering, *Macromolecules*. 53 (2020) 5950–5956. <https://doi.org/10.1021/acs.macromol.0c00610>.
- [151] R. Wetzel, Kinetics and thermodynamics of amyloid fibril assembly, *Acc. Chem. Res.* 39 (2006) 671–679. <https://doi.org/10.1021/ar050069h>.
- [152] J. Wang, K. Liu, R. Xing, X. Yan, Peptide self-assembly: Thermodynamics and kinetics, *Chem. Soc. Rev.* 45 (2016) 5589–5604. <https://doi.org/10.1039/c6cs00176a>.
- [153] Y. Cao, J. Adamcik, M. Diener, J.R. Kumita, R. Mezzenga, Different Folding States from the Same Protein Sequence Determine Reversible vs Irreversible Amyloid Fate, *J. Am. Chem. Soc.* 143 (2021) 11473–11481. <https://doi.org/10.1021/jacs.1c03392>.
- [154] D.M. Byler, H. Susi, Examination of the secondary structure of proteins by deconvolved FTIR spectra, *Biopolymers*. 25 (1986) 469–487. <https://doi.org/10.1002/bip.360250307>.
- [155] G. Zandomenighi, M.R.H. Krebs, M.G. McCammon, M. Fändrich, FTIR reveals structural differences between native β -sheet proteins and amyloid fibrils, *Protein Sci.* 13 (2004) 3314–3321. <https://doi.org/10.1110/ps.041024904>.
- [156] J. Foley, S.E. Hill, T. Miti, M. Mulaj, M. Ciesla, R. Robeel, C. Persichilli, R. Raynes, S. Westerheide, M. Muschol, Structural fingerprints and their evolution during oligomeric vs. oligomer-free amyloid fibril growth, *J. Chem. Phys.* 139 (2013) 121901. <https://doi.org/10.1063/1.4811343>.
- [157] N.J. Greenfield, Using circular dichroism spectra to estimate protein secondary structure, *Nat. Protoc.* 1 (2007) 2876–2890. <https://doi.org/10.1038/nprot.2006.202>.
- [158] L. Ma, M. Conover, H. Lu, M.R. Parsek, K. Bayles, D.J. Wozniak, Assembly and development of the *Pseudomonas aeruginosa* biofilm matrix, *PLoS Pathog.* 5 (2009) e1000354. <https://doi.org/10.1371/journal.ppat.1000354>.
- [159] J. Pansieri, M.A. Halim, C. Vendrely, M. Dumoulin, F. Legrand, M.M. Sallanon, S. Chierici, S. Denti, X. Dagany, P. Dugourd, C. Marquette, R. Antoine, V. Forge, Mass and charge distributions of amyloid fibers involved in neurodegenerative diseases: Mapping heterogeneity and polymorphism, *Chem. Sci.* 9 (2018) 2791–2796. <https://doi.org/10.1039/c7sc04542e>.

- [160] M. Sudagidan, A. Yemenicioğlu, Effects of nisin and lysozyme on growth inhibition and biofilm formation capacity of staphylococcus aureus strains isolated from raw milk and cheese samples, *J. Food Prot.* 75 (2012) 1627–1633. <https://doi.org/10.4315/0362-028X.JFP-12-001>.
- [161] R.S. Tobgi, L.P. Samaranayake, T.W. MacFarlane, In vitro susceptibility of *Candida* species to lysozyme, *Oral Microbiol. Immunol.* 3 (1988) 35–39. <https://doi.org/10.1111/j.1399-302X.1988.tb00603.x>.
- [162] E.Y. Lee, Y. Srinivasan, J. de Anda, L.K. Nicastro, Ç. Tükel, G.C.L. Wong, Functional Reciprocity of Amyloids and Antimicrobial Peptides: Rethinking the Role of Supramolecular Assembly in Host Defense, Immune Activation, and Inflammation, *Front. Immunol.* 11 (2020) 1629. <https://doi.org/10.3389/fimmu.2020.01629>.
- [163] C. Li, A.K. Born, T. Schweizer, M. Zenobi-Wong, M. Cerruti, R. Mezzenga, Amyloid-hydroxyapatite bone biomimetic composites, *Adv. Mater.* 26 (2014) 3207–3212. <https://doi.org/10.1002/adma.201306198>.
- [164] R. Cegielska-Radziejewska, G. Lesnierowski, T. Szablewski, J. Kijowski, Physico-chemical properties and antibacterial activity of modified egg white-lysozyme, *Eur. Food Res. Technol.* 231 (2010) 959–964. <https://doi.org/10.1007/s00217-010-1347-y>.
- [165] M.F.B.G. Gebbink, D. Claessen, B. Barend, L. Dijkhuizen, H.A.B. Wösten, Amyloids - A functional coat for microorganisms, *Nat. Rev. Microbiol.* 3 (2005) 333–341. <https://doi.org/https://doi.org/10.1038/nrmicro1127>.
- [166] M. Peydayesh, R. Mezzenga, Protein nanofibrils for next generation sustainable water purification, *Nat. Commun.* 12 (2021) 3248. <https://doi.org/10.1038/s41467-021-23388-2>.
- [167] M. Peydayesh, M. Bagnani, R. Mezzenga, Sustainable Bioplastics from Amyloid Fibril-Biodegradable Polymer Blends, *ACS Sustain. Chem. Eng.* 9 (2021) 11916–11926. <https://doi.org/10.1021/acssuschemeng.1c03937>.
- [168] T. Jin, M. Peydayesh, M. Li, Y. Yao, D. Wu, R. Mezzenga, Functional Coating from Amyloid Superwetting Films, *Adv. Mater.* 34 (2022) 2205072. <https://doi.org/10.1002/adma.202205072>.
- [169] R. Zhang, H.A. Andersson, M. Andersson, B. Andres, H. Edlund, P. Edström, S. Edvardsson, S. Forsberg, M. Hummelgård, N. Johansson, K. Karlsson, H.-E. Nilsson, M. Norgren, M. Olsen, T. Uesaka, T. Öhlund, H. Olin, Soap-film coating: High-speed deposition of multilayer nanofilms, *Sci. Rep.* 3 (2013) 1477. <https://doi.org/10.1038/srep01477>.
- [170] J. Li, R. Cha, K. Mou, X. Zhao, K. Long, H. Luo, F. Zhou, X. Jiang, Nanocellulose-Based Antibacterial Materials, *Adv. Healthc. Mater.* 7 (2018) 1800334. <https://doi.org/10.1002/adhm.201800334>.
- [171] T. Hakkarainen, R. Koivuniemi, M. Kosonen, C. Escobedo-Lucea, A. Sanz-Garcia, J. Vuola, J. Valtonen, P. Tammela, A. Mäkitie, K. Luukko, M. Yliperttula, H. Kavola, Nanofibrillar cellulose wound dressing in skin graft donor site treatment, *J. Control. Release.* 244 (2016) 292–301. <https://doi.org/10.1016/j.jconrel.2016.07.053>.
- [172] L. Amoroso, K.J. De France, C.I. Milz, G. Siqueira, T. Zimmermann, G. Nyström, Sustainable Cellulose Nanofiber Films from Carrot Pomace as Sprayable Coatings for Food Packaging Applications, *ACS Sustain. Chem. Eng.* 10 (2022) 342–352. <https://doi.org/10.1021/acssuschemeng.1c06345>.

- [173] P. Bertsch, M. Diener, J. Adamcik, N. Scheuble, T. Geue, R. Mezzenga, P. Fischer, Adsorption and Interfacial Layer Structure of Unmodified Nanocrystalline Cellulose at Air/Water Interfaces, *Langmuir*. 34 (2018) 15195–15202. <https://doi.org/10.1021/acs.langmuir.8b03056>.
- [174] F. Cheng, C. Liu, X. Wei, T. Yan, H. Li, J. He, Y. Huang, Preparation and Characterization of 2,2,6,6-Tetramethylpiperidine-1-oxyl (TEMPO)-Oxidized Cellulose Nanocrystal/Alginate Biodegradable Composite Dressing for Hemostasis Applications, *ACS Sustain. Chem. Eng.* 5 (2017) 3819–3828. <https://doi.org/10.1021/acssuschemeng.6b02849>.
- [175] C. Gruian, E. Vanea, S. Simon, V. Simon, FTIR and XPS studies of protein adsorption onto functionalized bioactive glass, *Biochim. Biophys. Acta - Proteins Proteomics*. 1824 (2012) 873–881. <https://doi.org/10.1016/j.bbapap.2012.04.008>.
- [176] A. Götz, R. Nikzad-Langerodi, Y. Staedler, A. Bellaire, J. Saukel, Apparent penetration depth in attenuated total reflection Fourier-transform infrared (ATR-FTIR) spectroscopy of *Allium cepa* L. epidermis and cuticle, *Spectrochim. Acta - Part A Mol. Biomol. Spectrosc.* 224 (2020) 117460. <https://doi.org/10.1016/j.saa.2019.117460>.
- [177] J.B. Gilbert, M.F. Rubner, R.E. Cohen, Depth-profiling X-ray photoelectron spectroscopy (XPS) analysis of interlayer diffusion in polyelectrolyte multilayers, *Proc. Natl. Acad. Sci. U. S. A.* 110 (2013) 6651–6656. <https://doi.org/10.1073/pnas.1222325110>.
- [178] S.L. McArthur, Applications of XPS in bioengineering, *Surf. Interface Anal.* 38 (2006) 1380–1385. <https://doi.org/10.1002/sia.2498>.
- [179] N. Kummer, C.E. Giacomini, P. Fischer, S. Campioni, G. Nyström, Amyloid fibril-nanocellulose interactions and self-assembly, *J. Colloid Interface Sci.* 641 (2023) 338–347. <https://doi.org/10.1016/j.jcis.2023.03.002>.
- [180] A.M. Carmona-Ribeiro, L.D. de Melo Carrasco, Cationic antimicrobial polymers and their assemblies, *Int. J. Mol. Sci.* 14 (2013) 9906–9946. <https://doi.org/10.3390/ijms14059906>.
- [181] O.G. Travkova, H. Moehwald, G. Brezesinski, The interaction of antimicrobial peptides with membranes, *Adv. Colloid Interface Sci.* 247 (2017) 521–532. <https://doi.org/10.1016/j.cis.2017.06.001>.
- [182] M.M. Barnhart, M.R. Chapman, Curli Biogenesis and Function, *Annu. Rev. Microbiol.* 60 (2010) 131–147. <https://doi.org/10.1146/annurev.micro.60.080805.142106>.
- [183] W. Thongsomboon, D.O. Serra, A. Possling, C. Hadjineophytou, R. Hengge, L. Cegelski, Phosphoethanolamine cellulose: A naturally produced chemically modified cellulose, 359 (2018) 334–338. <https://doi.org/https://doi.org/10.1126/science.aao4096>.
- [184] G. Wei, Z. Su, N.P. Reynolds, P. Arosio, I.W. Hamley, E. Gazit, R. Mezzenga, Self-assembling peptide and protein amyloids: From structure to tailored function in nanotechnology, *Chem. Soc. Rev.* 46 (2017) 4661–4708. <https://doi.org/10.1039/c6cs00542j>.
- [185] Y. Shen, A. Levin, A. Kamada, Z. Toprakcioglu, M. Rodriguez-Garcia, Y. Xu, T.P.J. Knowles, From Protein Building Blocks to Functional Materials, *ACS Nano*. 15 (2021) 5819–5837. <https://doi.org/10.1021/acsnano.0c08510>.
- [186] S. Bolisetty, R. Mezzenga, Amyloid-carbon hybrid membranes for universal

- water purification, *Nat. Nanotechnol.* 11 (2016) 365–371.
<https://doi.org/10.1038/nnano.2015.310>.
- [187] F. Yang, Z. Yan, J. Zhao, S. Miao, D. Wang, P. Yang, Rapid capture of trace precious metals by amyloid-like protein membrane with high adsorption capacity and selectivity, (2020). <https://doi.org/10.1039/C9TA12124B>.
- [188] M. Peydayesh, T. Suta, M. Usuelli, S. Handschin, G. Canelli, M. Bagnani, R. Mezzenga, Sustainable Removal of Microplastics and Natural Organic Matter from Water by Coagulation-Flocculation with Protein Amyloid Fibrils, *Environ. Sci. Technol.* 55 (2021) 8848–8858. <https://doi.org/10.1021/acs.est.1c01918>.
- [189] L. Severini, K.J. De France, D. Sivaraman, N. Kummer, G. Nyström, Biohybrid Nanocellulose–Lysozyme Amyloid Aerogels via Electrostatic Complexation, *ACS Omega.* 7 (2022) 578–586. <https://doi.org/10.1021/acsomega.1c05069>.
- [190] R. Weishaupt, G. Siqueira, M. Schubert, P. Tingaut, K. Maniura-Weber, T. Zimmermann, L. Thöny-Meyer, G. Faccio, J. Ihssen, TEMPO-Oxidized Nanofibrillated Cellulose as a High Density Carrier for Bioactive Molecules, *Biomacromolecules.* 16 (2015) 3640–3650.
<https://doi.org/10.1021/acs.biomac.5b01100>.
- [191] T. Nikolic, M. Korica, J. Milanovic, A. Kramar, Z. Petronijevic, M. Kostic, TEMPO-oxidized cotton as a substrate for trypsin immobilization: impact of functional groups on proteolytic activity and stability, *Cellulose.* 24 (2017) 1863–1875. <https://doi.org/10.1007/s10570-017-1221-1>.
- [192] R. Weishaupt, G. Siqueira, M. Schubert, M.M. Kämpf, T. Zimmermann, K. Maniura-Weber, G. Faccio, A Protein-Nanocellulose Paper for Sensing Copper Ions at the Nano- to Micromolar Level, *Adv. Funct. Mater.* 27 (2017) 1604291.
<https://doi.org/10.1002/adfm.201604291>.
- [193] R. Weishaupt, L. Heuberger, G. Siqueira, B. Gutt, T. Zimmermann, K. Maniura-Weber, S. Salentinig, G. Faccio, Enhanced Antimicrobial Activity and Structural Transitions of a Nanofibrillated Cellulose-Nisin Biocomposite Suspension, *ACS Appl. Mater. Interfaces.* 10 (2018) 20170–20181.
<https://doi.org/10.1021/acsami.8b04470>.
- [194] N.H.C.S. Silva, P. Figueira, E. Fabre, R.J.B. Pinto, M.E. Pereira, A.J.D. Silvestre, I.M. Marrucho, C. Vilela, C.S.R. Freire, Dual nanofibrillar-based biosorbent films composed of nanocellulose and lysozyme nanofibrils for mercury removal from spring waters, *Carbohydr. Polym.* 238 (2020) 116210.
<https://doi.org/10.1016/j.carbpol.2020.116210>.
- [195] Y. Huang, P. Yang, F. Yang, C. Chang, Self-supported nanoporous lysozyme/nanocellulose membranes for multifunctional wastewater purification, *J. Memb. Sci.* 635 (2021) 119537.
<https://doi.org/10.1016/j.memsci.2021.119537>.
- [196] J. Toro-Sierra, A. Tolkach, U. Kulozik, Fractionation of α -Lactalbumin and β -Lactoglobulin from Whey Protein Isolate Using Selective Thermal Aggregation, an Optimized Membrane Separation Procedure and Resolubilization Techniques at Pilot Plant Scale, *Food Bioprocess Technol.* 6 (2013) 1032–1043. <https://doi.org/10.1007/s11947-011-0732-2>.
- [197] C.A. Schneider, W.S. Rasband, K.W. Eliceiri, NIH Image to ImageJ: 25 years of image analysis, *Nat. Methods.* 9 (2012) 671–675.
<https://doi.org/10.1038/nmeth.2089>.
- [198] Y. Cao, S. Bolisetty, J. Adamcik, R. Mezzenga, Elasticity in Physically Cross-

- Linked Amyloid Fibril Networks, *Phys. Rev. Lett.* 120 (2018) 158103.
<https://doi.org/10.1103/PhysRevLett.120.158103>.
- [199] M.L. Gardel, J.H. Shin, F.C. MacKintosh, L. Mahadevan, P. Matsudaira, D.A. Weitz, Elastic behavior of cross-linked and bundled actin networks, *Science*. 304 (2004) 1301–1305. <https://doi.org/10.1126/science.1095087>.
- [200] O. Lieleg, M.M.A.E. Claessens, C. Heussinger, E. Frey, A.R. Bausch, Mechanics of bundled semiflexible polymer networks, *Phys. Rev. Lett.* 99 (2007) 3–6. <https://doi.org/10.1103/PhysRevLett.99.088102>.
- [201] Y.-C. Lin, N.Y. Yao, C.P. Broedersz, H. Herrmann, F.C. MacKintosh, D.A. Weitz, Origins of elasticity in intermediate filament networks, *Phys. Rev. Lett.* 104 (2010) 058101. <https://doi.org/10.1103/PhysRevLett.104.058101>.
- [202] F.C. Mackintosh, J. Kas, P.A. Janmey, Elasticity of Semi-flexible polymer networks, *Phys. Rev. Lett.* 75 (1995) 4425.
<https://doi.org/10.1103/PhysRevLett.75.4425>.
- [203] C.P. Broedersz, F.C. Mackintosh, Modeling semiflexible polymer networks, *Rev. Mod. Phys.* 86 (2014) 995–1036.
<https://doi.org/10.1103/RevModPhys.86.995>.
- [204] M.C.E. Van Dalen, J. Vaneyck, S.A. Semerdzhiev, M. Karperien, J.N. Post, M.M.A.E. Claessens, Protein Adsorption Enhances Energy Dissipation in Networks of Lysozyme Amyloid Fibrils, *Langmuir*. 37 (2021) 7349–7355.
<https://doi.org/10.1021/acs.langmuir.1c00657>.
- [205] L. Zhong, S. Fu, X. Peng, H. Zhan, R. Sun, Colloidal stability of negatively charged cellulose nanocrystalline in aqueous systems, *Carbohydr. Polym.* 90 (2012) 644–649. <https://doi.org/10.1016/j.carbpol.2012.05.091>.
- [206] R.J. Hill, Elastic modulus of microfibrillar cellulose gels, *Biomacromolecules*. 9 (2008) 2963–2966. <https://doi.org/10.1021/bm800490x>.
- [207] N. Quennouz, S.M. Hashmi, H.S. Choi, J.W. Kim, C.O. Osuji, Rheology of cellulose nanofibrils in the presence of surfactants, *Soft Matter*. 12 (2016) 157–164. <https://doi.org/10.1039/c5sm01803j>.
- [208] L. Jowkarderis, T.G.M. Van De Ven, Rheology of semi-dilute suspensions of carboxylated cellulose nanofibrils, *Carbohydr. Polym.* 123 (2015) 416–423.
<https://doi.org/10.1016/j.carbpol.2015.01.067>.
- [209] J. Mewis, N.J. Wagner, *Colloidal Suspension Rheology*, Cambridge University Press, 2011. <https://doi.org/10.1017/CBO9780511977978>.
- [210] S. Goda, K. Takano, K. Yutani, Y. Yamagata, R. Nagata, H. Akutsu, S. Maki, K. Namba, Amyloid protofilament formation of hen egg lysozyme in highly concentrated ethanol solution, *Protein Sci.* 9 (2008) 369–375.
<https://doi.org/10.1110/ps.9.2.369>.
- [211] A.K. Buell, Stability matters, too - the thermodynamics of amyloid fibril formation, *Chem. Sci.* 13 (2022) 10177–10192.
<https://doi.org/10.1039/d1sc06782f>.
- [212] S. Saffarionpour, Nanocellulose for Stabilization of Pickering Emulsions and Delivery of Nutraceuticals and Its Interfacial Adsorption Mechanism, *Food Bioprocess Technol.* 13 (2020) 1292–1328. <https://doi.org/10.1007/s11947-020-02481-2>.
- [213] I. Dueramae, S. Fukuzawa, N. Shinyashiki, S. Yagihara, R. Kita, Dynamics of amyloid-like aggregation and gel formation of hen egg-white lysozyme in highly concentrated ethanol solution, *J. Biorheol.* 31 (2017) 21–28.

- <https://doi.org/10.17106/jbr.31.21>.
- [214] T. Wu, Z. Zeng, G. Siqueira, K.J. De France, Dual-porous cellulose nanofibril aerogels via modular drying and cross-linking, *Nanoscale*. 12 (2020) 7383–7394. <https://doi.org/10.1039/d0nr00860e>.
- [215] Y. Han, Y. Cao, J. Zhou, Y. Yao, X. Wu, S. Bolisetty, M. Diener, S. Handschin, C. Lu, R. Mezzenga, Interfacial Electrostatic Self-Assembly of Amyloid Fibrils into Multifunctional Protein Films, *Adv. Sci.* 2206867 (2023) 2206867. <https://doi.org/10.1002/adv.202206867>.
- [216] A.S. Woods, S. Ferré, Amazing stability of the arginine-phosphate electrostatic interaction, *J. Proteome Res.* 4 (2005) 1397–1402. <https://doi.org/10.1021/pr050077s>.
- [217] I. Migneault, C. Dartiguenave, M.J. Bertrand, K.C. Waldron, Glutaraldehyde: behavior in aqueous solution, reaction with proteins, and application to enzyme crosslinking, *Biotechniques*. 37 (2004) 790–802. <https://doi.org/doi.org/10.2144/04375RV01>.
- [218] M. Linder, T.T. Teeri, The roles and function of cellulose-binding domains, *J. Biotechnol.* 57 (1997) 15–28. [https://doi.org/https://doi.org/10.1016/S0168-1656\(97\)00087-4](https://doi.org/https://doi.org/10.1016/S0168-1656(97)00087-4).
- [219] A. Chmielewska, M. Kozłowska, D. Rachwał, P. Wnukowski, R. Amarowicz, E. Nebesny, J. Rosicka-Kaczmarek, Canola/rapeseed protein–nutritional value, functionality and food application: a review, *Crit. Rev. Food Sci. Nutr.* 61 (2021) 3836–3856. <https://doi.org/10.1080/10408398.2020.1809342>.
- [220] L.A.A. Sluyterman, M.J.M. De Graaf, The effect of salts upon the pH dependence of the activity of papain and succinyl-papain, *Biochim. Biophys. Acta.* 258 (1972) 554–561. [https://doi.org/https://doi.org/10.1016/0005-2744\(72\)90247-1](https://doi.org/https://doi.org/10.1016/0005-2744(72)90247-1).
- [221] Y. Pei, Z. Li, D.J. McClements, B. Li, Comparison of structural and physicochemical properties of lysozyme/carboxymethylcellulose complexes and microgels, *Food Res. Int.* 122 (2019) 273–282. <https://doi.org/10.1016/j.foodres.2019.03.071>.
- [222] W. Huang, L. Wang, Y. Wei, M. Cao, H. Xie, D. Wu, Fabrication of lysozyme/k-carrageenan complex nanoparticles as a novel carrier to enhance the stability and in vitro release of curcumin, *Int. J. Biol. Macromol.* 146 (2020) 444–452. <https://doi.org/10.1016/j.ijbiomac.2020.01.004>.
- [223] M. Arcari, E. Zuccarella, R. Axelrod, J. Adamcik, A. Sánchez-Ferrer, R. Mezzenga, G. Nyström, Nanostructural Properties and Twist Periodicity of Cellulose Nanofibrils with Variable Charge Density, *Biomacromolecules*. 20 (2019) 1288–1296. <https://doi.org/10.1021/acs.biomac.8b01706>.
- [224] K.M.O. Håkansson, A.B. Fall, F. Lundell, S. Yu, C. Krywka, S. V Roth, G. Santoro, M. Kvick, L. Prah Wittberg, L. Wågberg, L.D. Söderberg, Hydrodynamic alignment and assembly of nanofibrils resulting in strong cellulose filaments., *Nat. Commun.* 5 (2014) 4018–4027. <https://doi.org/10.1038/ncomms5018>.
- [225] D. Klemm, E.D. Cranston, D. Fischer, M. Gama, S.A. Kedzior, D. Kralisch, F. Kramer, T. Kondo, T. Lindström, S. Nietzsche, K. Petzold-Welcke, F. Rauchfuß, Nanocellulose as a natural source for groundbreaking applications in materials science: Today's state, *Mater. Today*. 21 (2018) 720–748. <https://doi.org/10.1016/j.mattod.2018.02.001>.

- [226] J. Desmaisons, E. Boutonnet, M. Rueff, A. Dufresne, J. Bras, A new quality index for benchmarking of different cellulose nanofibrils, *Carbohydr. Polym.* 174 (2017) 318–329. <https://doi.org/10.1016/j.carbpol.2017.06.032>.
- [227] K. De France, Z. Zeng, T. Wu, G. Nyström, Functional Materials from Nanocellulose: Utilizing Structure–Property Relationships in Bottom-Up Fabrication, *Adv. Mater.* 33 (2020) 2000657. <https://doi.org/10.1002/adma.202000657>.
- [228] F. Rol, M.N. Belgacem, A. Gandini, J. Bras, Recent advances in surface-modified cellulose nanofibrils, *Prog. Polym. Sci.* 88 (2019) 241–264. <https://doi.org/10.1016/j.progpolymsci.2018.09.002>.
- [229] K. Löbmann, A.J. Svagan, Cellulose nanofibers as excipient for the delivery of poorly soluble drugs, *Int. J. Pharm.* 533 (2017) 285–297. <https://doi.org/10.1016/j.ijpharm.2017.09.064>.
- [230] C. Xu, B. Zhang Molino, X. Wang, F. Cheng, W. Xu, P. Molino, M. Bacher, D. Su, T. Rosenau, S. Willför, G. Wallace, 3D printing of nanocellulose hydrogel scaffolds with tunable mechanical strength towards wound healing application, *J. Mater. Chem. B.* 6 (2018) 7066–7075. <https://doi.org/10.1039/c8tb01757c>.
- [231] S. Shin, S. Park, M. Park, E. Jeong, K. Na, H.J. Youn, J. Hyun, Cellulose nanofibers for the enhancement of printability of low viscosity gelatin derivatives, *BioResources.* 12 (2017) 2941–2954. <https://doi.org/10.15376/biores.12.2.2941-2954>.
- [232] D.M. Eby, N.M. Schaeublin, K.E. Farrington, S.M. Hussain, G.R. Johnson, Lysozyme catalyzes the formation of antimicrobial silver nanoparticles, *ACS Nano.* 3 (2009) 984–994. <https://doi.org/10.1021/nn900079e>.
- [233] D.W. Horn, K. Tracy, C.J. Easley, V.A. Davis, Lysozyme dispersed single-walled carbon nanotubes: Interaction and activity, *J. Phys. Chem. C.* 116 (2012) 10341–10348. <https://doi.org/10.1021/jp300242a>.
- [234] G.G. Syngai, G. Ahmed, *Lysozyme: A Natural Antimicrobial Enzyme of Interest in Food Applications*, Elsevier, 2019. <https://doi.org/10.1016/b978-0-12-813280-7.00011-6>.
- [235] T. Wu, Q. Jiang, D. Wu, Y. Hu, S. Chen, T. Ding, X. Ye, D. Liu, J. Chen, What is new in lysozyme research and its application in food industry? A review, *Food Chem.* 274 (2019) 698–709. <https://doi.org/10.1016/j.foodchem.2018.09.017>.
- [236] A. Barbiroli, F. Bonomi, G. Capretti, S. Iametti, M. Manzoni, L. Piergiovanni, M. Rollini, Antimicrobial activity of lysozyme and lactoferrin incorporated in cellulose-based food packaging, *Food Control.* 26 (2012) 387–392. <https://doi.org/10.1016/j.foodcont.2012.01.046>.
- [237] X. Liu, L.H. Nielsen, H. Qu, L.P. Christensen, J. Rantanen, M. Yang, Stability of lysozyme incorporated into electrospun fibrous mats for wound healing, *Eur. J. Pharm. Biopharm.* 136 (2019) 240–249. <https://doi.org/10.1016/j.ejpb.2019.01.003>.
- [238] T. Zhang, P. Zhou, Y. Zhan, X. Shi, J. Lin, Y. Du, X. Li, H. Deng, Pectin/lysozyme bilayers layer-by-layer deposited cellulose nanofibrous mats for antibacterial application, *Carbohydr. Polym.* 117 (2015) 687–693. <https://doi.org/10.1016/j.carbpol.2014.10.064>.
- [239] S. Dekina, I. Romanovska, A. Ovsepyan, V. Tkach, E. Muratov, Gelatin/carboxymethyl cellulose mucoadhesive films with lysozyme:

- Development and characterization, *Carbohydr. Polym.* 147 (2016) 208–215. <https://doi.org/10.1016/j.carbpol.2016.04.006>.
- [240] J.V. Edwards, N.T. Prevost, B. Condon, A. French, Covalent attachment of lysozyme to cotton/cellulose materials: Protein versus solid support activation, *Cellulose*. 18 (2011) 1239–1249. <https://doi.org/10.1007/s10570-011-9563-6>.
- [241] K. Zhu, T. Ye, J. Liu, Z. Peng, S. Xu, J. Lei, H. Deng, B. Li, Nanogels fabricated by lysozyme and sodium carboxymethyl cellulose for 5-fluorouracil controlled release, *Int. J. Pharm.* 441 (2013) 721–727. <https://doi.org/10.1016/j.ijpharm.2012.10.022>.
- [242] Z. Li, W. Xu, C. Zhang, Y. Chen, B. Li, Self-assembled lysozyme/carboxymethylcellulose nanogels for delivery of methotrexate, *Int. J. Biol. Macromol.* 75 (2015) 166–172. <https://doi.org/10.1016/j.ijbiomac.2015.01.033>.
- [243] Z. Li, Y. Wang, Y. Pei, W. Xiong, W. Xu, B. Li, J. Li, Effect of substitution degree on carboxymethylcellulose interaction with lysozyme, *Food Hydrocoll.* 62 (2017) 222–229. <https://doi.org/10.1016/j.foodhyd.2016.07.020>.
- [244] M. Tavakolian, M. Okshevsky, T.G.M. Van De Ven, N. Tufenkji, Developing Antibacterial Nanocrystalline Cellulose Using Natural Antibacterial Agents, *ACS Appl. Mater. Interfaces*. 10 (2018) 33827–33838. <https://doi.org/10.1021/acsami.8b08770>.
- [245] A. Basu, M. Strømme, N. Ferraz, Towards tunable protein-carrier wound dressings based on nanocellulose hydrogels crosslinked with calcium ions, *Nanomaterials*. 8 (2018) 550. <https://doi.org/10.3390/nano8070550>.
- [246] A. Abouhmad, T. Dishisha, M.A. Amin, R. Hatti-Kaul, Immobilization to Positively Charged Cellulose Nanocrystals Enhances the Antibacterial Activity and Stability of Hen Egg White and T4 Lysozyme, *Biomacromolecules*. 18 (2017) 1600–1608. <https://doi.org/10.1021/acs.biomac.7b00219>.
- [247] S. Gustafsson, L. Manukyan, A. Mihranyan, Protein – Nanocellulose Interactions in Paper Filters for Advanced Separation Applications, *Langmuir*. 33 (2017) 4729–4736. <https://doi.org/10.1021/acs.langmuir.7b00566>.
- [248] C. Ben Amara, P. Degraeve, N. Oulahal, A. Gharsallaoui, pH-dependent complexation of lysozyme with low methoxyl (LM) pectin, *Food Chem.* 236 (2017) 127–133. <https://doi.org/10.1016/j.foodchem.2017.03.124>.
- [249] L. Mendoza, W. Batchelor, R.F. Tabor, G. Garnier, Gelation mechanism of cellulose nanofibre gels: A colloids and interfacial perspective, *J. Colloid Interface Sci.* 509 (2018) 39–46. <https://doi.org/10.1016/j.jcis.2017.08.101>.
- [250] L. Alves, E. Ferraz, A.F. Lourenço, P.J. Ferreira, M.G. Rasteiro, J.A.F. Gamelas, Tuning rheology and aggregation behaviour of TEMPO-oxidised cellulose nanofibrils aqueous suspensions by addition of different acids, *Carbohydr. Polym.* 237 (2020) 116109. <https://doi.org/10.1016/j.carbpol.2020.116109>.
- [251] N. Masruchin, B.D. Park, V. Causin, Dual-responsive composite hydrogels based on TEMPO-oxidized cellulose nanofibril and poly(N-isopropylacrylamide) for model drug release, *Cellulose*. 25 (2018) 485–502. <https://doi.org/10.1007/s10570-017-1585-2>.
- [252] H. Meng, P. Xiao, J. Gu, X. Wen, J. Xu, C. Zhao, J. Zhang, T. Chen, Self-healable macro-/microscopic shape memory hydrogels based on supramolecular interactions, *Chem. Commun.* 50 (2014) 12277–12280.

<https://doi.org/10.1039/c4cc04760e>.

- [253] S. Voutilainen, A. Paananen, M. Lille, M.B. Linder, Modular protein architectures for pH-dependent interactions and switchable assembly of nanocellulose, *Int. J. Biol. Macromol.* 137 (2019) 270–276. <https://doi.org/10.1016/j.ijbiomac.2019.06.227>.
- [254] S. Josset, P. Orsolini, G. Siqueira, A. Tejado, P. Tingaut, T. Zimmermann, Energy consumption of the nanofibrillation of bleached pulp, wheat straw and recycled newspaper through a grinding process, *Nord. Pulp Pap. Res. J.* 29 (2014) 167–175. <https://doi.org/10.3183/npprj-2014-29-01-p167-175>.
- [255] S. Dutta, P. Samanta, D. Dhara, Temperature, pH and redox responsive cellulose based hydrogels for protein delivery, *Int. J. Biol. Macromol.* 87 (2016) 92–100. <https://doi.org/10.1016/j.ijbiomac.2016.02.042>.
- [256] T.S. Anirudhan, S.R. Rejeena, Poly(acrylic acid)-modified poly(glycidylmethacrylate)-grafted nanocellulose as matrices for the adsorption of lysozyme from aqueous solutions, *Chem. Eng. J.* 187 (2012) 150–159. <https://doi.org/10.1016/j.cej.2012.01.113>.
- [257] N. Gull, M. Ishtikhar, M.S. Alam, S.N. Sabah Andrabi, R.H. Khan, Spectroscopic studies on the comparative refolding of guanidinium hydrochloride denatured hen egg-white lysozyme and *Rhizopus niveus* lipase assisted by cationic single-chain/gemini surfactants via artificial chaperone protocol, *RSC Adv.* 7 (2017) 28452–28460. <https://doi.org/10.1039/c6ra21528a>.
- [258] Q. Zhu, Q. Yao, J. Sun, H. Chen, W. Xu, J. Liu, Q. Wang, Stimuli induced cellulose nanomaterials alignment and its emerging applications: A review, *Carbohydr. Polym.* 230 (2020) 115609. <https://doi.org/10.1016/j.carbpol.2019.115609>.
- [259] D. Mallamace, E. Fazio, F. Mallamace, C. Corsaro, The role of hydrogen bonding in the folding/unfolding process of hydrated lysozyme: A review of recent NMR and FTIR results, *Int. J. Mol. Sci.* 19 (2018) 3825. <https://doi.org/10.3390/ijms19123825>.
- [260] S. Sudhakar, P.B. Santhosh, E. Mani, Dual Role of Gold Nanorods: Inhibition and Dissolution of A β Fibrils Induced by Near IR Laser, *ACS Chem. Neurosci.* 8 (2017) 2325–2334. <https://doi.org/10.1021/acscchemneuro.7b00238>.
- [261] T. Al Kayal, S. Nappini, E. Russo, D. Berti, M. Bucciantini, M. Stefani, P. Baglioni, Lysozyme interaction with negatively charged lipid bilayers: Protein aggregation and membrane fusion, *Soft Matter.* 8 (2012) 4524–4534. <https://doi.org/10.1039/c2sm06906g>.
- [262] G. Albornoz-Palma, F. Betancourt, R.T. Mendonça, G. Chinga-Carrasco, M. Pereira, Relationship between rheological and morphological characteristics of cellulose nanofibrils in dilute dispersions, *Carbohydr. Polym.* 230 (2020) 115588. <https://doi.org/10.1016/j.carbpol.2019.115588>.
- [263] B. Zhang, B. Sun, X. Li, Y. Yu, Y. Tian, X. Xu, Z. Jin, Synthesis of pH- and ionic strength-responsive microgels and their interactions with lysozyme, *Int. J. Biol. Macromol.* 79 (2015) 392–397. <https://doi.org/10.1016/j.ijbiomac.2015.05.011>.
- [264] J. Li, Y. Zhang, Q. Fan, C. Teng, W. Xie, Y. Shi, Y. Su, Y. Yang, Combination effects of NaOH and NaCl on the rheology and gel characteristics of hen egg white proteins, *Food Chem.* 250 (2018) 1–6. <https://doi.org/10.1016/j.foodchem.2018.01.031>.

- [265] Y.C. Kim, S. Late, A.K. Banga, P.J. Ludovice, M.R. Prausnitz, Biochemical enhancement of transdermal delivery with magainin peptide: Modification of electrostatic interactions by changing pH, *Int. J. Pharm.* 362 (2008) 20–28. <https://doi.org/10.1016/j.ijpharm.2008.05.042>.
- [266] L. Alves, B. Lindman, B. Klotz, A. Böttcher, H.M. Haake, F.E. Antunes, Rheology of polyacrylate systems depends strongly on architecture, *Colloid Polym. Sci.* 293 (2015) 3285–3293. <https://doi.org/10.1007/s00396-015-3715-4>.
- [267] K. Järbrink, G. Ni, H. Sönnergren, A. Schmidtchen, C. Pang, R. Bajpai, J. Car, Prevalence and incidence of chronic wounds and related complications : a protocol for a systematic review, *Syst. Rev.* 5 (2016) 152. <https://doi.org/10.1186/s13643-016-0329-y>.
- [268] K. Järbrink, G. Ni, H. Sönnergren, A. Schmidtchen, C. Pang, R. Bajpai, J. Car, The humanistic and economic burden of chronic wounds: a protocol for a systematic review, *Syst. Rev.* 6 (2017) 15. <https://doi.org/10.1186/s13643-016-0400-8>.
- [269] G.A. James, E. Swogger, R. Wolcott, E. Pulcini, P. Secor, J. Sestrich, J.W. Costerton, P.S. Stewart, Biofilms in chronic wounds, *Wound Repair Regen.* 16 (2008) 37–44. <https://doi.org/10.1111/j.1524-475X.2007.00321.x>.
- [270] F. Gottrup, E. Henneberg, R. Trangbaek, N. Baekmark, K. Zollner, J. Sorensen, Point prevalence of wounds and cost impact in the acute and community setting in Denmark, *J. Wound Care.* 22 (2013) 413. <https://doi.org/10.12968/jowc.2013.22.8.413>.
- [271] S.R. Nussbaum, M.J. Carter, C.E. Fife, J. Davanzo, R. Haught, M. Nusgart, D. Cartwright, An Economic Evaluation of the Impact , Cost , and Medicare Policy Implications of Chronic Nonhealing Wounds, *Value Heal.* 21 (2018) 27–32. <https://doi.org/10.1016/j.jval.2017.07.007>.
- [272] C.K. Sen, Human Wounds and Its Burden: An Updated Compendium of Estimates, *Adv. Wound Care.* 8 (2019) 39–48. <https://doi.org/10.1089/wound.2019.0946>.
- [273] Y. Habibi, L.A. Lucia, O.J. Rojas, Cellulose nanocrystals: Chemistry, self-assembly, and applications, *Chem. Rev.* 110 (2010) 3479–3500. <https://doi.org/10.1021/cr900339w>.
- [274] M. Roman, Toxicity of Cellulose Nanocrystals: A Review, *Ind. Biotechnol.* 11 (2015) 25–33. <https://doi.org/10.1089/ind.2014.0024>.
- [275] R.M.A. Domingues, M.E. Gomes, R.L. Reis, The Potential of Cellulose Nanocrystals in Tissue Engineering Strategies, *Biomacromolecules.* 15 (2014) 2327–2346. <https://doi.org/10.1021/bm500524s>.
- [276] M. Jorfi, E.J. Foster, Recent advances in nanocellulose for biomedical applications, *J. Appl. Polym. Sci.* 132 (2015) 41719. <https://doi.org/10.1002/app.41719>.
- [277] K.J. De France, E.D. Cranston, T. Hoare, Mechanically Reinforced Injectable Hydrogels, *ACS Appl. Polym. Mater.* 2 (2020) 1016–1030. <https://doi.org/10.1021/acsapm.9b00981>.
- [278] J. Catalán, M. Ilves, H. Järventausta, K. Hannukainen, E. Kontturi, E. Vanhala, H. Alenius, K.M. Savolainen, H. Norppa, Genotoxic and Immunotoxic Effects of Cellulose Nanocrystals In Vitro, *Environ. Mol. Mutagen.* 56 (2015) 171–182. <https://doi.org/https://doi.org/10.1002/em.21913>.

- [279] M.S. Reid, M. Villalobos, E.D. Cranston, Benchmarking Cellulose Nanocrystals: From the Laboratory to Industrial Production, *Langmuir*. 33 (2017) 1583–1598. <https://doi.org/10.1021/acs.langmuir.6b03765>.
- [280] F. V. Ferreira, C.G. Otoni, K.J. De France, H.S. Barud, L.M.F. Lona, E.D. Cranston, O.J. Rojas, Porous nanocellulose gels and foams: Breakthrough status in the development of scaffolds for tissue engineering, *Mater. Today*. 37 (2020) 126–141. <https://doi.org/10.1016/j.mattod.2020.03.003>.
- [281] K.J. De France, M. Badv, J. Dorogin, E. Siebers, V. Panchal, M. Babi, J.M. Moran-Mirabal, M. Lawlor, E.D. Cranston, T. Hoare, Tissue Response and Biodistribution of Injectable Cellulose Nanocrystal Composite Hydrogels, *ACS Biomater. Sci. Eng.* 5 (2019) 2235–2246. <https://doi.org/10.1021/acsbiomaterials.9b00522>.
- [282] N. Lin, A. Dufresne, Nanocellulose in biomedicine: Current status and future prospect, *Eur. Polym. J.* 59 (2014) 302–325. <https://doi.org/10.1016/j.eurpolymj.2014.07.025>.
- [283] J.A. Kelly, M. Giese, K.E. Shopsowitz, W.Y. Hamad, M.J. MacLachlan, The development of chiral nematic mesoporous materials, *Acc. Chem. Res.* 47 (2014) 1088–1096. <https://doi.org/10.1021/ar400243m>.
- [284] J.P.F. Lagerwall, C. Schütz, M. Salajkova, J. Noh, J. Hyun Park, G. Scalia, L. Bergström, J.H. Park, G. Scalia, L. Bergström, Cellulose nanocrystal-based materials: from liquid crystal self-assembly and glass formation to multifunctional thin films, *NPG Asia Mater.* 6 (2014) e80. <https://doi.org/10.1038/am.2013.69>.
- [285] A. Tran, C.E. Boott, M.J. MacLachlan, Understanding the Self-Assembly of Cellulose Nanocrystals — Toward Chiral Photonic Materials, *Adv. Mater.* (2020) 1905876. <https://doi.org/10.1002/adma.201905876>.
- [286] K.J. De France, K.G. Yager, T. Hoare, E.D. Cranston, Cooperative Ordering and Kinetics of Cellulose Nanocrystal Alignment in a Magnetic Field, *Langmuir*. 32 (2016) 7564–7571. <https://doi.org/10.1021/acs.langmuir.6b01827>.
- [287] K.J. De France, Z. Zeng, T. Wu, G. Nyström, Functional Materials from Nanocellulose: Utilizing Structure - Property Relationships in Bottom-Up Fabrication, *Adv. Mater.* 33 (2020) 2000657. <https://doi.org/10.1002/adma.202000657>.
- [288] B.L. Tardy, B.D. Mattos, L.G. Greca, T. Kämäräinen, K.W. Klockars, O.J. Rojas, Tessellation of Chiral-Nematic Cellulose Nanocrystal Films by Microtemplating, *Adv. Funct. Mater.* 29 (2019) 1808518. <https://doi.org/10.1002/adfm.201808518>.
- [289] M. Giese, L.K. Blusch, M.K. Khan, M.J. MacLachlan, Functional Materials from Cellulose-Derived Liquid-Crystal Templates, *Angew. Chemie Int. Ed.* 54 (2015) 2888–2910. <https://doi.org/10.1002/anie.201407141>.
- [290] B. Natarajan, A. Krishnamurthy, X. Qin, C.D. Emiroglu, A. Forster, E.J. Foster, C. Weder, D.M. Fox, S. Ketten, J. Obrzut, J.W. Gilman, Binary Cellulose Nanocrystal Blends for Bioinspired Damage Tolerant Photonic Films, *Adv. Funct. Mater.* 28 (2018) 1800032. <https://doi.org/10.1002/adfm.201800032>.
- [291] L.N. Johnson, The structure and function of lysozyme, *Sci. Prog.* 54 (1966) 367–385. <https://doi.org/https://www.jstor.org/stable/43425692>.
- [292] A. Jebali, S. Hekmatimoghaddam, A. Behzadi, I. Rezapour, B.H. Mohammadi, T. Jasemizad, S.A. Yasini, M. Javadzadeh, A. Amiri, M. Soltani, Z. Rezaei, N.

- Sedighi, M. Seyfi, M. Rezaei, M. Sayadi, Antimicrobial activity of nanocellulose conjugated with allicin and lysozyme, *Cellulose*. 20 (2013) 2897–2907. <https://doi.org/10.1007/s10570-013-0084-3>.
- [293] J.V. Edwards, N.T. Prevost, B. Condon, A. French, Q. Wu, Immobilization of lysozyme-cellulose amide-linked conjugates on cellulose I and II cotton nanocrystalline preparations, *Cellulose*. 19 (2012) 495–506. <https://doi.org/10.1007/s10570-011-9637-5>.
- [294] K.M.A. Uddin, H. Orelma, P. Mohammadi, M. Borghei, J. Laine, M. Linder, O.J. Rojas, Retention of lysozyme activity by physical immobilization in nanocellulose aerogels and antibacterial effects, *Cellulose*. 24 (2017) 2837–2848. <https://doi.org/10.1007/s10570-017-1311-0>.
- [295] S. Beck-Candanedo, M. Roman, D.G. Gray, Effect of Reaction Conditions on the Properties and Behavior of Wood Cellulose Nanocrystal Suspensions, *Biomacromolecules*. 6 (2005) 1048–1054. <https://doi.org/10.1021/bm049300p>.
- [296] I. Usov, R. Mezzenga, FiberApp: An open-source software for tracking and analyzing polymers, filaments, biomacromolecules, and fibrous objects, *Macromolecules*. 48 (2015) 1269–1280. <https://doi.org/10.1021/ma502264c>.
- [297] L.A. Morozova-Roche, J. Zurdo, A. Spencer, W. Noppe, V. Receveur, D.B. Archer, M. Joniau, C.M. Dobson, Amyloid fibril formation and seeding by wild-type human lysozyme and its disease-related mutational variants, *J. Struct. Biol.* 130 (2000) 339–351. <https://doi.org/10.1006/jsbi.2000.4264>.
- [298] I. Burgert, K. Frühmann, J. Keckes, P. Fratzl, S.E. Stanzl-Tschegg, Microtensile Testing of Wood Fibers Combined with Video Extensometry for Efficient Strain Detection, *Holzforschung*. 57 (2003) 661–664. <https://doi.org/10.1515/HF.2003.099>.
- [299] M. Schlesinger, W.Y. Hamad, M.J. MacLachlan, Optically tunable chiral nematic mesoporous cellulose films, *Soft Matter*. 15 (2015) 4686–4694. <https://doi.org/10.1039/C5SM00745C>.
- [300] B.L. Tardy, M. Ago, J. Guo, M. Borghei, T. Kämäräinen, O.J. Rojas, Optical Properties of Self-Assembled Cellulose Nanocrystals Films Suspended at Planar–Symmetrical Interfaces, *Small*. 13 (2017) 1702084. <https://doi.org/10.1002/smll.201702084>.
- [301] K.W. Klockars, B.L. Tardy, M. Borghei, A. Tripathi, L.G. Greca, O.J. Rojas, Effect of Anisotropy of Cellulose Nanocrystal Suspensions on Stratification, Domain Structure Formation, and Structural Colors, *Biomacromolecules*. 19 (2018) 2931–2943. <https://doi.org/10.1021/acs.biomac.8b00497>.
- [302] M.F. Mossuto, A. Dhulesia, G. Devlin, E. Frare, J.R. Kumita, P.P. de Laureto, M. Dumoulin, A. Fontana, C.M. Dobson, X. Salvatella, The Non-Core Regions of Human Lysozyme Amyloid Fibrils Influence Cytotoxicity, *J. Mol. Biol.* 402 (2010) 783–796. <https://doi.org/10.1016/j.jmb.2010.07.005>.
- [303] J. Milosevic, J. Petric, B. Jovic, B. Jankovic, N. Polovic, Exploring the potential of infrared spectroscopy in qualitative and quantitative monitoring of ovalbumin amyloid fibrillation, *Spectrochim. Acta Part A Mol. Biomol. Spectrosc.* 229 (2020) 117882. <https://doi.org/10.1016/j.saa.2019.117882>.
- [304] B. Wang, A. Walther, Self-Assembled, Iridescent, Crustacean-Mimetic Nanocomposites with Tailored Periodicity and Layered Cuticular Structure, *ACS Nano*. 9 (2015) 10637–10646. <https://doi.org/10.1021/acs.nano.5b05074>.
- [305] K. Yao, Q. Meng, V. Bulone, Q. Zhou, Flexible and Responsive Chiral Nematic

- Cellulose Nanocrystal/Poly(ethylene glycol) Composite Films with Uniform and Tunable Structural Color, *Adv. Mater.* 29 (2017) 1701323. <https://doi.org/10.1002/adma.201701323>.
- [306] Z. Dong, Z. Ye, Z. Zhang, K. Xia, P. Zhang, Chiral Nematic Liquid Crystal Behaviors of Core-shell Hybrid Rods Consisting of Chiral Cellulose Nanocrystals dressed with Non-Chiral Conformal Polymeric Skins, *Biomacromolecules*. 21 (2020) 2376–2390. <https://doi.org/10.1021/acs.biomac.0c00320>.
- [307] C. Schütz, J.R. Bruckner, C. Honorato-Rios, Z. Tosheva, M. Anyfantakis, J.P.F. Lagerwall, From Equilibrium Liquid Crystal Formation and Kinetic Arrest to Photonic Bandgap Films Using Suspensions of Cellulose Nanocrystals, *Crystals*. 10 (2020) 199. <https://doi.org/10.3390/cryst10030199>.
- [308] S. Beck, J. Bouchard, R. Berry, Controlling the Reflection Wavelength of Iridescent Solid Films of Nanocrystalline Cellulose, *Biomacromolecules*. 12 (2011) 167–172. <https://doi.org/10.1021/bm1010905>.
- [309] Y.P. Zhanga, V.P. Chodavarapua, A.G. Kirka, M.P. Andrews, Structured color humidity indicator from reversible pitch tuning in self-assembled nanocrystalline cellulose films, *Sensors Actuators B Chem.* 176 (2013) 692–697. <https://doi.org/10.1016/j.snb.2012.09.100>.
- [310] B. Zhu, R. Merindol, A. Benitez, B. Wang, A. Walther, Supramolecular Engineering of Hierarchically Self-assembled, Bioinspired, Cholesteric Nanocomposites formed by Cellulose Nanocrystals and Polymers, *ACS Appl. Mater. Interfaces*. 8 (2016) 11031–11040. <https://doi.org/10.1021/acsami.6b00410>.
- [311] B. Natarajan, J.W. Gilman, Bioinspired Bouligand cellulose nanocrystal composites: a review of mechanical properties, *Philos. Trans. R. Soc. A*. 376 (2018) 20170050. <https://doi.org/10.1098/rsta.2017.0050>.
- [312] K.J. De France, K.G. Yager, K.J.W. Chan, B. Corbett, E.D. Cranston, T. Hoare, Injectable Anisotropic Nanocomposite Hydrogels Direct in Situ Growth and Alignment of Myotubes, *Nano Lett.* 17 (2017) 6487–6495. <https://doi.org/10.1021/acs.nanolett.7b03600>.
- [313] B. Masschalck, C.W. Michiels, Antimicrobial properties of lysozyme in relation to foodborne vegetative bacteria, *Crit. Rev. Microbiol.* 29 (2003) 191–214. <https://doi.org/10.1080/713610448>.
- [314] S. Nikolov, M. Petrov, L. Lymperakis, M. Friák, C. Sachs, H.O. Fabritius, D. Raabe, J. Neugebauer, Revealing the design principles of high-performance biological composites using Ab initio and multiscale simulations: The example of lobster cuticle, *Adv. Mater.* 22 (2010) 519–526. <https://doi.org/10.1002/adma.200902019>.
- [315] P. Egan, R. Sinko, P.R. Leduc, S. Keten, The role of mechanics in biological and bio-inspired systems, *Nat. Commun.* 6 (2015) 7418. <https://doi.org/10.1038/ncomms8418>.
- [316] C. Zhang, D.A. McAdams, J.C. Grunlan, Nano/micro-manufacturing of bioinspired materials: A review of methods to mimic natural structures, *Adv. Mater.* 28 (2016) 6292–6321. <https://doi.org/10.1002/adma.201505555>.
- [317] K. Li, C.M. Clarkson, L. Wang, Y. Liu, M. Lamm, Z. Pang, Y. Zhou, J. Qian, M. Tajvidi, D.J. Gardner, H. Tekinalp, L. Hu, T. Li, A.J. Ragauskas, J.P. Youngblood, S. Ozcan, Alignment of Cellulose Nanofibers: Harnessing

- Nanoscale Properties to Macroscale Benefits, *ACS Nano*. 15 (2021) 3646–3673. <https://doi.org/10.1021/acsnano.0c07613>.
- [318] O.M. Vanderfleet, E.D. Cranston, Production routes to tailor the performance of cellulose nanocrystals, *Nat. Rev. Mater.* 6 (2021) 124–144. <https://doi.org/10.1038/s41578-020-00239-y>.
- [319] R. Kádár, S. Spirk, T. Nypelö, Cellulose Nanocrystal Liquid Crystal Phases: Progress and Challenges in Characterization Using Rheology Coupled to Optics, Scattering, and Spectroscopy, *ACS Nano*. 15 (2021) 7931–7945. <https://doi.org/10.1021/acsnano.0c09829>.
- [320] R. Xiong, A. Singh, S. Yu, S. Zhang, H. Lee, Y.G. Yingling, D. Nepal, T.J. Bunning, V. V. Tsukruk, Co-Assembling Polysaccharide Nanocrystals and Nanofibers for Robust Chiral Iridescent Films, *ACS Appl. Mater. Interfaces*. 12 (2020) 35345–35353. <https://doi.org/10.1021/acsmi.0c08571>.
- [321] K. Adstedt, E.A. Popenov, K.J. Pierce, R. Xiong, R. Geryak, V. Cherpak, D. Nepal, T.J. Bunning, V. V. Tsukruk, Chiral Cellulose Nanocrystals with Intercalated Amorphous Polysaccharides for Controlled Iridescence and Enhanced Mechanics, *Adv. Funct. Mater.* 30 (2020) 2003597. <https://doi.org/10.1002/adfm.202003597>.
- [322] B.L. Tardy, J.J. Richardson, L.G. Greca, J. Guo, H. Ejima, O.J. Rojas, Exploiting Supramolecular Interactions from Polymeric Colloids for Strong Anisotropic Adhesion between Solid Surfaces, *Adv. Mater.* 32 (2020) 1906886. <https://doi.org/10.1002/adma.201906886>.
- [323] L.G. Greca, K.J. De France, J. Majoinen, N. Kummer, O.I.V. Luotonen, S. Campioni, O.J. Rojas, G. Nyström, B.L. Tardy, Chitin-amyloid synergism and their use as sustainable structural adhesives, *J. Mater. Chem. A*. 9 (2021) 19741–19753. <https://doi.org/10.1039/d1ta03215a>.
- [324] M. Kim, K. Pierce, M. Krecker, D. Bukharina, K. Adstedt, D. Nepal, T. Bunning, V. V. Tsukruk, Monolithic Chiral Nematic Organization of Cellulose Nanocrystals under Capillary Confinement, *ACS Nano*. 15 (2021) 19418–19429. <https://doi.org/10.1021/acsnano.1c05988>.
- [325] L. Lemetti, J. Tersteegen, J. Sammaljärvi, A.S. Aranko, M.B. Linder, Recombinant Spider Silk Protein and Delignified Wood Form a Strong Adhesive System, *ACS Sustain. Chem. Eng.* 10 (2022) 552–561. <https://doi.org/10.1021/acssuschemeng.1c07043>.
- [326] O.I.V. Luotonen, L.G. Greca, G. Nyström, J. Guo, J.J. Richardson, O.J. Rojas, B.L. Tardy, Benchmarking supramolecular adhesive behavior of nanocelluloses, cellulose derivatives and proteins, *Carbohydr. Polym.* 292 (2022) 119681. <https://doi.org/10.1016/j.carbpol.2022.119681>.
- [327] X. Liu, C. Liang, X. Zhang, J. Li, J. Huang, L. Zeng, Z. Ye, B. Hu, W. Wu, Amyloid fibril aggregation: An insight into the underwater adhesion of barnacle cement, *Biochem. Biophys. Res. Commun.* 493 (2017) 654–659. <https://doi.org/10.1016/j.bbrc.2017.08.136>.
- [328] C. Zhong, T. Gurry, A.A. Cheng, J. Downey, Z. Deng, C.M. Stultz, T.K. Lu, Strong underwater adhesives made by self-assembling multi-protein nanofibres, *Nat. Nanotechnol.* 9 (2014) 858–866. <https://doi.org/10.1038/nnano.2014.199>.
- [329] D.E. Barlow, G.H. Dickinson, B. Orihuela, J.L. Kulp, D. Rittschof, K.J. Wahl, Characterization of the adhesive plaque of the barnacle *Balanus amphitrite*:


- Amyloid-like nanofibrils are a major component, *Langmuir*. 26 (2010) 6549–6556. <https://doi.org/10.1021/la9041309>.
- [330] A.S. Mostaert, M.J. Higgins, T. Fukuma, F. Rindi, S.P. Jarvis, Nanoscale mechanical characterisation of amyloid fibrils discovered in a natural adhesive, *J. Biol. Phys.* 32 (2006) 393–401. <https://doi.org/10.1007/s10867-006-9023-y>.
- [331] R.S. Jacob, S. Das, N. Singh, K. Patel, D. Datta, S. Sen, S.K. Maji, Amyloids Are Novel Cell-Adhesive Matrices, in: K. Chattopadhyay, S.C. Basu (Eds.), *Biochem. Biophys. Roles Cell Surf. Mol.*, Springer Singapore, 2018: pp. 79–97. https://doi.org/10.1007/978-981-13-3065-0_7.
- [332] L. Comez, P.L. Gentili, M. Paolantoni, A. Paciaroni, P. Sassi, Heat-induced self-assembling of BSA at the isoelectric point, *Int. J. Biol. Macromol.* 177 (2021) 40–47. <https://doi.org/10.1016/j.ijbiomac.2021.02.112>.
- [333] M. Bhattacharya, N. Jain, S. Mukhopadhyay, Insights into the mechanism of aggregation and fibril formation from bovine serum albumin, *J. Phys. Chem. B.* 115 (2011) 4195–4205. <https://doi.org/10.1021/jp111528c>.
- [334] N.K. Holm, S.K. Jespersen, L. V. Thomassen, T.Y. Wolff, P. Sehgal, L.A. Thomsen, G. Christiansen, C.B. Andersen, A.D. Knudsen, D.E. Otzen, Aggregation and fibrillation of bovine serum albumin, *Biochim. Biophys. Acta - Proteins Proteomics.* 1774 (2007) 1128–1138. <https://doi.org/10.1016/j.bbapap.2007.06.008>.
- [335] F.G. Pearce, S.H. Mackintosh, J.A. Gerrard, Formation of amyloid-like fibrils by ovalbumin and related proteins under conditions relevant to food processing, *J. Agric. Food Chem.* 55 (2007) 318–322. <https://doi.org/10.1021/jf062154p>.
- [336] I. Usov, J. Adamcik, R. Mezzenga, Serum albumin fibrils: Morphology and statistical analysis, *Faraday Discuss.* 166 (2013) 151–162. <https://doi.org/10.1039/c3fd00083d>.
- [337] A. Aliyan, N.P. Cook, A.A. Martí, Interrogating Amyloid Aggregates using Fluorescent Probes, *Chem. Rev.* 119 (2019) 11819–11856. <https://doi.org/10.1021/acs.chemrev.9b00404>.
- [338] E. van der Linden, P. Venema, Self-assembly and aggregation of proteins, *Curr. Opin. Colloid Interface Sci.* 12 (2007) 158–165. <https://doi.org/10.1016/j.cocis.2007.07.010>.
- [339] D.C. Carter, J.X. Ho, Structure of serum albumin, *Adv. Protein Chem.* 45 (1994) 153–176. [https://doi.org/10.1016/S0065-3233\(08\)60640-3](https://doi.org/10.1016/S0065-3233(08)60640-3).
- [340] J.F. Revol, H. Bradford, J. Giasson, R.H. Marchessault, D.G. Gray, Helicoidal self-ordering of cellulose microfibrils in aqueous suspension, *Int. J. Biol. Macromol.* 14 (1992) 170–172. [https://doi.org/10.1016/S0141-8130\(05\)80008-X](https://doi.org/10.1016/S0141-8130(05)80008-X).
- [341] C. Honorato-Rios, J.P.F. Lagerwall, Interrogating helical nanorod self-assembly with fractionated cellulose nanocrystal suspensions, *Commun. Mater.* 1 (2020) 69. <https://doi.org/10.1038/s43246-020-00069-z>.
- [342] F. Azzam, L. Heux, B. Jean, Adjustment of the Chiral Nematic Phase Properties of Cellulose Nanocrystals by Polymer Grafting, *Langmuir*. 32 (2016) 4305–4312. <https://doi.org/10.1021/acs.langmuir.6b00690>.
- [343] M.D. Xue, T. Kimura, J.F. Revol, D.G. Gray, Effects of ionic strength on the isotropic-chiral nematic phase transition of suspensions of cellulose crystallites, *Langmuir*. 12 (1996) 2076–2082. <https://doi.org/10.1021/la950133b>.
- [344] G. Guidetti, H. Sun, A. Ivanova, B. Marelli, B. Frka-Petescic, Co-Assembly of

- Cellulose Nanocrystals and Silk Fibroin into Photonic Cholesteric Films, *Adv. Sustain. Syst.* 5 (2021) 2000272. <https://doi.org/10.1002/adsu.202000272>.
- [345] H. Thérien-Aubin, A. Lukach, N. Pitch, E. Kumacheva, Structure and properties of composite films formed by cellulose nanocrystals and charged latex nanoparticles, *Nanoscale*. 7 (2015) 6612–6618. <https://doi.org/10.1039/c5nr00660k>.
- [346] C. Schütz, M. Agthe, A.B. Fall, K. Gordeyeva, V. Guccini, M. Salajková, T.S. Plivelic, J.P.F. Lagerwall, G. Salazar-Alvarez, L. Bergström, Rod Packing in Chiral Nematic Cellulose Nanocrystal Dispersions Studied by Small-Angle X-ray Scattering and Laser Diffraction, *Langmuir*. 31 (2015) 6507–6513. <https://doi.org/10.1021/acs.langmuir.5b00924>.
- [347] C. Honorato-Rios, A. Kuhnhold, J.R. Bruckner, R. Dannert, T. Schilling, J.P.F. Lagerwall, Equilibrium Liquid Crystal Phase Diagrams and Detection of Kinetic Arrest in Cellulose Nanocrystal Suspensions, *Front. Mater.* 3 (2016) 21. <https://doi.org/10.3389/fmats.2016.00021>.
- [348] Y. Mao, M.E. Cates, H.N.W. Lekkerkerker, Depletion stabilization by semidilute rods, *Phys. Rev. Lett.* 75 (1995) 4548–4551. <https://doi.org/10.1103/PhysRevLett.75.4548>.
- [349] P.J. Flory, Phase equilibria in solutions of rod-like particles, *Proc. R. Soc. A.* 234 (1956) 73–89. <https://doi.org/10.1098/rspa.1956.0016>.
- [350] C.D. Edgar, D.G. Gray, Influence of dextran on the phase behavior of suspensions of cellulose nanocrystals, *Macromolecules*. 35 (2002) 7400–7406. <https://doi.org/10.1021/ma0204195>.
- [351] S. Beck-Candanedo, D. Viet, D.G. Gray, Induced phase separation in low-ionic-strength cellulose nanocrystal suspensions containing high-molecular-weight blue dextrans, *Langmuir*. 22 (2006) 8690–8695. <https://doi.org/10.1021/la061310j>.
- [352] S. Asakura, F. Oosawa, On interaction between two bodies immersed in a solution of macromolecules, *J. Chem. Phys.* 22 (1954) 1255–1256. <https://doi.org/10.1063/1.1740347>.
- [353] B. V. Derjaguin, Theory of the Stability of Strongly Charged Lyophobic Sol and of the Adhesion of Strongly Charged Particles in Solutions of Electrolytes, *Acta Phys. Chim. U. R. S. S.* 14 (1941) 633–662.
- [354] E.J.W. Verwey, Theory of the stability of lyophobic colloids, *J. Phys. Chem.* 51 (1947) 631–636. <https://doi.org/https://doi.org/10.1021/j150453a001>.
- [355] X. Xing, L. Hua, T. Ngai, Depletion versus stabilization induced by polymers and nanoparticles: The state of the art, *Curr. Opin. Colloid Interface Sci.* 20 (2015) 54–59. <https://doi.org/10.1016/j.cocis.2014.11.012>.
- [356] M.P.B. Van Bruggen, F.M. Van Der Kooij, H.N.W. Lekkerkerker, Liquid crystal phase transitions in dispersions of rod-like colloidal particles, *J. Phys. Condens. Matter*. 8 (1996) 9451–9456. <https://doi.org/10.1088/0953-8984/8/47/044>.
- [357] Z. Gu, M. Lu, K. Feng, Z. Jin, The different composites of cellulose nanocrystals with d- or l-histidine, *Nanoscale*. 13 (2021) 8174–8180. <https://doi.org/10.1039/d1nr00946j>.
- [358] X. Mu, D.G. Gray, Droplets of cellulose nanocrystal suspensions on drying give iridescent 3-D “coffee-stain” rings, *Cellulose*. 22 (2015) 1103–1107. <https://doi.org/10.1007/s10570-015-0569-3>.

- [359] R.D. Deegan, O. Bakajin, T.F. Dupont, G. Huber, S.R. Nagel, T.A. Witten, Capillary flow as the cause of ring stains from dried liquid drops, *Nature*. 389 (1997) 827–829. <https://doi.org/https://doi.org/10.1038/39827>.
- [360] T. Still, P.J. Yunker, A.G. Yodh, Surfactant-induced Marangoni eddies alter the coffee-rings of evaporating colloidal drops, *Langmuir*. 28 (2012) 4984–4988. <https://doi.org/10.1021/la204928m>.
- [361] M. Parsa, S. Harmand, K. Sefiane, M. Bigerelle, R. Deltombe, Effect of substrate temperature on pattern formation of nanoparticles from volatile drops, *Langmuir*. 31 (2015) 3354–3367. <https://doi.org/10.1021/acs.langmuir.5b00362>.
- [362] S. Beisl, J. Adamczyk, A. Friedl, H. Ejima, Confined evaporation-induced self-assembly of colloidal lignin particles for anisotropic adhesion, *Colloids Interface Sci. Commun.* 38 (2020) 100306. <https://doi.org/10.1016/j.colcom.2020.100306>.
- [363] A.D. Roberts, W. Finnigan, P.P. Kelly, M. Faulkner, R. Breitling, E. Takano, N.S. Scrutton, J.J. Blaker, S. Hay, Non-covalent protein-based adhesives for transparent substrates—bovine serum albumin vs. recombinant spider silk, *Mater. Today Bio.* 7 (2020) 100068. <https://doi.org/10.1016/j.mtbio.2020.100068>.
- [364] J. Majoinen, E. Kontturi, O. Ikkala, D.G. Gray, SEM imaging of chiral nematic films cast from cellulose nanocrystal suspensions, *Cellulose*. 19 (2012) 1599–1605. <https://doi.org/10.1007/s10570-012-9733-1>.

Curriculum Vitae

Nico Kummer

 Swiss citizen, born 13 September 1992 in Bern



Higher Education

Empa / ETH Zürich: Doctorate

Dübendorf / Zürich (CH)

2019-2023 Preparation of antimicrobial lysozyme amyloid fibrils, characterization (AFM, spectroscopies: fluorescence, FTIR, UV-vis, CD), studying amyloid-nanocellulose interactions and self-assembly, project management, scientific communication, supervision of 4 students.

Paul Scherrer Institute / ETH Zürich: Master Thesis

Villigen / Zürich (CH)

2017-2018 Characterization of interactions between water and polysaccharide, their dynamics and structure with neutron scattering techniques.

National University of Singapore: Student Exchange

Singapore (SIN)

2016 Following courses in Food Science and Chemistry

ETH Zürich: Master in Food Science

Zürich (CH)

2015-2018 Major: Food Process Engineering Minor: Food Chemistry
GPA: 5.58/6

ETH Zürich: Bachelor in Food Science

Zürich (CH)

2012-2015 GPA: 5.18/6

Professional Experience

Bühler Insect Technology Solutions: Internship

Wuxi (PRC)

2018-2019 Support of the R&D team with the establishment of lab-scale processes to optimize insect processing into a protein-rich meal.

ETH Zürich: Research Assistant

Zürich (CH)

2018-2019 Analysis of phytochemicals in various types of cereals, including method development and optimization, HPLC analysis and data analysis.

ETH Zürich: Teaching Assistant

Zürich (CH)

2015 & 2017 Tutoring the lecture "Selected Topics in Physical Chemistry", correction of the weekly exercise sheets, exam correction and grading.

Skills

Software: MS Office, Origin, Adobe Illustrator, Python (basic), Matlab (basic)

Soft Skills: Analytical thinking, Problem-solving, Teamwork, Leadership, Discipline, Communication

Languages: German (native), English (fluent), French (advanced), Mandarin (advanced), Russian (basic)

Activities

Sports: I am an outdoorsy person and love road cycling, running, hiking and ski tours

Food: As a trained food scientist I enjoy cooking and eating a lot, especially after sports

Languages: I am a hobby linguist trying to speak some more or less exotic languages

Publications (as of 23 November 2023)

Kummer, N.; Wu, T.; De France, K. J.; Zuber, F.; Ren, Q.; Fischer, P.; Campioni, S.; Nyström, G. Self-Assembly Pathways and Antimicrobial Properties of Lysozyme in Different Aggregation States. *Biomacromolecules* 2021, 22 (10), 4327–4336.

Kummer, N.; Giacomini, C. E.; Fischer, P.; Campioni, S.; Nyström, G. Amyloid Fibril-Nanocellulose Interactions and Self-Assembly. *J. Colloid Interface Sci.* 2023, 641, 338–347.

Kummer, N.; Huguenin-Elie, L.; Zeller, A.; Chandorkar, Y.; Schoeller, J.; Zuber, F.; Ren, Q.; Sinha, A.; De France, K.; Fischer, P.; Campioni, S.; Nyström, G. 2D Foam Film Coating of Antimicrobial Lysozyme Amyloid Fibrils onto Cellulose Nanopapers. *Nanoscale Adv.* 2023, 5, 5276–5285.

as co-author

De France, K. J.; **Kummer, N.;** Ren, Q.; Campioni, S.; Nyström, G. Assembly of Cellulose Nanocrystal-Lysozyme Composite Films with Varied Lysozyme Morphology. *Biomacromolecules* 2020, 21 (12), 5139–5147.

Wu, T.; **Kummer, N.;** France, K. J. De; Campioni, S.; Zeng, Z.; Siqueira, G.; Dong, J.; Nyström, G. Nanocellulose-Lysozyme Colloidal Gels via Electrostatic Complexation. *Carbohydr. Polym.* 2021, 251, 117021.

Bergfreund, J.; Diener, M.; Geue, T.; Nussbaum, N.; **Kummer, N.;** Bertsch, P.; Nyström, G.; Fischer, P. Globular Protein Assembly and Network Formation at Fluid Interfaces: Effect of Oil. *Soft Matter* 2021, 17 (6), 1692–1700.

Greca, L. G.; De France, K. J.; Majoinen, J.; **Kummer, N.;** Luotonen, O. I. V.; Campioni, S.; Rojas, O. J.; Nyström, G.; Tardy, B. L. Chitin-Amyloid Synergism and Their Use as Sustainable Structural Adhesives. *J. Mater. Chem. A* 2021, 9 (35), 19741–19753.

Zeng, Z.; Mavrona, E.; Sacré, D.; **Kummer, N.;** Cao, J.; Müller, L. A. E.; Hack, E.; Zolliker, P.; Nyström, G. Terahertz Birefringent Biomimetic Aerogels Based on Cellulose Nanofibers and Conductive Nanomaterials. *ACS Nano* 2021, 15 (4), 7451–7462.

Wu, N.; Zeng, Z.; **Kummer, N.**; Han, D.; Zenobi, R.; Nyström, G. Ultrafine Cellulose Nanofiber-Assisted Physical and Chemical Cross-Linking of MXene Sheets for Electromagnetic Interference Shielding. *Small Methods* **2021**, *5*, 2100889.

Mishra, K.; Kohler, L.; **Kummer, N.**; Zimmermann, S.; Ehrenguber, S.; Kämpf, F.; Dufour, D.; Nyström, G.; Fischer, P.; Windhab, E. J. Rheology of Cocoa Butter. *J. Food Eng.* **2021**, *305*, 110598.

Mishra, K. S.; Kämpf, F.; Ehrenguber, S.; Merkel, J.; **Kummer, N.**; Pauer, R.; Fischer, P.; Windhab, E. The Rheology and Foamability of Crystal-Melt Suspensions Composed of Triacylglycerols. *Soft Matter* **2022**, *accepted*.

Severini, L.; De France, K. J.; Sivaraman, D.; **Kummer, N.**; Nyström, G. Biohybrid Nanocellulose–Lysozyme Amyloid Aerogels via Electrostatic Complexation. *ACS Omega* **2022**, *7* (1), 578–586.

Mishra, K.; **Kummer, N.**; Bergfreund, J.; Kämpf, F.; Bertsch, P.; Pauer, R.; Nyström, G.; Fischer, P.; Windhab, E. J. Controlling Lipid Crystallization across Multiple Length Scales by Directed Shear Flow. *J. Colloid Interface Sci.* **2023**, *630*, 731–741.

De France, K. J.; **Kummer, N.**; Campioni, S.; Nyström, G. Phase Behavior, Self-Assembly, and Adhesive Potential of Cellulose Nanocrystal-Bovine Serum Albumin Amyloid Composites. *ACS Appl. Mater. Interfaces* **2023**, *15* (1), 1958–1968.

Benselfelt, T.; **Kummer, N.**; Nordenström, M.; Fall, A. B.; Nyström, G.; Wågberg, L. The Colloidal Properties of Nanocellulose. *ChemSusChem* **2023**, e202201955.

Sinha, A.; **Kummer, N.**; Wu, T.; De France, K. J.; Pinotsi, D.; Thoma, J. L.; Fischer, P.; Campioni, S.; Nyström, G. Nanocellulose Aerogels as 3D Amyloid Templates. *Nanoscale* **2023**, *15*, 17785–17792.

Conferences

Kummer, N.; Wu, T.; De France, K. J.; Zuber, F.; Ren, Q.; Fischer, P.; Campioni, S.; Nyström, G. Self-Assembly of Lysozyme Aggregates With Enhanced Antimicrobial Activity (Talk). *ACS Spring Meeting 2022*.

Kummer, N.; Huguenin-Elie, L.; Fischer, P.; Campioni, S.; Nyström, G. Amyloid stabilized air-water interfaces for functional coatings (Poster). *ACS Spring Meeting 2022*.

Kummer, N.; Giacomini, C. E.; Fischer, P.; Campioni, S.; Nyström, G. Nanocellulose interactions with different protein aggregates (Talk). *Nanocellulose Days at Monte Verità 2022*.

Kummer, N.; Giacomini, C. E.; Fischer, P.; Campioni, S.; Nyström, G. Amyloid-Nanocellulose Interactions and Self-assembly (Talk). *MRS Fall Meeting 2022*.